Self-Assembly of Amphiphilic Oligophosphates into Supramolecular Polymers

Inauguraldissertation
der Philosophisch-naturwissenschaftlichen Fakultät
der Universität Bern

vorgelegt von
Edouard Ehret
von Jongny

Leiter der Arbeit:
Prof. Dr. Robert Häner
Departement für Chemie, Biochemie und Pharmazie der Universität Bern

Self-Assembly of Amphiphilic Oligophosphates into Supramolecular Polymers

Inauguraldissertation
der Philosophisch-naturwissenschaftlichen Fakultät
der Universität Bern

vorgelegt von
Edouard Ehret
von Jongny

Leiter der Arbeit:
Prof. Dr. Robert Häner
Departement für Chemie, Biochemie und Pharmazie der Universität Bern

Von der Philosophisch-naturwissenschaftlichen Fakultät angenommen.

Bern, 28. October 2024

Der Dekan
Prof. Dr. Jean-Louis Reymond

Acknowledgements

First of all, I would like to sincerely thank Prof. Dr. Robert Häner for his supervision over the past four years. I greatly appreciated your constant availability for discussions about ongoing projects and your continuous encouragement.

I extend my gratitude to Prof. Dr. Jonathan Hall and Prof. Dr. Philippe Renaud for agreeing to be part of the jury and for dedicating their time to evaluate my work.

Additionally, I would like to thank the cryo-EM specialists, Prof. Dr. Benoît Zuber and Dr. Ioan Iacovache, for their valuable contributions to this research. Their experiments provided detailed insights into the morphology of the cholane-derived self-assemblies.

Thank you to all former and current members of the Häner group. From the very beginning, I felt warmly welcomed, and I carry only fond memories from our time together, both in the lab and outside of it. A special thanks to Dr. Simon Langenegger for your mentoring over the years, our many constructive discussions, and, more importantly, your friendship. I would also like to express my gratitude to Jan and Isabelle for the countless hours spent Aareböötle together. During my time in the Häner group, I had the privilege of collaborating with three talented students. Thank you, Léon, Marc, and Silène, for your dedication and contributions to this thesis.

I would like to express my gratitude to the DCBP staff members, including all in-house services, as well as for the financial support provided by the Swiss National Science Foundation (SNF) and the University of Bern.

A huge thank you to all the amazing people I have met over the past four years in Olten and Bern, whom I am lucky enough to call friends! Among all of you, I have to give a special shoutout to Keir and Neil, who have supported me since day one and ensured that this chapter of my life was filled with great memories and anything but sober. Another heartfelt thanks to Célia for the incredible friendship we've developed

over the past four years and all the hilarious moments we've shared.

Thank you, Nicolas, Sylvain, and Cedric, for all the memories we've created throughout our studies. Life may have pushed us in different directions, but we've always found a way to reconnect and share important moments.

I am deeply grateful to my long-time friends, who are too numerous to name here, but who will undoubtedly recognise themselves. Thanks to the proximity of my studies to home, I could always count on you whenever I needed support, and your presence throughout this journey has meant the world to me.

Enfin, mais non des moindres, je tiens à remercier mes parents et mes grands-parents pour leur soutien et leur patience à mon égard depuis le premier jour jusqu'à aujourd'hui. Rien de tout cela n'aurait été possible sans vous. Je remercie également mon frère, Xavier, ma petite sœur, Élodie, et son mari, Frédéric, pour votre soutien constant, votre amour, et votre humour un brin particulier.

If we knew what it was we were doing,
it would not be called research,
would it?
- Albert Einstein

Table of Contents

Summary

Supramolecular polymers are a unique class of materials. They offer dynamic and reversible characteristics which separate them from conventional polymers.

Their self-assembling behavior, as well as their singular properties, are described in Chapter 1. This introduction, with a focus on the self-assembly of oligomers in aqueous media, explores the possibility of introducing chemical modifications into oligomers to form functionalized supramolecular polymers. The introduction is followed by elucidating the aim of the thesis in Chapter 2.

Chapter 3 investigates the incorporation of a carbohydrate moiety into phosphodiester-linked pyrene oligomers. The synthesis and self-assembly behavior of several carbohydrate-modified pyrene oligomers are described. The controlled aggregation of the oligomers, resulting in the formation of two distinct supramolecular polymers whose morphology was dictated by the pyrene isomer present in the oligomer construct.

The Chapter 4 explores the possibility of observing the self-assembly of oligomers lacking intramolecular π-π interactions, in aqueous media. The synthesis of a small library of cholane-PAH-cholane oligomers (CPC) and their self-assembly properties and morphologies are detailed. The supramolecular assembly of the different CPCs resulted in the observation of three distinct nanostructures - sheets, tubes and worms.

Chapter 5 describes the light-harvesting properties of the different phenanthrene CPC assemblies, in the presence of the pyrene CPCs, under different aggregation conditions. The efficiency of the different donor-acceptor couples are discussed and the most efficient system is presented.

The final chapter provides an overall conclusion on the work performed and highlights potential future perspectives.

Chapter 1

Introduction

1.1 Supramolecular Polymers

Supramolecular polymers consist of recurring monomeric units held together through directional, non-covalent interactions rather than traditional covalent bonds. This fundamental distinction confers several unique properties to the supramolecular polymers, distinguishing them from their covalent counterparts.[1–4] The non-covalent interactions, such as van der Waals forces, hydrophobic effects, hydrogen-bonding, and π-π interactions, are inherently weaker than covalent bonds, making them more reversible. This reversibility gives supramolecular polymers (SPs) an adaptive and dynamic nature, leading to self-healing, recyclable, and stimuli-responsive behaviors.[5–9]

Recent progress in materials science has been aimed towards finding smart or intelligent materials that can change their behavior by responding to external stimuli such as light, pH, temperature, force, electric fields, *etc.*[10–13] These innovative materials play an essential role in many fields, such as biosensing, automobiles, construction, the aviation industry, and electronic and medical applications.[14–19] The versatility offered by supramolecular polymers makes them ideal candidates for such applications.

A notable example of a smart self-healable material was presented by Weder and coworkers, who have demonstrated the formation of optically responsive supramolecular polymer glass based on a tri-functional monomer (see Figure 1.1a).[20] They demonstrated that the self-assembly process is driven by strong hydrogen-bonding dimers between the ureido-4-pyrimidinone (UPy) moieties present in the monomer, forming a clear glassy material (Figure 1.1c). The supramolecular nature of the material gave it high stiffness when glassy, along with viscoelastic behavior, coating, and adhesive properties when melted.

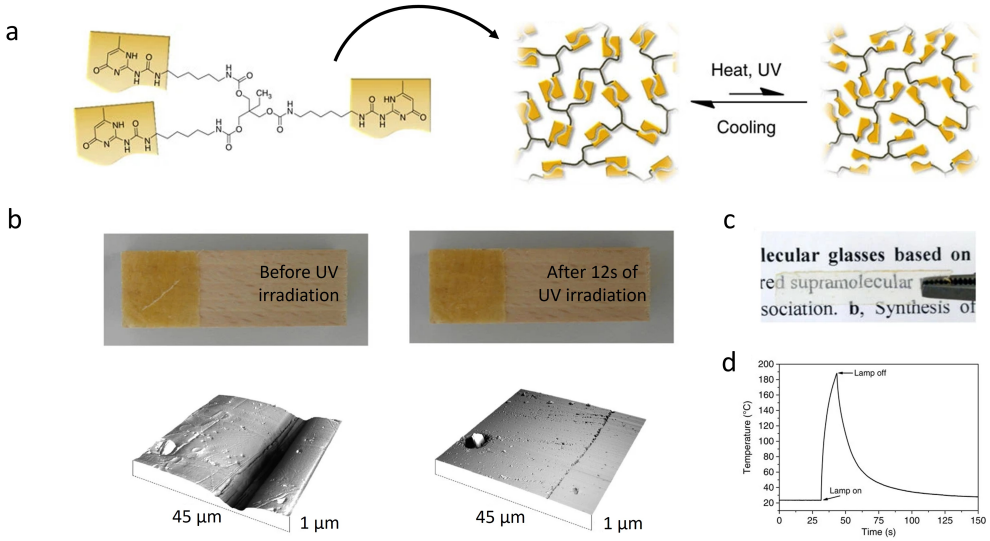

Figure 1.1: (a) Chemical structure of the $(UPy)_3TMP$ monomer and a schematic representation of the supramolecular network formed after self-assembly. The monomer is composed of three ureido-4-pyrimidinone (UPy) moieties highlighted in yellow and a 1,1,1-tris(hydroxymethyl)propane (TMP) center. (b) Pictures (top) and AFM images (bottom) showing the optical healing of a damaged coating after exposure to UV light for 12 seconds. The film present on top was found to be 300 µm thin, while the one determined by AFM was 45 µm. (c) Picture of the $(UPy)_3TMP$ film. (d) Illustration taken and adapted from ref.[20]

The self-healing nature of the supramolecular glass was demonstrated by intentionally cutting the glass before exposing it to ultraviolet (UV) irradiation. Atomic force microscopy (AFM) revealed the rapid disappearance of the cut after a 12-second exposure time (Figure 1.1b). The transition to glass was shown to take place around 105 °C. The optical responsiveness depended on converting optical energy into heat through the non-radiative relaxation of the excited state.

Extensive research has also been conducted to implement SPs in the development of new catalysts and catalytic platforms. The self-assembly driven by metal coordination bonds has led to the formation of acid-base,[21] redox[22,23] and photocleavage-sensitive[24] metallosupramolecular polymers. In the presence of a lanthanide core, the metallosupramolecular polymers were shown to be luminescent while being sensitive to heat, pH, metal ion competition, and even pressure, allowing for the tuning of metal ion luminescence.[25] Additionally, the possibility of combining aromatic compounds with these metallosupramolecular polymers to absorb specific wavelengths has been studied, leading to the formation of donor-acceptor systems in which energy transfer or charge transfer was observed.[26–29]

Many biological systems and natural processes also rely on supramolecular chemistry to function.[30–32] All of the previously mentioned SPs are formed and stable in organic solvents, making them difficult to incorporate into biocompatible materials or use in biological applications. The study of SPs in aqueous media is therefore of particular interest in diagnostic, drug delivery, and/or medical applications for example.[33,34] An important supramolecular system is the guest-host complex - the most studied ones include cyclodextrin- and calixarene-based supramolecular polymers.[35–39] These amphiphilic, cyclic oligomers are composed of a hydrophobic cavity and a hydrophilic rim that can be chemically modified and are used in biomedical applications, catalysis, and purification. An example of a cyclodextrin (CD)-based supramolecular polymer in aqueous media was reported by Chen, Huang, and co-workers.[40] It was shown that their monomer, composed of β-CD (host) linked to the anticancer drug, camptothecin (CPT, guest), *via* a disulfide bond (CD-SS-CPT in Figure 1.2), self-assembles linearly into rod-like fibers. However, through co-assembly with CPT-PEG-NOTA and CPT-PEG-RGD, the system self-assembles into micelles or nanoparticles that can be used for radio-labeling and drug delivery (see Figure 1.2).

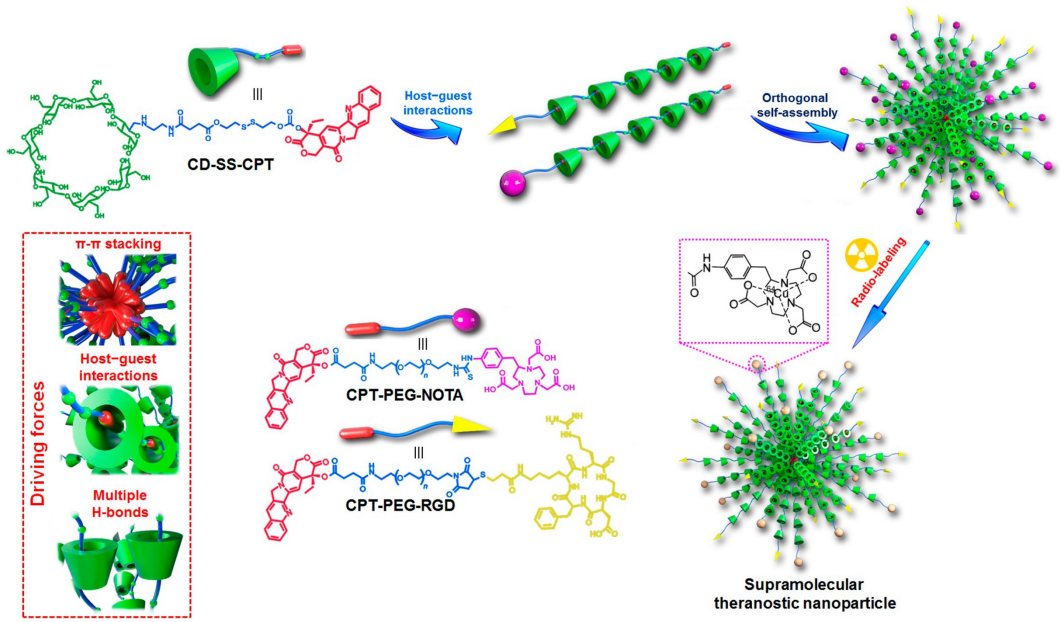

Figure 1.2: Schematic illustration showing the self-assembly of CD-SS-CPT into rod-like supramolecular polymers as well as co-polymers formed by CD-SS-CPT and other functionalized building blocks: CPT-PEG-NOTA and/or CPT-PEG-RGD. Illustration adapted from ref.[40]

Transmission electron microscopy (TEM) data revealed the supramolecular self-

assemblies, while *in vitro* and *in vivo* experiments showed increased anticancer efficacy of CPT along with an anti-metastasis effect. Multiple hydrogen-bonding, host-guest interactions, and π-π stacking can explain the driving forces involved in the formation of these supramolecular polymers.

The amphiphilic behavior of monomeric units is crucial for studying supramolecular polymers in aqueous media, where they create a bridge between the hydrophobic core and the hydrophilic environment. This has led our group to focus our research on the self-assembly of supramolecular polymers from phosphodiester-linked amphiphilic oligomers. A wide variety of polyaromatic hydrocarbon (PAH) building blocks, such as pyrene,[41,42] phenanthrene[43] and squarine,[44] were used in developing these supramolecular polymers. These were initially incorporated into DNA single strands, which have been shown to hybridize and self-assemble into a multitude of different morphologies, ranging from vesicles[45] to ribbons,[46] and even a rare and remarkable aggregation pattern: asterosomes.[47] Further experimentation demonstrated that the DNA bases present in the construct were not necessary to observe self-assembly of the oligomer. The first oligoarenotide to exhibit self-assembly behavior was composed of a pyrene heptamer (see Figure 1.3a) which, under TEM, revealed the presence of "extended structures of a relatively uniform thickness (4–6 nm) and variable length (up to 200 nm)".[48] This discovery led to interesting and surprising results - several different morphologies were observed, including nanosheets and nanotoroids, which had not been previously observed with PAH-modified DNA. Once again, the nature of the building block and its substitutions were key to observing different kinds of self-assembled supramolecular polymers. Work performed with 1,6-disubstituted pyrene trimers has led to the observation of nanosheets,[49] while nanofibers were detected when working with 1,8-disubstituted pyrene[50] and 3,6-disubstituted phenanthrene[51] (see Figure 1.3b). A unique stimuli-responsive supramolecular polymer composed of azobenzene trimers was shown to undergo photoisomerization, resulting in a switch between nanosheets and nanotoroids upon irradiation (see Figure 1.3c).[52]

All these supramolecular polymers were assembled *via* a controlled cooling process. The self-assembly of the oligomers is mainly driven by π-π interactions between the hydrophobic PAHs, and the interactions between the phosphodiester groups and the medium. The sample is first heated to elevated temperatures (70 to 80 °C) to ensure reproducibility of the self-assembly process and complete disaggregation. After stabilization at this temperature, the sample is cooled using a controlled cooling gradient (*e.g.*, 0.5 °C/min). The cooling gradient is an essential factor for the self-assembly process, as it can lead to the formation of either the thermodynamically controlled supramolecular polymer or the kinetically controlled polymer.[53]

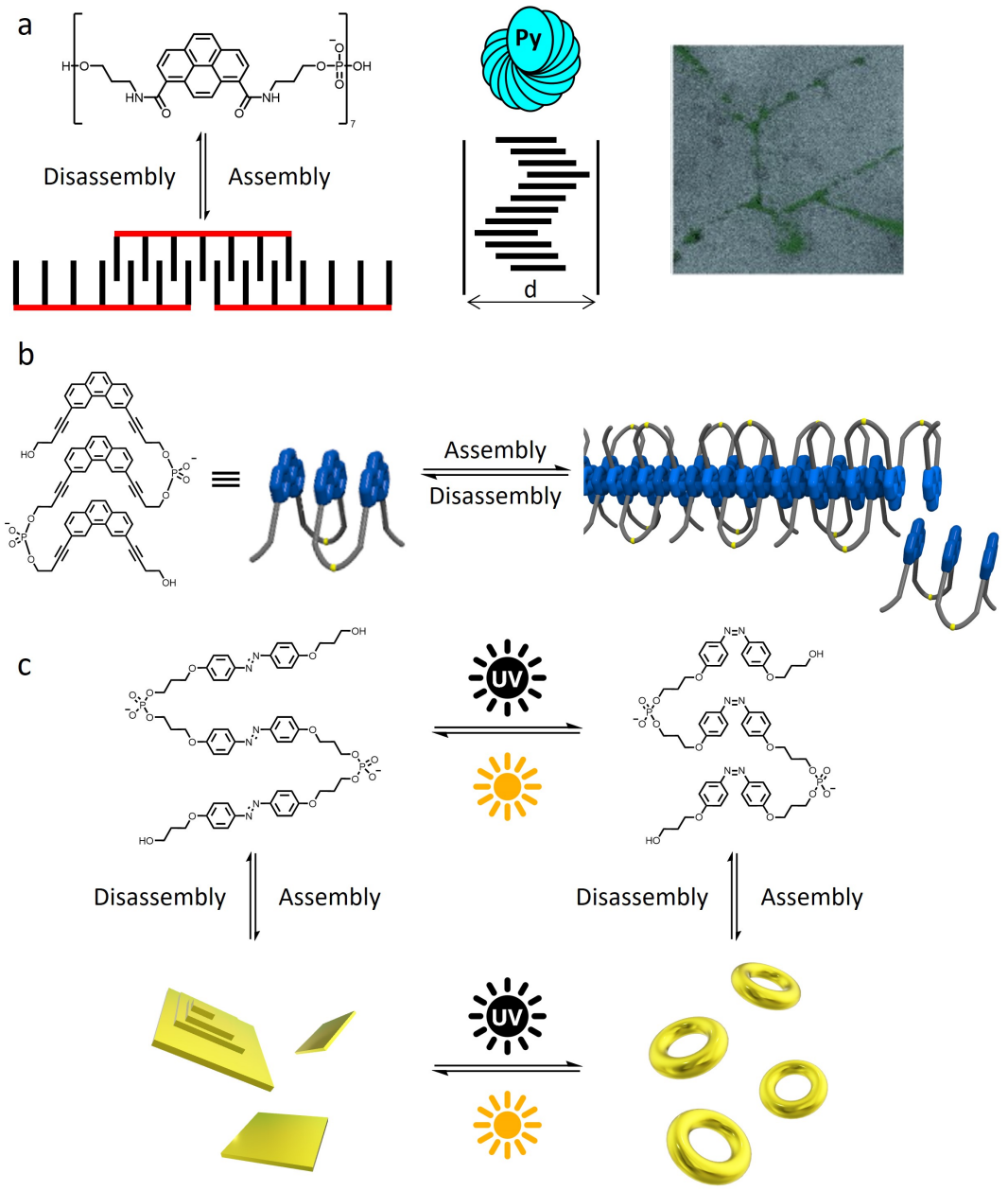

Figure 1.3: Schematic illustration of an idealized self-assembly process with: (a) A 1,8-disubstituted pyrene heptamer; (b) A 3,6-disubstituted phenanthrene trimer; (c) An azobenzene trimer, into supramolecular polymers. Illustrations adapted from refs.[48,51,52].

The supramolecular polymerization process of oligomers has been extensively studied and described.[54,55] Meijer *et al.* have reported two predominant self-assembly mecha-

nisms: isodesmic and cooperative polymerization.[56,57] These two mechanisms can be used to describe systems containing either single or multiple monomeric units.

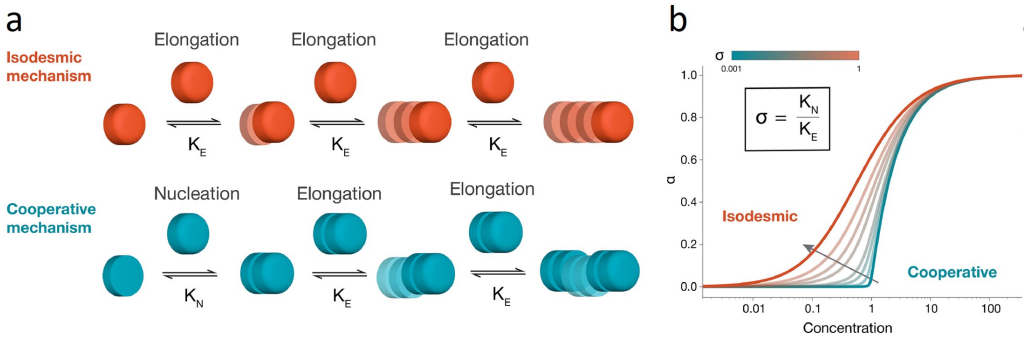

Figure 1.4: (a) Illustration of the two major self-assembly processes, the isodesmic pathway is highlighted in red and the cooperative one in blue. (b) Graphical illustration of the different mechanisms based on the nucleation and elongation association constant, in the isodesmic process they are identical. Illustration is taken from ref.[58].

Isodesmic polymerization features identical reactivity for the formation of a single non-covalent bond (Figure 1.4a). This reversible bond forms at the same rate at every step of the polymerization process, resulting in a single binding constant. This mechanism can be easily identified as it follows a sigmoidal curve when the aggregation is plotted as a function of concentration (illustrated in orange in Figure 1.4b).[54]

In contrast, the cooperative pathway (Figure 1.4a) is composed of two steps: first, nucleation, followed by elongation of the polymer (also known as the nucleation-elongation process). The rate at which monomeric units are incorporated in both steps differs, and the mechanism is therefore considered a non-linear process (illustrated in blue in Figure 1.4b). The system first forms a nuclei as the concentration increases (or the temperature decreases), and once the critical concentration (or temperature) is reached, these units start growing into large assemblies.[54,59]

1.2 Design of Functionalized Oligomers

Supramolecular polymers have been shown to self-assemble into a wide variety of morphologies. Through the functionalization of their various building blocks, either pre- or post-assembly, supramolecular polymers become ideal platforms for precise molecular arrangement.[60] These systems can precisely position compounds, ranging from catalysts[61] to chromophores[62] and even enzymes.[63] This property allows these molecules to

further bind (covalently or not) to other species, such as proteins,[64] cells[65] or materials.[66]

A reliable approach to control the arrangement of monomers while incorporating functional groups into a material is to use supramolecular scaffolds. These structures have been developed to possess multiple well-defined binding sites inside or on the surface of their architecture, while allowing pre- or post-functionalization of the building blocks through non-covalent or covalent bonds. Ishiwari and co-workers have classified these supramolecular scaffolds into four categories, based on the dimensions of the self-assembled structures (Figure 1.5).[67]

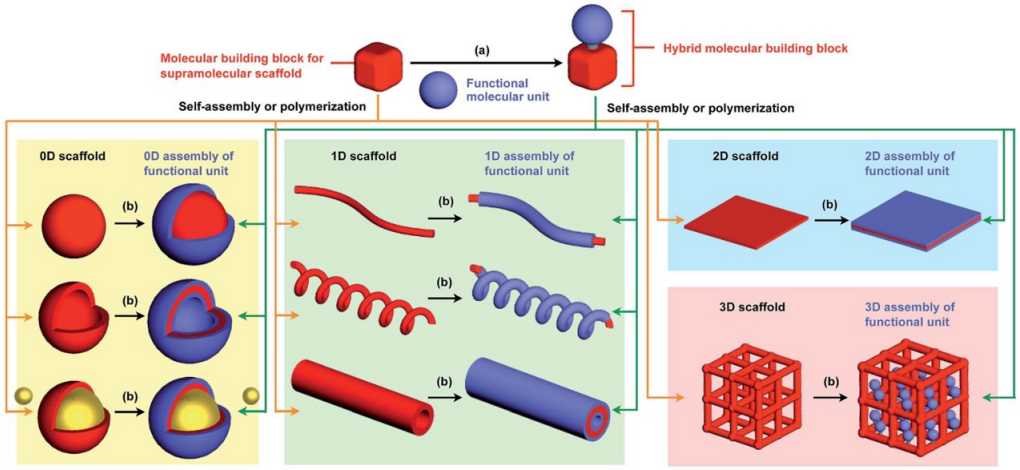

Figure 1.5: Illustration of the four categories of supramolecular scaffolds. (a) Pre-self-assembly functionalization (green lines); (b) Post-self-assembly functionalization (orange lines). Reproduced from ref.[67].

DNA itself may be used as a scaffold for supramolecular polymerization. This option offers multiple advantages, including biocompatibility, precise control over distance and arrangement of molecules, along with the possibility to include stimuli-responsive compounds.[68] One example consists of the creation of artificial multienzyme constructs. Niemayer and co-workers have generated di-enzymatic complexes using oligonucleotide conjugates of glucose oxidase (GOx) and horseradish peroxidase (HRP), which both bind to the same surface attached DNA single strand (see Figure 1.6a).[69] The ability to precisely tune the distance between the two enzymes allowed them to find the optimal distance for the enzymatic cascade to take place. With the same enzymes, Willner and co-workers went even further by creating 2D nanoarrays to which the enzymes could bind through DNA "hinges" (see Figure 1.6b).[70] The DNA, modified with enzyme strips, forms singular and bundled fiber-like nanostructures upon hybridization, up to tens of micrometers long and about 3.5 nm high (see Figure 1.6c). This second method achieved even greater proximity, leading to higher reaction rates than the ones previ-

ously observed.

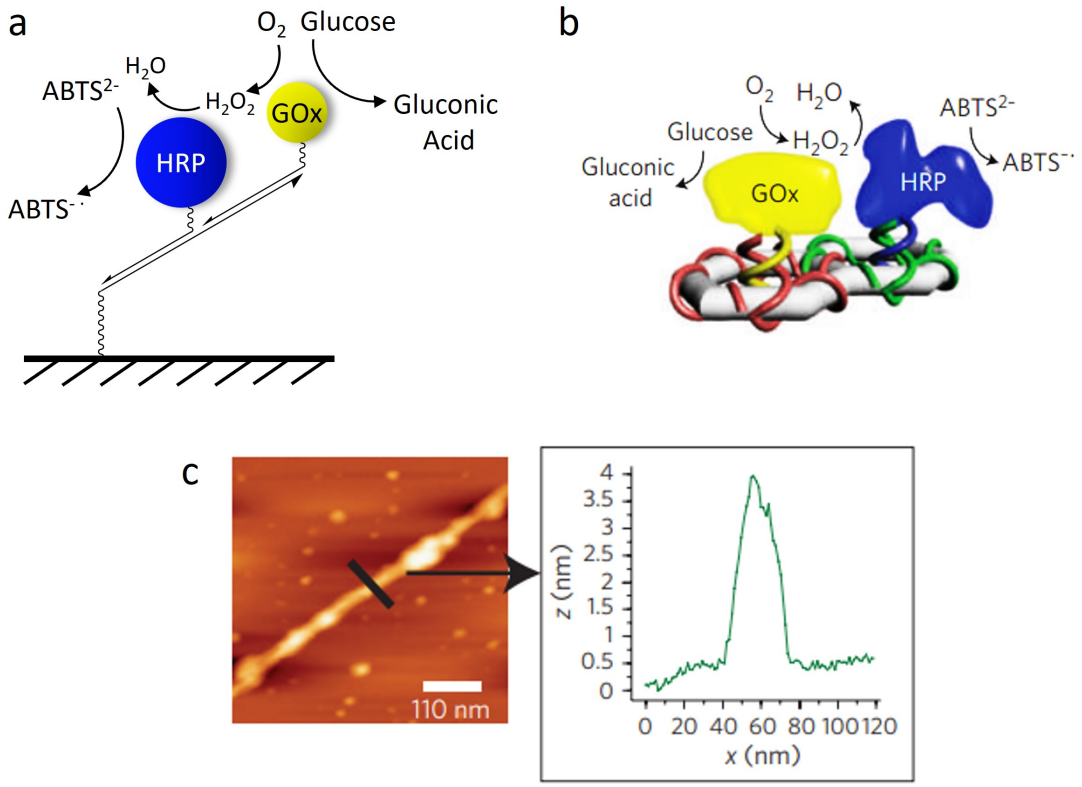

Figure 1.6: Schematic illustration of the DNA-protein complexes with (a) A surface-attached system; (b) A directed assembly on DNA nanoarrays; (c) AFM image and cross section of the two enzyme system assembled on the hexagon strips in (b). Illustration adapted from ref[69] and taken from ref.[70,71].

The simplest way to functionalize supramolecular scaffolds without extensively altering the supramolecular morphology is by using chemical handles. Many different handles have been developed and made commercially available (*e.g.*, azide, thiols and streptavidin), offering a plethora of options for post-synthesis modifications.[72,73] Nevertheless, the required post-assembly reaction conditions may lead to certain limitations that can disrupt the self-assemblies. A well-documented example is the use of copper-catalysed azide-alkyne cycloadditions, which can damage DNA through the formation of radicals inducing the oxidation of the bases, along with the formation of crosslinks between adjacent base pairs.[74–77] As a solution to this shortcoming, researchers have developed systems where post-assembly modifications are performed through non-covalent interactions. Carbohydrates are an example of compounds that allow such functionalization. Some of them are specifically recognized by proteins - for example; lectins are proteins which interact and bind specific carbohydrate moieties to initiate the ag-

glutination of cells.[78–80] In combination with amphiphilic aromatic building blocks, the self-assembly process is driven by π-π stacking, hydrophobic effects and carbohydrate-carbohydrate interactions. The possibility of equipping supramolecular scaffolds with bioactive compounds, such as sugars, is particularly appealing as such a system would allow the formation of biomimetic, programmable materials.[81–83]

Another class of smart nanomaterials that could benefit from the specific arrangement of molecules present in supramolecular polymers are artificial light-harvesting complexes (LHCs). The possibility of precisely controlling the position of chromophores in supramolecular polymers makes them highly attractive for the development of new optoelectronic devices. The optimization of fluorescence-based sensors and LHCs requires the rapid and efficient transfer of electronic energy over long distances. According to the Förster theory (described in Section 1.3), the optimization of the geometrical arrangement between the donor and acceptor molecule would result in an increased rate of electronic energy transfer (EET).[84]

Robust supramolecular scaffolds are also used in the design of nano-artificial light-harvesting systems (ALHSs).[85–87] Many ALHSs have been developed based on host-guest complexations - in these systems, the donor is selected and designed to co-assemble in the presence of a supramolecular scaffold such as pillararenes,[88,89] cyclodextrin[90] and other macrocycles.[91] The acceptor chromophores are then added and energy transfer is observed, resulting in efficient ALHSs with donor:acceptor ratios of 100:1 to 200:1 in some cases.[92,93]

The use of non-toxic biomacromolecules to construct nano-ALHSs has great potential for biosensing and cell imaging. ALHSs have also been developed based on DNA,[94,95] protein, and peptide scaffolds. A great example involving the latter has been shown by Perrier and co-workers, who reported a co-assembly of three modified cyclic peptides (see Figure 1.7).[96] They have demonstrated that their dye-modified cyclic peptides self-assemble in aqueous media due to the strong interactions between the flat rings and the amphiphilic properties of the construct. The energy transfer cascade was made possible by carefully selecting the chromophores to ensure the overlap between the emission spectra of the donor and the absorption spectra of the acceptor in both steps. By adjusting the ratio of the different peptides in solution they were able to efficiently tune the emission color of the ALHS from blue to green and orange, including pure white.

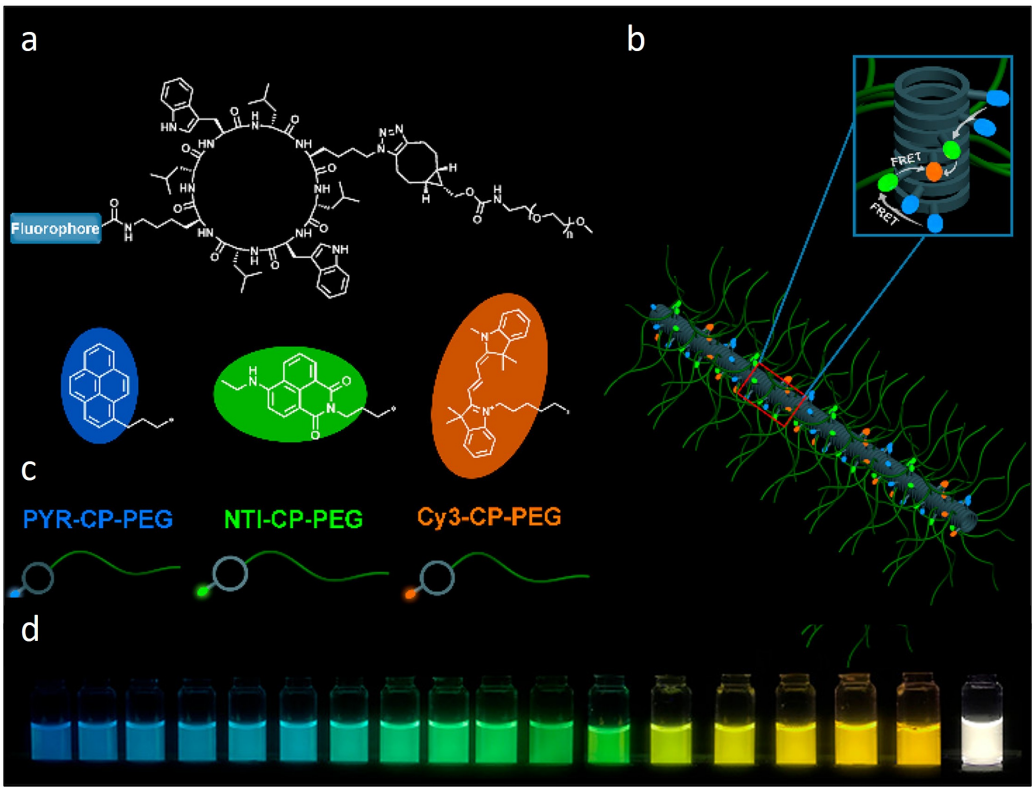

Figure 1.7: (a) Chemical structure of the three fluorophore - cyclic peptide - polymer conjugates. (b) Cartoon illustration of the supramolecular light-harvesting system. (c) Schematic illustration of the different conjugates. (d) Photograph of the colors emitted by different cyclic peptide ratios. Illustration is taken from ref.[96].

The introduction of building blocks to these supramolecular nano-ALHSs can render them sensitive to external stimuli, such as pH,[97] temperature[98] or light[99] which is of significant interest for potential anti-counterfeiting, cell imaging and photocatalytic applications.[100,101]

1.3 Energy Transfer in Supramolecular Polymers

In LHCs, light excites an initial chromophore and the excitation energy is then transferred to the system following multiple pathways. This photophysical process is known as electronic energy transfer (EET). Within multi-chromophoric systems, the transfer of excitation energy can be done over large distances by a series of energy hops and is limited by the excited state lifetime.[102] Electronic energy transfer can be divided into two categories: incoherent and coherent energy transfer (Figure 1.8).

Incoherent EET, also known as classical EET, is observed when a weak electronic coupling between the chromophores is present. It is best described by Förster theory, where

Förster resonance energy transfer (FRET) is based on the electronic dipole-dipole interactions. FRET therefore depends on the relative orientation between the chromophores, the distance between them (1 to 10 nm) and the overlap of the donor's fluorescence and acceptor's absorption bands.[103–106] In these systems, the excitation energy is seen to hop between the different chromophores in a random walk manner (see Figure 1.8a).

However, when strong electronic couplings are present between the donor and acceptor, the electronic excited states are no longer localized on one chromophore. Instead, they become delocalized over several chromophores. In extended, ordered systems, such as crystals or certain supramolecular polymers, the energy is seen to spread coherently, like a wave (see Figure 1.8b).[107]

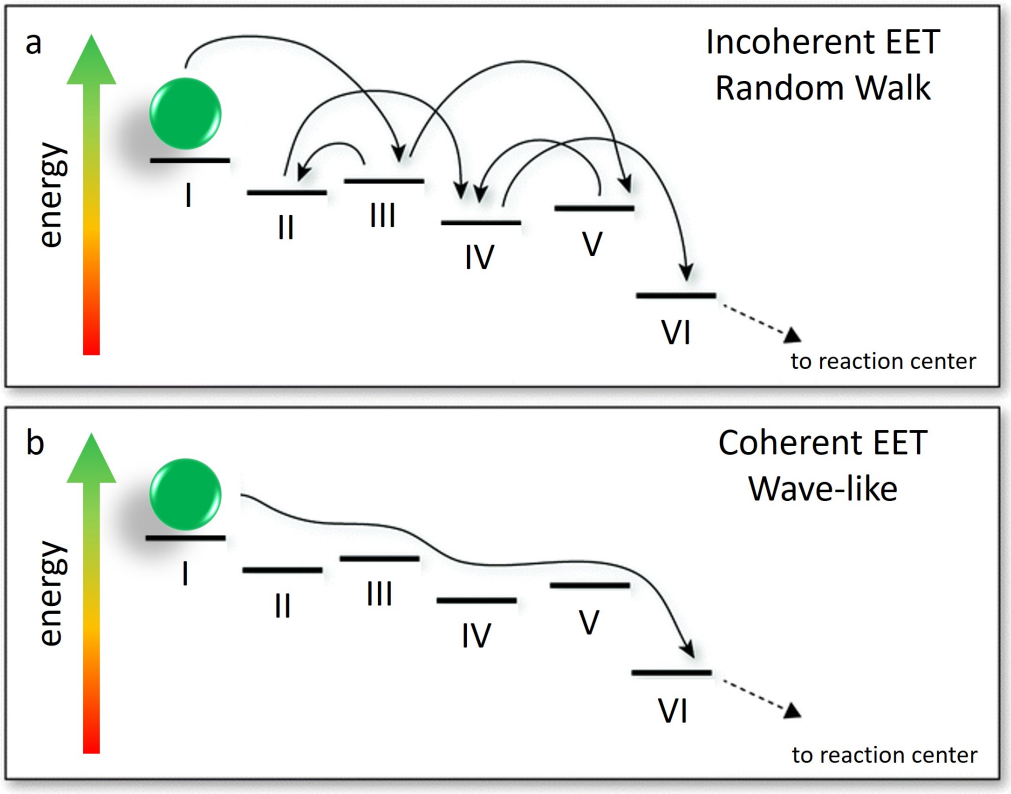

Figure 1.8: Illustration of the two EET categories. (a) Non-coherent EET: the excitation energy hops randomly from one chromophore to the other in the manner of a random walk; (b) Coherent EET: the excitation energy is distributed over several chromophores and spreads like a wave. Figure adapted from ref.[107].

Not all the parameters influencing quantum coherent energy transfer are fully understood, and new models are being developed to incorporate and observe this quantum theory in natural LHCs.[108–110]

1.4 Preparation of Synthetic Oligomers

Two major methods are employed in synthesising phosphodiester-linked oligomers, each suited for specific requirements depending on the scale and the length of the desired oligomer.

Solid-phase synthesis is a robust, efficient, and automated technique for producing long oligonucleotides with defined sequences, up to as long as 200-mers.[111–114] This method was initially developed for the synthesis of DNA strands. However, it quickly became possible to incorporate modified-DNA bases and non-nucleosidic compounds.[115] The synthesis pathway involves a repeating cycle of four steps performed for each building block addition (Figure 1.9).

The first nucleoside is initially attached to an insoluble solid-support, usually *via* a succinyl linker. The first step of the cycle - detritylation - involves deprotecting the 5'-4,4'-dimethoxytrityl (DMT) group using acidic conditions (*e.g.*, 3% trichloroacetic acid, TCA). The following step is to couple the next nucleoside in the presence of an activator (*e.g.*, 5-(Ethylthio)-1H-tetrazole, ETT). Once the coupling is executed, the unreacted hydroxyl groups are capped with a base-labile protecting group (*e.g.*, acetyl group) to prevent the presence of failed sequences. In the fourth and last step, the phosphite triester is oxidized to the phosphate triester (*e.g.*, I_2). The cycle then repeats until the desired oligonucleotide is obtained. The oligomer is then released from the solid support and the protecting groups are removed in the same step in basic conditions (*e.g.*, aqueous NH_3). The crude oligomer is finally purified by high-performance liquid chromatography (HPLC).

The second method requires the synthesis of the oligomer in solution using the same phosphoramidite chemistry. This method is used for short oligomers and allows their preparation on a much larger scale. The synthesis of symmetrical oligomers requires the formation of two different building blocks (see Figure 1.10). The first one, **A**, is a diol protected on one side with a base-labile protecting group (usually acetyl). The second, **B**, is a diol on which both hydroxyl groups have been derivatized to the corresponding phosphoramidite.

The two building blocks are then coupled with an activating agent in 1,2-dichloroethane (1,2-DCE). The resulting phosphite triester is then oxidized to the corresponding phosphate triester using a ^{t}BuOOH solution, giving **C**. The compound is then purified and finally, the protecting groups are removed from the oligomer under basic conditions, yielding **D**.

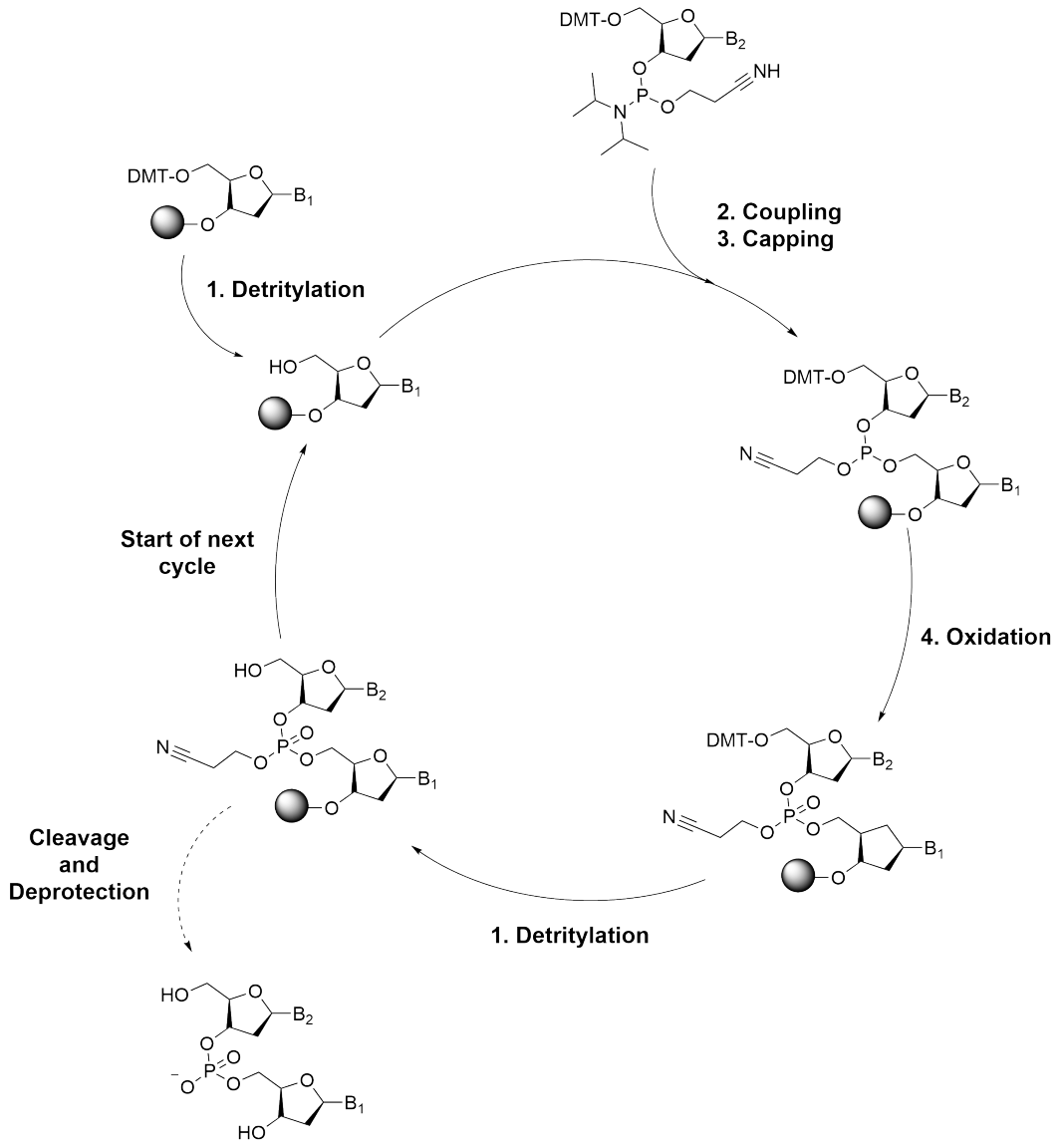

Figure 1.9: Solid phase oligonucleotide synthesis cycle. Conditions: 1. 3% trichloroacetic acid in DCM; 2. DMT-protected nucleoside phosphoramidite, 4,5-dicyanoimidazole in acetonitrile; 3. *in situ* mixing of acetic acid and 2,6-lutidine in THF with *N*-methylimidazole in THF; 4. I_2, pyridine, water and THF. Cleavage from the solid support and deprotection is done with NH_3.[116]

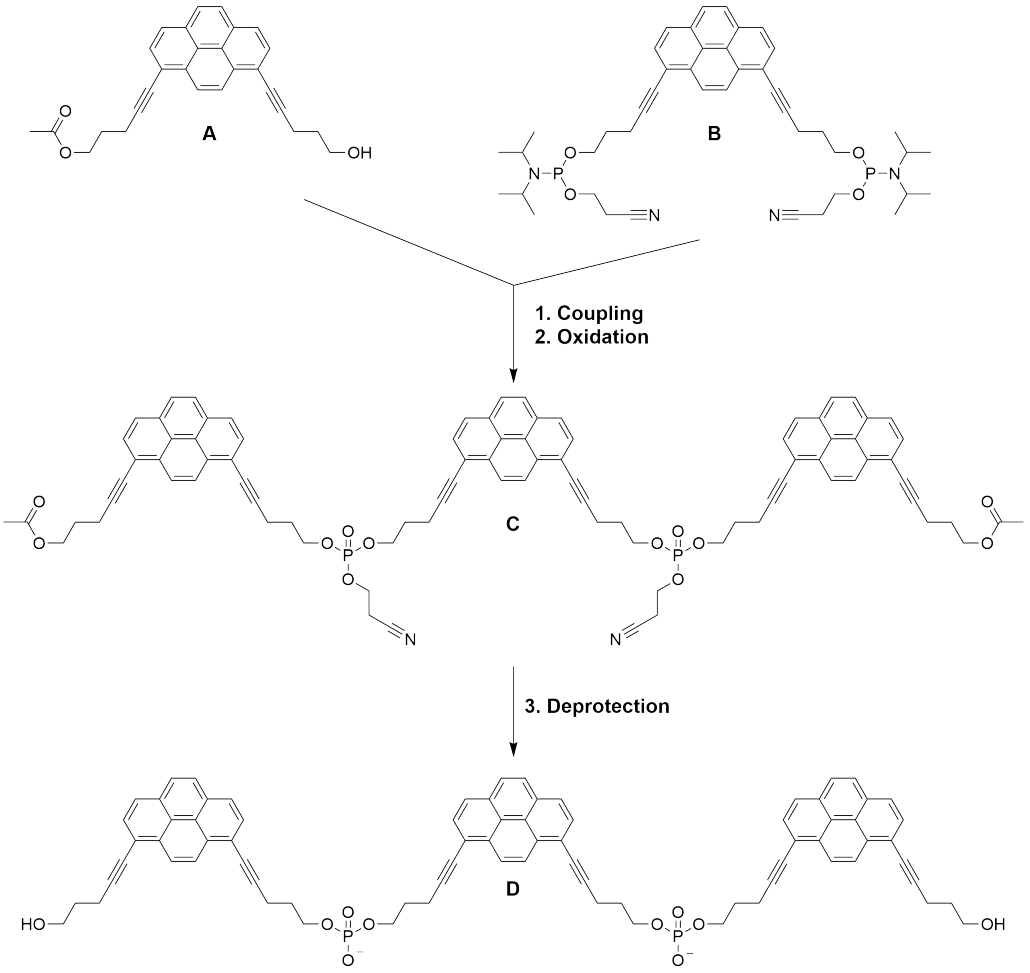

Figure 1.10: Solution phase oligomer synthesis. Conditions: 1. **A**, **B**, ETT in 1,2-DCE; 2. ^{t}BuOOH in water; 3. 2 M NH_3 in MeOH.

Chapter 2

Aim of the Thesis

The precise control of the arrangement of individual components within intricate, self-assembled supramolecular arrays plays an essential role in numerous chemical and biochemical processes.[117,118]

The previous work conducted within our group regarding the self-assembly of pyrene trimers[50,119] and the light-harvesting properties of phenanthrene trimers[51,120] has initiated this research. This thesis aims to enhance our understanding of the supramolecular self-assembly process of different oligomers, through the study of different polyaromatic hydrocarbon derivatives and chemical modifications.

The possibility of creating a novel carbohydrate supramolecular platform is very attractive for observing possible carbohydrate-protein interactions. For this reason, the robust phosphodiester-linked pyrene trimer scaffold we have previously synthesized will be functionalized with a sugar moiety (α-mannose). The morphology of the self-assembled nanostructures will be further investigated by changing the pyrene isomer present in the oligomer construct and by increasing the number of pyrene units (Chapter 3).

In addition, the opportunity of designing supramolecular polymers based on a new class of oligomers will be investigated. The substitution of a couple of polyaromatic hydrocarbon moieties by a non-aromatic, hydrophobic, chiral molecule, cholane, will be explored. In more detail, two pyrene and/or phenanthrene building blocks present in our trimers were replaced by cholane. The influence of the absence of intramolecular π-π interactions in our construct will be studied along with the impact of having different pyrene or phenanthrene derivatives in the oligomer. Finally, the light-harvesting abilities of the phenanthrene trimers will be explored (Chapters 4 and 5).

Chapter 3

Self-Assembly of Carbohydrate-Modified Pyrene Oligomers

This chapter focuses on the synthesis of carbohydrate-modified pyrene oligomers and the investigation of their self-assembling properties. The use of α-mannose as the carbohydrate source in this project is of particular interest as it is specifically recognized by certain proteins, such as lectins (*e.g.*, concanavalin A, Con A). The resulting supramolecular polymers could be used for the development of new carbohydrate-based materials or functional platforms.[121–127] A schematic illustration of this work is present in Figure 3.1.

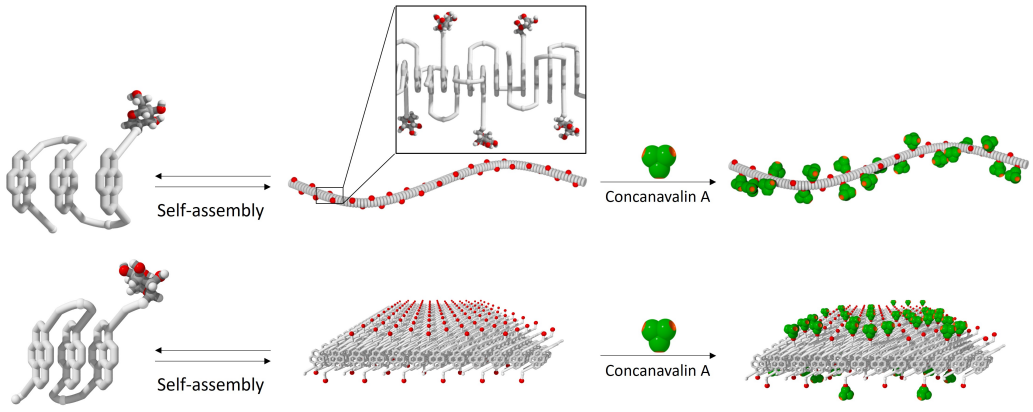

Figure 3.1: Schematic illustration from the self-assembly process of α-mannose-modified 1,8-disubstituted pyrene oligomers into nanofibers, followed by the addition of Con A (top). Identical procedure illustrated with α-mannose-modified 1,6-disubstituted pyrene oligomers (bottom).

Upon synthesis of the different oligomers, spectroscopic measurements were performed to gain information on their aggregation process. Atomic force microscopy

(AFM) experiments revealed the formation of several distinct supramolecular polymers based on the different pyrene isomers present in the construct. Following the self-assembly of carbohydrate-modified pyrene oligomers into nano-sized supramolecular polymers, an attempt was made to bind Con A to the self-assembled nanostructures.

3.1 Results and Discussion

3.1.1 Overview of α-Mannose-Modified Pyrene Oligomers

The oligomers used throughout this research project are presented in Table 3.1. These compounds were prepared *via* solid-phase synthesis and were further purified by HPLC - detailed procedures are provided in Sections 7.2.1 to 7.2.3.

Table 3.1: (Left) The oligomers and their sequence. (Right) Building blocks used to synthesis the oligomers. Note: The building blocks are all connected through phosphate groups.

Oligomer	Sequence
O1	$Py_{1,8}$ - $Py_{1,8}$ - $Py_{1,8}$
O2	$Py_{1,8}$ - $Py_{1,8}$ - $Py_{1,8}$ - αMan
O3	$Py_{1,8}$ - $Py_{1,8}$ - $Py_{1,8}$ - Peg 3 - αMan
O4	$Py_{1,8}$ - $Py_{1,8}$ - $Py_{1,8}$ - $Py_{1,8}$ - Peg 3 - αMan
O5	$Py_{1,8}$ - $Py_{1,8}$ - $Py_{1,8}$ - $Py_{1,8}$ - $Py_{1,8}$ - Peg 3 - αMan
O6	$Py_{1,6}$ - $Py_{1,6}$ - $Py_{1,6}$ - Peg 3 - αMan
O7	$Py_{1,6}$ - $Py_{1,6}$ - $Py_{1,6}$ - $Py_{1,6}$ - Peg 3 - αMan
O8	$Py_{1,6}$ - $Py_{1,6}$ - $Py_{1,6}$ - $Py_{1,6}$ - $Py_{1,6}$ - Peg 3 - αMan

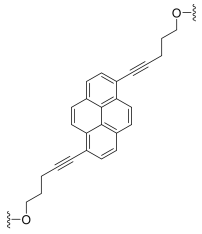

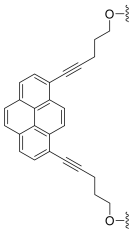

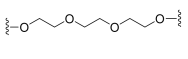

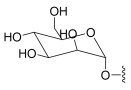

3.1.2 Supramolecular Assembly of α-Mannose-Modified Oligomers

Previous work performed with pyrene trimers highlighted the importance of the substituted position on the pyrene core. The self-assembly of 1,6-disubstituted pyrene trimers led to the formation of nanosheets,[49] while aggregation of 1,8-disubstituted pyrene trimers resulted in the formation of nanofibers.[50] This work has led us to study the effect of a modification on both trimers, as it would ultimately result in a different crowding environment.

Initially, three different oligomers were synthesized with 1,8-disubstituted pyrene (see Figure 3.2a). The first one, **O1**, was left unmodified. The second, **O2**, contained the α-mannose moiety, while the third one, **O3**, possessed a PEG-3 linker between the pyrene trimer and the carbohydrate. This last addition was done to ensure access of the Con A binding pocket to the α-mannose as it is situated between 8 to 10 Å from the protein surface.[128,129]

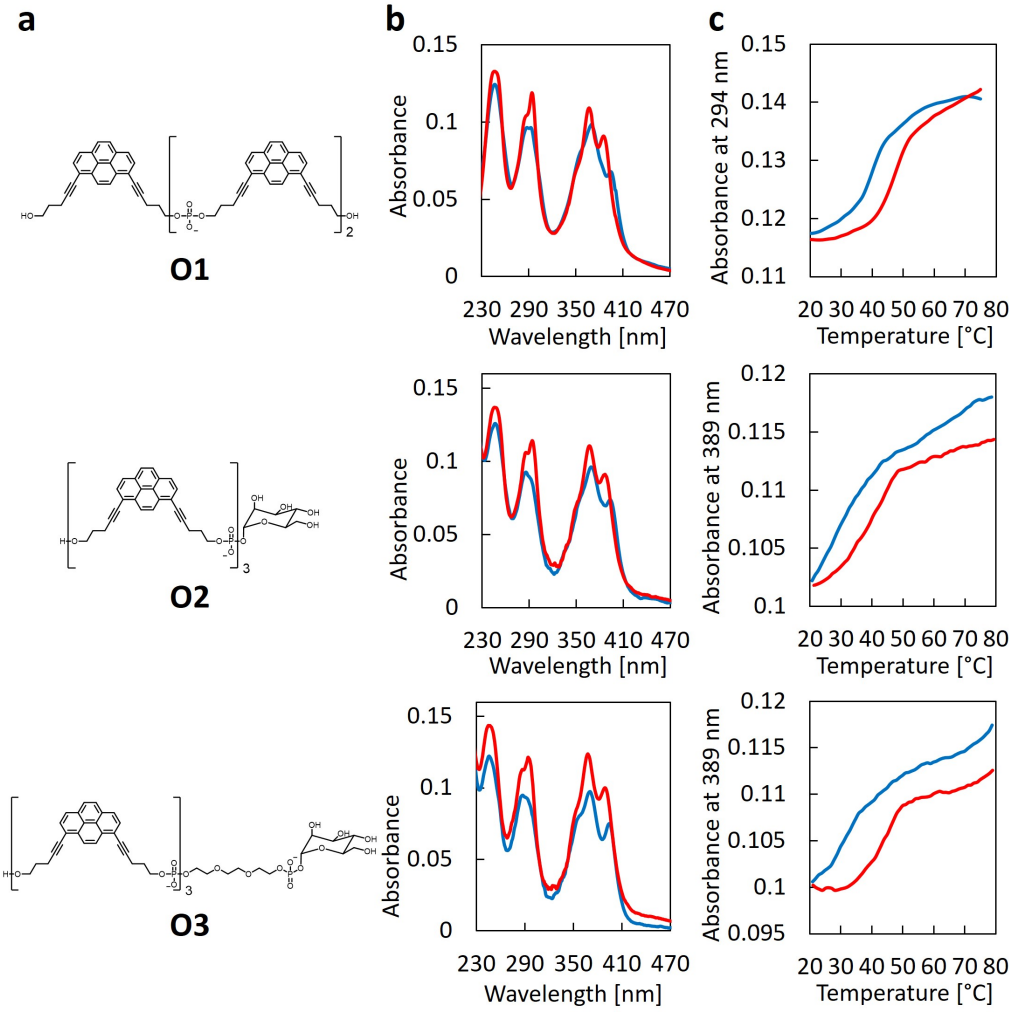

Figure 3.2: (a) Chemical structures of **O1**, **O2** and **O3**; (b) Absorption spectra at 20 °C (blue) and 75 °C (red); (c) Cooling (blue) and heating (red) curves. Conditions: 1 µM **O1**, 10 mM sodium phosphate buffer pH 7.2, 10% EtOH, 10 mM NaCl; 1 µM **O2**, 10 mM sodium phosphate buffer pH 7.2, 200 mM NaCl; 1 µM **O3**, 10 mM sodium phosphate buffer pH 7.2, 800 mM NaCl. Temperature gradient: 0.5 °C/min.

The spectroscopic behavior of both oligomers were compared to that of the unmodified trimer (**O1**). The UV-vis temperature-dependent absorption spectra of **O1**, **O2** and **O3** are shown in Figure 3.2b. The conditions necessary to observe the supramolecular

polymer disassembled at 75 °C and assembled at 20 °C were optimised. Upon cooling with a temperature gradient of 0.5 °C/min, all three absorption spectra display identical features: a hypochromic shift at 295 nm along with two bathochromic shifts from 370 nm to 376 nm and from 392 nm to 396 nm, implying aggregation is taking place at 20 °C.

To understand when the aggregation takes place, the absorption at one wavelength was monitored when cooling the sample from 75 °C to 20 °C and when heating from 20 °C to 75 °C. In the case of **O1**, **O2** and **O3**, these curves (Figure 3.2c) are similar, with slight changes in the aggregation and de-aggregation temperatures (see Table 3.2). These temperatures were defined respectively as the onset temperature of the cooling and heating curves.

Table 3.2: Aggregation and de-aggregation temperatures of oligomers **O1** to **O3**.

	O1	**O2**	**O3**
Aggregation Temp.	50 °C	45 °C	50 °C
De-aggregation Temp.	28 °C	22 °C	35 °C

AFM measurements were performed to observe the aggregated nanostructures. The assembled oligomers were deposited on a (3-amino-propyl)triethoxy-silane (APTES)-modified mica sheet. As depicted in Figure 3.3, ill-defined nanostructures were observed for **O2**.

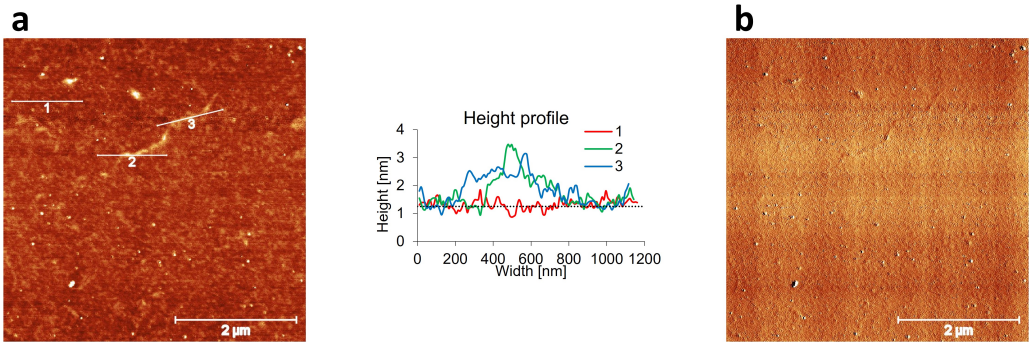

Figure 3.3: (a) AFM with corresponding cross sections; (b) Amplitude scan of self-assembled **O2**. Conditions: 1 µM **O2**, 10 mM sodium phosphate buffer pH 7.2, 200 mM NaCl.

In contrast, measurements realized with **O3** revealed well-defined fiber-like nanostructures (Figure 3.4). This is a direct consequence of the de-aggregation temperature being close room temperature for **O2** (see Table 3.2), resulting in the low stability of the nanostructures. The supramolecular fibers observed with **O3** are present in two

different sizes. The larger fibers are the ones that stand out in Figure 3.4a, they are between 1 to 4 µm long, 0.7 nm high and 100 nm wide. The smaller ones are present in the background, underneath the major fiber and seem to coat the mica sheet.

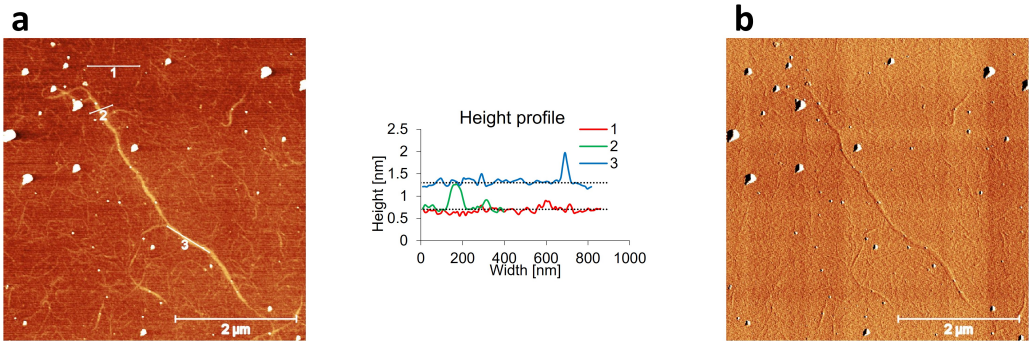

Figure 3.4: (a) AFM with corresponding cross sections; (b) Amplitude scan of self-assembled **O3**. Conditions: 1 µM **O3**, 10 mM sodium phosphate buffer pH 7.2, 800 mM NaCl.

In summary, the self-assembly of α-mannose-modified 1,8-disubstituted pyrene oligomers results in the formation of supramolecular fibers. While this is a success, the possibility to increase the aggregation temperature to improve the stability of the supramolecular polymer was explored.

3.1.3 Stabilization of the Nanostructures

In order to increase the hydrophobic interactions present within the oligomer and thus improve its stability, the number of pyrene units present in the construct was increased. The two synthesized oligomers - **O4** and **O5** - possess four and five pyrene units, respectively (Figure 3.5a).

The conditions necessary for the aggregation of the two oligomers were optimised by monitoring the changes taking place in the UV-vis absorption spectra between 75 °C and 20 °C. The spectroscopic data recorded for these oligomers were comparable to those observed for **O3** (see in Figure 3.5b). Upon controlled cooling (gradient: 0.5 °C/min), the absorption spectra at 20 °C exhibited the same spectroscopic shifts as the ones observed previously (Figure 3.2b): a hypochromic shift from the band present at 295 nm and two bathochromic shifts from the bands at 370 nm and 392 nm to 376 nm and 396 nm respectively. Upon measuring the cooling and heating curves of these oligomers (see Figure 3.5c), their de-aggregation temperature was found not to increase. An attempt was made with higher salt concentrations to induce the aggregation process to begin at a higher temperature. However, these conditions did not allow the full dissociation of

the oligomers at 75 °C (see Figure 7.32).

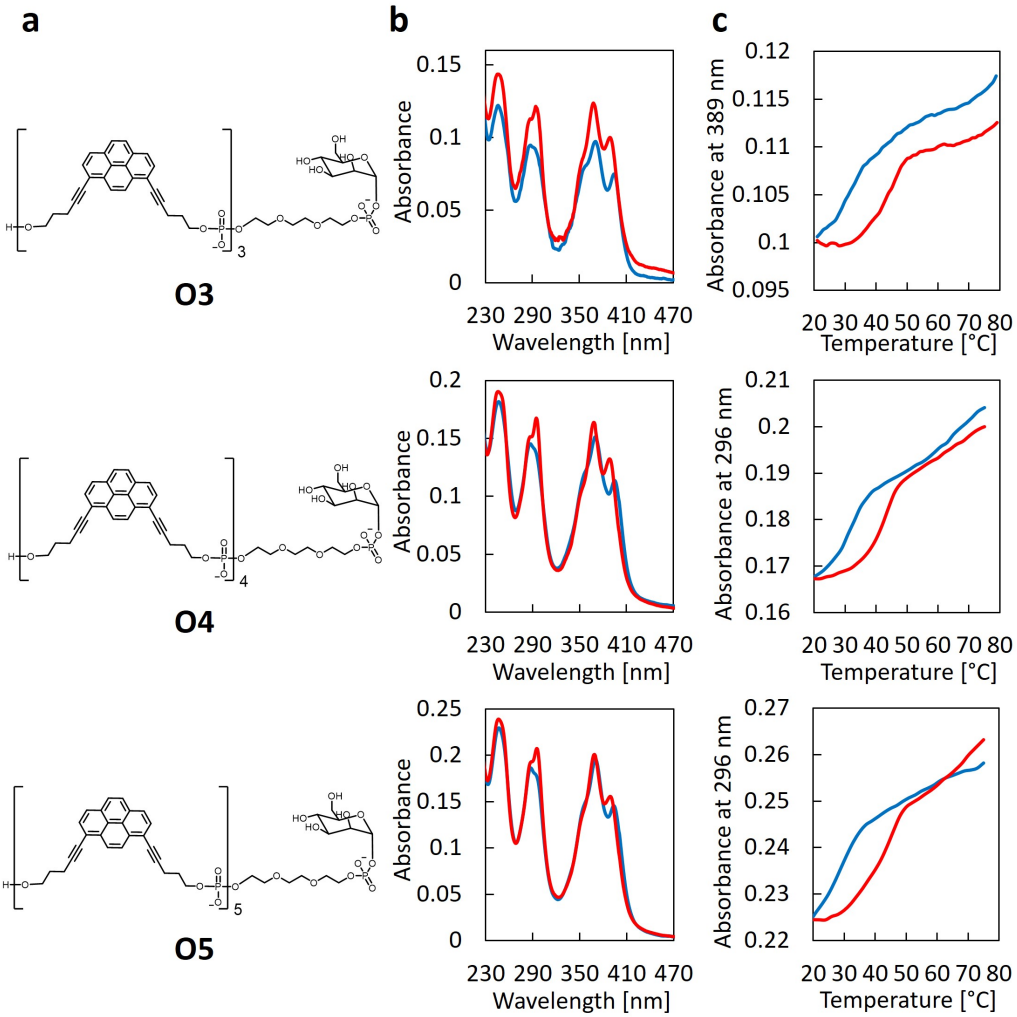

Figure 3.5: (a) Chemical structures of **O3**, **O4** and **O5**; (b) Absorption spectra at 20 °C (blue) and 75 °C (red); (c) Cooling (blue) and heating (red) curves. Conditions: 1 µM **O3**, 10 mM sodium phosphate buffer pH 7.2, 800 mM NaCl; 1 µM **O4**, 10 mM sodium phosphate buffer pH 7.2, 100 mM NaCl; 1 µM **O5**, 10 mM sodium phosphate buffer pH 7.2, 75 mM NaCl. Temperature gradient: 0.5 °C/min.

In summary, the effort to improve the stability of the oligomer by increasing the amount of pyrene units present in the monomer was not conclusive. Optimization of the self-assembly conditions for the different oligomers did not allow to have full dissociation of the oligomer at high temperature and a higher aggregation temperature at the same time. The possibility to observe the interaction between a protein and the α-mannose-modified pyrene supramolecular polymer was then explored with **O3**.

3.1.4 Decoration of Supramolecular fibers with Concanavalin A

The addition of Con A - a protein with 2 to 4 α-mannose binding pockets, depending on its dimeric or tetrameric form - to the previously formed supramolecular assemblies was done after immobilization of the self-assembled nanofibers on the APTES-modified mica sheets. This was made possible by mounting the mica sheet on a magnetic metallic plate, allowing the precise measurement of a specific area several times (Kinematic Nanosurf, see Figure 3.6). With this technique, the same nanostructures can be observed before and after the addition of the protein.

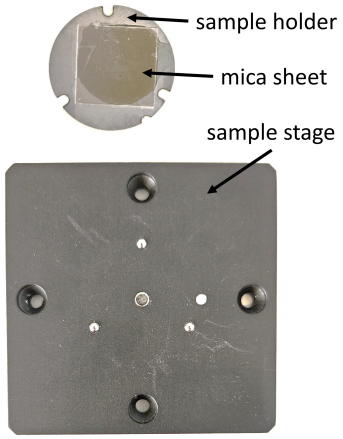

Figure 3.6: Atomic force microscopy setup. (Top) mica sheet mounted on the sample holder, (bottom) sample stage.

In Figure 3.7, one may observe the self-assembled **O3** in the presence of nanofibers before (a) and after (b) the addition of Con A. Upon addition of the protein, the background present in Figure 3.7b changed and appeared to be crowded. This is highlighted by the difference in height between the different cross sections. In both AFM measurements, the first cross section is a measure of the background. Initially, when the polymer alone is observed, the background was seen to be regular (Figure 3.7c). However, after the addition of the protein, the background became irregular (Figure 3.7d). Upon further analysis, an increase in the height profile on the nanofibers of around 0.3 nm was noticed.

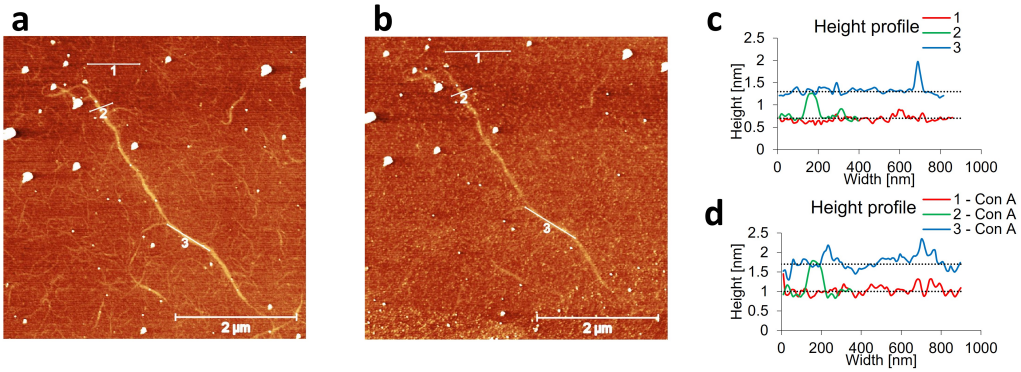

Figure 3.7: (a) AFM of **O3**; (b) AFM of **O3** after addition of Con A; (c) Cross section of (a); (d) Cross section of (b). Conditions: 1 µM **O3**, 10 mM sodium phosphate buffer pH 7.2, 800 mM NaCl; Con A: 0.2 µM Con A, 10 mM phosphate buffer pH 6.8, 1 mM $CaCl_2$, 1 mM $MnCl_2$.

To understand whether the changes in height present on the supramolecular polymers were induced by the interaction of Con A with the α-mannose residues present on our oligomers, a couple of control experiments were carried out. The protein buffer, with and without the protein, was added to an APTES-modified mica sheet and monitored through AFM measurements (Figure 3.8a and b respectively). The height profile of the protein buffer sample without the protein (Figure 3.8c) showed a noise signal of 0.2 to 0.3 nm high which is comparable to that of a freshly prepared mica sheet (see Figure 7.33). The same profile was observed for the second sample containing Con A (Figure 3.8d). Both these results indicate that the protein buffer does not interact directly with an APTES-modified mica sheet.

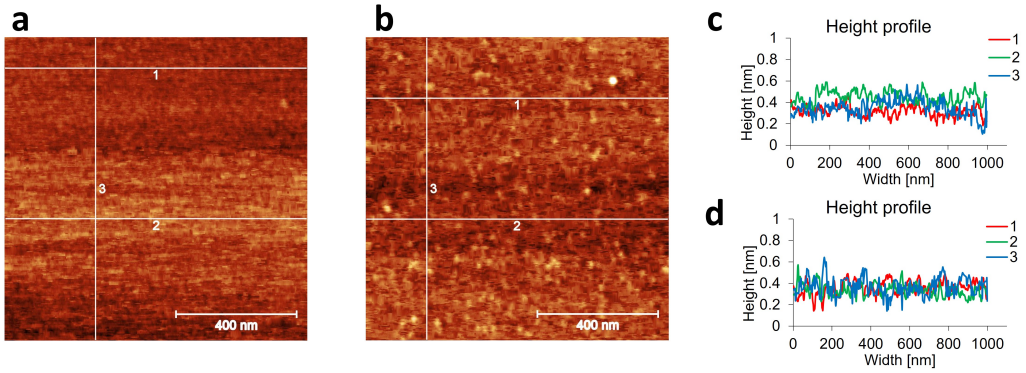

Figure 3.8: (a) AFM of Con A buffer; (b) AFM of Con A solution; (c) Cross section of (a); (d) Cross section of (b). Conditions: Con A buffer: 10 mM phosphate buffer pH 6.8, 1 mM $CaCl_2$, 1 mM $MnCl_2$; Con A solution: 0.2 µM Con A, 10 mM phosphate buffer pH 6.8, 1 mM $CaCl_2$, 1 mM $MnCl_2$.

It is therefore possible to attribute the difference in height to the interaction between Con A and the self-assembled nanofibers. The presence of the protein interaction with the background is due to the presence of smaller aggregates covering the APTES-modified mica sheet, leading Con A to cover the mica sheet.

3.1.5 Influence of the Pyrene Isomer

Previous studies have shown the importance of the pyrene isomer used in the monomer construct. Changes in the pyrene substitution pattern can influence the self-assembly process and the morphology of the supramolecular polymer.[49,50,130] Therefore, the study of the carbohydrate-modified pyrene oligomer was extended by synthesizing 1,6-disubstituted oligomers (Figure 3.9a).

Upon optimization of the conditions necessary to observe supramolecular assem-

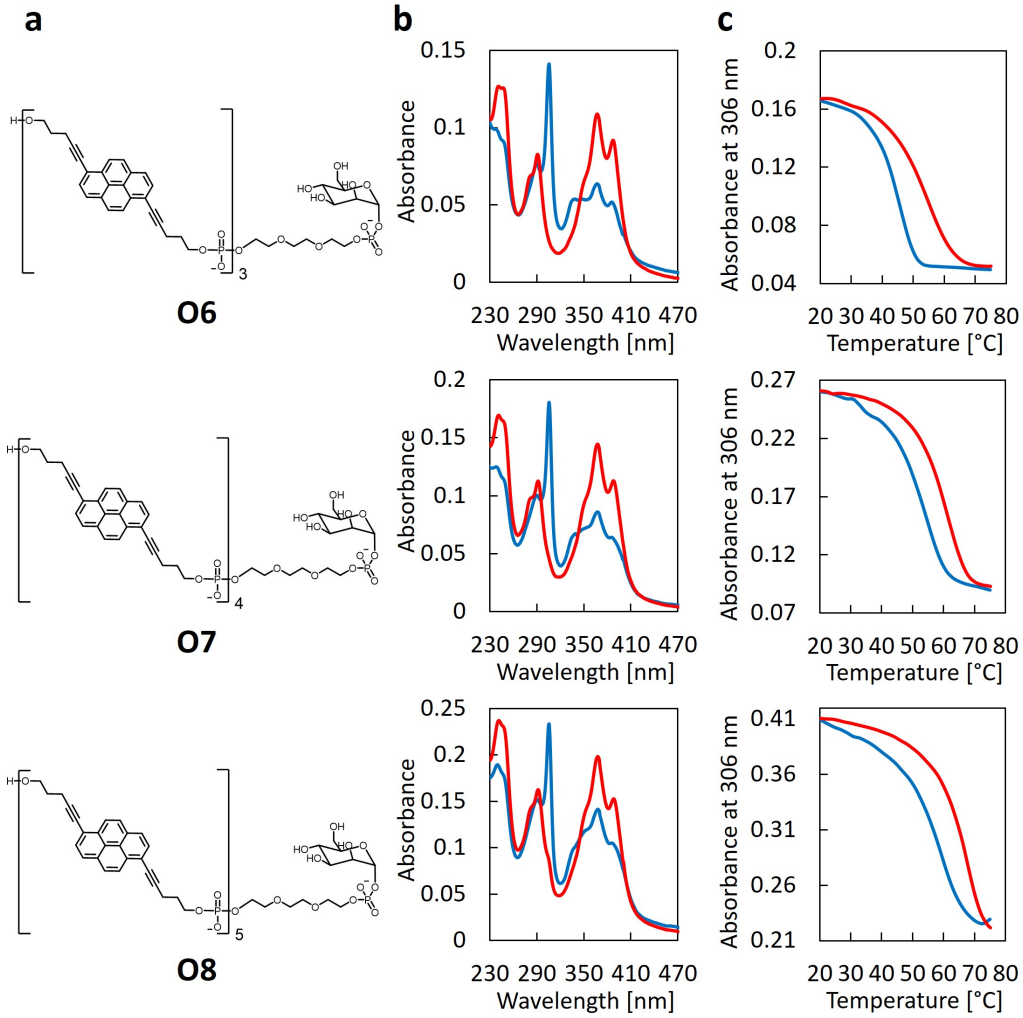

Figure 3.9: (a) Chemical structures of **O6**, **O7** and **O8**; (b) Absorption spectra at 20 °C (blue) and 75 °C (red); (c) Cooling (blue) and heating (red) curves. Conditions: 1 µM **O6**, 10 mM sodium phosphate buffer pH 7.2, 200 mM NaCl; 1 µM **O7**, 10 mM sodium phosphate buffer pH 7.2, 75 mM NaCl; 1 µM **O8**, 10 mM sodium phosphate buffer pH 7.2, 50 mM NaCl. Temperature gradient: 0.5 °C/min.

blies, different UV-vis spectroscopic features were observed upon cooling (temperature gradient: 0.5 °C/min) in the presence of this isomer. As it can be observed in Figure 3.9b, unlike for the 1,8-disubstituted pyrene oligomers, a strong *J*-band was found to be present at 305 nm upon aggregation along with a small *H*-band at 335 nm indicating an aggregation. The cooling and heating curves measured (Figure 3.9c) showed a higher stability at room temperature than for the previous oligomers (see Table 3.3). Once more, the aggregation and de-aggregation temperatures were defined as the onset temperature of the cooling and heating curves.

Table 3.3: Aggregation and de-aggregation temperatures of oligomers **O6** to **O8**.

	O6	**O7**	**O8**
Aggregation Temp.	56 °C	62 °C	70 °C
De-aggregation Temp.	40 °C	45 °C	54 °C

The melting temperature of the last oligomer - **O8** - was observed to be the highest, indicating a higher stability of the supramolecular assembly at room temperature. For this reason, a focus was placed on **O8** for microscopy measurements. Upon deposition of the self-assembled oligomer on APTES-modified mica sheets, sheet-like nanostructures were observed (Figure 3.10).

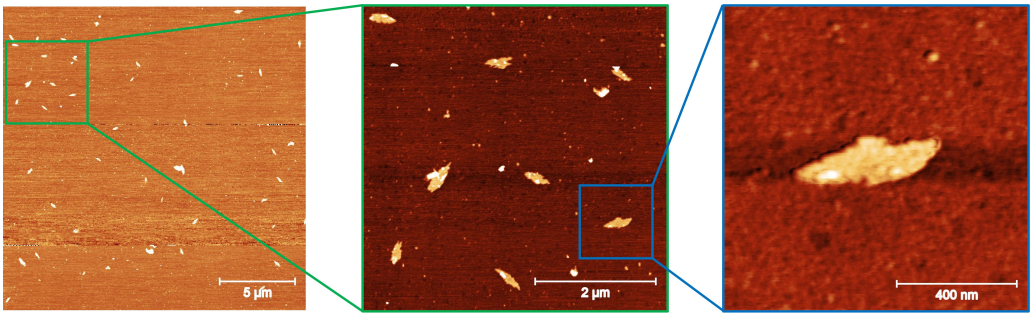

Figure 3.10: AFM scan of **O8** magnified several times. Conditions: 1 µM **O8**, 10 mM sodium phosphate buffer pH 7.2, 50 mM NaCl.

The size of these nanosheets are very regular - the cross section measured on the nanosheet (Figure 3.11a) indicated a height of about 2.5 nm, a width between 50 and 200 nm and a length of 200 to 700 nm.

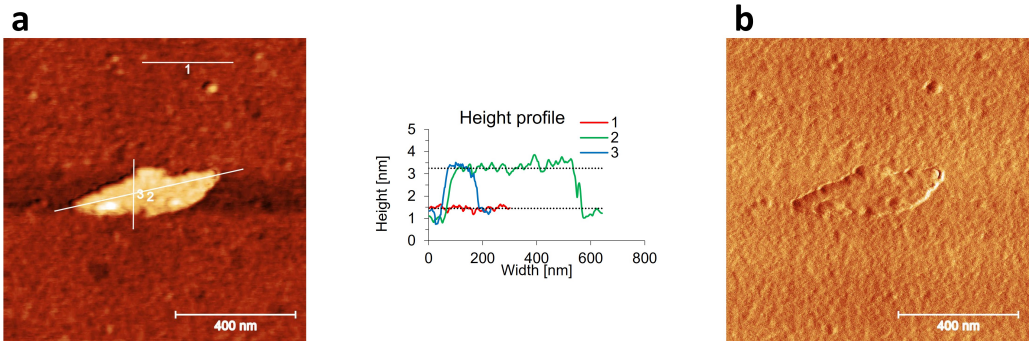

Figure 3.11: (a) AFM with corresponding cross sections; (b) Amplitude scan of self-assembled **O8**. Conditions: 1 µM **O8**, 10 mM sodium phosphate buffer pH 7.2, 50 mM NaCl.

Following the successful aggregation of the α-mannose-modified oligomer into sheet-like nanostructures, an attempt was made to observe the non-covalent interactions between Con A and the supramolecular polymer. As previously described (Section 3.1.4), in a first step, the aggregates were deposited on the mica sheet and measured (Figure 3.12a) before Con A was added in a second step. As witnessed in Figure 3.12b, upon the addition of the protein, the surface of the sheet was no longer regular and the height profile of the nanosheet was increased by 0.5 to 1 nm (Figure 3.12d).

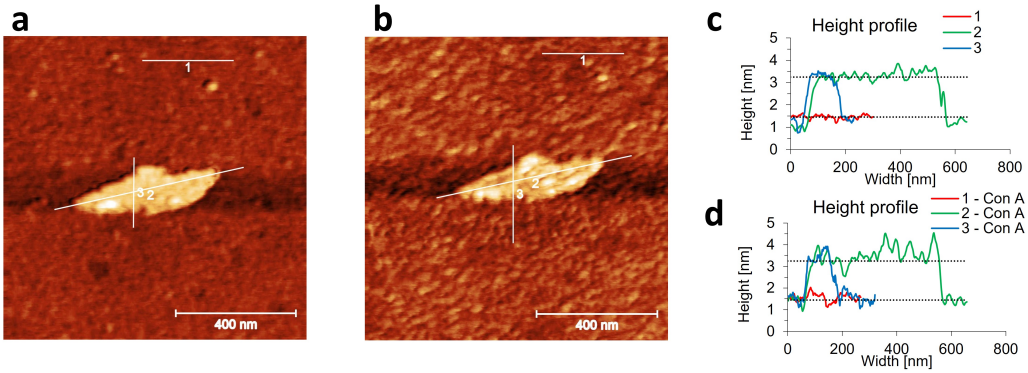

Figure 3.12: (a) AFM of **O8**; (b) AFM of **O8** after addition of Con A; (c) Cross section of (a); (d) Cross section of (b). Conditions: 1 µM **O8**, 10 mM sodium phosphate buffer pH 7.2, 50 mM NaCl; Con A: 0.2 µM Con A, 10 mM phosphate buffer pH 6.8, 1 mM $CaCl_2$, 1 mM $MnCl_2$.

However, the same crowding effect as previously seen with **O3** was observed to be present. This observation is surprising as no intermediate supramolecular species seemed to be present in the background. With the hypothesis of the Con A protein binding to the background being ruled out by previous measurements (see Figure 3.8), the possibility of having monomers sticking to the modified mica-sheet leading to the interaction of the protein to the background was then explored.

This assumption was studied by observing the possible interaction between Con A and the non-modified 1,6-disubstituted pyrene oligomer, **JJ** (see Scheme 3.1).[131] This measurement would as well answer the question of the specificity of the interaction between Con A and the α-mannose present on the supramolecular polymer.

The oligomer was measured on AFM before (Figure 3.13a) and after (Figure 3.13b) the addition of Con A. The supramolecular nanosheets observed upon self-assembly of **JJ** measured between 1 and 2 µm long and wide and are 2 nm high. The addition of the protein to this sample induced an increase in the height profile of the supramolec-

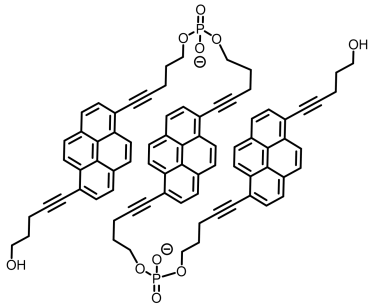

JJ

Scheme 3.1: 1,6-disubstituted pyrene trimer, **JJ**.

ular polymer of 1 to 2 nm (in green between Figure 3.13c and d). Even though the height profile of the background is not as strongly changed as the nanosheet, a rougher pattern was observed upon analysis of the red cross-section. The origin of the bonding between the non-modified trimer and the protein may be explained by the presence of local positively-charged surface area on Con A which interacts with the negatively-charged surface of the nanosheets.

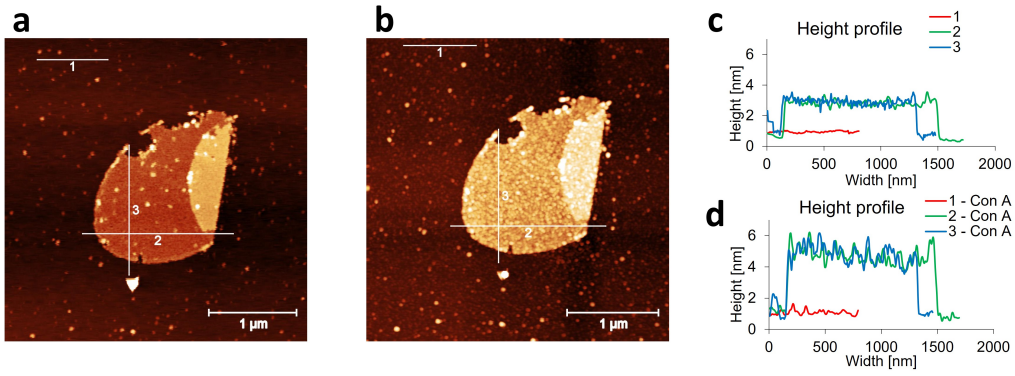

Figure 3.13: (a) AFM of **JJ**; (b) AFM of **JJ** after addition of Con A; (c) Cross section of (a); (d) Cross section of (b). Conditions: 2 µM **JJ**, 10 mM phosphate buffer pH 7.2, 10 mM NaCl, 10% EtOH; Con A: 0.2 µM Con A, 10 mM phosphate buffer pH 6.8, 1 mM $CaCl_2$, 1 mM $MnCl_2$.

In summary, the formation of self-assembled supramolecular nanosheets with the α-mannose-modified 1,6-disubstituted pyrene oligomer was successfully observed. These sheets measured between 50 and 200 nm in width, 200 and 700 nm in length and approximately 2.5 nm high. The control measurement performed with the non-modified pyrene oligomer **JJ** revealed the interaction between the carbohydrate-modified oligomer and the Con A protein is not carbohydrate-specific.

3.2 Conclusions and Outlook

The synthesis and self-assembly behavior of carbohydrate-modified pyrene oligomers has been described. The resulting supramolecular polymers possessed distinct nanostructures based on their different substitutions. In the case of 1,8-disubstituted pyrene oligomers (**O3**), AFM measurements revealed the formation of fiber-like nanostructures with sizes of 1 to 4 µm long and a height of 0.8 nm. In contrast, the α-mannose-modified 1,6-disubstituted pyrene supramolecular polymers (**O8**) displayed sheet-like nanostructures upon AFM analysis. The observed nanosheets size varied between 200 to 700 nm long and about 2.5 nm high.

Intriguingly, the subsequent hypothesis - to increase the stability of the polymer by increasing the hydrophobic interaction - was not completely verified. Indeed, the presence of additional 1,8-disubstituted pyrene units did not induce any additional stability to the supramolecular polymer. However, the addition of 1,6-disubstituted pyrene unit resulted in a higher disassembly temperature.

The interaction between Con A - a protein with a specific binding pocket for the α-mannose units present in the oligomer - and the self-assembled supramolecular polymers was observed with the two types of morphologies. However, it was shown this interaction was non-specific as it was also observed between the protein and the non-modified pyrene trimer, **JJ**.

So far, it has been assumed that the negative charges present at the surface of the supramolecular polymer are enough for the protein to bind electrostatically to the polymer. In order to overcome this shortcoming, one may replace the negatively-charged phosphodiester bridges with a positively charged species, such as amine bridges, to prevent the formation of electrostatic interactions between the surface of the nanostructures and the protein.[131]

Chapter 4

Self-Assembly of Isomeric Pyrene-Cholane and Phenanthrene-Cholane Amphiphiles

In this Chapter, the focus is placed on the self-assembly of several phosphodiester-linked cholane-pyrene-cholane and cholane-phenanthrene-cholane (CPCs) oligomers, as well as the investigation of their supramolecular assembly properties.

All of the previously studied monomers in our group and the ones described in the previous Chapter possess several covalently-linked polyaromatic hydrocarbon (PAH) molecules. In addition to strong hydrophobic effects, their self-assembly process relies on intra- and inter-molecular π-π interactions. The substitution of two PAH building blocks with the non-aromatic, lipophilic and chiral cholane molecule allows us to study what happens when intramolecular π-π interactions are absent.

Previous work showed that the substituted positions on pyrene[50] and on phenanthrene[41,51] have a major influence on the morphology of self-assembled supramolecular polymers (SPs). Therefore, a small library composed of five oligomers, three pyrene-based and two phenanthrene-based, each with a different substitution pattern, was synthesized to observe a variety of morphologies.

After the successful synthesis of the different cholane-pyrene-cholane and cholane-phenanthrene-cholane oligomers, their aggregation process was explored. The spectroscopic properties of the SPs were investigated with UV-vis absorption, fluorescence and circular dichroism measurements, while their morphologies were studied with AFM and

Cryo-EM.

Part of this work has been submitted for publication.

4.1 Results and Discussion

4.1.1 Overview of Cholane - PAH - Cholane Oligomers

The various oligomers used throughout this research project are presented in Scheme 4.1. They were all synthesized in solution and purified by HPLC - detailed procedures are presented in Section 7.3.1. These five trimers consist of either a pyrene or a phenanthrene unit embedded between two phosphodiester-linked cholane moieties.

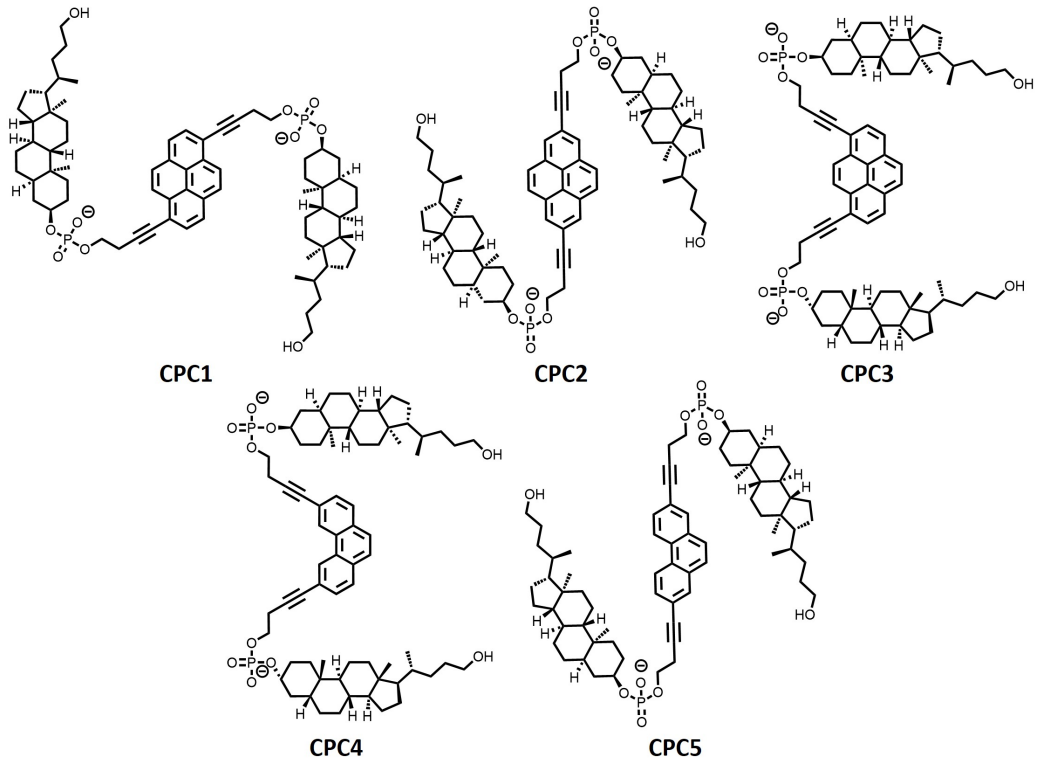

Scheme 4.1: Chemical structure of the different cholane-pyrene-cholane and cholane-phenanthrene-cholane oligomers.

4.1.2 Supramolecular Self-Assembly of Cholane-Pyrene-Cholane Oligomers

In a first series of experiments, the three cholane-pyrene-cholane oligomers (**CPC1** to **CPC3**) were studied and compared. The goal was to characterize the spectroscopic

changes occurring upon self-assembly for all three oligomers and to examine the different supramolecular morphologies upon aggregation. Additionally, the chiral properties of the oligomers during aggregation were recorded.

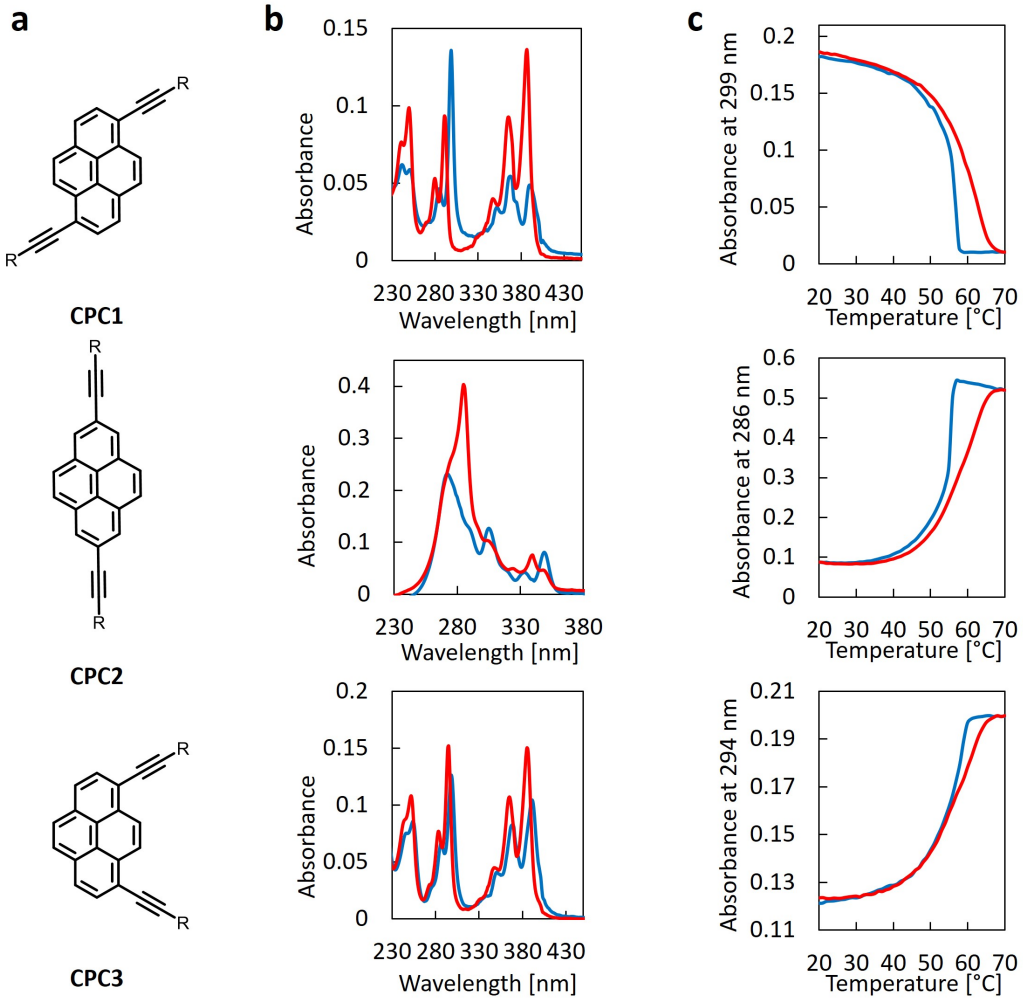

Figure 4.1: (a) Chemical structures of the three pyrene oligomers; (b) UV-Vis absorption spectra at 70 °C (red) and 20 °C (blue); (c) Cooling (blue) and heating (red) curves of the respective CPC trimers. Conditions: 3 µM oligomer, 10 mM sodium phosphate buffer pH 7.2, 10 mM NaCl and EtOH (20% for **CPC1**, 25% for **CPC2** and 15% for **CPC3**).

The self-assembly behavior of the oligomers was first studied through UV-vis absorption (Figure 4.1), followed by fluorescence excitation and emission (Figure 4.2). Temperature-dependent UV-vis absorption spectra were recorded for all three oligomers. Upon controlled cooling from 70 °C to 20 °C (0.5 °C/min), significant changes were observed in the absorbance of the oligomers. **CPC1** exhibited strong hypochromicity for

the bands present between 355 nm and 405 nm along with the appearance of a sharp *J*-band at 298 nm. These changes have been previously described in 1,6-disubstituted pyrene trimers[49] (see also in Chapter 3, Section 3.1.5). The 2,7-disubstituted pyrene oligomer (**CPC2**) displayed a strong hypochromic effect and a hypsochromic shift from 285 nm to 272 nm along with a bathochromic shift from 339 nm to 350 nm. The final oligomer, **CPC3**, showed a combination of hypochromicity and bathochromic shifts for all its bands, these latter varying between 3 to 6 nm.

Upon analysis of the absorption of the different oligomers during the cooling and the heating process (Figure 4.1c), it was determined that the self-assembly followed a nucleation-elongation process.[132,133] The beginning of the self-assembly process is highlighted by a sharp change in the absorption upon cooling. The nucleation temperature was found to be between 56 °C and 59 °C, depending on the oligomer (see Table 4.1).

Table 4.1: Nucleation temperature of oligomers **CPC1** to **CPC3**.

	CPC1	**CPC2**	**CPC3**
Nucleation Temp.	57 °C	56 °C	59 °C

Excitation and emission fluorescence temperature-dependent spectra were recorded for all three trimers (Figure 4.2). Unlike the previously reported 1,6-disubstituted pyrene trimers,[49] **CPC1** did not exhibit any excimer fluorescence upon self-assembly, and only very little monomer fluorescence (Figure 4.2a). In contrast, oligomers **CPC2** and **CPC3** exhibit fluorescence upon aggregation at 20 °C. In the case of **CPC2**, monomer emission was observed to decrease by half upon self-assembly, whereas for **CPC3**, the monomer emission vanished, but the excimer emission at 515 nm was increased, indicating a close proximity between the pyrene units of the different monomers upon aggregation. A minor excimer fluorescence at 70 °C is observed, likely due to the interaction of some monomers.

AFM (Figure 4.3) and cryo-EM (Figure 4.4) measurements were performed to visualize the formed supramolecular aggregates. The self-assembled nanostructures were deposited on (3-aminopropyl)-triethoxysilane (APTES)-modified mica sheets. Three different kinds of morphologies were observed. Upon cooling, **CPC1** showed tube- and sheet-like supramolecular polymers (Figure 4.3a and Figure 7.63). It is important to note that the ratio of nanosheets to nanotubes may be influenced by changing the cooling rate during sample preparation. A lower cooling rate (0.1 °C/min) results in a higher amount of nanosheets forming and an increase in their length (see Figure 7.64). In both cases, the nanosheets were found to be 2 nm high, while their side lengths varied between

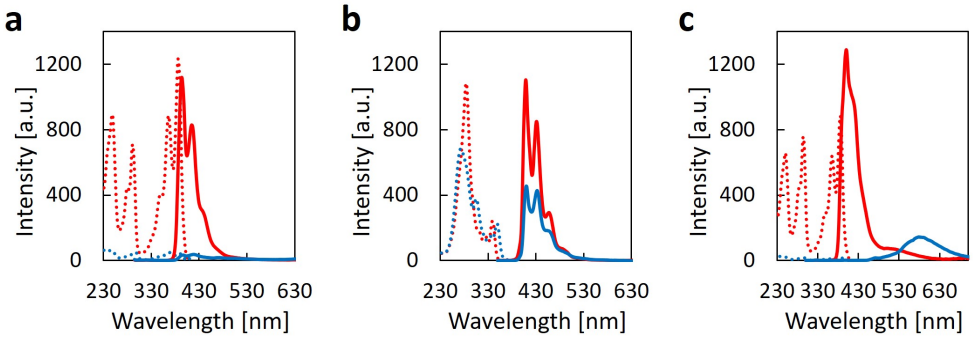

Figure 4.2: Fluorescence excitation (dotted line) and emission (solid line) spectra of the different pyrene oligomers at 70°C (red) and 20 °C (blue). (a) **CPC1** λ_{ex}: 290 nm and λ_{em}: 415 nm; (b) **CPC2** λ_{ex}: 284 nm and λ_{em}: 409 nm; (c) **CPC3** λ_{ex}: 294 nm and λ_{em}: 415 nm. Conditions: 3 µM oligomer, 10 mM sodium phosphate buffer pH 7.2, 10 mM NaCl and EtOH (20% for **CPC1**, 25% for **CPC2** and 15% for **CPC3**.)

0.3 to 5 µm. The height of 2 nm corresponds well with the molecular dimensions of the trimer (Scheme 7.6). On the other hand, the observed nanotubes are up to 2 µm long and have heights up to 12 nm with increments of 4 nm. This last value correlates well with a collapsed tube with a membrane thickness of 2 nm.[41] Unlike AFM images, only one species was observed in cryo-EM (Figure 4.4a and Figure 7.71). Measurements revealed hollow linear objects indicating the presence of nanotubes that co-exist as single- and multi-walled species. The diameter of these tubes varies between 30 and 80 nm. Over their whole length, the diameter stays very regular with differences only up to 4%. The absence of sheets in cryo-EM images can be explained by their small cross-section, which makes them difficult to detect.

Unlike **CPC1**, **CPC2** only exhibited one species in AFM (Figure 4.3b and Figure 7.65) and in cryo-EM measurements (Figure 4.4b and Figure 7.72) upon self-assembly. The nanotubes were determined to be up to 10 µm long and between 4 and 24 nm high, with increments of 4 nm. The membrane thickness of the tubes observed with **CPC2**, is the same as for **CPC1**, about 2 nm. Their diameter varies between 30 and 65 nm.

In opposition to its counterparts, the trimer containing the 1,8-disubstituted-pyrene, **CPC3**, displayed nanostructures that are best described as *worm-like* upon aggregation. AFM measurements (Figure 4.3c and Figure 7.66) reveal structures possessing a height of 8 nm and are up to 20 µm long. After observation of a broken part of the worm (see cross section 1, in red), 2 nm steps are present, corresponding to the membrane thickness of the nanostructure. The worm-like supramolecular polymer were confirmed through cryo-EM measurements (Figure 4.4c and Figure 7.73). The observed structures

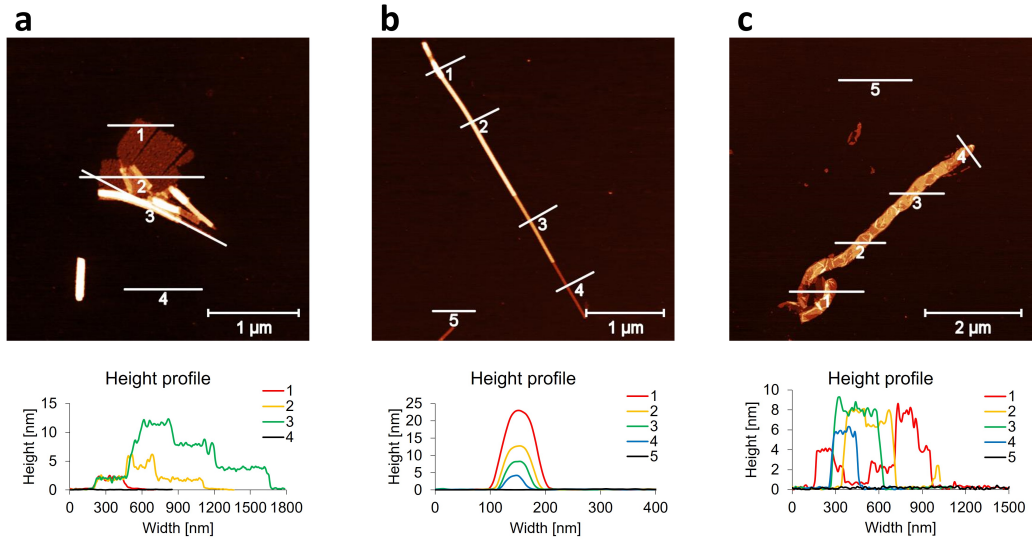

Figure 4.3: (Top) AFM measurements of (a) **CPC1**; (b) **CPC2**; (c) **CPC3**. (Bottom) Their respective cross-sections. Conditions: 3 µM oligomer, 10 mM sodium phosphate buffer pH 7.2, 10 mM NaCl and EtOH (20% for **CPC1**, 25% for **CPC2** and 15% for **CPC3**.)

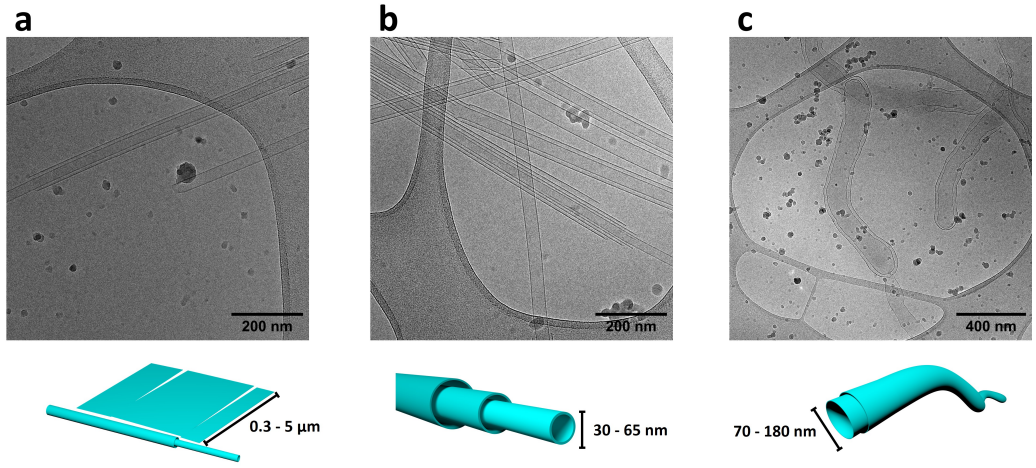

Figure 4.4: (Top) Cryo-EM measurements of (a) **CPC1**; (b) **CPC2**; (c) **CPC3**. (Bottom) Schematic representation of the supramolecular polymers. Conditions: 3 µM oligomer, 10 mM sodium phosphate buffer pH 7.2, 10 mM NaCl and EtOH (20% for **CPC1**, 25% for **CPC2** and 15% for **CPC3**.)

are composed of two membranes with a diameter ranging between 70 and 180 nm. The SPs presumably collapse on the mica sheet which results in the formation of four layered objects with a total height of 8 nm.

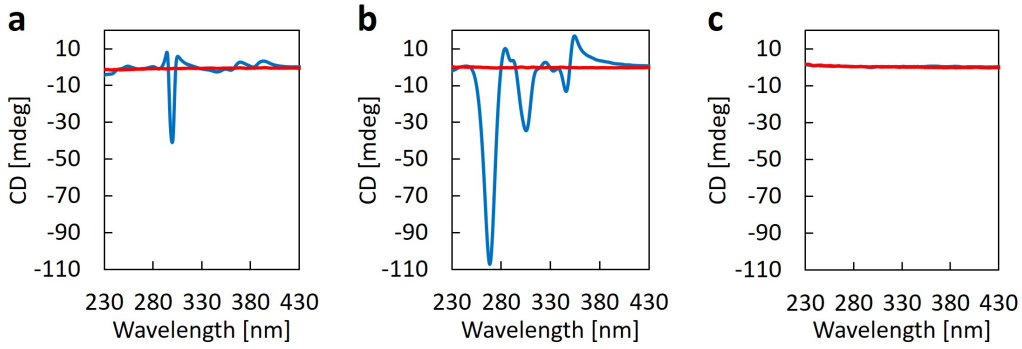

Figure 4.5: Circular dichroism of (a) **CPC1**; (b) **CPC2**; (c) **CPC3** at 70°C (red) and 20 °C (blue). Conditions: 3 µM oligomer, 10 mM sodium phosphate buffer pH 7.2, 10 mM NaCl and EtOH (20% for **CPC1**, 25% for **CPC2** and 15% for **CPC3**.)

The oligomers possess several chiral centers, therefore circular dichroism measurements were performed before and after self-assembly (Figure 4.5). None of the three oligomers were optically active in their dissociated form at 70 °C. However, the supramolecular polymers formed by **CPC1** and **CPC2** exhibited some optical activity upon self-assembly. Highlighted by the blue spectra, both oligomers absorbed circular-polarized light. The supramolecular worm-like polymer on the other hand did not exhibit any chiroptical properties.

In summary, the self-assembly of cholane-pyrene-cholane trimers was demonstrated. Several different morphologies were observed depending on the pyrene isomer present in the oligomer. **CPC1** revealed the formation of tubes and sheet-like nanostructures (with an increase of the observed sheets upon a slower cooling gradient). The thermal assembly of **CPC2** resulted in the formation of single- and multi-walled species while **CPC3** displayed worm-like nanostructures upon aggregation.

4.1.3 Supramolecular Self-Assembly of Cholane-Phenanthrene-Cholane Oligomers

In a similar fashion as for their pyrene counterparts, the aggregation behavior of cholane-phenanthrene-cholane trimers (**CPC4** and **CPC5** present in Scheme 4.1) were studied in aqueous conditions. This was done by monitoring the spectroscopic changes in their UV-vis absorption spectra (Figure 4.6), their fluorescence excitation and emission spectra (Figure 4.7) and in their circular dichroism absorption (Figure 4.10). In addition, the morphology of the supramolecular polymers was observed though AFM (Figure 4.8) and cryo-EM measurements (Figure 4.9).

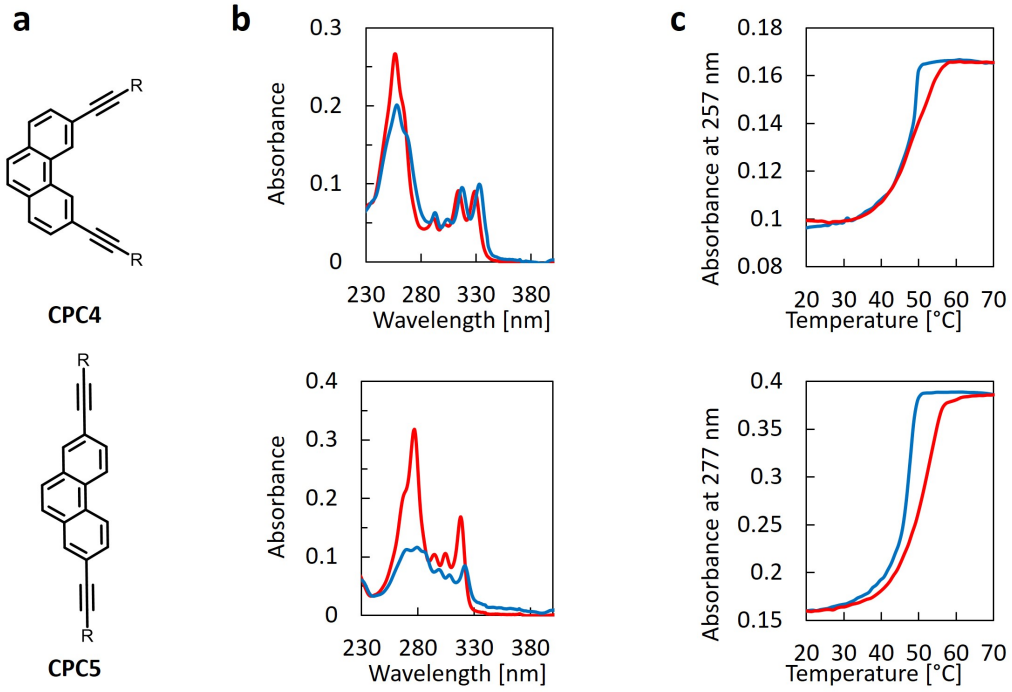

Figure 4.6: (a) Chemical structure of the two phenanthrene oligomers; (b) UV-Vis absorption spectra at 70 °C (red) and 20 °C (blue); (c) Cooling (blue) and heating (red) curves of the respective CPC trimers. Conditions: 3 µM oligomer, 10 mM sodium phosphate buffer pH 7.2, 10 mM NaCl and EtOH (15% for **CPC4**, 20% for **CPC5**.)

As previously described, the self-assembly process was initially studied through temperature dependent UV-vis absorption (Figure 4.6). Upon thermal assembly (0.5 °C/min), **CPC4** exhibits hypochromicity from its band at 257 nm along with a small bathochromic shift from its bands between 314 nm and 328 nm of 3 to 5 nm. On the other hand, **CPC5** displays a hypochromic effect over its whole spectra - with a major reduction of its band at 277 nm - along with small bathochromic shifts in the region between 294 and 318 nm of 3 nm. The aggregation process followed by both oligomers was a nucleation-elongation process, which is identical to the one followed by the cholane-pyrene-cholane trimers. This was determined by monitoring the absorption of the trimers during the cooling and heating process (Figure 4.6c). The nucleation process was determined to start at the same temperature, 51 °C, for both oligomers (Table 4.2).

Pursuing the spectroscopic characterization of the different phenanthrene trimers, excitation and emission fluorescence were recorded before and after aggregation (Figure 4.7). In contrast to its pyrene counterpart (**CPC3**), **CPC4** exhibited an increased

Table 4.2: Nucleation temperature of oligomers **CPC4** and **CPC5**.

	CPC4	**CPC5**
Nucleation Temp.	51 °C	51 °C

phenanthrene monomer fluorescence upon self-assembly while excimer fluorescence was absent. On the other hand, the linear phenanthrene isomer, **CPC5**, displayed a monomer fluorescence reduced by half upon aggregation between 360 and 490 nm, which is comparable to **CPC2** (see Figure 4.2c).

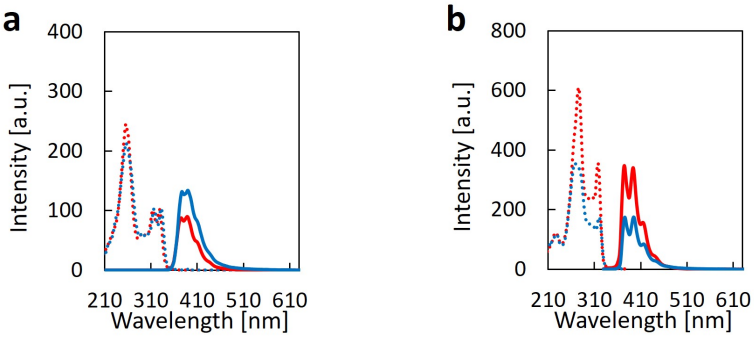

Figure 4.7: Fluorescence excitation (dotted line) and emission (solid line) spectra of the different phenanthrene oligomers at 70 °C (red) and 20 °C (blue). (a) **CPC4** λ_{ex}: 333 nm and λ_{em}: 375 nm; (b) **CPC5** λ_{ex}: 320 nm and λ_{em}: 394 nm. Conditions: 3 µM oligomer, 10 mM sodium phosphate buffer pH 7.2, 10 mM NaCl and EtOH (15% for **CPC4**, 20% for **CPC5**).

The morphology of the different self-assembled phenanthrene oligomers was then investigated through AFM and cryo-EM. AFM measurements performed on the first phenanthrene isomer, **CPC4**, revealed the formation of worm-like nanostructures (see Figure 4.8a and Figure 7.67), while **CPC5** aggregates into nanotubes (see Figure 4.8b and Figure 7.69). The overall dimensions of the worms observed with **CPC4** are similar to the ones formed with its pyrene counterpart, **CPC3**. The height of these structures is about 8 nm high while their length varies between 2 and 30 µm. In addition, cryo-EM measurements (see Figure 4.9a and Figure 7.74) revealed the presence of a double membrane with a diameter ranging from 100 to 310 nm. Through AFM measurements, the **CPC5** nanotubes were observed to be between 8 and 16 nm high and up to 2 µm long. While cryo-EM images (see Figure 4.9b and Figure 7.75) revealed diameters between 30 and 80 nm, along with the presence of mostly bi-layered tubes. For both oligomers, the observation of a double layer correlates well with the data recorded with AFM, the height resulting from four membrane stacked on top of each other reaching about 8 nm.

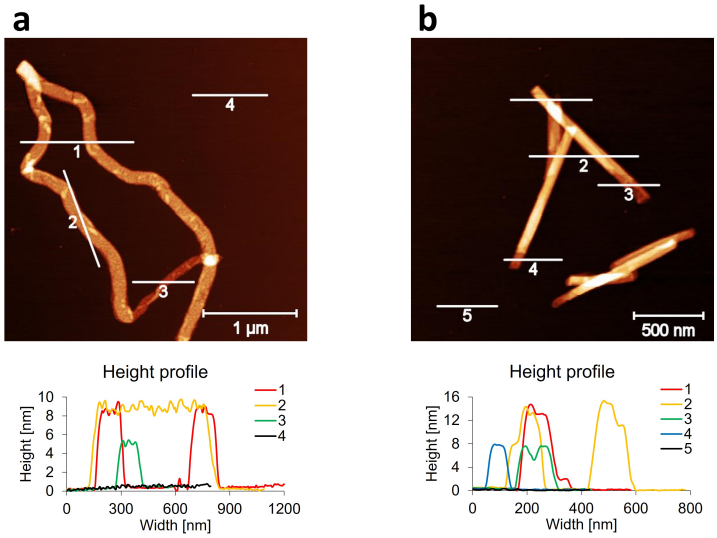

Figure 4.8: (Top) AFM measurements of (a) **CPC4**; (b) **CPC5**. (Bottom) Their respective cross-sections. Conditions: 3 µM oligomer, 10 mM sodium phosphate buffer pH 7.2, 10 mM NaCl and EtOH (15% for **CPC4**, 20% for **CPC5**)

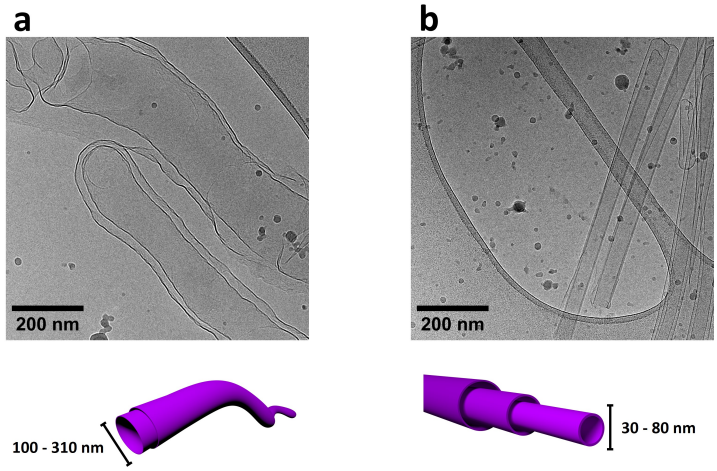

Figure 4.9: (Top) Cryo-EM measurements of (a) **CPC4**; (b) **CPC5**. (Bottom) Schematic representation of the supramolecular polymers. Conditions: 3 µM oligomer, 10 mM sodium phosphate buffer pH 7.2, 10 mM NaCl and EtOH (15% for **CPC4**, 20% for **CPC5**.)

As for their pyrene counterparts, these oligomers are chiral. Circular dichroism experiments were performed before and after self-assembly (Figure 4.10). None of the two oligomers were optically active in their dissociated form at 70 °C. In a similar fashion as

for the worm-like supramolecular polymer formed by **CPC3**, the worm-like nanostructures formed by **CPC4** did not exhibit any optical activity upon aggregation. However, the self-assemblies formed by **CPC5** displayed some chiroptical properties as highlighted by the blue spectra in Figure 4.10b.

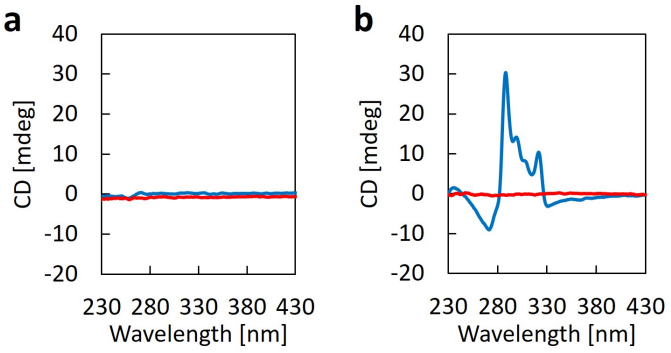

Figure 4.10: Circular dichroism of (a) **CPC4**; (b) **CPC5** at 70 °C (red) and 20 °C (blue). Conditions: 3 µM oligomer, 10 mM sodium phosphate buffer pH 7.2, 10 mM NaCl and EtOH (15% for **CPC4** and 20% for **CPC5**.)

In summary, the self-assembly of the two different cholane-phenanthrene-cholane oligomers **CPC4** and **CPC5** gave rise to two different types of supramolecular polymers. The 3,6-disubstituted isomer (**CPC4**) exhibited a worm-like nanostructures, while **CPC5** (the 2,7-disubstituted isomer) self-assembled into optically active nanotubes.

4.1.4 Influence of the Temperature Gradient on the Aggregation

Previous work performed with phenanthrene trimers have shown that the temperature gradient applied to the system did not have an influence on the spectroscopic properties of the oligomer.[120] The presence of various substitution patterns on the PAHs present in our trimers construct have led us to study the spectroscopic and self-assembling properties of both phenanthrene oligomers upon application of a faster temperature gradient (10 °C/min).

The spectroscopic properties of both oligomers were recorded after cooling with both cooling gradients (Figure 4.11). The 3,6-disubstituted phenanthrene oligomer (**CPC4**) exhibited minor changes in both UV-vis absorption (Figure 4.11b, top) and fluorescence excitation and emission spectra (Figure 4.11c, top). In contrast, the spectroscopic properties of **CPC5** were altered when different temperature gradients were applied to the system. The hypochromic effect, in the UV-vis spectra (Figure 4.11b, bottom), of the band at 276 nm was found not to be identical upon slow and fast cooling. Differences

also arise in the fluorescence excitation and emission spectra (Figure 4.11c, bottom). The fluorescence intensity was found to be lower when a faster cooling gradient was applied. Both observations led into considering a disordered aggregation of **CPC5** in such conditions.

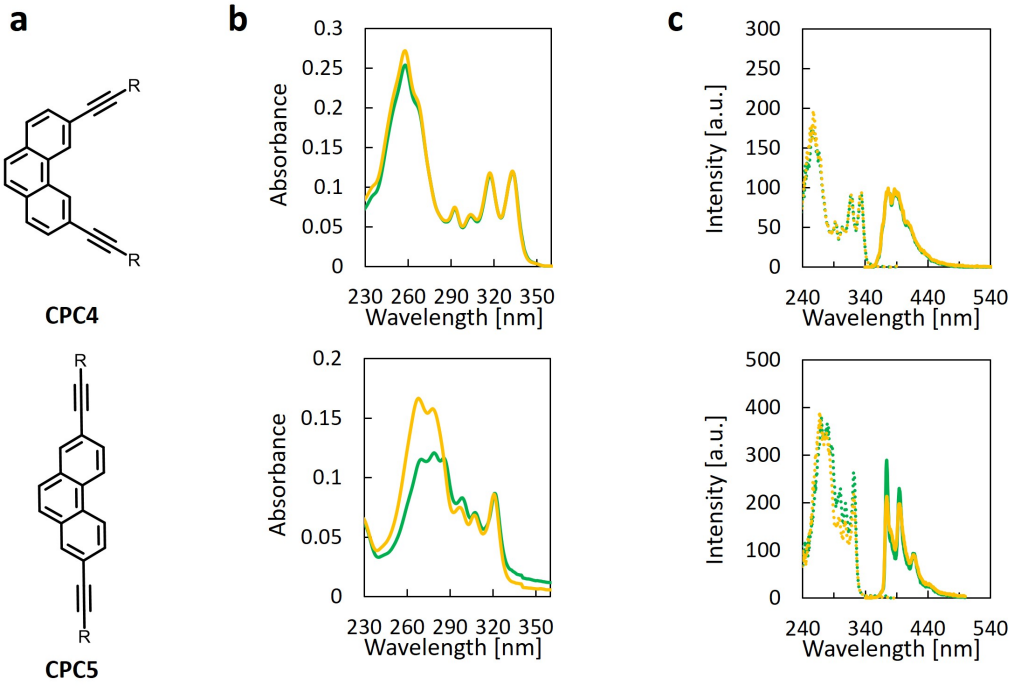

Figure 4.11: (a) Chemical structure of **CPC4** (top) and **CPC5** (bottom); (b) UV-Vis absorption spectra at 20 °C after a gradient of 0.5 °C per min (green) and after a gradient of 10 °C/min (yellow); (c) Fluorescence excitation (dotted line) and emission (solid line) spectra of the different phenanthrene oligomers at 20 °C after a gradient of 0.5 °C/min (green) and after a gradient of 10 °C/min (yellow); **CPC4** λ_{ex}: 333 nm and λ_{em}: 375 nm, **CPC5** λ_{ex}: 320 nm and λ_{em}: 394 nm. Conditions: 3 µM oligomer, 10 mM sodium phosphate buffer pH 7.2, 10 mM NaCl and EtOH (15% for **CPC4**, 20% for **CPC5**.)

From the slight changes taking place in the spectroscopic properties of **CPC4**, it was assumed the morphology of the aggregates formed with a faster cooling rate would lead to the formation of worm-like nanostructures. However, AFM measurements revealed the presence of small circular nanostructures possessing a height of approximately 4 nm and a width between 40 and 150 nm (see Figure 4.12a). The larger structures observed are very likely to be several aggregates interacting together as their height is always a multiple of 4. An identical morphology was observed for the fast self-assembly of **CPC5** (Figure 4.12b). However, in this case, the nanostructures are thinner with a height varying between 2 and 10 nm high with 2 nm increments, while their width is ranging

from 50 to 400 nm.

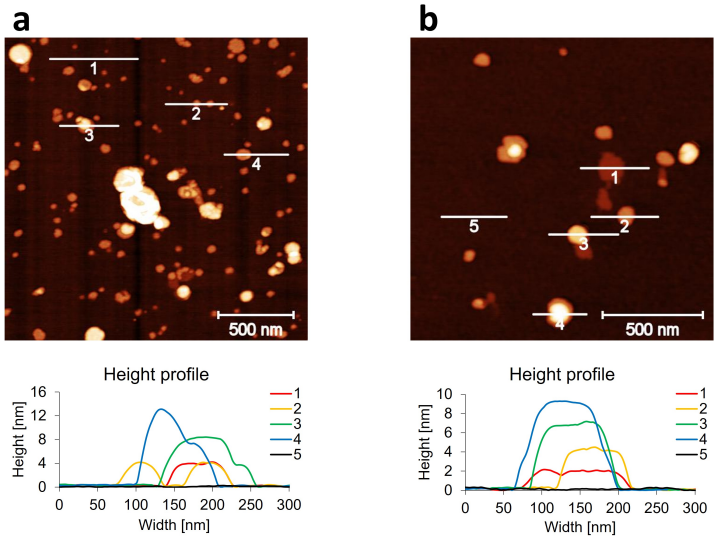

Figure 4.12: AFM measurements of (a) **CPC4**; (b) **CPC5** with their respective cross-sections with a temperature gradient of 10 °C/min. Conditions: 3 µM oligomer, 10 mM sodium phosphate buffer pH 7.2, 10 mM NaCl and EtOH (15% for **CPC4**, 20% for **CPC5**).

These structures may be associated with two different kinds of morphologies, sheets and/or vesicles. Previous work has shown that observation of nanosheets is highly unlikely with this method. Whereas the observation of vesicles has been reported numerous amount of times. Therefore, the absence of nanostructures observed in cryo-EM measurements led us to assume **CPC4** and **CPC5** aggregate into nanosheets when a cooling rate of 10 °C/min is applied.

4.2 Conclusions and Outlook

The synthesis and self-assembly behavior of cholane-pyrene-cholane and cholane-phenanthrene-cholane oligomers have been described. The structural diversity present within the oligomer constructs were found to be a major influence in the self-assembly process, resulting in different supramolecular morphologies (see Table 4.3).

CPC1 revealed the formation of tubes and sheet-like nanostructures. The nanosheets had a height of about 2 nm while their side length varied between 0.3 to 5 µm depending on the cooling gradient. The nanotubes observed through AFM and cryo-EM possess a membrane thickness of about 2 nm, their diameter fluctuated between 30 to 80 nm and are up to 2 µm long. The thermal assembly of **CPC2** resulted in the formation of single- and multi-walled nanotubes. These structures had a membrane thickness of 2

Table 4.3: Summary of the aggregation patterns of **CPC1** to **CPC5** with a temperature gradient of 0.5 °C/min.

	CPC1		**CPC2**	**CPC3**	**CPC4**	**CPC5**
Chemical Structure	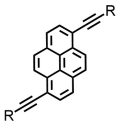			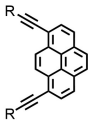	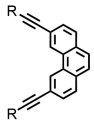	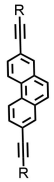
Morphology						
Chiroptical Activity	Yes			Yes	No	No	Yes
Length [µm]	Sheet	Tube		10	20	30	2
	0.3 - 5	2					
Diameter [nm]	-		30 - 80	30 - 65	70 - 180	100 - 310	30 - 80
Membrane	-		1	1	2	2	1

nm, a diameter varying between 30 and 65 nm and up to 10 µm long. While **CPC3** displayed worm-like nanostructures upon aggregation, which was found to be structurally hollow, composed of a double membrane with a 2 nm thickness, a diameter between 70 and 180 nm, and were found to be up to 20 µm long.

The phenanthrene oligomers on the other hand self-assembled into two different kinds of supramolecular polymers, worms and tubes. The worm-like nanostructures were observed with **CPC4** and possess morphological properties close to **CPC3**, and possessed two membranes which were 2 nm thick, up to 30 µm long, and had a diameter between 100 and 310 nm. The single and multi-walled nanotubes observed with **CPC5** exhibited similar morphological properties with the ones observed with **CPC2**, having a diameter varying between 30 and 80 nm and were up to 2 µm long. Additional information about the self-assemblies of all five oligomers may be obtained through cryo-EM tomography.

It is to be noted that the cooling rate for the self-assembly process plays a direct role on the morphology and the spectroscopic properties of the assembled supramolecular polymers. Reducing the cooling rate from 0.5 °C/min to 0.1 °C/min for **CPC1** resulted in a change in the tube/sheet ratio and in the formation of larger sheets. On the other hand, an increase of the cooling gradient to 10 °C/min for **CPC4** and **CPC5** resulted in the formation of small circular nanosheets. The increase in the thermal as-

sembly process also had an impact on the spectroscopic properties of the latter oligomer.

Additionally, the supramolecular polymers formed by the self-assembly of **CPC1**, **CPC2** and **CPC5**, were found to be optically active while the ones formed by the aggregation of **CPC3** or **CPC4** did not exhibit any optical properties.

Finally, structurally-close oligomers such as **CPC2** and **CPC5** or **CPC3** and **CPC4** had similar morphologies indicating an analogous self-assembly process. This could lead to further investigation regarding a potential light-harvesting system bearing both oligomers.

The supramolecular diversity shown by the oligomers could also lead to their use as supramolecular scaffolds. The different morphologies observed with the change in the pyrene substitution pattern could lead to having different applications such as the internalization of compounds with the worms or the use of nanosheets as a platform for screening specific interactions.

Chapter 5

Light-Harvesting Properties of Self-Assembled Cholane-Phenanthrene-Cholane Amphiphiles

This Chapter highlights the light-harvesting properties of four co-assemblies, based on combinations of the different phenanthrene and pyrene oligomers previously presented. The energy transfer capabilities and the self-assembly behavior of the different systems have been investigated.

The energy transfer properties of phenanthrene have been thoroughly studied. It has been shown that this PAH is very versatile as it can act as an energy acceptor as well as an energy donor. It is present in a wide variety of fields, and is used to transfer energy to various species, such as gases,[134] metal complexes,[135] lanthanide ions in aqueous micellar solutions,[136] polymers,[137] and even supramolecular polymers.[51,120] However, in most of the work previously cited, phenanthrene, when acting as an energy donor, is in very close proximity to the energy acceptor, either through direct covalent bonding or through non-covalent interactions. Herein, the presence of a non-chromophoric species in the oligomer (cholane) dilutes the system and increases the distance between the acceptor and the donor chromophore.

A schematic illustration of this work is present in Scheme 5.1. It was conducted by adding increasing amounts of the acceptor oligomer (blue) to the donor oligomer (purple). The solution was first heated to ensure a full dissociated state and then cooled to observe self-assembled supramolecular polymers. Previous work presented in Chapter 4 highlighted changes in the spectroscopic properties of **CPC4** and **CPC5**, along with

their morphologies, when different cooling rates are applied. The following work has therefore been performed at two different temperature gradients: 0.5 °C/min and 10 °C/min, referred to hereafter as slow and fast cooling respectively.

The quantum yield of each addition was calculated and the different systems were compared to one another. The spectroscopic measurements revealed a strong capability to transfer energy, while AFM indicated in one case a self-sorting behavior.

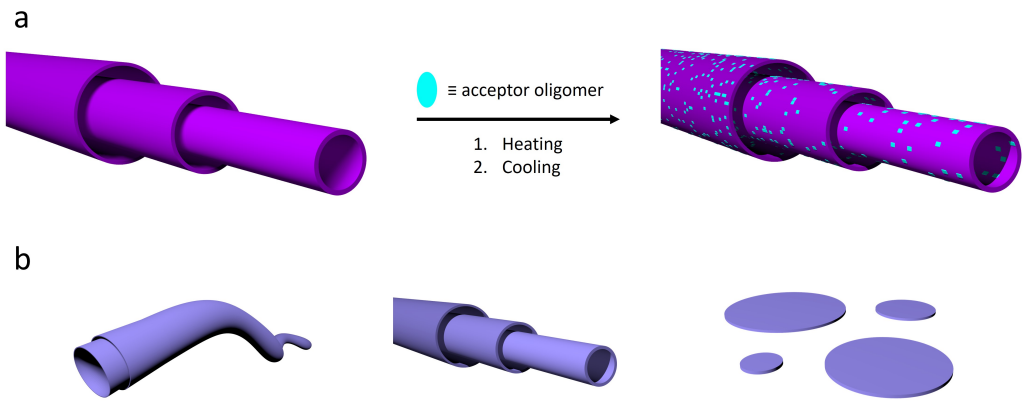

Scheme 5.1: (a) Schematic illustration of self-assembled phenanthrene CPC supramolecular polymer (purple) before and after the addition of the acceptor oligomer (blue). (b) Schematic illustration of the doped systems based on the previously observed phenanthrene morphologies, for clarity due to the size of the illustrations, these systems will be colored in Lila throughout this chapter.

5.1 Results and Discussion

The different oligomers used throughout this chapter are presented in Scheme 5.2. The study of their UV-vis absorption and fluorescence spectra show that a pronounced spectral overlap is present between the absorption bands of the acceptor oligomers, **CPC1** and **CPC3**, and the emission bands of the donor oligomers, **CPC4** and **CPC5** (see Figure 5.1). This observation is important as it is a requirement to observe excitation energy transfer *via* Förster resonance energy transfer (FRET).[106]

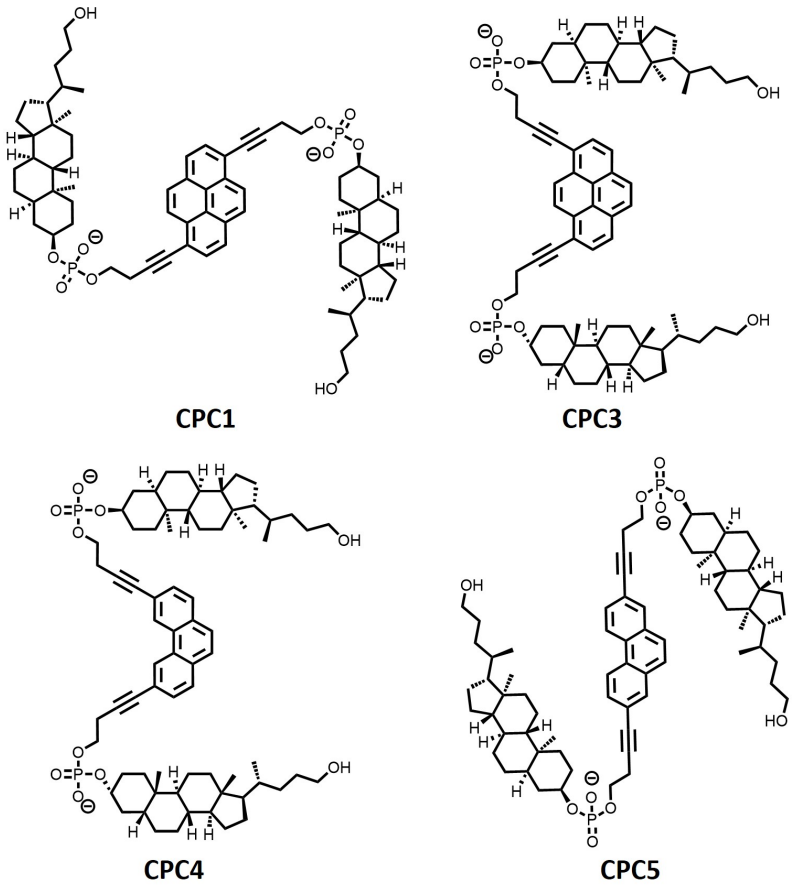

Scheme 5.2: Chemical structure of the cholane-pyrene-cholane oligomers (**CPC1** and **CPC3**) and cholane-phenanthrene-cholane oligomers (**CPC4** and **CPC5**).

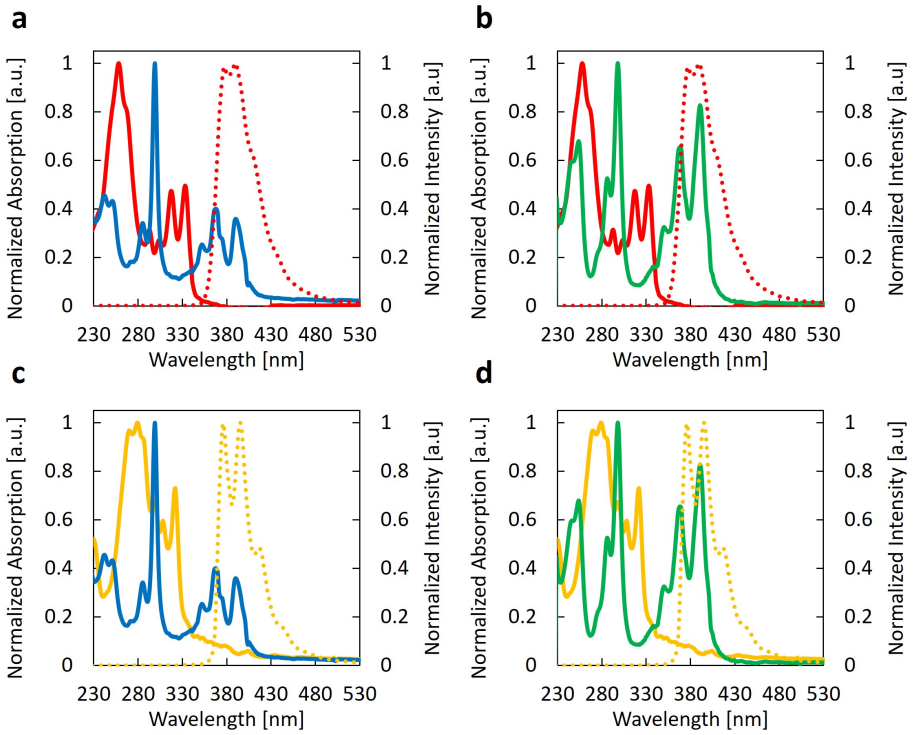

Figure 5.1: Normalized UV-vis absorption (solid line) of all self-assembled oligomers and fluorescence emission (dotted) of self-assembled phenanthrene oligomers. (a) **CPC4** (red) and **CPC1** (blue); (b) **CPC4** (red) and **CPC3** (green); (c) **CPC5** (orange) and **CPC1** (blue); (d) **CPC5** (orange) and **CPC3** (green). Conditions: 3 µM oligomer, 10 mM sodium phosphate buffer pH 7.2, 10 mM NaCl and EtOH (20% for **CPC1**, 15% for **CPC3**, 15% for **CPC4**, 20% for **CPC5**), λ_{ex}: 333 nm for **CPC4** and λ_{ex}: 320 nm for **CPC5**.

5.1.1 Light-Harvesting Properties of CPC4

The 3,6-disubstituted phenanthrene oligomer, **CPC4**, has previously shown to self-assemble into round sheets and worm-like nanostructures when different cooling rates were applied. It was however established that the morphological differences did not have any effect on the spectroscopic properties of the assembly (see Section 4.1.4, Chapter 4). The light-harvesting properties of both morphological self-assemblies were studied upon excitation of **CPC4** (at 333 nm) and the addition of increasing amounts of **CPC1** or **CPC3** (0.3% to 24%). The fluorescence emission spectra of the different systems were recorded (Figure 5.2a, b, d and e). The quantum yield was then calculated for every addition (Figure 5.2c and f) and AFM measurements were performed for the addition inducing the highest changes (Figure 5.3 and Figure 5.4).

Immediately after the addition of 0.3% of **CPC1** to **CPC4**, and a fast cooling (Fig-

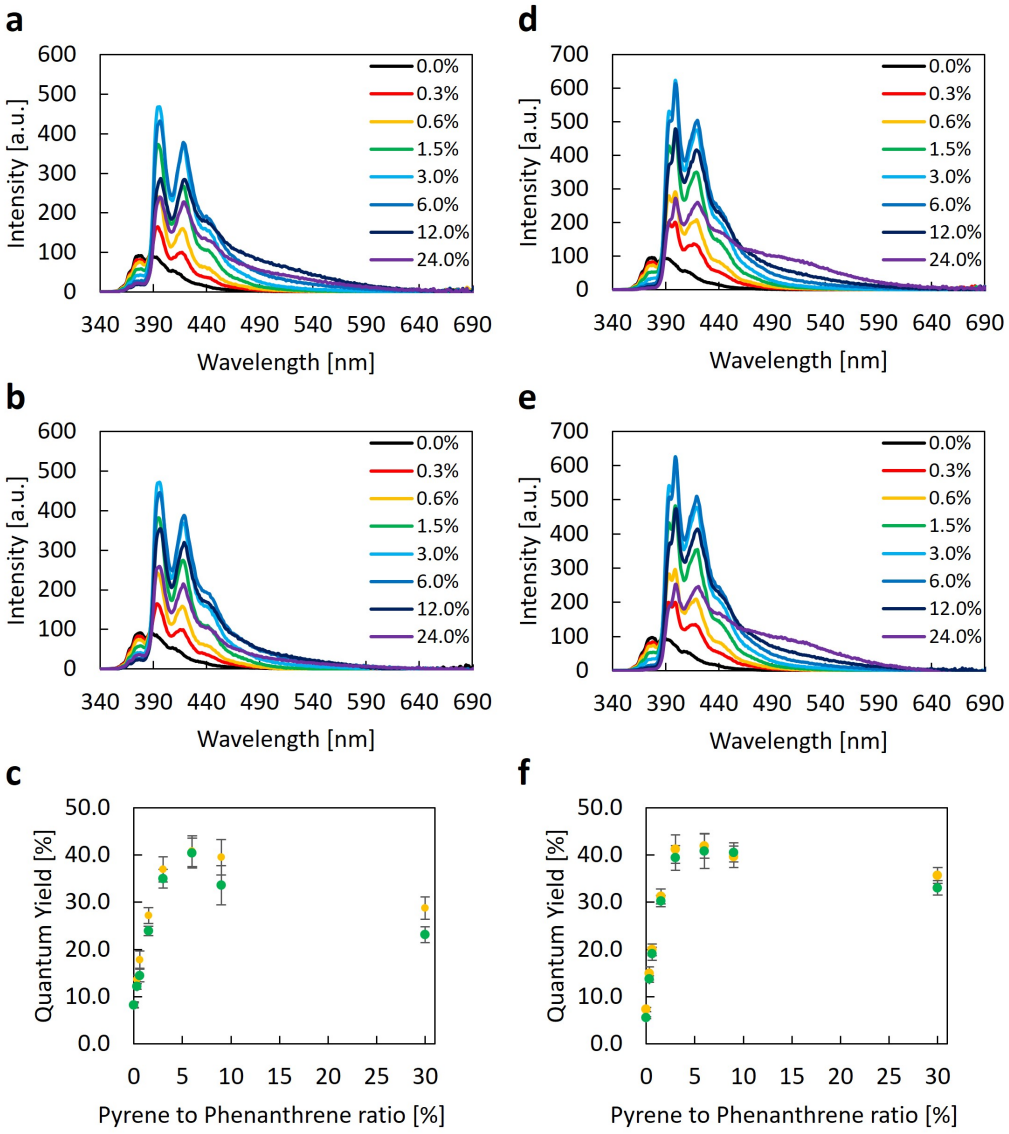

Figure 5.2: Fluorescence emission spectra of **CPC4** in presence of increasing amounts of **CPC1** (0 to 24%) with a cooling rate of (a) 10 °C/min; (b) 0.5 °C/min; (c) Quantum yield of both systems, in yellow at 10 °C/min and in green at 0.5 °C/min. Fluorescence emission spectra of **CPC4** in presence of increasing amounts of **CPC3** (0 to 8%) with a cooling rate of (d) 10 °C/min; (e) 0.5 °C/min; (f) Quantum yield of both systems, in yellow at 10 °C/min and in green at 0.5 °C/min. Conditions: 3 µM oligomer, 10 mM sodium phosphate buffer pH 7.2, 10 mM NaCl and 15 % EtOH, λ_{ex}: 333 nm.

ure 5.2a, red line), a strong pyrene monomer fluorescence was observed (with two local maxima at 396 nm and 418 nm, identical to those observed for **CPC1** alone as seen in Figure 4.2a). This indicates that energy transfer takes place between the phenanthrene oligomer (donor) and the pyrene oligomer (acceptor). The decrease in the phenanthrene

monomer fluorescence coupled to the increase in pyrene monomer fluorescence implies the presence of a FRET mechanism. The combined increase in quantum yield from 8% to 13% reveals an additional excitation energy transfer mechanism (*e.g.*, coherent EET). As the amount of **CPC1** increased, the phenanthrene fluorescence emission decreased and the monomer pyrene fluorescence rose until reaching a maximum at 6% before decreasing again after the addition of 24% of **CPC1**. This decrease occurs simultaneously with the appearance of a broad band around 520 nm, characteristic of the presence of a pyrene excimer which indicates van der Waals interactions between the pyrene units.[138] The origin of the pyrene excimer can be explained by the rising concentration of pyrene oligomer in the system, increasing their probability to interact directly with one another. The quantum yields (Figure 5.2c, yellow) follow the same trend, with a maximum of 40.8 ± 3.2% observed after the addition of 6% of **CPC1** to **CPC4** which corresponds to a five-fold increase compared to **CPC4** alone.

The use of a slower cooling rate did not result in any significant differences with a maximal pyrene monomer fluorescence observed after the addition of 6% of **CPC1** (Figure 5.2b). A quantum yield of 40.4 ± 3.2% was observed with this temperature gradient which corresponds as well to a five-fold increase to the undoped **CPC4.** A minor change occurred after the addition of 12% of **CPC1**, where the reduction in phenanthrene fluorescence was not accompanied by a pyrene excimer fluorescence. The corresponding quantum yields no longer overlap with the ones obtained after a fast cooling (Figure 5.2c, green).

The second system formed by **CPC4** with **CPC3** exhibited a similar behavior to the previous one. As shown in Figure 5.2d, after a fast cooling, a strong fluorescence was observed upon the addition of the 1,8-disubstituted pyrene to **CPC4**. This fluorescence is once again associated with the pyrene monomer fluorescence and is present after the addition of 0.3% of the pyrene oligomer. It reaches a maximum after the addition of 6% of **CPC3** before a slow reduction after adding 24% of it. This decline was accompanied by an increase in the pyrene excimer fluorescence emission observed between 480 and 590 nm. The quantum yield associated with this couple of oligomers after a fast self-assembly process also reach a maximum of 41.9 ± 2.6% after the addition of 6% of **CPC3** corresponding once more to a five-fold increase to the native **CPC4**. A slight reduction in the quantum yield took place (see Figure 5.2f, yellow) after the addition of higher amounts of **CPC3**.

The use of a cooling gradient of 0.5 °C/min did not have a significant impact on the spectroscopic properties of the system composed of oligomers **CPC4** and **CPC3**. The fluorescence emission spectra recorded after a slower self-assembly process (Figure 5.2e)

were similar to the ones measured after a fast cooling process. The quantum yields calculated for this system were identical (within the error margins) to the ones previously measured (see Figure 5.2f, green).

The maximal quantum yield measured for all the previously stated conditions are summarized in Table 5.1.

Table 5.1: Quantum yields of **CPC4** in presence of 6% **CPC1** or 6% **CPC3**.

	CPC1		**CPC3**	
Cooling Gradient	10 °C/min	0.5 °C/min	10 °C/min	0.5 °C/min
Φ_F [%]	40.8 ± 3.2	40.4 ± 3.2	41.9 ± 2.6	40.9 ± 3.7
Increase vs $\Phi_{\mathbf{CPC4}}$	5x	5x	5x	5x

In all four experiments, a decrease in the phenanthrene emission was observed while the pyrene emission increased. This observation, along with the spectral overlap between the emission spectra of **CPC4** and the absorption spectra of **CPC1** or **CPC3**, clearly indicates the presence of a FRET mechanism. However, the increase in the quantum yield of the system indicates that additional energy transfer mechanisms are also involved, *e.g.*, coherent ETT.

The morphology of the self-assembled systems were studied at both fast and slow cooling rates in the presence of 6% of the pyrene oligomer. Measurements taken after cooling the sample with a gradient of 0.5 °C/min (Figure 5.3) revealed the presence of worm-like nanostructures, identical to those observed in the absence of the acceptor oligomer (see Figure 4.8a). In the presence of **CPC1** or **CPC3**, the worms had heights of 8 nm and were between 1 to 5 µm long.

With a faster temperature gradient (10 °C/min), small circular sheets were observed to be present in the AFM measurements (Figure 5.4). These sheets had heights of 4 nm and a diameter between 50 and 200 nm. These values match those previously measured for **CPC4** without the presence of pyrene oligomers (see Figure 4.12a).

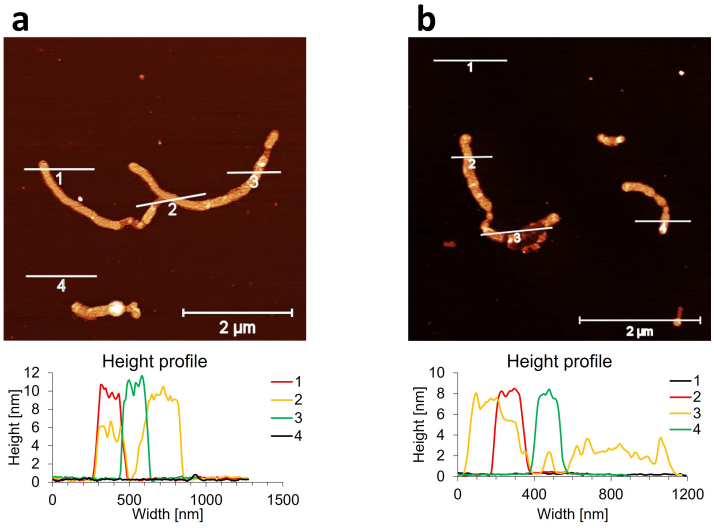

Figure 5.3: AFM measurements of the self-assemble **CPC4** with a cooling rate of 0.5 °C/min in presence of (a) 6 % **CPC1** and (b) 6 % **CPC3** with their respective cross sections. Conditions: 3 µM **CPC4**, 10 mM sodium phosphate buffer pH 7.2, 10 mM NaCl and 15 % EtOH.

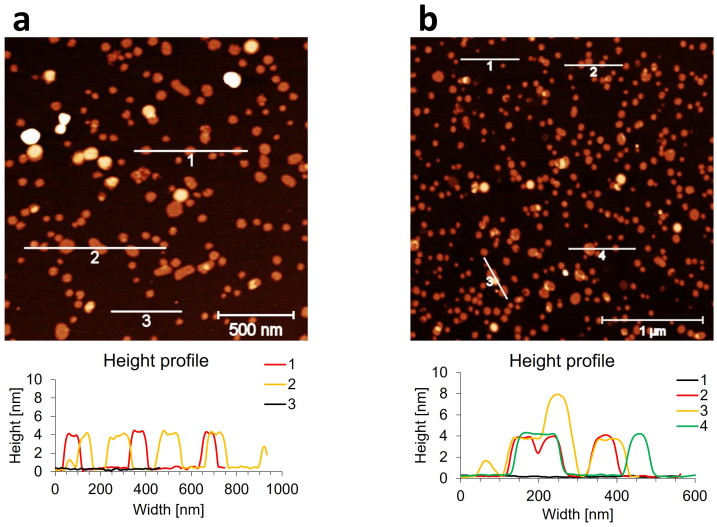

Figure 5.4: AFM measurements of the self-assemble **CPC4** with a cooling rate of 10 °C/min in presence of (a) 6 % **CPC1** and (b) 6 % **CPC3** with their respective cross sections. Conditions: 3 µM **CPC4**, 10 mM sodium phosphate buffer pH 7.2, 10 mM NaCl and 15 % EtOH.

In summary, a significant energy transfer is observed between **CPC4** and **CPC1** or **CPC3**. The addition of small amounts of the pyrene oligomer resulted in a five-fold increase in the system's quantum yield, reaching a maximum in both cases after the

addition of 6% of the pyrene oligomers. Although the difference in the cooling gradient did not have a major influence on the light-harvesting system, it did result in different supramolecular polymer morphologies, identical to the ones observed with **CPC4** alone.

5.1.2 Light-Harvesting Properties of CPC5

The 2,7-disubstituted phenanthrene oligomer **CPC5** has formerly shown to self-assemble into two distinct morphologies depending on the cooling gradient used (see Section 4.1.4, Chapter 4). Nanotubes composed of single- and multi-walls were observed after applying a slow (0.5 °C/min) temperature gradient while circular nanosheets were seen after applying a faster one (10 °C/min). Unlike the first phenanthrene isomer (**CPC4**), the difference in the cooling rate had a major influence on the spectroscopic properties of the self-assemblies formed by this oligomer. The self-assembled oligomer displayed a higher absorption between 260 and 280 nm, along with a reduced phenanthrene fluorescence (see Figure 4.11 bottom).

The following light-harvesting experiments were performed by adding increasing amounts of **CPC1** or **CPC3** (0.3% to 27%) to **CPC5** and thermal assembly of the supramolecular polymer was done with both temperature gradients. Following the same methodology as previously described, the fluorescence emission spectra of the four different systems were recorded (Figure 5.5a, b, d and e) and their quantum yield were then calculated (Figure 5.5c and f). AFM measurements were performed to observe the systems presenting the highest excitation energy transfer potential (Figure 5.6 to Figure 5.8).

When the **CPC5** oligomer was doped with **CPC1**, excitation energy transfer from the phenanthrene to the pyrene was observed. As shown in Figure 5.5a, the phenanthrene monomer fluorescence (black curve) decreased nearly completely while the pyrene monomer fluorescence was observed to increase. This increase seemed to reach a plateau at 9% before rising again when adding up to 27% of **CPC1**. When calculating the quantum yield associated with the system, a similar trend could be observed with a maximum of 34.6 ± 2.5 reached after the addition of 6% of **CPC1** (Figure 5.5c, yellow). This increase in quantum yield corresponds to about a four-fold increase compared to the native **CPC5**, which had a quantum yield of 10%. It is important to note that after the last addition, the quantum yield decreased by approximately 2% and did not increase as displayed on the fluorescence emission spectra.

The study of the same system with a slower cooling rate led to different fluorescence results (see Figure 5.5b). The fluorescence of the pyrene monomer reached a plateau at 9%, with a maximum quantum yield of 35.1 ± 3.8 after the addition of 6% of **CPC1**

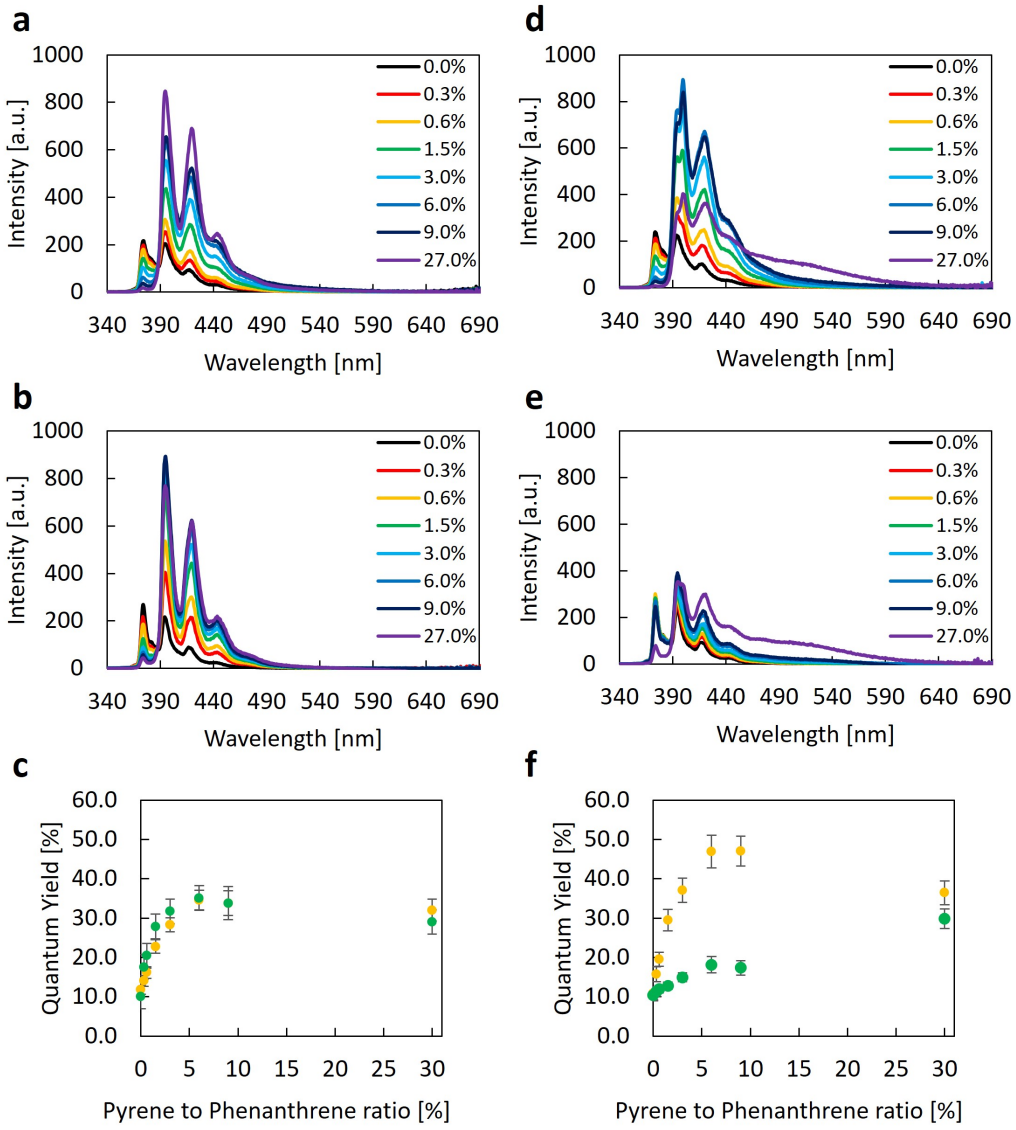

Figure 5.5: Fluorescence emission spectra of **CPC5** in presence of increasing amounts of **CPC1** (0 to 27%) with a cooling rate of (a) 10 °C/min; (b) 0.5 °C/min; (c) Quantum yield of both systems, in yellow at 10 °C/min and in green at 0.5 °C/min. Fluorescence emission spectra of **CPC5** in presence of increasing amounts of **CPC3** (0 to 8%) with a cooling rate of (d) 10 °C/min; (e) 0.5 °C/min; (f) Quantum yield of both systems, in yellow at 10 °C/min and in green at 0.5 °C/min. Conditions: 3 µM oligomer, 10 mM sodium phosphate buffer pH 7.2, 10 mM NaCl and 20 % EtOH, λ_{ex}: 320 nm.

(identical to the fast cooling quantum yield). However, two differences arose when a gradient of 0.5 °C/min was applied. First, after the addition of small amounts of **CPC1** the fluorescence of the pyrene monomer increased a lot, suggesting a more favorable alignment of the oligomers in the system for excitation energy transfer. Secondly, the ratio

between the vibronic bands (394 nm and 420 nm) changes, indicating a modification in the relative orientation of the oligomers resulting in different spectroscopic behavior.

The fourth system, composed of **CPC5** and **CPC3**, exhibited higher excitation energy transfer properties in its self-assembled nanostructures in comparison to the other systems. Indeed, after a fast cooling of the system, the fluorescence of the phenanthrene monomer decreased completely, while a strong fluorescence from the pyrene monomer was detected (Figure 5.5d). This fluorescence reached a plateau at 9% before decreasing again after the addition of 27% of **CPC3**. Along with the decrease in the fluorescence of the pyrene monomer, the appearance of a broad pyrene excimer fluorescence band was observed. This band was identical to the one seen previously in the LHC composed of **CPC3** and **CPC4** (Figure 5.2d). The maximum quantum yield calculated for this system with fast cooling was 47.0 ± 3.8, reached after the addition of 6% of **CPC3** (Figure 5.5f) which is about a five-fold increase compared to the original **CPC5** by itself.

Unlike all donor-acceptor couples previously presented in this chapter, those composed of **CPC5** and **CPC3** saw their light-harvesting capabilities strongly influenced by the applied cooling rate. When a gradient of 0.5 °C/min was applied, a very small amount pyrene monomer fluorescence was observed (Figure 5.5e). This observation, along with the absence of a decrease in the phenanthrene fluorescence, suggests that the two oligomers do not interact together. The addition of 27% of **CPC3** seems to bring structural changes to the system and force an interaction between the two oligomers. The controls made for this experiment (Figure 7.87 and Figure 7.91) showed only excitation of **CPC3** through **CPC5** and nor direct excitation of the pyrene oligomer.

As previously suggested for the donor-acceptor systems composed of **CPC4**, a FRET mechanism is partly responsible for the excitation energy transfer in the systems containing **CPC5**. The observed decrease in the phenanthrene emission accompanied by an increase in the pyrene fluorescence is a clear sign of it in addition to the overlap spectral overlap between the fluorescence emission of the donor and the absorption of the donor. However, the increase in the quantum yield suggests once more that FRET is not the only energy transfer mechanism at play here.

The maximal quantum yields of these two couples after the application of two different cooling gradients are all present in Table 5.2.

Table 5.2: Quantum yields of **CPC5** in presence of 6% **CPC1** or 6% **CPC3**.

	CPC1		**CPC3**	
Cooling	10 °C/min	0.5 °C/min	10 °C/min	0.5 °C/min
Φ_F [%]	34.6 ± 2.5	35.1 ± 3.8	47.0 ± 3.8	17.4 ± 1.9
Increase vs $\Phi_{\mathbf{CPC5}}$	4x	4x	5x	2x

As observed for the previous doping systems, the morphology of the supramolecular polymers formed by a combination of **CPC5** and 6% of **CPC1** resulted in identical aggregates as in the absence of the pyrene oligomer. With a cooling rate of 10 °C/min, small sheets with a thickness of 2 nm are observed (Figure 5.6a). When the temperature gradient was reduced to 0.5 °C/min, the system self-assembles into nanotubes which were observed to be 4 nm high and up to 5 µm long (Figure 5.6b). These dimensions are identical to the ones previously measured in the absence of **CPC1** (see Figure 4.12b).

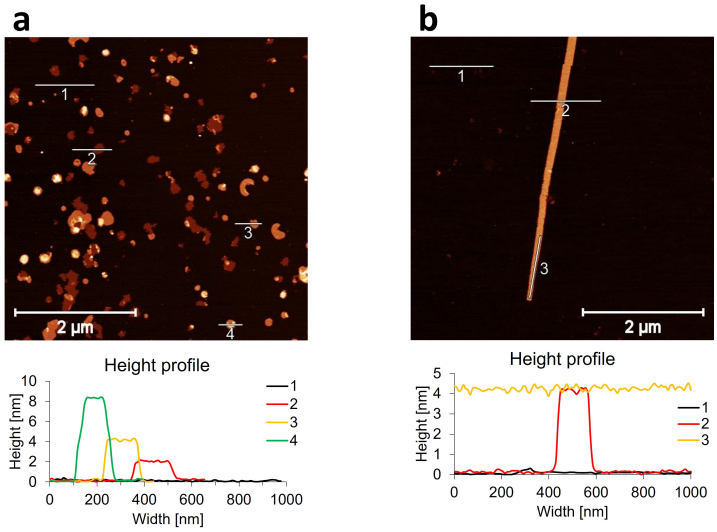

Figure 5.6: AFM measurements of the self-assemble **CPC5** with a cooling rate of (a) 10 °C/min; (b) 0.5 °C/min in presence of 6 % **CPC1** with their respective cross sections. Conditions: 3 µM **CPC5**, 10 mM sodium phosphate buffer pH 7.2, 10 mM NaCl and 20 % EtOH.

The addition of 6% **CPC3** to **CPC5** followed the same trend when a cooling rate of 10 °C/min was applied (see Figure 5.7) with the formation of nanosheets that were 2 nm high.

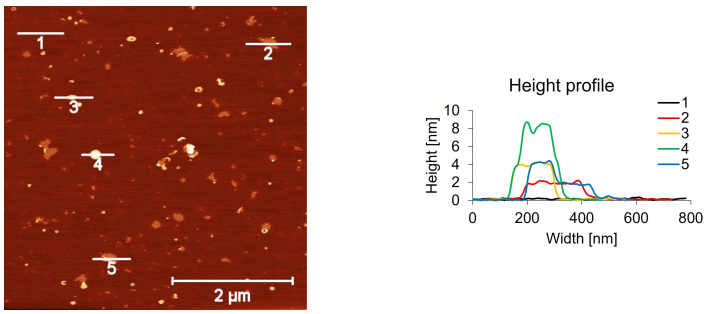

Figure 5.7: AFM measurement of the self-assemble **CPC5** with a cooling rate of 10 °C/min in presence of 6 % **CPC3** with its cross sections. Conditions: 3 µM **CPC5**, 10 mM sodium phosphate buffer pH 7.2, 10 mM NaCl and 20 % EtOH.

However, when the slower temperature gradient was used, several types of morphologies were present. As observed in Figure 5.8, nanotubes and spherical nanosheets co-exist. The tubes were observed to be 4 nm high and measure up to 6 µm long which is comparable to the sizes previously measured with **CPC5**. On the other hand, spherical nanosheets with a height of 2 nm is an unusual self-assembly pattern for probably **CPC3**, which previously formed worm-like nanostructures. This may be due to the small amount of **CPC3** present in solution being insufficient to form larger aggregates.

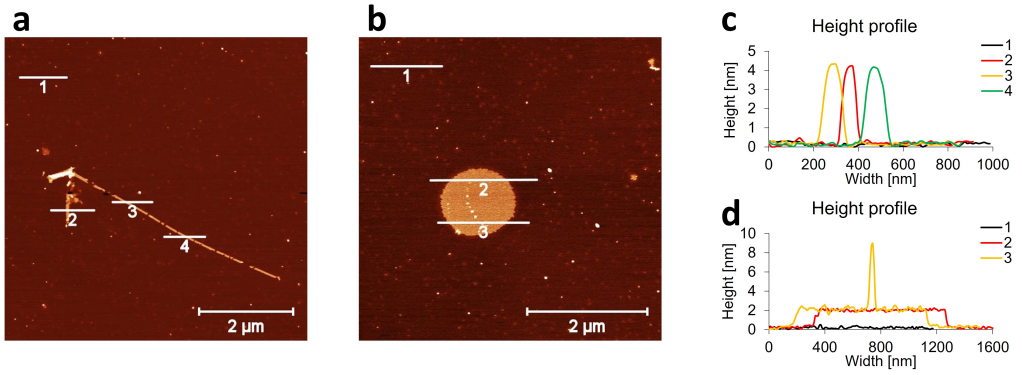

Figure 5.8: AFM measurements of **CPC5** with a cooling rate of 0.5 °C/min in presence of 6 % **CPC3**. (a) Nanotube; (b) Nanosheet; (c) Cross sections of the nanotube present in (a); (d) Cross sections of the nanosheet present in (b). Conditions: 3 µM **CPC5**, 10 mM sodium phosphate buffer pH 7.2, 10 mM NaCl and 20 % EtOH.

These different morphologies present, could hint for a self-sorting process. The big structural differences in the substitution of the phenanthrene and the pyrene could be a reason for it to occur. Similar to previous work,[120] the fast cooling of **CPC5** would trap **CPC3** in its self-assembled nanostructures while a slower cooling would result in the formation of two distinct supramolecular polymers.

In summary, the donor-acceptor couple showing the highest excitation energy transfer is composed of **CPC5** and **CPC3** with a maximal quantum yield of 47.0 ± 3.8 in the presence of 6% of the acceptor which corresponds to a five-fold increase compared to the native **CPC5**. However, the energy transfer was observed to occur only when using a 10 °C/min cooling gradient. When the cooling process was slowed down, some self-sorting was observed, with two distinct self-assemblies present in AFM images.

In addition to all these measurements, preliminary data was collected for the energy transfer from **CPC4** and **CPC5** to **CPC2**. However, the results obtained were not as conclusive as the data presented previously and further investigations into the oligomer were dropped (see Figure 7.79).

5.2 Conclusion and Outlook

The light-harvesting properties of the self-assemblies formed with phosphodiester-linked cholane-phenanthrene-cholane oligomers have been established. The structural diversity present in both the donor and acceptor oligomers, along with the use of different cooling rates, led to a wide range of results (see Table 5.3 and Table 5.4).

The light-harvesting systems formed with **CPC4** in the presence of increasing amounts of **CPC1** or **CPC3** were revealed to be very similar. Both systems behaved identically upon the addition of the acceptor oligomer, with the appearance of strong fluorescence of the pyrene monomer. A fluorescence maximum was observed after the addition of 6% of **CPC1** or **CPC3** resulting in quantum yields of approximately 40% (a five-fold increase compared to **CPC4** alone (see Table 5.3)). The use of different cooling gradients did not influence these two systems, with identical quantum yields observed between fast and slow cooling (within the margin of error).

The morphologies of the self-assemblies formed by **CPC4** in the presence of 6% of **CPC1** or 6% of **CPC3** were identical to the nanostructures observed for **CPC4** alone.

The systems formed with **CPC5** as the donor oligomer also showed promising results. As for the previous two systems, the cooling rate used when adding **CPC1** to the system resulted in similar results with a identical (within the margin of error) maximum quantum yield in both cases of 35% observed after addition of 6% of **CPC1**. The supramolecular polymers observed after cooling in presence of 6% of **CPC1** were identical to those seen with **CPC5** alone. Fast cooling resulted in small spherical nanosheets,

Table 5.3: Summary of the morphology and the spectroscopic properties of the supramolecular polymers formed by **CPC4** in presence of 6% **CPC1** or 6% **CPC3**.

	CPC4			
	CPC1		**CPC3**	
Temperature Gradient	10 °C/min	0.5 °C/min	10 °C/min	0.5 °C/min
Φ_F [%]	40.8 ± 3.2	40.4 ± 3.2	41.9 ± 2.6	40.9 ± 3.7
Increase vs $\Phi_{\mathbf{CPC4}}$	5x	5x	5x	5x
Morphology				
Height [nm]	4	8	4	8

while a slower cooling produced nanotubes.

When **CPC3** was used instead of **CPC1**, the differences in energy transfer and morphologies between fast and slow cooling rates were pronounced. A slow temperature gradient led to self-sorting until about 27% of **CPC3** was added, resulting in a strong pyrene excimer fluorescence band around 520 nm, which also appeared during fast cooling. Consequently, the quantum yields for this system varied significantly with 47% reached with a 10 °C/min gradient and 17% with a 0.5 °C/min gradient. This self-sorting phenomena was also observed through AFM measurements, which revealed the co-existence of two distinct supramolecular polymers: nanotubes and spherical nanosheets.

Future work may involve to study the influence of the cholane units present in the acceptor oligomer on the light-harvesting properties of **CPC4** and **CPC5**. For this, the pyrene diols can be used as acceptor molecules. Additional chromophores can be introduced to observe different kind of interactions between the donor oligomer and acceptor dyes. This last proposal has been performed by Silène Gobeil in the context of a Bachelor's thesis (Silène Gobeil, *Light-harvesting antennas based on a cholane-phenanthrene-cholane oligomer*, Bachelor's thesis, University of Bern, 2024).

The spectroscopic properties of the donor-acceptor couples can be further studied. Transient absorption spectroscopy performed on them would give us information on the different excited states as well as more information on the energy transfer mechanism. The potential use of total internal reflection fluorescence (TIRF) microscopy could bring

Table 5.4: Summary of the morphology and the spectroscopic properties of the supramolecular polymers formed by **CPC5** in presence of 6% **CPC1** or 6% **CPC3**.

	CPC5			
	CPC1		**CPC3**	
Temperature Gradient	10 °C/min	0.5 °C/min	10 °C/min	0.5 °C/min
Φ_F [%]	34.6 ± 2.5	35.1 ± 3.8	47.0 ± 3.8	17.4 ± 1.9
Increase vs $\Phi_{\mathbf{CPC5}}$	4x	4x	5x	2x
Morphology		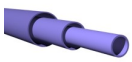		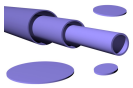
Height [nm]	2 - 4	4	2	Tube 4 / Sheet 2

some insight on the location of the acceptor dye in the supramolecular polymer.

Another way to gain more information on the aggregation pattern could be small angle X-ray scattering (SAXS). However, the growth of the crystal has to following specific temperature gradients and solvents rendering it complicated to realize. Cryo-EM tomography may also be a technique that can be used to get more insights on the structural arrangement of the donor and acceptor oligomers within our systems.

Chapter 6

Overall Conclusions and Future Perspectives

Overall the use of previously developed 1,6-disubstituted pyrene trimer and 1,8-disubstituted pyrene trimer as scaffolds for the development of functionalized supramolecular platforms was successful. The addition of a carbohydrate moiety did not alter their supramolecular morphologies, with the oligomers self-assembling into nanofibers and nanosheets. The addition of increasing units of pyrene in the oligomer surprisingly had different effects depending on the pyrene isomer present. It was expected that the increase of pyrene molecules would enhance hydrophobic interactions, leading to a higher melting temperature of the supramolecular polymer. For the 1,8-disubstituted pyrene, no significant changes in the de-aggregation temperature were observed. In contrast, the 1,6-pyrene isomer exhibited a higher melting temperature of the supramolecular sheets.

The interaction between the supramolecular polymer and Con A was observed after the addition of the protein solution to the self-assembled supramolecular polymer. However, this interaction was proven to be non-specific to the presence of α-mannose on our polymers. The presence of electrostatic interactions between the surface of the protein and the supramolecular polymer could be at the origin of this shortcoming. To address this issue, replacing the negatively charged phosphate groups linking the pyrene units with positively charged amine bridges could improve the system and potentially enable specific interactions. Another approach to explore is using different molecular handles that do not involve electrostatic interactions. For example, incorporating a small azide functionality to the oligomer and coupling it to a strained alkyne (*e.g.*, dibenzocyclooctyne, DIBO) through soft coupling conditions could be an interesting direction for further investigation.

Furthermore, the removal of intramolecular π-π interactions within the oligomer con-

struct proved not to be a liability for the self-assembly process. The different cholane-PAH-cholane oligomers demonstrated the ability to aggregate into a wide variety of supramolecular polymer ranging from nanosheets to nanotubes and worms. The cooling rate used for the assemblies proved to be important as different morphologies were observed using the same oligomer. The co-assemblies formed by combining phenanthrene and pyrene oligomers showed potential to be light-harvesting systems with a few cases leading to a five-fold increase in the quantum yield compared to the native phenanthrene oligomer.

Future work could focus on performing faster cooling experiments with the pyrene-based CPCs to determine if all the self-assemblies are influenced by the temperature gradient. Their potential as scaffolds for supramolecular assemblies is promising, as they offer a diversity of morphologies to work with. For instance, the worm-like nanostructures could be used to internalize compounds, while the tubes might be used to capture small molecules on the inside and larger ones on the outside. The light-harvesting properties of these systems could be further studied through the incorporation of additional chromophores. A particularly interesting direction would be optimizing the systems to absorb visible light and transfer it through excitation energy.

Chapter 7

Experimental Section

7.1 General Methods

NMR Spectroscopy

A Bruker AV 300 (300 MHz) spectrometer at 298 K at the Department of Chemistry, Biochemistry and Pharmaceutical Sciences of the University of Bern was used to measure all the NMR spectra.

Mass Spectrometry

A Thermo Fischer LTQ Orbitrap XL mass spectrometer was used to obtain MS spectra with High resolution ESI-MS/MS mode.

UV-Vis Measurements

A Jasco V-730 spectrophotometer equipped with a Varian-Cary-block temperature controller was used to record UV-vis spectra. All measurements were done using quartz cuvette with an optical path of 1 cm. The samples measurements were performed between 75 °C and 25 °C with the temperature being controlled and monitored by a reference cuvette.

Fluorescence Measurements

A Jasco FP-8300 spectrofluorometer was used to record fluorescence measurements. If not mentioned otherwise, the excitation bandwidth was of 1 nm and the emission slit was of 2.5 nm.

AFM Measurements

A Nanoflex AFM instrument (Nanosurf AG, Switzerland) was used to measure AFM images, with measurements performed with the tapping mode. Tap190-Al-G cantilevers

from Budget-Sensors were used, with a resonant frequency of 190 kHz, a force constant of 48 N/m and a tip radius of 10 nm. All samples were prepared in the same way. The mica sheets were first modified with APTES by incubating them 2 h in presence of 10 µL DIPEA and 30 µL APTES in a desiccator under argon, after which the reagents were removed and the sheets were left to cure overnight. 20 µL of the sample of interested were then added to the sheets and let to adsorb for 10 minutes before being washed away with 2 mL MilliQ-H_2O and dried under argon. Measurements were then performed with the Nanosurf C3000 program while the graphical illustrations were done with Gwyddion. In order to measure the same structures before and after the addition of Con A, a screw-on sample stage with magnetic anchors was used. The mica was glued to a steel sample holder with Araldite® Rapid and prepared as stated above (see Figure 3.6 in Section 3.1.4, Chapter 3).

Cryo-EM

A Gatan 626 cryo holder on a Falcon III equipped FEI Tecnai F20 in nanoprobe mode was used to acquire the images. Due to the nature of the sample, acquisition settings had to be adjusted for a low total electron dose (less than 20 $e^-/\mathring{A}^2$) using EPU software. All samples for were plunge frozen using the FEI Vitrobot Mark 4 at room temperature and 100% humidity. Copper lacey carbon grids were glow discharged (air -10 mA for 20 seconds). 3 µL of then sample were pipetted on the girds and blotted for 3 seconds before plunging into liquid ethane. Sample grids were stored in liquid nitrogen. Distance measurements were done in Fiji[139,140] using the multi-point tool to set marks.

7.2 Appendix - Chapter 3

7.2.1 Organic Synthesis

The synthesis of 1,6- and 1,8-pyrene phosphoramidites **8** and **9** respectively were performed as described in literature (Scheme 7.1).[138]

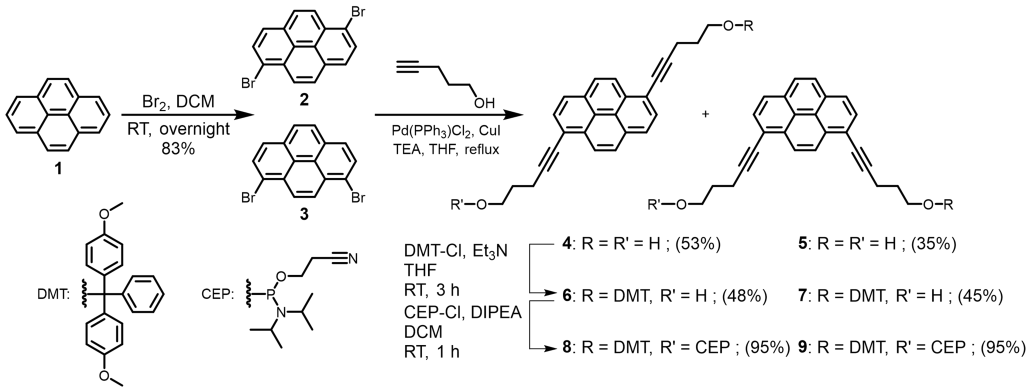

Scheme 7.1: Synthesis of 1,6-pyrene phosphoramidite **8** and 1,8-pyrene phosphoramidite **9**.

1,6-dibromopyrene (2) and 1,8-dibromopyrene (3)

To a solution of pyrene, **1** (20 g, 99 mmol, 1 eq.), dissolved in HPLC grade DCM (360 mL) was added dropwise a solution of Br_2 (10.2 mL, 198 mmol, 2 eq.) diluted in HPLC grade DCM (280 mL). After overnight stirring at RT, the reaction was filtered and washed with ice-cold MeOH (3x) and ice-cold DCM (1x). Compounds **2** and **3** were obtained as a mixture of gray solid (29.7 g, 83%). The dibromopyrene mixture was used without any further purification in the next step. ^{1}H NMR **2** and **3** (300 MHz, $CDCl_3$; sample contained traces of DCM) δ = 8.51 (s, 1H), 8.44 (d, J = 9.2 Hz, 1H), 8.26 (dd, J = 1.8 Hz, 8.2 Hz, 2H), 8.13 – 8.00 (m, 4H).

5,5'-(pyrene-1,6-diyl)bis(pent-4-yn-1-ol)) (4) and 5,5'-(pyrene-1,8-diyl)-bis-(pent-4-yn-1-ol)) (5)

To a mixture of compounds **2** and **3** (5 g, 13.9 mmol, 1 eq.) dissolved in dry THF (130 mL), was added, under oxygen free conditions, $Pd(PPh_3)_2Cl_2$ (244 mg, 0.4 mmol, 0.03 eq.) and CuI (34 mg, 0.2 mmol, 0.01 eq.). The solution was heated to 80 °C before freshly degassed TEA (80 mL) was added along with pent-4-yn-1-ol (5.17 mL, 55.6 mmol, 4 eq.). The reaction was stirred under reflux overnight. The mixture was then filtered and solvent removed under reduced pressure. The crude was then dissolved in EtOAc and washed with citric acid (10%) and saturated $NaHCO_3$. The organic phase was dried over Na_2SO_4, filtered, and concentrated under reduced pressure. The residue was

then purified by column chromatography (SiO_2, DCM / toluene / isopropanol 87:10:3 to 80:10:10). Compound **4** was isolated as a pure yellow solid (2.7 g, 53%) while compound **5** was recrystallized from MeOH, yielding a yellow solid (1.8 g, 35%). ^{1}H NMR **4** (300 MHz, DMSO-d_6; sample contained traces of DCM) δ = 8.51 (d, J = 9.1 Hz, 2H), 8.31 (d, J = 8.5 Hz, 4H), 8.14 (d, J = 7.9 Hz, 2H), 4.65 (t, J = 5.2 Hz, 2H), 3.66 (dt, J = 6.2 Hz, 5.3 Hz, 4H), 2.73 (t, J = 7.1 Hz, 4H), 1.87 (p, J = 6.7 Hz, 4H). ^{1}H NMR **5** (300 MHz, DMSO-d_6) δ = 8.60 (s, 2H), 8.28 (d, J = 8.0 Hz, 2H), 8.21 (s, 2H), 8.14 (d, J = 8.0 Hz, 2H), 4.66 (t, J = 5.2 Hz, 2H), 3.68 (dt, J = 6.2 Hz, 5.3 Hz, 4H), 2.74 (t, J = 7.1 Hz, 4H), 1.88 (p, J = 6.7 Hz, 4H).

5-(6-(5-(bis(4-methoxyphenyl)(phenyl)methoxy)pent-1-yn-1-yl)pyren-1-yl) pent-4-yn-1-ol (6)

To a solution of **4** (1 g, 2.7 mmol, 1 eq.) in dry THF (40 mL) under argon, was added freshly degassed pyridine (25 mL), followed by a solution of dimethoxytrityl chloride (0.9 g, 2.7 mmol, 1 eq.) in dry THF (10 mL). After stirring at RT for 3 h, the solvents were removed and the crude was dissolved in EtOAc. It was then washed with saturated NH_4Cl (2x), saturated $NaHCO_3$ (2x) and brine (2x). The organic phase was dried over Na_2SO_4, filtered, and concentrated under reduced pressure. The crude was purified by column chromatography (SiO_2, heptane / EtOAc / NEt_3 2:1:2% to 0:1:2%, then EtOAc / MeOH / NEt_3 95:5:2%). Compound **6** was isolated as a pure yellow foam (871 mg, 48%). ^{1}H NMR **6** (300 MHz, $CDCl_3$; sample contained traces of DCM) δ = 8.40 (m, 2H), 8.06 – 7.94 (m, 4H), 7.91 (m, 2H), 7.47 – 7.38 (m, 2H), 7.42 – 7.26 (m, 4H), 7.31 – 7.02 (m, 4H), 6.76 – 6.65 (m, 4H), 3.88 (t, J = 6.2 Hz, 2H), 3.59 (s, 6H), 3.29 (t, J = 6.1 Hz, 2H), 2.73 (m, 4H), 2.06 – 1.89 (m, 4H).

5-(8-(5-(bis(4-methoxyphenyl)(phenyl)methoxy)pent-1-yn-1-yl)pyren-1-yl) pent-4-yn-1-ol (7)

To a solution of **5** (320 mg, 0.9 mmol, 1 eq.) in dry THF (13 mL) under argon was added freshly degassed pyridine (8.1 mL), followed by a solution of 4,4'-dimethoxytrityl chloride (296 mg, 0.9 mmol, 1 eq.) in dry THF (3.1 mL). After stirring at RT for 3 h, the solvent was removed and the crude was dissolved in EtOAc. It was then washed with saturated NH_4Cl (2x), saturated $NaHCO_3$ (2x) and brine (2x). The organic phase was dried over Na_2SO_4, filtered, and concentrated under reduced pressure. The crude was purified by column chromatography (SiO_2, heptane / EtOAc / NEt_3 2:1:2% to 0:1:2%, then EtOAc / MeOH / NEt_3 95:5:2%). Compound **7** was isolated as a pure yellow foam (265.2 mg, 45%). ^{1}H NMR **7** (300 MHz, $CDCl_3$; sample contained traces of DCM and heptane) δ = 8.63 – 8.50 (m, 2H), 8.13 – 7.96 (m, 6H), 7.55 – 7.50 (m, 2H), 7.46 – 7.35 (m, 4H), 7.38 – 7.15 (m, 3H), 6.86 – 6.75 (m, 4H), 3.98 (m, 2H), 3.69 (s, 6H), 3.39 (t, J

= 6.0 Hz, 2H), 2.85 (m, 4H), 2.14 – 1.99 (m, 4H).

5-(6-(5-(bis(4-methoxyphenyl)(phenyl)methoxy)pent-1-yn-1-yl)pyren-1-yl) pent-4-yn-1-yl (cyanoethyl) diisopropylphosphoramidite (8)

To a solution of **6** (1.2 g, 1.8 mmol, 1 eq.) in dry DCM under argon was added freshly degassed DIPEA (927 µL, 5.3 mmol, 3 eq.) followed by the dropwise addition of CEP-Cl (514 µL, 2.3 mmol, 1.3 eq.). The reaction was stirred at RT for 1 h. The solvents were removed and the residue was purified by column chromatography (SiO_2, heptane / EtOAc / NEt_3 2:1:2%). The solvent mixture was dried over aluminum oxide prior to the column. Compound **8** was isolated as a pure yellow foam (1.4 g, 95%). ^{1}H NMR **8** (300 MHz, $CDCl_3$; sample contained traces od DCM and heptane) δ = 8.49 (m, 2H), 8.08 (m, 4H), 8.00 (m, 2H), 7.52 – 7.46 (m, 2H), 7.41 – 7.33 (m, 4H), 7.31 – 7.14 (m, 3H), 6.84 – 6.73 (m, 4H), 4.00 – 3.79 (m, 2H), 3.67 (s, 6H), 3.74 – 3.56 (m, 1H), 3.36 (m, 2H), 2.80 (m, 4H), 2.65 (t, J = 6.5 Hz, 2H), 2.08 (m, 4H), 1.22 (m, 13H). ^{31}P NMR **8** (121 MHz, $CDCl_3$) δ = 147.84.

5-(8-(5-(bis(4-methoxyphenyl)(phenyl)methoxy)pent-1-yn-1-yl)pyren-1-yl) pent-4-yn-1-yl (cyanoethyl) diisopropylphosphoramidite (9)

To a solution of **7** (355 mg, 0.5 mmol, 1 eq.) in dry DCM under argon was added freshly degassed DIPEA (278 µL, 1.6 mmol, 3 eq.) followed by the dropwise addition of CEP-Cl (154 µL, 0.7 mmol, 1.3 eq.). The reaction was stirred at RT for 1 h. The solvents were removed and the residue was purified by column chromatography (SiO_2, heptane / EtOAc / NEt_3 2:1:2%). The solvent mixture was dried over aluminum oxide prior to the column. Compound **9** was isolated as a pure yellow foam (431 mg, 95%). ^{1}H NMR **9** (300 MHz, $CDCl_3$; sample contained traces of heptane) δ = 8.56 (m, 2H), 8.08 – 7.95 (m, 7H), 7.54 – 7.45 (m, 2H), 7.43 – 7.33 (m, 4H), 7.33 – 7.23 (m, 2H), 7.24 – 7.13 (m, 1H), 6.87 – 6.73 (m, 4H), 4.02 – 3.74 (m, 3H), 3.66 (s, 6H), 3.74 – 3.55 (m, 1H), 3.36 (m, 2H), 2.81 (m, 4H), 2.62 m, 2H), 2.08 (m, 4H), 1.21 (m, 14H). ^{31}P NMR **9** (121 MHz, $CDCl_3$) δ = 147.79.

1.6-pyrene-modified solid-support (11)

The synthesis of solid-support **11**, was adapted from literature.[41] To a solution of **6** (50 mg, 0.1 mmol, 1 eq.) in DCM (0.4 mL), was added succinic anhydride (30 mg, 0.3 mmol, 3.8 eq.) followed by DMAP (15 mg, 0.1 mmol, 1.5 eq.). The reaction mixture was stirred at RT for 4 h. The reaction was then diluted with DCM (10 mL). The organic phase was washed with 10% citric acid (15 mL), brine (15 mL), dried over Na_2SO_4, filtered, and concentrated under reduced pressure yielding compound **10**. Compound **10** was redissolved in ACN (6 mL), 5.4 mL of this solution was added to LCAA-CPG

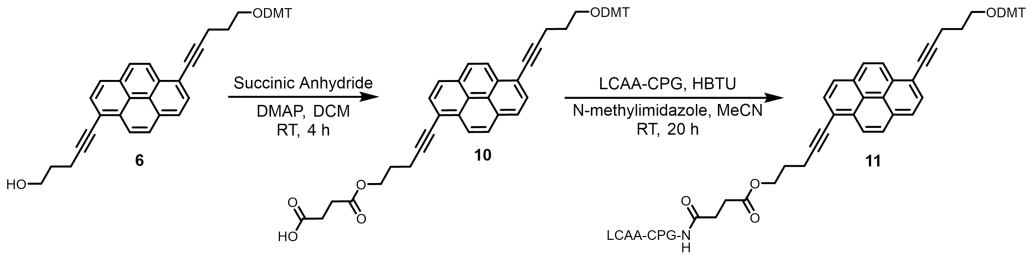

Scheme 7.2: Synthetic approach for the preparation of 1.6-pyrene-modified solid-support **11**.

(500 mg, 500 Å, amine loading 82 µmol/g). HBTU (61 mg, 0.2 mmol, 2 eq.) and N-methylimidazole (24 µL, 0.3 mmol, 3.8 eq.) were added. The reaction was stirred at RT for 16 h. The solid support **11** was then filtered off and washed with DCM. The loading was determined according to the Beer-Lambert law; **11** (3.1 mg) was added to 3% trichloroacetic acid in DCM (10 mL). After a 1:1 dilution in the same solvent, the absorbance was recorded at 498 nm. The loading was calculated using a molar absorptivity for the DMT cation of ε = 70'000 $L^{*}mol^{-1*}cm^{-1}$ and was determined to be 75 µmol/g.

1.8-pyrene-modified solid-support (13)

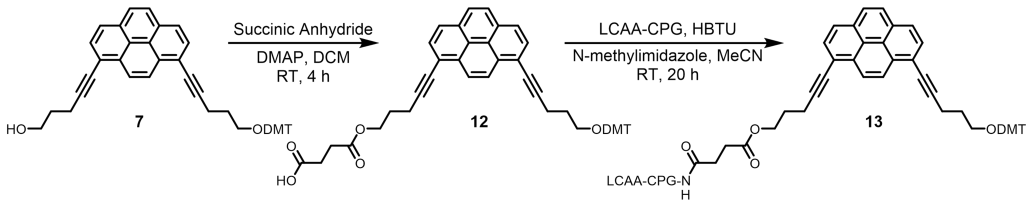

Scheme 7.3: Synthetic approach for the preparation of 1.8-pyrene-modified solid-support **13**.

The synthesis of solid-support **13**, was adapted from literature.[41] To a solution of **7** (50 mg, 0.1 mmol, 1 eq.) in DCM (0.4 mL), was added succinic anhydride (30 mg, 0.3 mmol, 3.8 eq.) followed by DMAP (15 mg, 0.1 mmol, 1.5 eq.). The reaction mixture was stirred at RT for 4 h. The reaction was then diluted with DCM (10 mL). The organic phase was washed with 10% citric acid (15 mL), brine (15 mL), dried over Na_2SO_4, filtered, and concentrated under reduced pressure yielding compound **12**. Compound **12** was redissolved in ACN (6 mL), 5.4 mL of this solution was added to LCAA-CPG (500 mg, 500 Å, amine loading 82 µmol/g). HBTU (61 mg, 0.2 mmol, 2 eq.) and N-methylimidazole (25 µL, 0.3 mmol, 3.8 eq.) were added. The reaction was stirred at RT for 16 h. The solid support **13** was then filtered off and washed with DCM. The

loading was determined according to the Beer-Lambert law; **13** (3.1 mg) was added to 3% trichloroacetic acid in DCM (10 mL). After a 1:1 dilution in the same solvent, the absorbance was recorded at 498 nm. The loading was calculated using a molar absorptivity for the DMT cation of ε = 70'000 L*mol^{-1}*cm^{-1} and was determined to be 29 µmol/g.

α-Mannose Phosphoramidite (15)

The synthesis of α-mannose phosphoramidite **15** was performed as described in literature (see Scheme 7.4).[141]

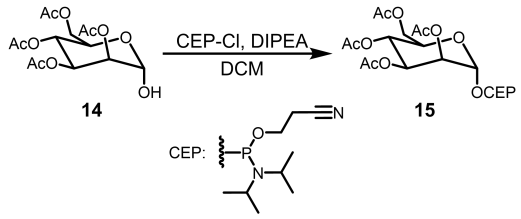

Scheme 7.4: Phosphoramidite substitution on α-mannose yielding compound **15**.

To a solution of 2,3,4,6-tetra-O-acetyl-D-mannopyranose, **14**, (200 mg, 0.6 mmol, 1 eq.) in dry DCM (4 mL) under argon, was added freshly degassed DIPEA (150 µL, 0.9 mmol, 1.5 eq.) followed by the dropwise addition of CEP-Cl (153 µL, 0.7 mmol, 1.2 eq.). The reaction was stirred at RT for 1 h. The solvents were removed under reduced pressure and the crude was purified by column chromatography (SiO_2, heptane / EtOAc / NEt_3 1:1:2%). The solvent mixture was dried over aluminum oxide prior to the column. Compound **15** was isolated as a pure colorless oil (290.7 mg, 95%). ^{1}H NMR **15** (300 MHz, $CDCl_3$; sample contained traces of heptane) δ = 5.47 – 5.13 (m, 4H), 4.38 – 4.08 (m, 3H), 3.89 (m, 2H), 3.68 (m, 2H), 2.69 (m, 2H), 2.19 (s, 3H), 2.12 (d, J = 4.4 Hz, 3H), 2.10 – 2.04 (m, 4H), 2.02 (s, 3H), 1.26 – 1.22 (m, 10H). ^{31}P NMR **15** (121 MHz, $CDCl_3$) δ = 153.41, 151.82, 150.08, 149.61.

PEG3 Phosphoramidite (18)

The synthesis of triethylene glycol phosphoramidite **18** was performed as described in literature (see Scheme 7.5).[142]

2-(2-(2-(bis(4-methoxyphenyl)(phenyl)methoxy)ethoxy)ethoxy) ethan-1-ol (17)

To a solution of triethylene glycol, **16**, (0.3 mL, 2.2 mmol, 1 eq.) in dry DCM (10 mL) under argon, was added freshly degassed pyridine (4.2 mL). Once the solution was clear, a solution of 4,4'-dimethoxytrityl chloride (760 mg, 2.2 mmol, 1 eq.) in dry DCM (10

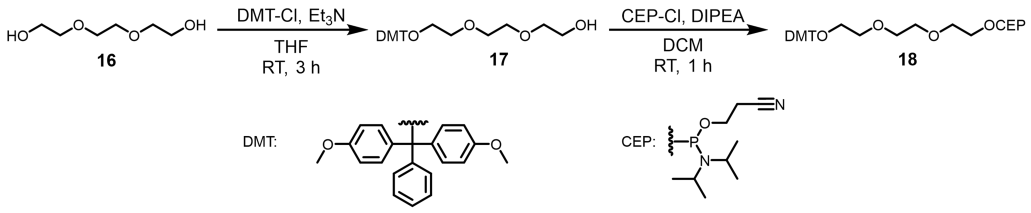

Scheme 7.5: Synthetic approach for the preparation of triethylene glycol phosphoramidite **18**.

mL) under argon was added dropwise. After stirring at RT for 3 h, the solvent were removed under reduced pressure and the crude was dissolved in EtOAc, washed with saturated NH_4Cl (2x), saturated $NaHCO_3$ (2x) and brine (2x). The organic phase was dried over Na_2SO_4, filtered, and concentrated over reduced pressure. The crude was purified by column chromatography (SiO_2, heptane / EtOAc / NEt_3 1:1:2% to 0:1:2%.). Compound **17** was isolated as a transparent oil (524 mg, 52%). ^{1}H NMR **17** (300 MHz, $CDCl_3$) δ = 7.51 – 7.40 (m, 2H), 7.40 – 7.14 (m, 7H), 6.86 – 6.77 (m, 4H), 4.12 (q, J = 7.1 Hz, 2H), 3.81 – 3.58 (m, 16H), 3.24 (t, J = 5.2 Hz, 2H), 2.40 (s, 1H), 2.04 (s, 2H), 1.26 (t, J = 7.1 Hz, 3H).

2-(2-(2-(bis(4-methoxyphenyl)(phenyl)methoxy)ethoxy)ethoxy) ethyl(2-cyanoethyl) diisopropylphosphoramidite (18)

To a solution of **17** (524 mg, 1.2 mmol, 1 eq.) in dry DCM (6 mL) under argon was added freshly degassed DIPEA (353 µL, 2.0 mmol, 1.75 eq.) followed by the dropwise addition of CEP-Cl (336 µL, 1.5 mmol, 1.3 eq.). The reaction was stirred at RT for 1 h. The solvents were removed under reduced pressure and the crude was purified by column chromatography (SiO_2, heptane / EtOAc / NEt_3 2:1:2%). The solvent mixture was dried over aluminum oxide prior to the column. Compound **18** was isolated as a pure colorless oil (414.2 mg, 55%). ^{1}H NMR **18** (300 MHz, $CDCl_3$; sample contained traces of heptane) δ = 7.53 – 7.43 (m, 2H), 7.42 – 7.16 (m, 7H), 6.90 – 6.79 (m, 4H), 3.94 – 3.80 (m, 2H), 3.81 (s, 6H), 3.80 – 3.68 (m, 2H), 3.73 – 3.53 (m, 8H), 3.25 (t, J = 5.3 Hz, 2H), 2.66 – 2.55 (m, 2H), 1.28 (s, 2H), 1.19 (dd, J = 6.8 Hz, 5.5 Hz, 12H). ^{31}P NMR **18** (121 MHz, $CDCl_3$) δ = 148.48.

7.2.2 NMR Spectra

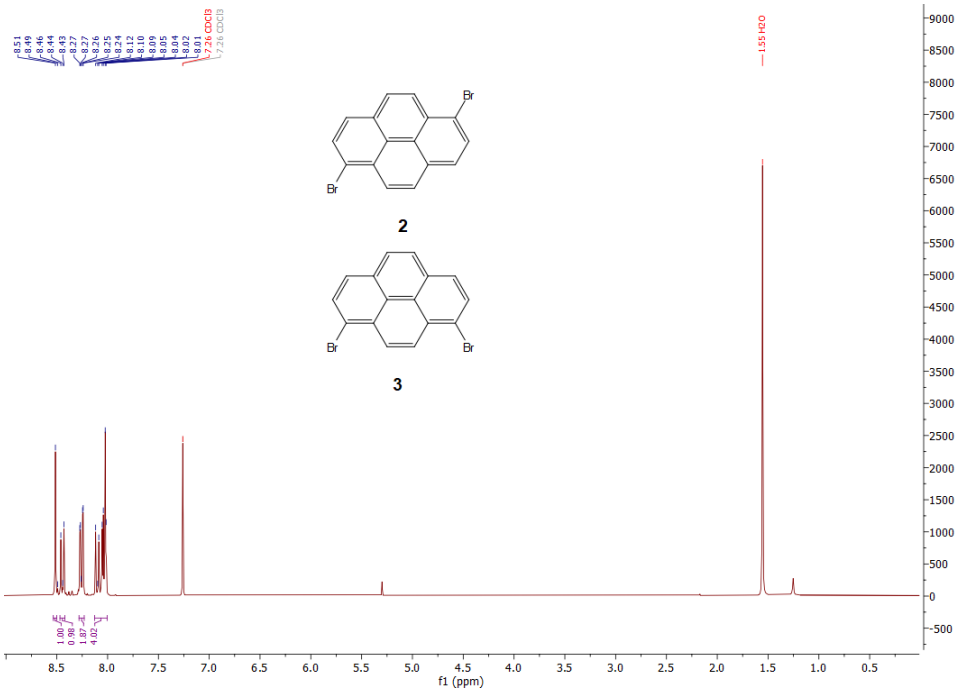

Figure 7.1: ^{1}H NMR of a mixture of compounds **2** and **3** in $CDCl_3$.

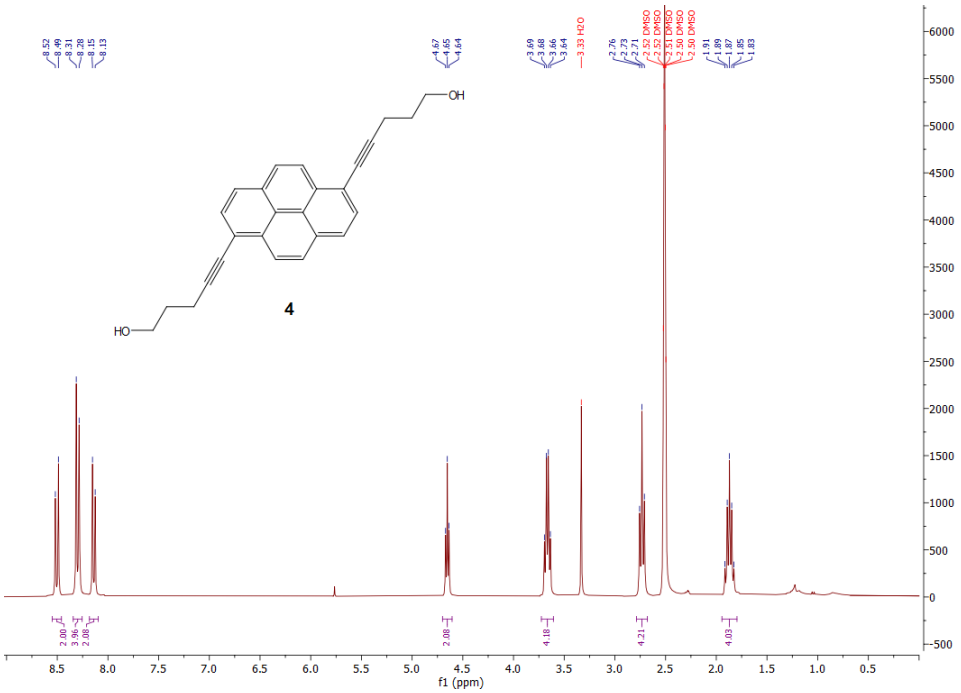

Figure 7.2: ^{1}H NMR of compound **4** in DMSO-d_6.

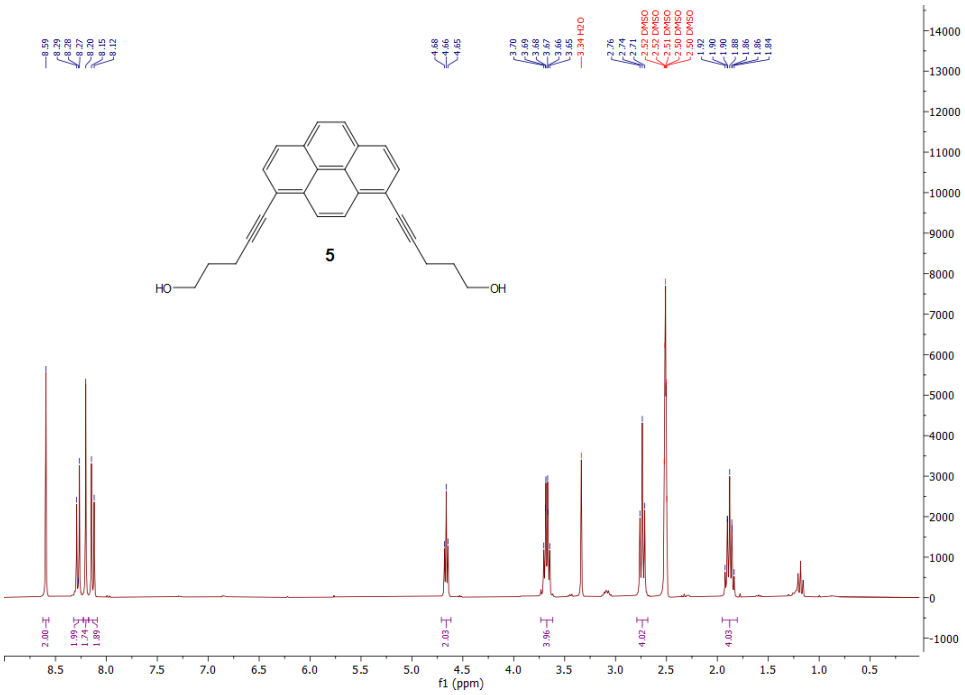

Figure 7.3: ^{1}H NMR of compound **5** in DMSO-d_6.

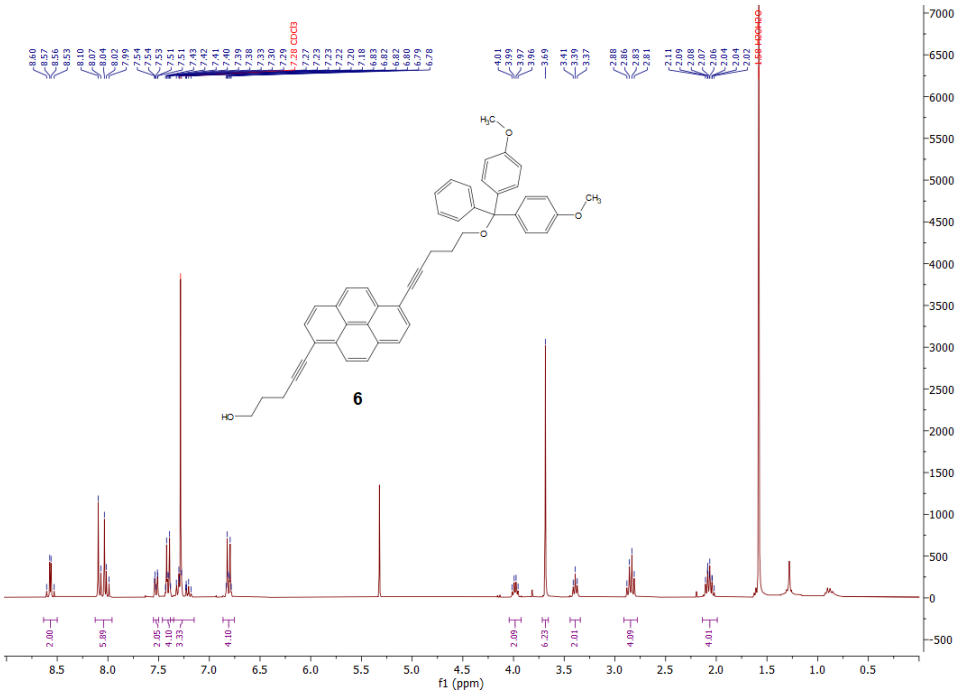

Figure 7.4: ^{1}H NMR of compound **6** in $CDCl_3$.

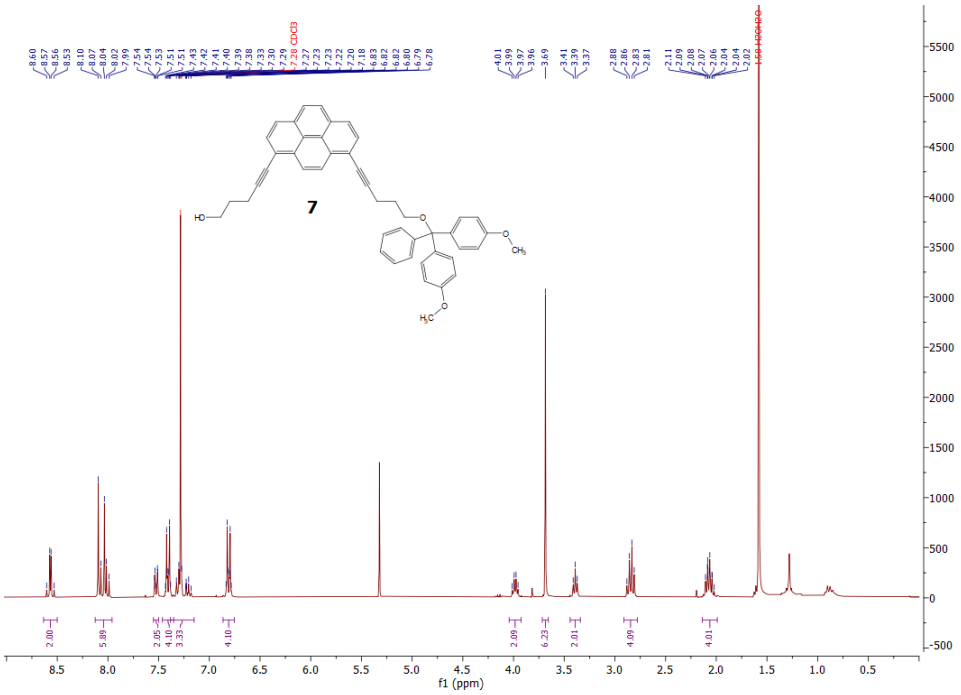

Figure 7.5: ^{1}H NMR of compound **7** in $CDCl_3$.

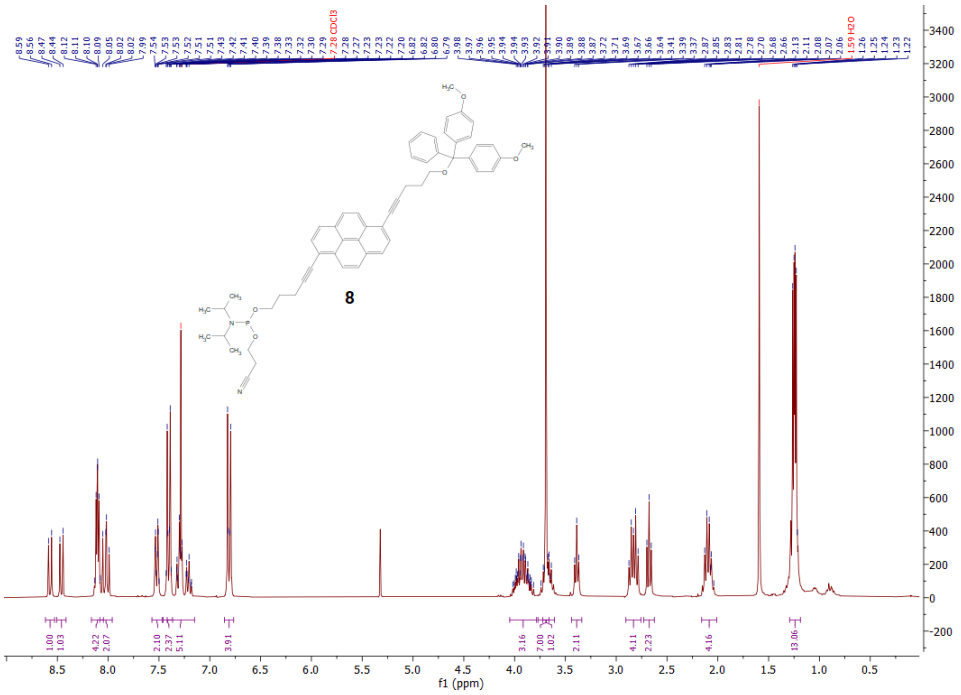

Figure 7.6: ^{1}H NMR of compound **8** in $CDCl_3$.

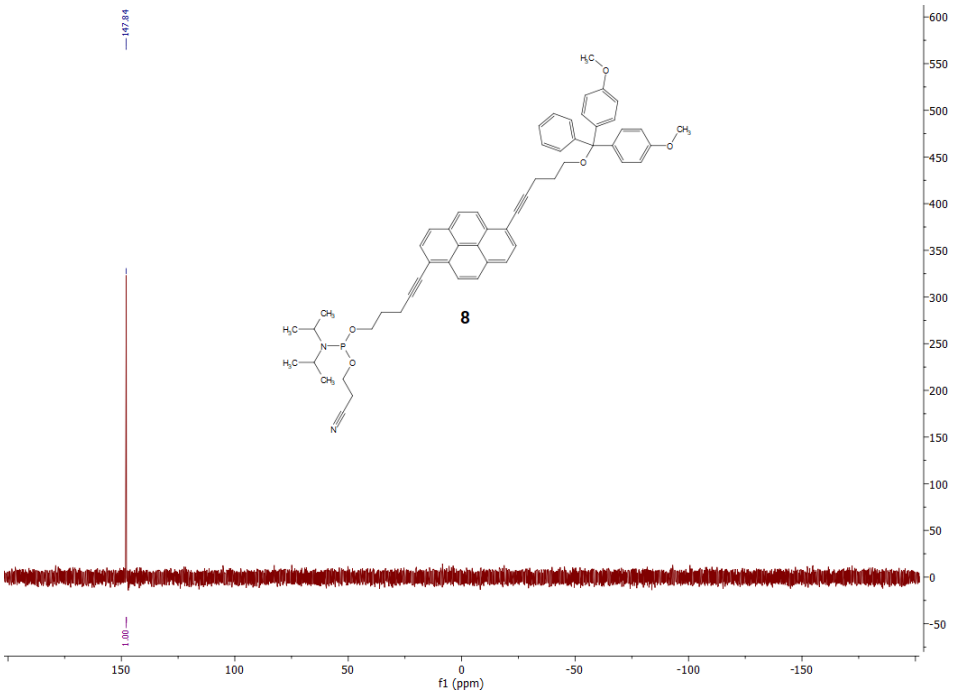

Figure 7.7: ^{31}P NMR of compound **8** in $CDCl_3$.

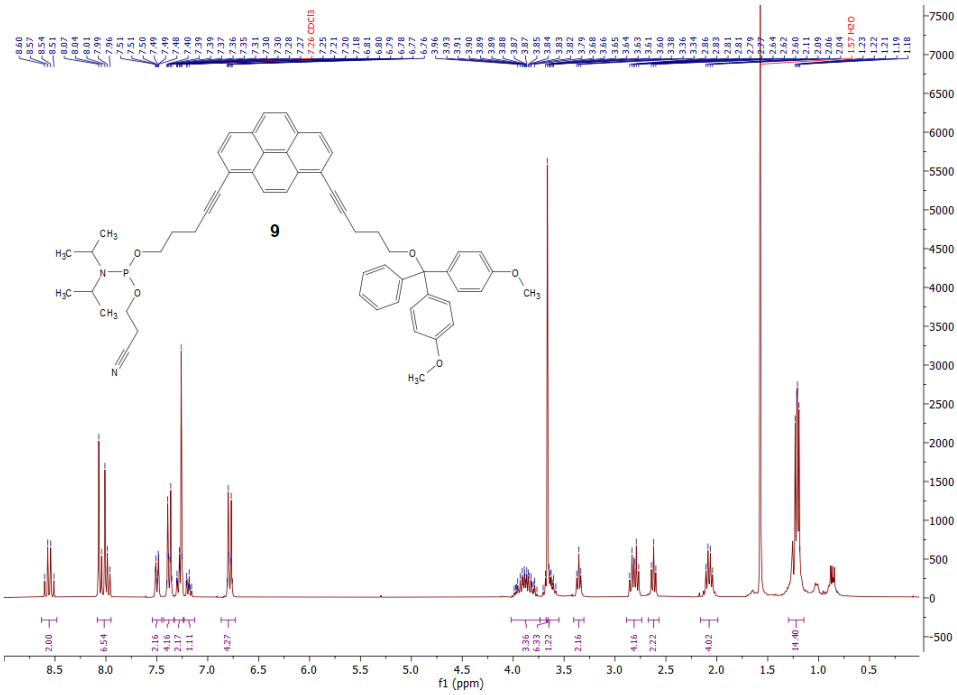

Figure 7.8: ^{1}H NMR of compound **9** in $CDCl_3$.

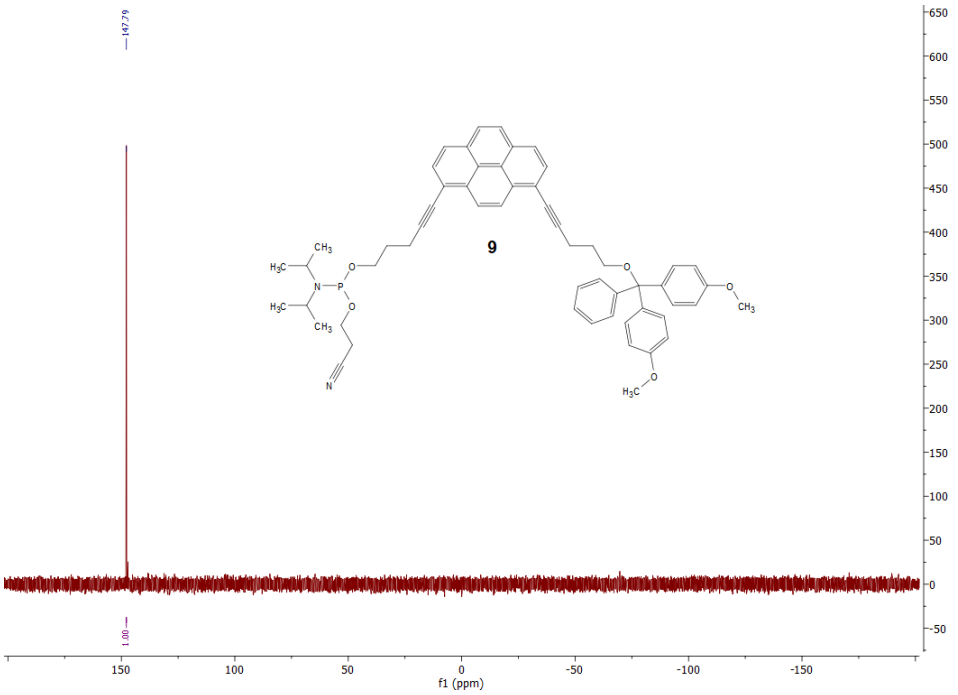

Figure 7.9: ^{31}P NMR of compound **9** in $CDCl_3$.

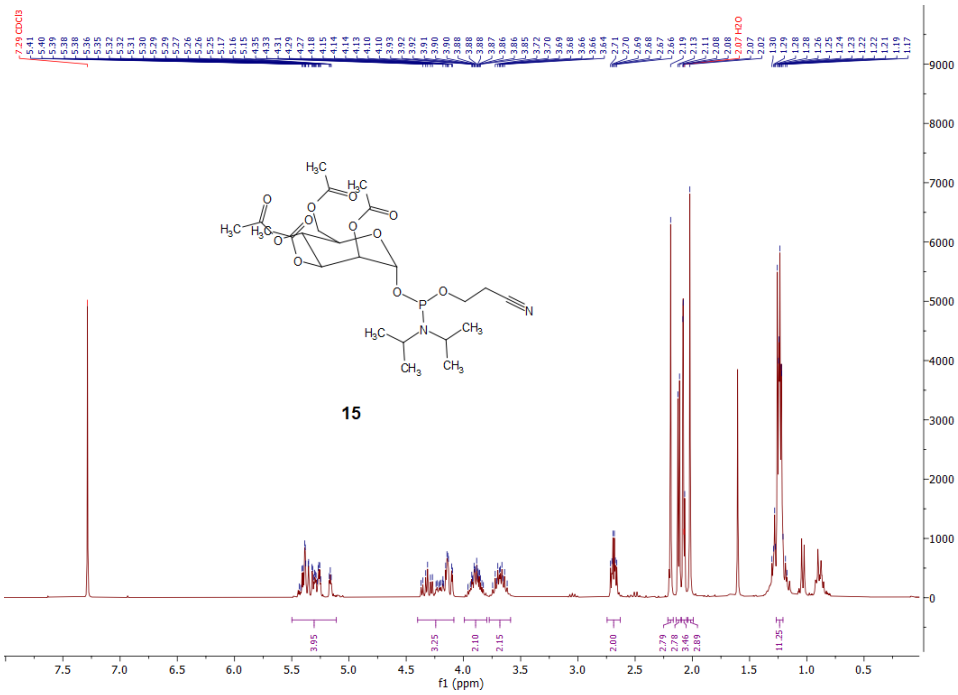

Figure 7.10: ^{1}H NMR of compound **15** in $CDCl_3$.

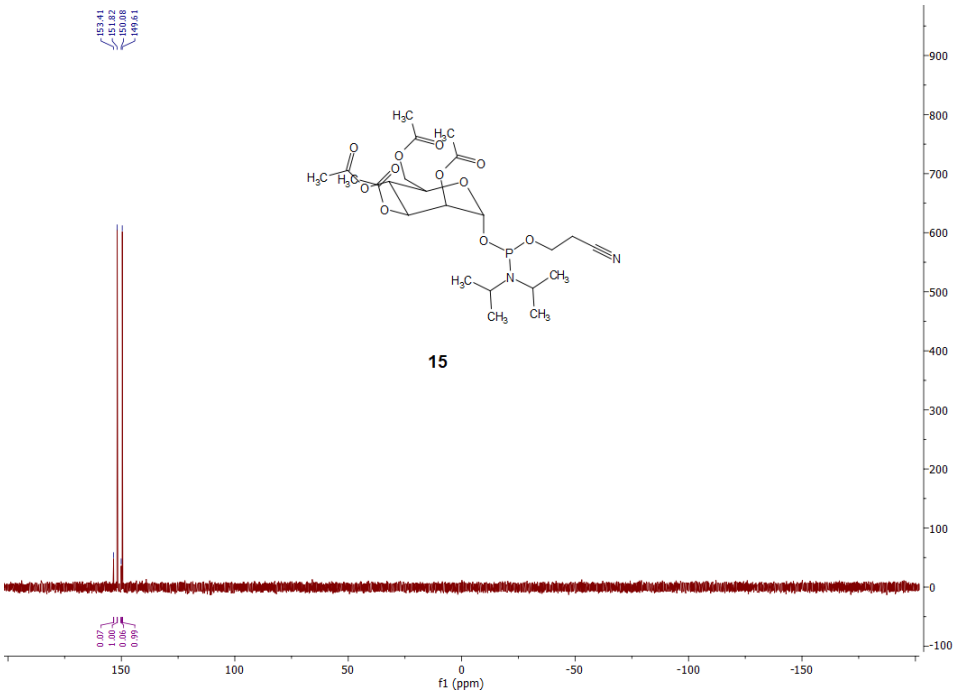

Figure 7.11: ^{31}P NMR of compound **135** in $CDCl_3$.

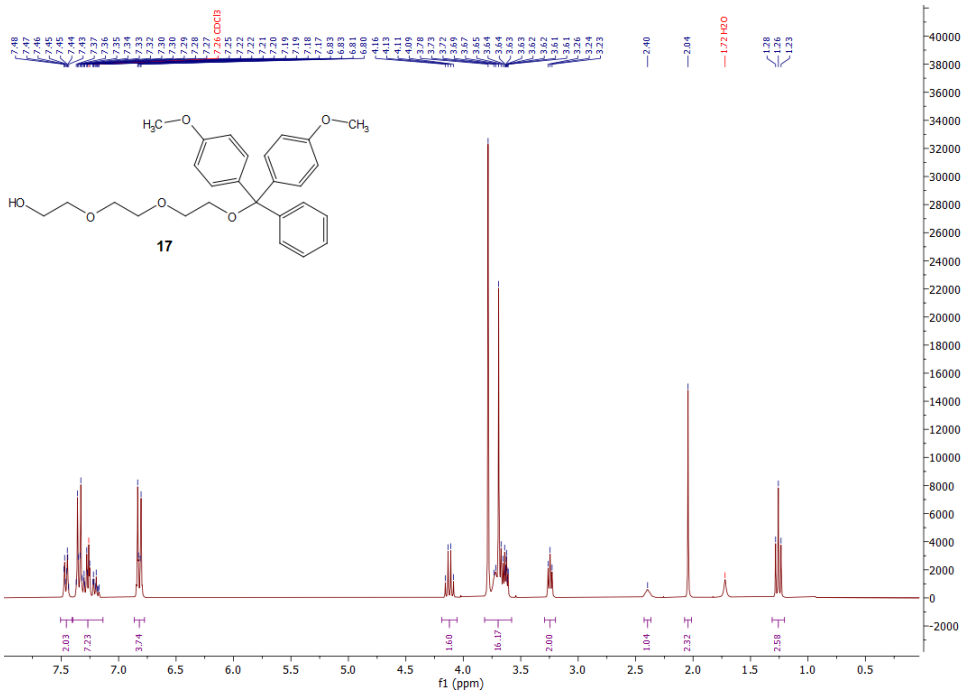

Figure 7.12: ^{1}H NMR of compound **17** in $CDCl_3$.

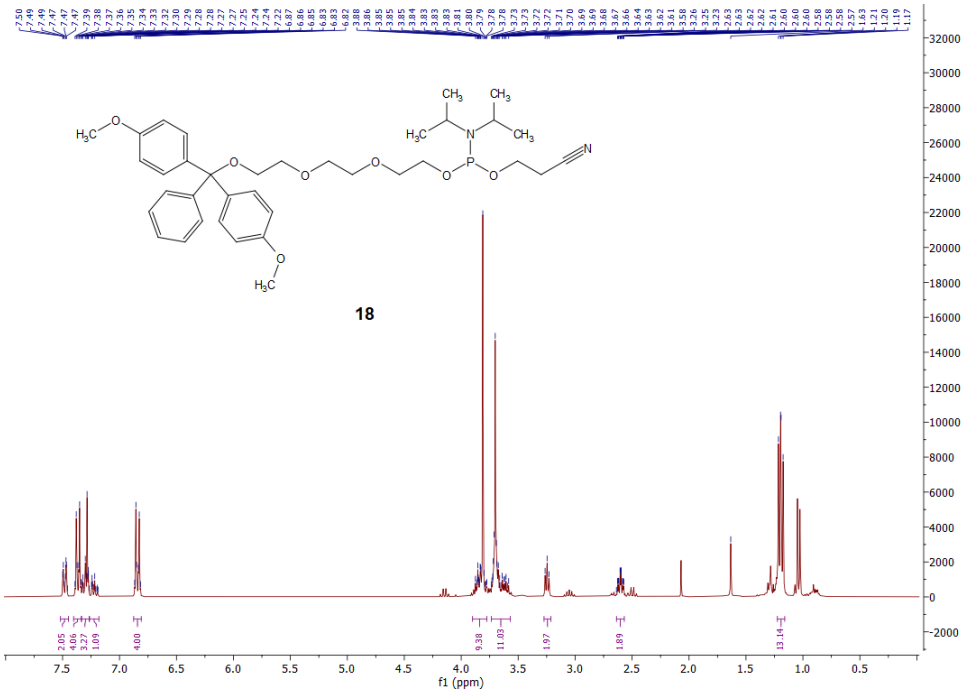

Figure 7.13: ^{1}H NMR of compound **18** in $CDCl_3$.

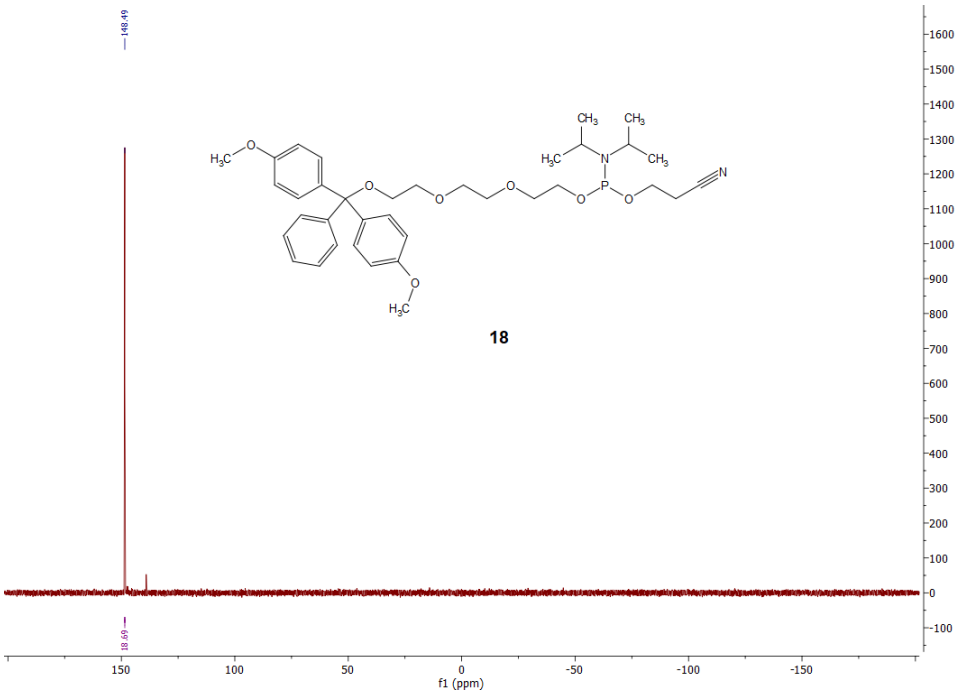

Figure 7.14: ^{31}P NMR of compound **18** in $CDCl_3$.

7.2.3 Synthesis of Oligomers

Oligomers 1 to 8 were all synthesized with an *Applied Biosystems 394 DNA/RNA synthesizer* on a 1 µM scale using a standard cyanoethyl-phosphoramidite coupling protocol. A prolonged coupling time was used for all modifications (3 minutes). Both pyrene phosphoramidites were dissolved to 0.1 M in 1,2-DCE, while PEG 3 and α-mannose phosphoramidites were dissolved to 0.1 M in amidite diluent (dry acetonitrile from Sigma Aldrich). After synthesis, the oligomers were cleaved from the solid support using a 2 M NH_3 in MeOH solution at RT overnight. The supernatents were collected and the solid supports were washed with a solution of MilliQ·H_2O and EtOH (1:1, 3 x 1 mL) before the crude oligomers were lyophilized. The crude oligomers were purified on a reversed phase HPLC (Shimadzu LC-20AT, ReproSil 100 C8, 5 µm, 250 x 4 mm) with a flow of 1 mL/min at 40 °C. Solvent A: 25 mM 1,1,1,3,3,3-hexafluoropropan-2-ol (HFIP) / 2.1 mM triethylamine (TEA) in MilliQ·H_2O pH 8; Solvent B: acetonitrile. The gradient used for the purification are indicated in Table 7.1.

Table 7.1: Oligomer HPLC gradients, calculated and found masses by ESI-MS, and yields.

Oligomer	HPLC gradient B [%] ($t_{R\ [min]}$)	Calc. mass	Found mass	Yield [%]
O1	20 (2), 40 (24)	1221.3902	1221.3944	3.9
O2	15 (2), 40 (24)	1464.4166	1464.4209	4
O3	15 (2), 40 (24)	1676.4616	1676.4654	3.7
O4	20 (0), 50 (24)	2105.5856	2105.5880	3.7
O5	20 (0), 50 (24)	2533.8465	2533.7015	5.3
O6	15 (2), 40 (24)	1676.4616	1676.4656	1.5
O7	20 (0), 50 (24)	2105.5863	2105.5884	3.1
O8	20 (0), 50 (24)	2533.7041	2533.7025	3.2

All oligomers were dissolved in a 1:1 solution of EtOH / MilliQ·H_2O. Their concentration were determined by measuring their absorption at 384 nm for oligomers containing $Py_{1,6}$ and 386 nm for oligomers containing $Py_{1,8}$. The molar absorptivity used in [L*mol^{-1}*cm^{-1}] for the two building blocks were respectively: $\varepsilon_{Py_{1,6}}$: 54'000 and $\varepsilon_{Py_{1,8}}$: 62'000. The HPLC traces of all oligomers are presented in Figure 7.15, the corresponding MS results are listed in Table 7.1 and the MS spectra are displayed in Figure 7.16 to Figure 7.31.

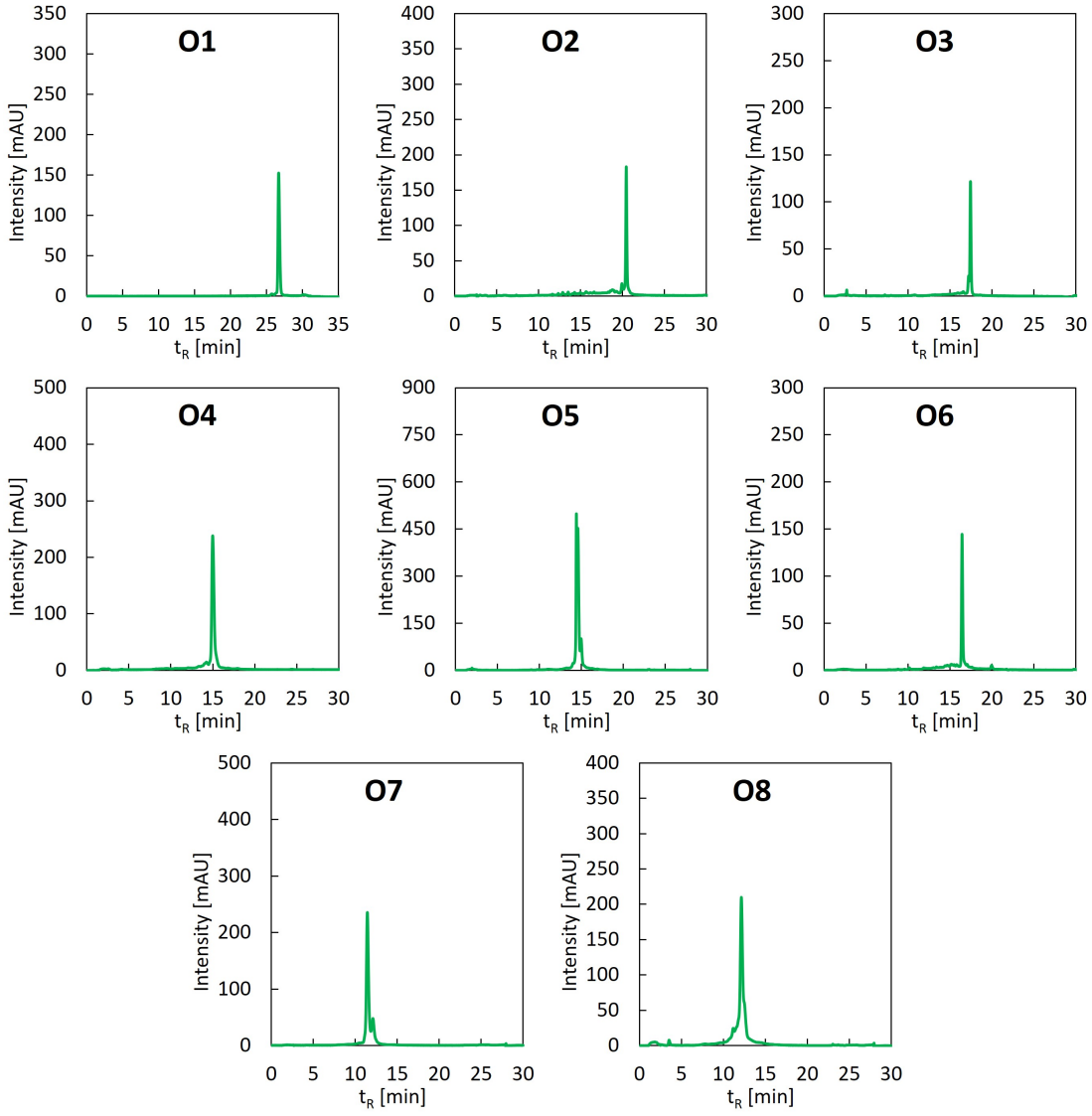

Figure 7.15: HPLC traces of α-mannose modified oligomers.

7.2.4 MS Spectra

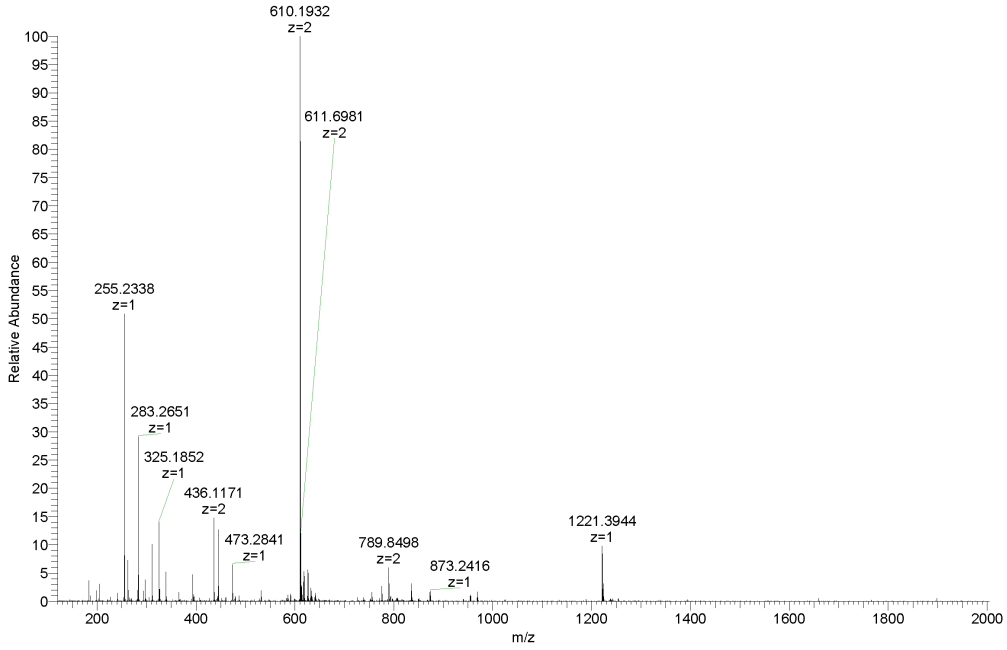

Figure 7.16: Mass spectrum of oligomer 1.

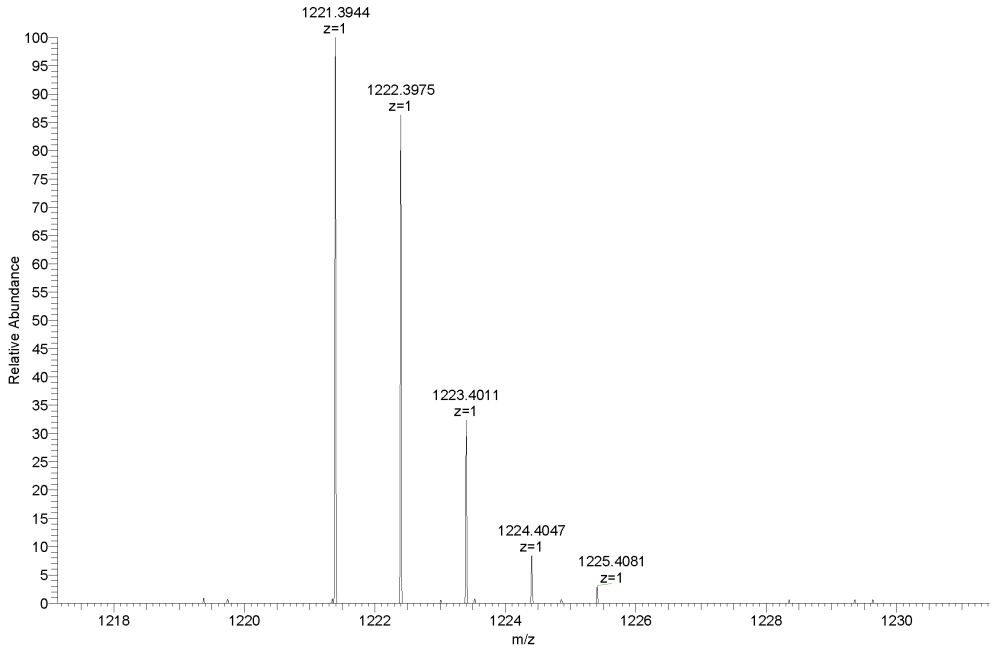

Figure 7.17: Mass spectrum (zoom) of oligomer 1.

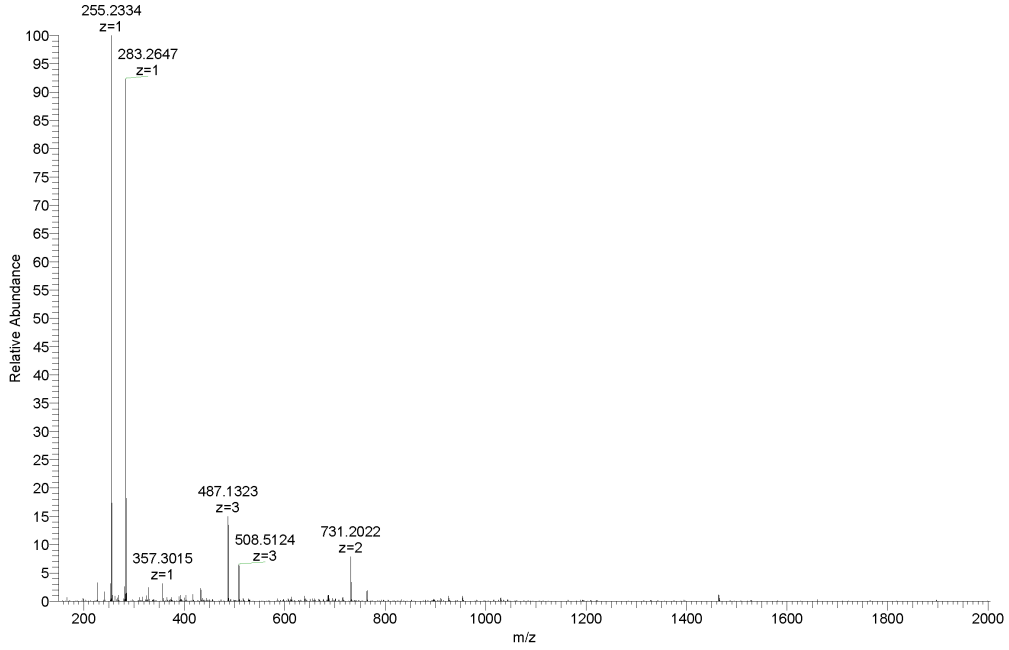

Figure 7.18: Mass spectrum of oligomer 2.

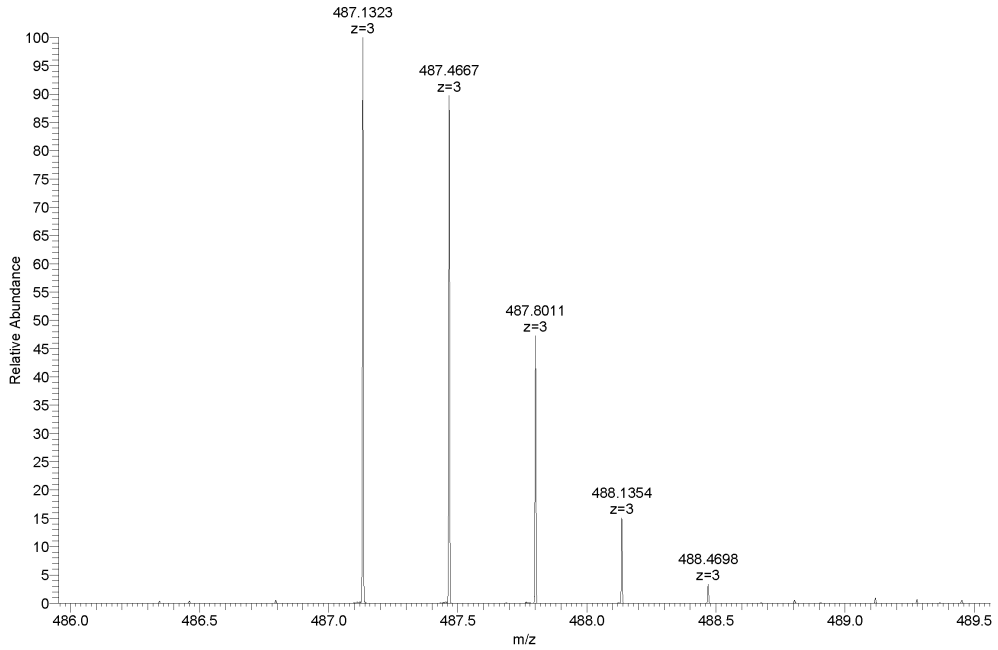

Figure 7.19: Mass spectrum (zoom) of oligomer 2.

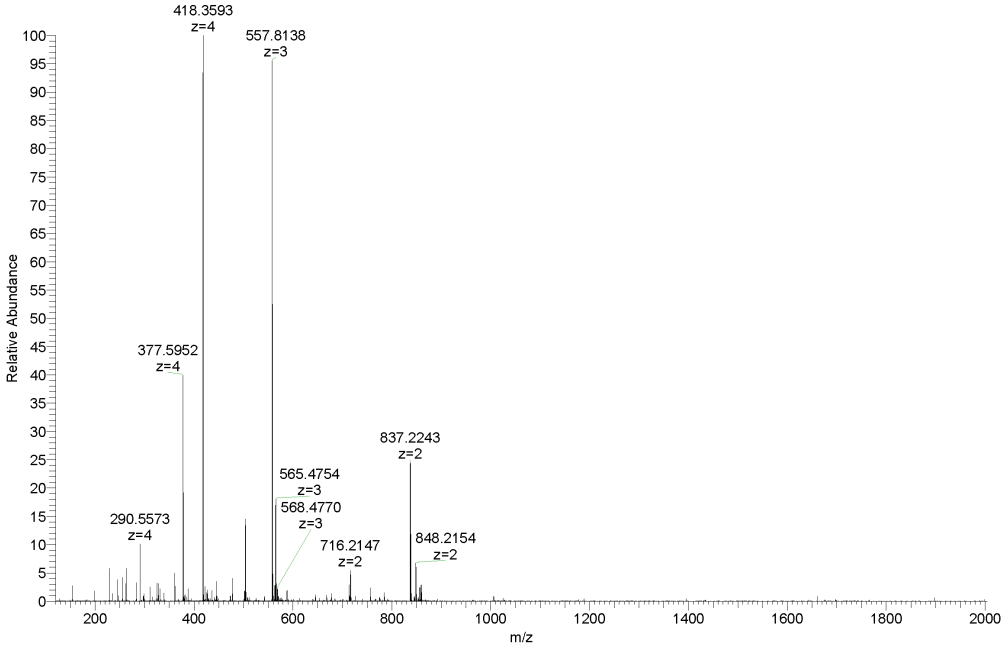

Figure 7.20: Mass spectrum of oligomer 3.

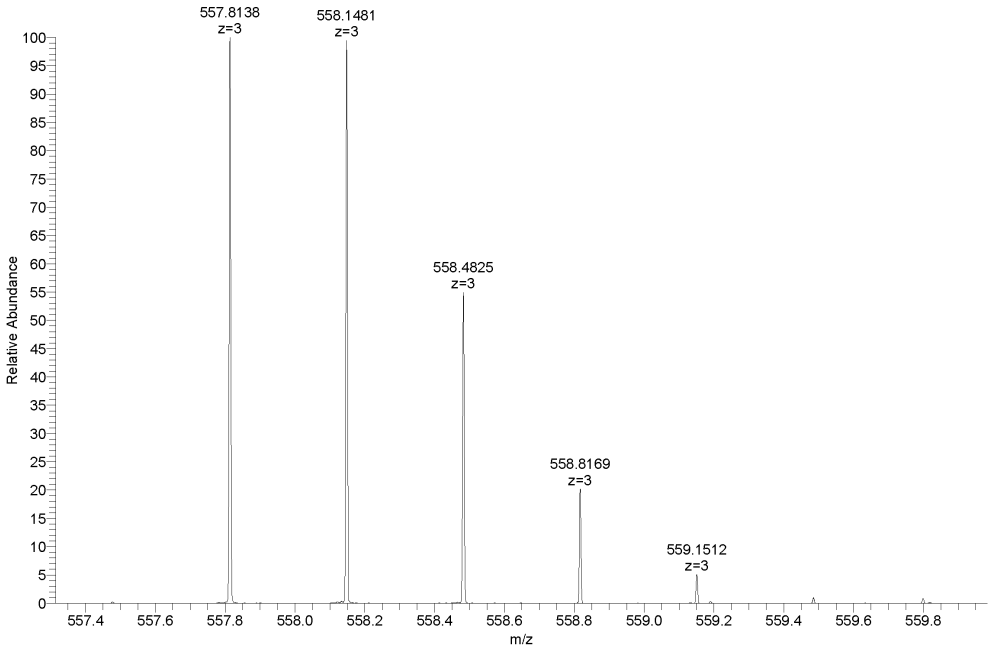

Figure 7.21: Mass spectrum (zoom) of oligomer 3.

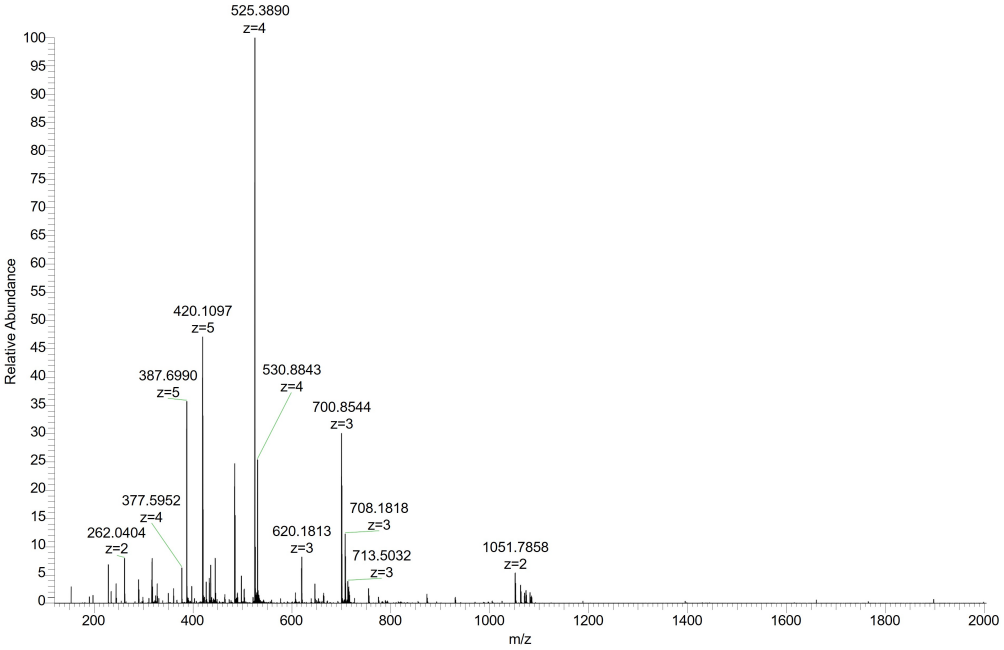

Figure 7.22: Mass spectrum of oligomer 4.

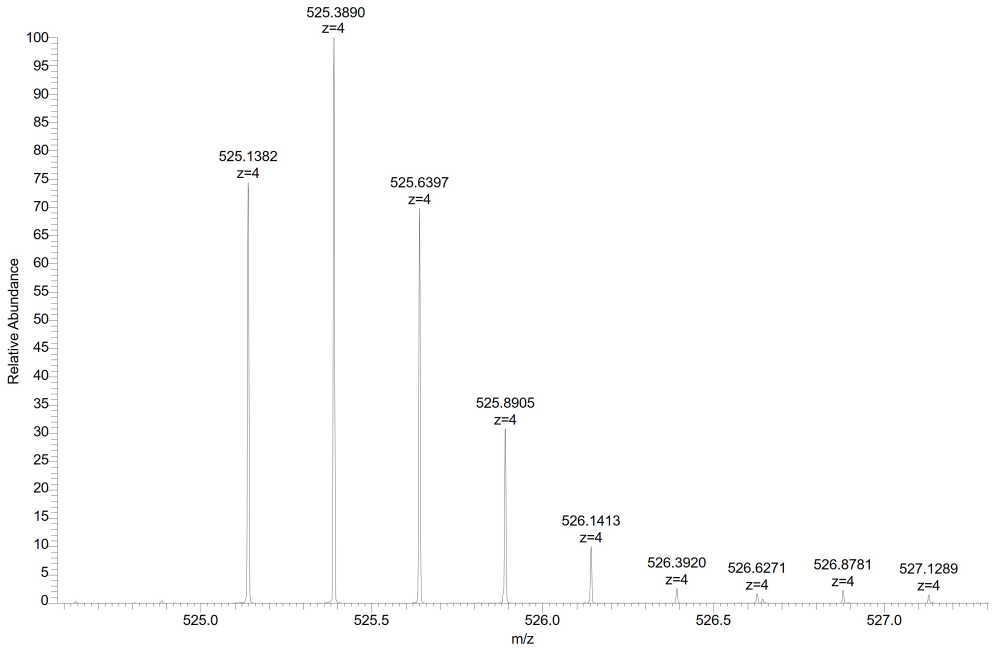

Figure 7.23: Mass spectrum (zoom) of oligomer 4.

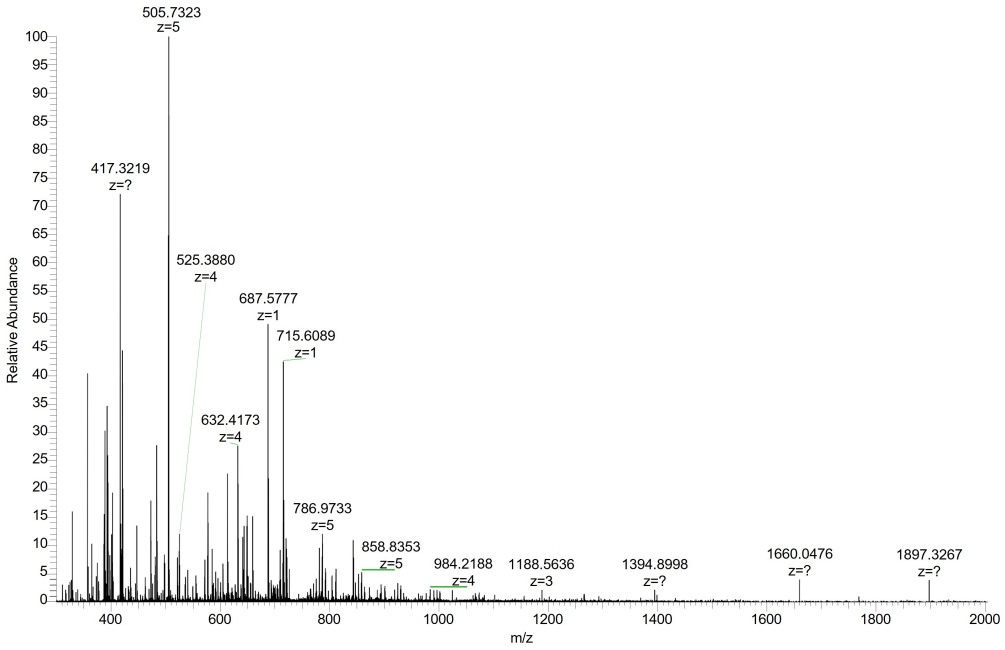

Figure 7.24: Mass spectrum of oligomer 5.

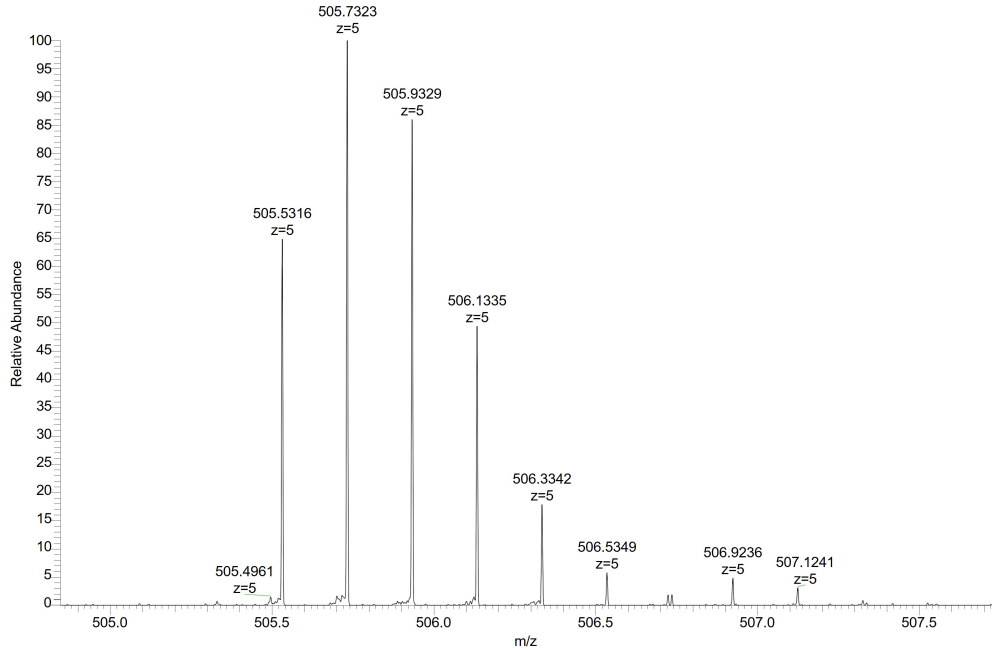

Figure 7.25: Mass spectrum (zoom) of oligomer 5.

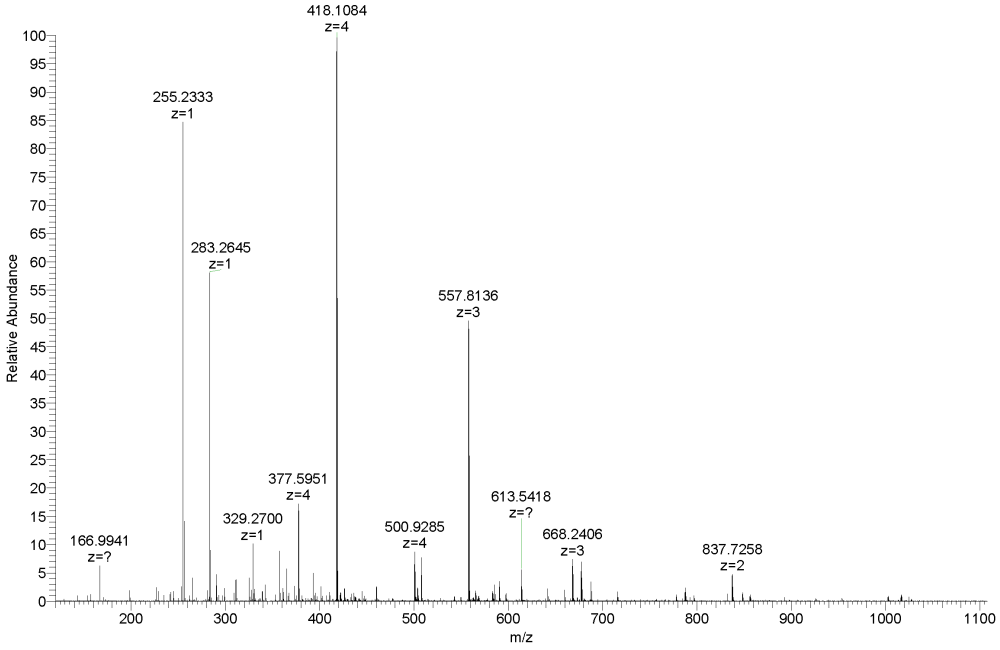

Figure 7.26: Mass spectrum of oligomer 6.

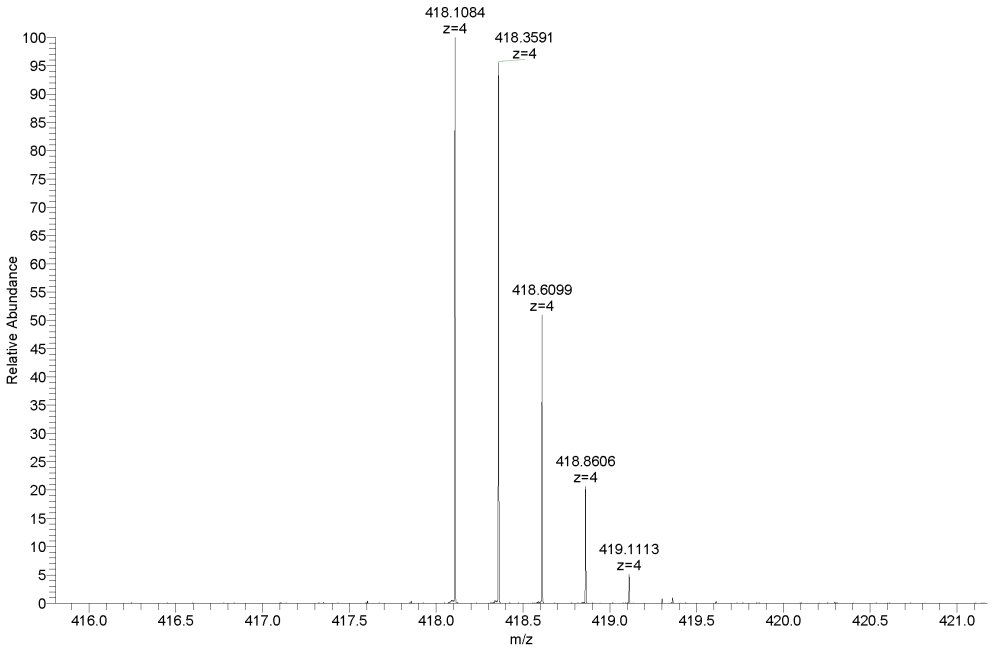

Figure 7.27: Mass spectrum (zoom) of oligomer 6.

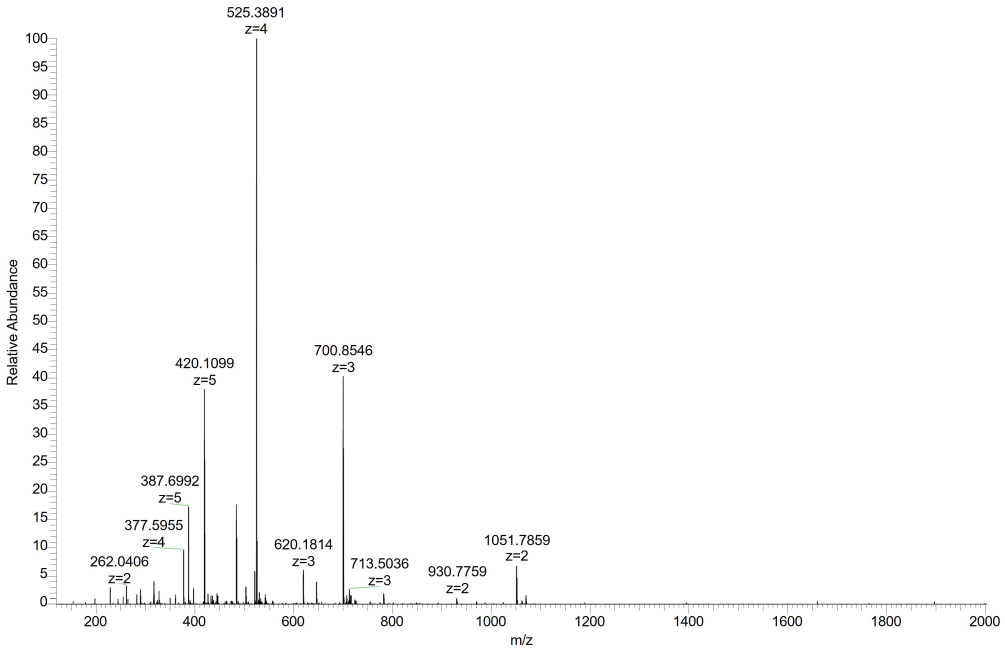

Figure 7.28: Mass spectrum of oligomer 7.

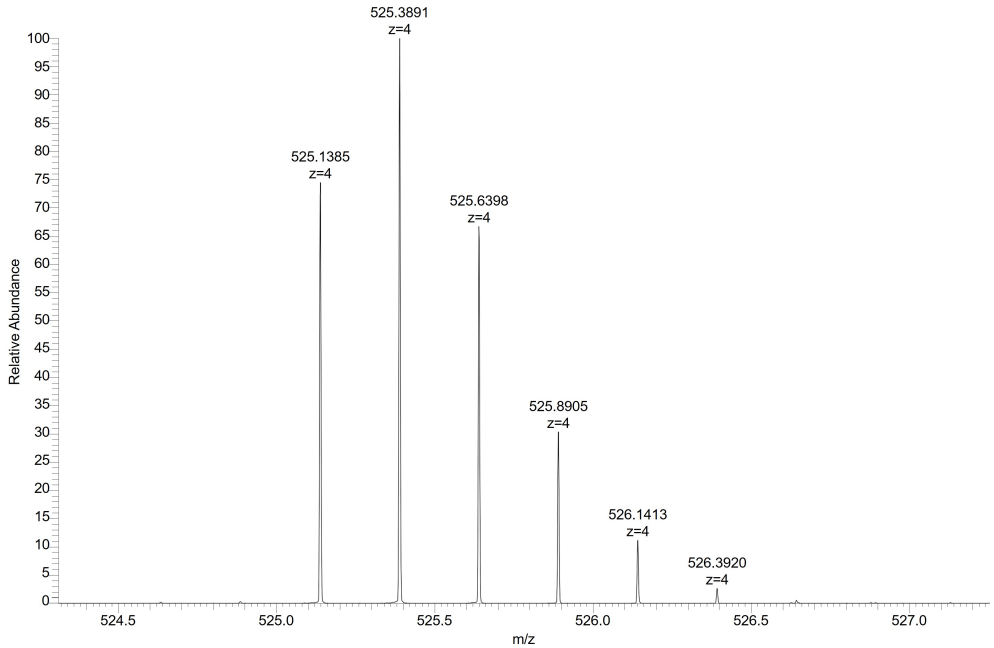

Figure 7.29: Mass spectrum (zoom) of oligomer 7.

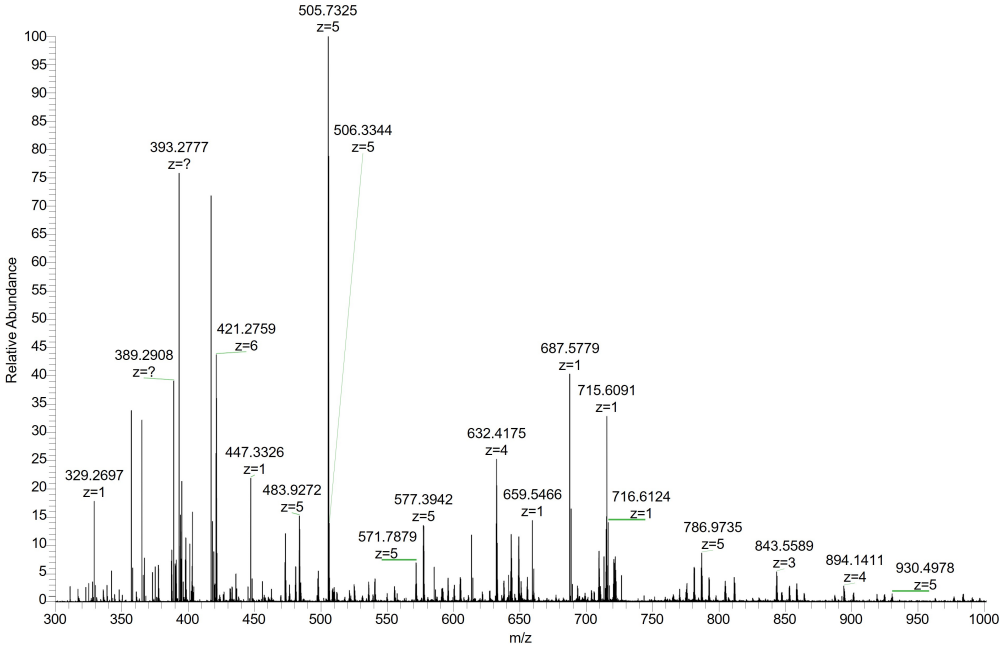

Figure 7.30: Mass spectrum of oligomer 8.

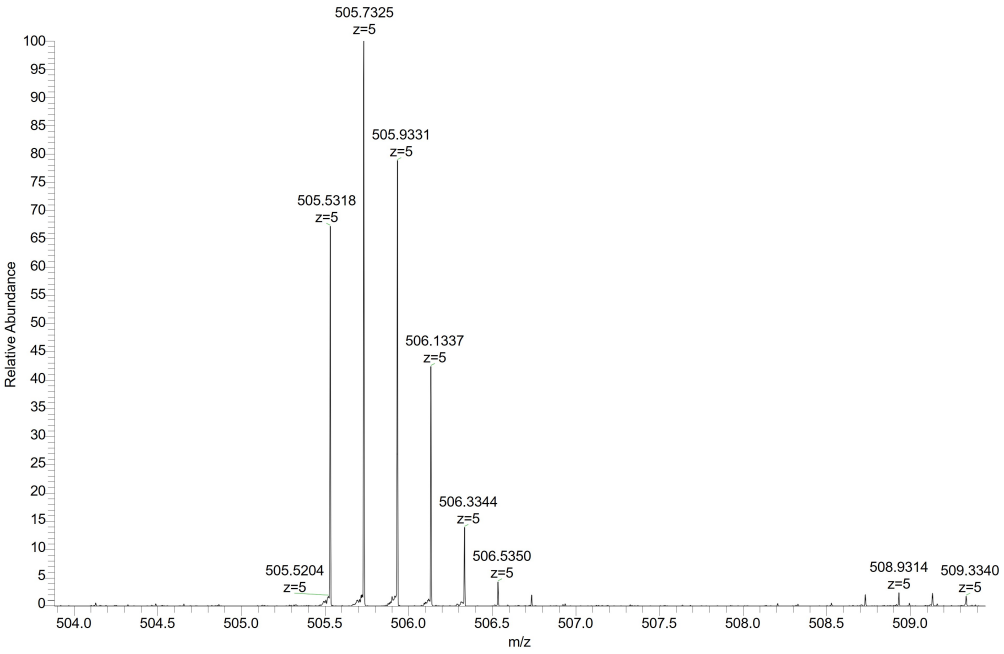

Figure 7.31: Mass spectrum (zoom) of oligomer 8.

7.2.5 Spectroscopic and Microscopic Measurements

Additionnal UV-vis absorption spectra for **O4** and **O5**.

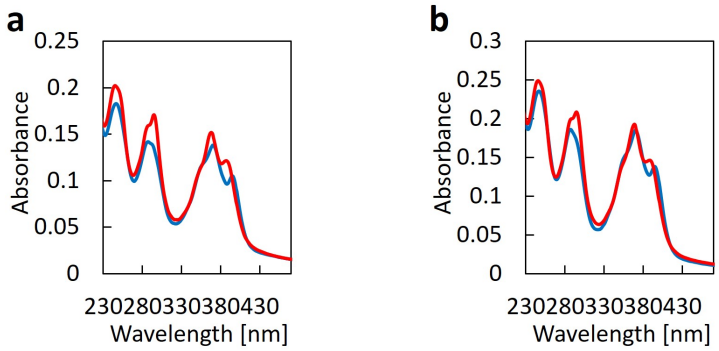

Figure 7.32: UV-Vis absorption spectra of (a) **O4**; and (b) **O5** at 20 °C (blue) and 70 °C (red) curves of the respective oligomer in aqueous media. Conditions: 1 µM **O4**, 10 mM sodium phosphate buffer pH 7.2, 200 mM NaCl; 1 µM **O5**, 10 mM sodium phosphate buffer pH 7.2, 200 mM NaCl.

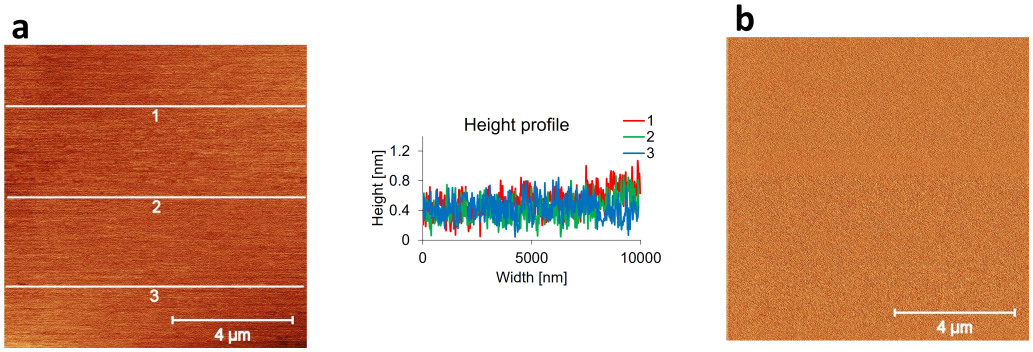

Figure 7.33: (a) AFM with corresponding cross section and (b) amplitude scan of an APTES-modified mica sheet.

7.2.6 Buffer Solutions

Sodium Phosphate Buffer 10x

To $Na_2HPO_4{\cdot}2H_2O$ (5.5 g, 0.06 mol) in MilliQ·H_2O was added $NaH_2PO_4{\cdot}H_2O$ (2.6 g, 0.04 mol). The buffer was adjusted to pH 7.2 using NaOH and the volume completed to 500 mL with MilliQ·H_2O. The buffer was then filtered over 0.20 µm pore size polyester filters, divided into 1 mL aliquots, and stored at -30 °C.

Phosphate-Buffered Saline 10x

To $Na_2HPO_4 \cdot 2H_2O$ (4.5 g, 0.1 mol) in MilliQ·H_2O was added KH_2PO_4 (0.6 g, 0.02 mol), KCl (0.5 g, 0.03 mol) and NaCl (20 g, 1,37 mol). The buffer was adjusted to pH 6.8 using NaOH and the volume completed to 250 mL with MilliQ·H_2O. The buffer changes to pH 7.2 upon 10x dilution. The buffer was then filtered over 0.20 µm pore size polyester filters, divided into 1 mL aliquots, and stored at -30 °C.

Protein Stock Solutions

From the documentation furnished by Sigma Aldrich, a buffer was prepared to dissolve the protein. A Con A stock solution in PBS pH 6.8 was prepared as follow: to ± 0.3 mg of Con A was added 100 µL of 10x PBS pH 6.8 along with 20 µL of 5 M $CaCl_2$, 20 µL of 5 M $MnCl_2$ and 860 mL of MilliQ·H_2O. The concentration measured by nanodrop was 0.748 mg / mL (29.33 µM). From this, a second stock solution was prepared at 0.2 µM for the AFM measurements.

7.3 Appendix - Chapter 4

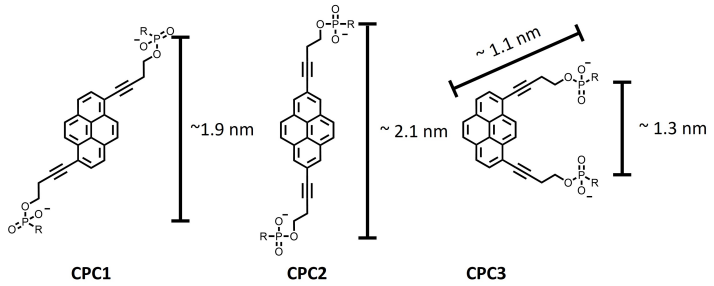

Scheme 7.6: Molecular length of the different pyrene molecules (determined with Chem3D).

7.3.1 Organic Chemistry

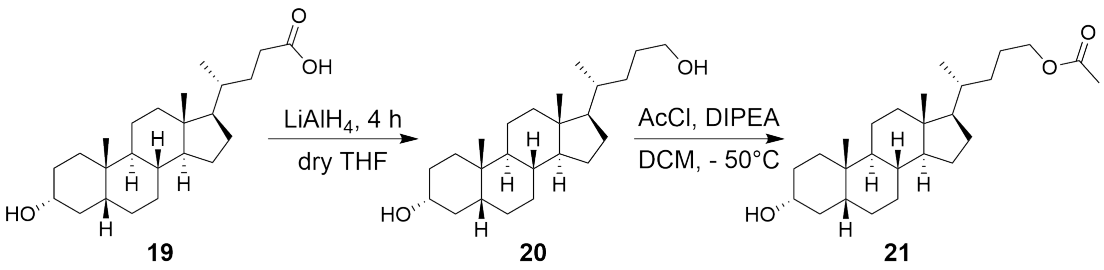

Scheme 7.7: Synthesis of acetyl protected cholane **21** from lithocholic acid **19**.

(3R,8R,9S,10S,13R,14S,17R)-17-((R)-5-hydroxypentan-2-yl)-10,13-dimethylhexadecahydro-1H-cyclopenta[a]phenanthren-3-ol (20)

The synthesis of cholane-3,24-diol (3α,5β), **20**, was performed as described in literature.[143] To a solution of **19** (1 g, 2.7 mmol, 1 eq.) in dry THF (60 mL) at 0°C was slowly added a 1 M solution of $LiAlH_4$ (12.6 mL, 12.6 mmol, 4 eq.). The reaction was then stirred 2.5 h at RT. The reaction was then quenched subsequently with H_2O (0.5 mL), 15% aqueous NaOH (0.5 mL) and additional H_2O (1.5 mL). The precipitate was removed by filtration and the organic phase was dried with Na_2SO_4, filtered, and concentrated under reduced pressure. Compound **20** was isolated as a white solid (693 mg, 1.9 mmol, 72 %). ^{1}H NMR **20** (300 MHz, $CDCl_3$) δ = 3.70 – 3.52 (m, 3H), 2.02 – 0.93 (m, 24H), 0.94 – 0.89 (m, 6H), 0.64 (s, 3H).

(4R)-4-((3R,8R,9S,10S,13R,14S,17R)-3-hydroxy-10,13-dimethylhexadecahydro-1H-cyclopenta[a]phenanthren-17-yl)pentyl acetatel (21)

The synthesis of **21** was adapted from literature.[144] To a solution of **20** (575 mg, 1.6 mmol, 1 eq.) in dry THF (50 mL) at -50 °C were added DIPEA (0.58 mL, 3.3 mmol, 2.1 eq.) and AcCl (135 µL, 1.9 mmol, 1.9 eq.). The reaction was stirred 2 h at -50 °C followed by 1 h at RT. It was quenched with 3.7% aqueous HCl (10 mL), extracted with ether, dried over Na_2SO_4, filtered, and concentrated under reduced pressure. The crude was then purified by column chromatography (SiO_2, heptane / EtOAc 8:2, Rf = 0.16). Compound **21** was isolated as an oil (180 mg, 0.4 mmol, 28%). ^{1}H NMR **21** (300 MHz, $CDCl_3$; sample contained traces of DCM) δ = 4.01 (m, 2H), 3.62 (m, 1H), 2.04 (s, 3H), 2.00 – 0.94 (m, 21H), 0.91 (m, 6H), 0.64 (s, 3H). HRMS-NSI (m/z): $[M+H+K]^+$ calcd for $C_{26}H_{44}O_3K$, 443.2922; found, 443.2929.

bis(2-cyanoethyl)(pyrene-1,6-diylbis(but-3-yne-4,1-diyl))bis(diisopropylphosphoramidite) (23)

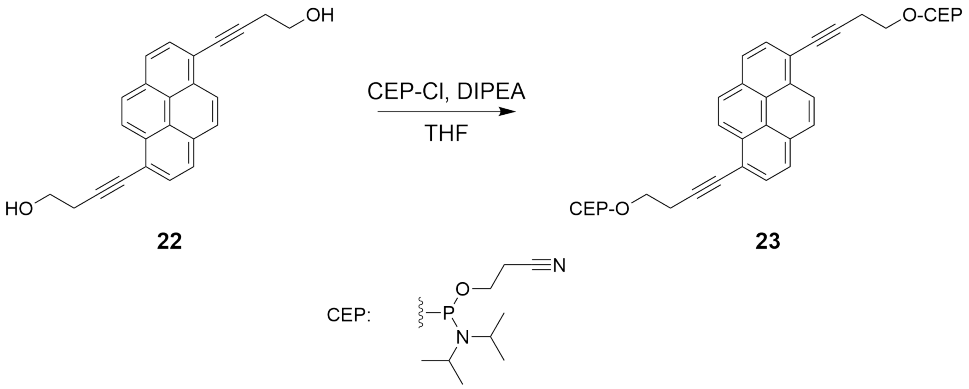

Scheme 7.8: Diphosphitylation of compound **22** to obtain compound **23**.

Compound **22** (50 mg, 0.2 mmol, 1 eq.) was dissolved in anhydrous THF (3 mL) and DIPEA (0.3 mL, 1.5 mmol, 10 eq.). CEP-Cl (73 µL, 0.3 mmol, 2.2 eq.) was added dropwise at RT and the reaction stirred for 1 h under argon. The reaction was concentrated under reduced pressure. The crude was purified by a short flash column chromatography on silica gel (heptane / EtOAc / NEt_3 7:3:1%). Product **23** was isolated as a yellow oil (112 mg, 97%). ^{1}H NMR **23** (300 MHz, $CDCl_3$; sample contained traces of heptane) δ = 8.60 (d, J = 9.1 Hz, 2H), 8.18 – 8.06 (m, 6H), 4.13 – 3.81 (m, 9H), 3.70 (dp, J = 10.4 Hz, 6.8 Hz, 4H), 3.00 (t, J = 6.8 Hz, 4H), 2.67 (td, J = 6.5 Hz, 4.8 Hz, 5H), 1.32 – 1.20 (m, 33H).^{31}P NMR **23** (121 MHz, $CDCl_3$) δ = 148.25. HRMS-NSI (m/z): $[M+H]^+$ calcd for $C_{42}H_{53}N_4O_4P_2$, 739.3537; found, 739.3553.

Protected Oligomer CPC1 (24)

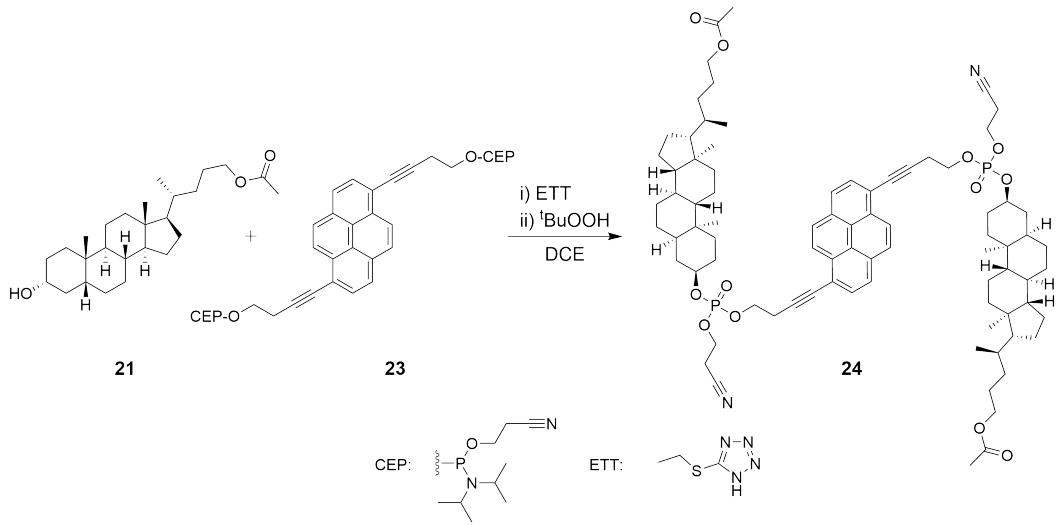

Scheme 7.9: Coupling of **21** and **23** to obtain compound **24**.

To a solution of **23** (20 mg, 0.03 mmol, 1 eq.) in DCE (0.19 mL) was added 5-(ethylthio)-1H-tetrazole (12 mg, 0.1 mmol, 3.5 eq.) in DCE (0.31 mL) under argon atmosphere. Compound **21** (32 mg, 0.1 mmol, 3 eq.) was dissolved in DCE (0.64 mL) and added to the activated compound **23**. The reaction was stirred at RT for 3 h. Tert-butyl hydroperoxide solution (70% in water, 23 µL, 0.2 mmol) was added. After 10 minutes, the reaction was diluted with $CHCl_3$ (15 mL) and washed with aq. sat. $NaHCO_3$ (15 mL) and brine (15 mL). The organic layer was dried over Na_2SO_4, filtered, and concentrated under reduced pressure. The crude was purified by a preparative TLC (DCM/toluene/MeOH 86:10:4) and subsequently used in the next step.

Oligomer CPC1

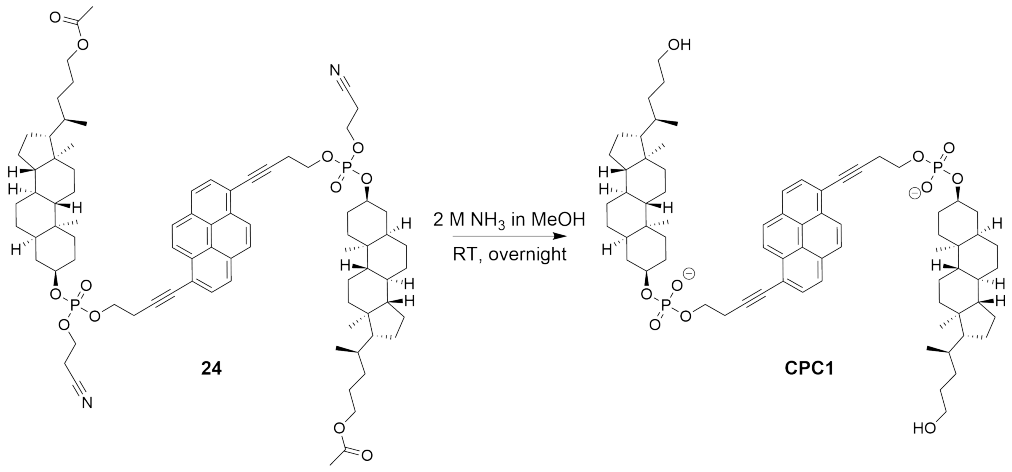

Scheme 7.10: Deprotection of **24** yielding **CPC1**.

Compound **24** was dissolved in a solution of 2 M NH_3 in MeOH (5 mL) and stirred at RT for 72 h. The sample was lyophilized and then purified by RP-HPLC (for conditions see Table 7.2 on page 112). HRMS-NSI (m/z): $[M-H]^-$ calcd for $C_{72}H_{98}O_{10}P_2$, 592.3323; found, 592.3315.

bis(2-cyanoethyl)(pyrene-2,7-diylbis(but-3-yne-4,1-diyl))bis (diisopropylphosphoramidite) (26)

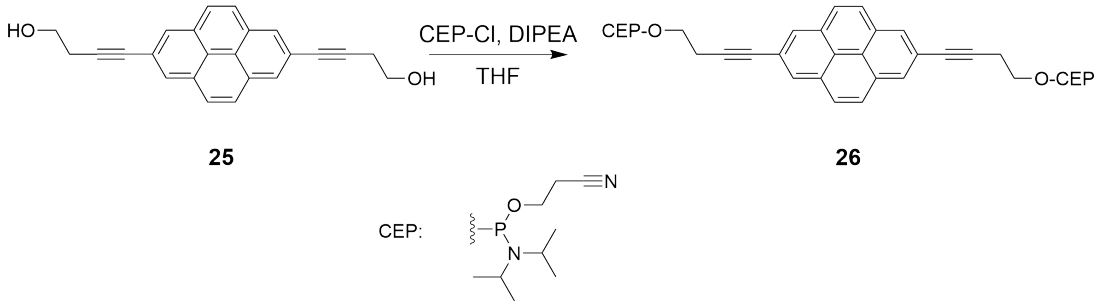

Scheme 7.11: Diphosphitylation of compound **25** to obtain compound **26**.

Compound **25** (100 mg, 0.3 mmol, 1 eq.) was dissolved in anhydrous THF (6 mL) and DIPEA (0.5 mL, 2.9 mmol, 10 eq.). CEP-Cl (145 µL, 0.7 mmol, 2.2 eq.) was added dropwise at RT and the reaction stirred for 1 h under argon. The reaction was concentrated under reduced pressure. The crude was purified by a short flash column chromatography on silica gel (heptane / EtOAc / NEt_3 7:3:1%). Product **26** was isolated as a colorless oil (190 mg, 87%). ^{1}H NMR **26** (300 MHz, $CDCl_3$; sample contained traces of heptane) δ = 8.18 (s, 4H), 7.98 (s, 4H), 4.05 – 3.78 (m, 6H), 3.67 (m, 3H), 2.85 (t, J =

6.9 Hz, 4H), 2.67 (m, 4H), 1.23 (m, 27H). ^{31}P NMR **26** (121 MHz, $CDCl_3$) δ = 148.23. HRMS-NSI (m/z): $[M+H]^+$ calcd for $C_{42}H_{53}N_4O_4P_2$, 739.3537; found, 739.3546.

Protected Oligomer CPC2 (27)

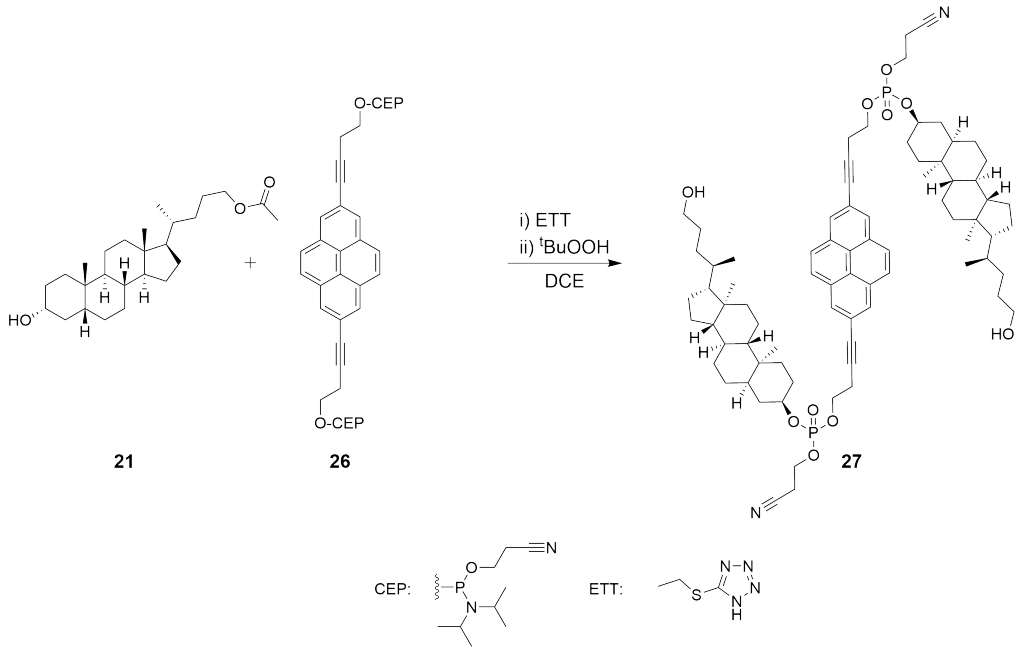

Scheme 7.12: Coupling of **21** and **26** to obtain compound **27**.

To a solution of **26** (30 mg, 0.04 mmol, 1 eq.) in DCE (0.28 mL) was added 5-(ethylthio)-1H-tetrazole (18.5 mg, 0.1 mmol, 3.5 eq.) in DCE (0.47 mL) under argon atmosphere. Compound **21** (49 mg, 0.1 mmol, 3 eq.) was dissolved in DCE (0.96 mL) and added to the activated compound **26**. The reaction was stirred at RT for 3 h. Tert-butyl hydroperoxide solution (70% in water, 34 µL, 0.2 mmol) was added. After 10 min, the reaction was diluted with $CHCl_3$ (15 mL) and washed with aq. sat. $NaHCO_3$ (15 mL) and brine (15 mL). The organic layer was dried over Na_2SO_4, filtered, and concentrated under reduced pressure. The crude was purified by a preparative TLC (DCM/toluene/MeOH 88:10:2) and subsequently used in the next step.

Oligomer CPC2

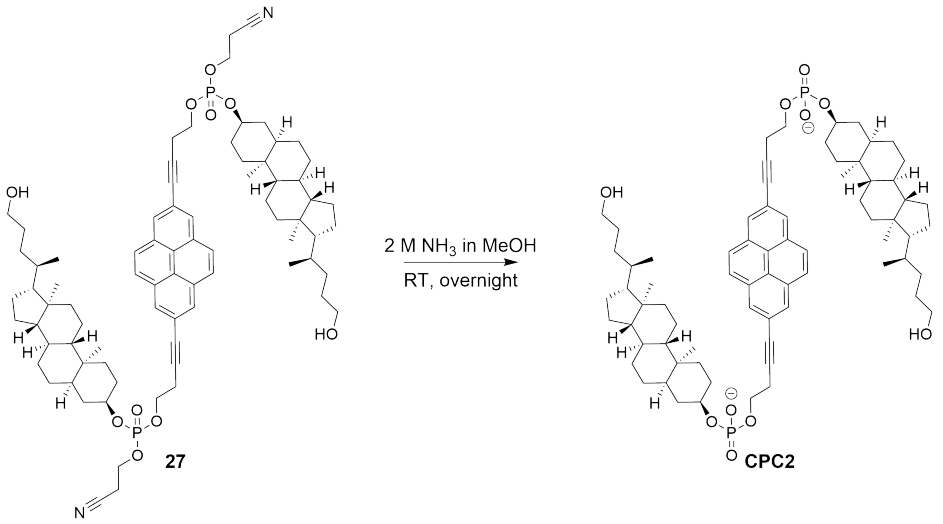

Scheme 7.13: Deprotection of **27** yielding **CPC2**.

Compound **27** was dissolved in a solution of 2 M NH_3 in MeOH (5 mL) and stirred at RT for 72 h. The sample was lyophilized and then purified by RP-HPLC (for conditions see Table 7.2 on page 112). HRMS-NSI (m/z): $[M-H]^-$ calcd for $C_{72}H_{98}O_{10}P_2$, 592.3323; found, 592.3312.

bis(2-cyanoethyl)(pyrene-1,8-diylbis(but-3-yne-4,1-diyl)) bis(diisopropylphosphoramidite) (29)

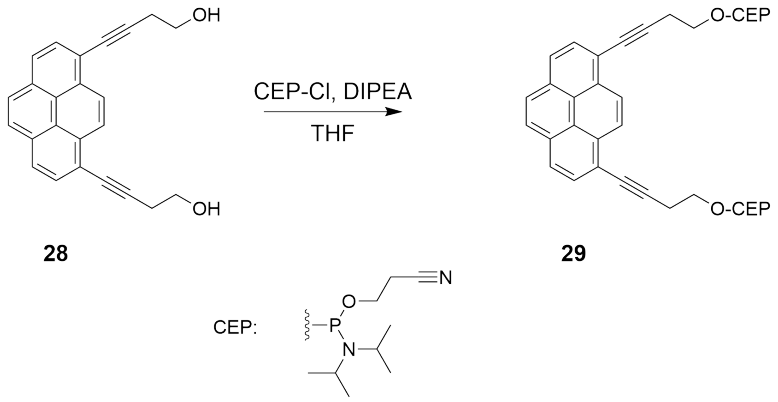

Scheme 7.14: Diphosphitylation of compound **28** to obtain compound **29**.

Compound **28** (50 mg, 0.2 mmol, 1 eq.) was dissolved in anhydrous THF (3 mL) and DIPEA (0.3 mL, 1.5 mmol, 10 eq.). CEP-Cl (72.5 µL, 0.3 mmol, 2.2 eq.) was added dropwise at RT and the reaction stirred for 1 h under argon. The reaction was concentrated under reduced pressure. The crude was purified by a short flash column

chromatography on silica gel (heptane / EtOAc / NEt_3 8:2:1%). Product **29** was isolated as a yellow oil (95 mg, 87%). ^{1}H NMR **29** (300 MHz, $CDCl_3$) δ = 8.63 (s, 2H), 8.07 (s, 3H), 8.01 (s, 2H), 3.94 (m, 7H), 3.75 – 3.56 (m, 4H), 2.99 (m, 4H), 2.64 (m, 4H), 1.22 (m, 31H). ^{31}P NMR **29** (121 MHz, $CDCl_3$) δ = 148.28. HRMS-NSI (m/z): $[M+H]^+$ calcd for $C_{42}H_{53}N_4O_4P_2$, 739.3537; found, 739.3550.

Protected Oligomer CPC3 (30)

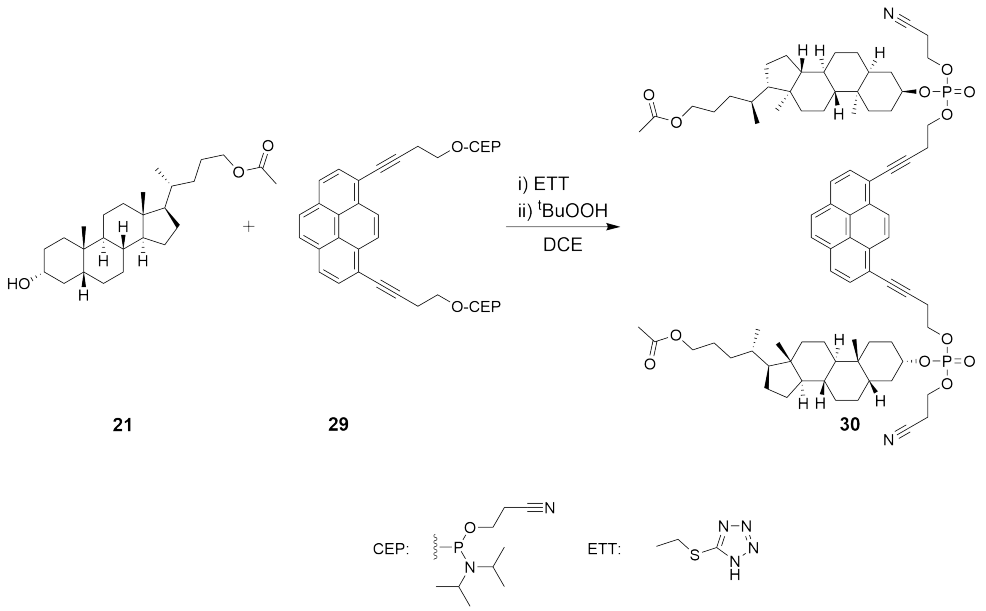

Scheme 7.15: Coupling of **21** and **29** to obtain compound **30**.

To a solution of **29** (30 mg, 0.04 mmol, 1 eq.) in DCE (0.29 mL) was added 5-(ethylthio)-1H-tetrazole (19.1 mg, 0.2 mmol, 3.5 eq.) in DCE (0.48 mL) under argon atmosphere. Compound **21** (51 mg, 0.1 mmol, 3 eq.) was dissolved in DCE (0.99 mL) and added to the activated compound **29**. The reaction was stirred at RT for 3 h. Tert-butyl hydroperoxide solution (70% in water, 35 µL, 0.3 mmol) was added. After 10 minutes, the reaction was diluted with $CHCl_3$ (15 mL) and washed with aq. sat. $NaHCO_3$ (15 mL) and brine (15 mL). The organic layer was dried over Na_2SO_4, filtered, and concentrated under reduced pressure. The crude was purified by a preparative TLC (DCM/toluene/MeOH 88:10:2) and subsequently used in the next step.

Oligomer CPC3

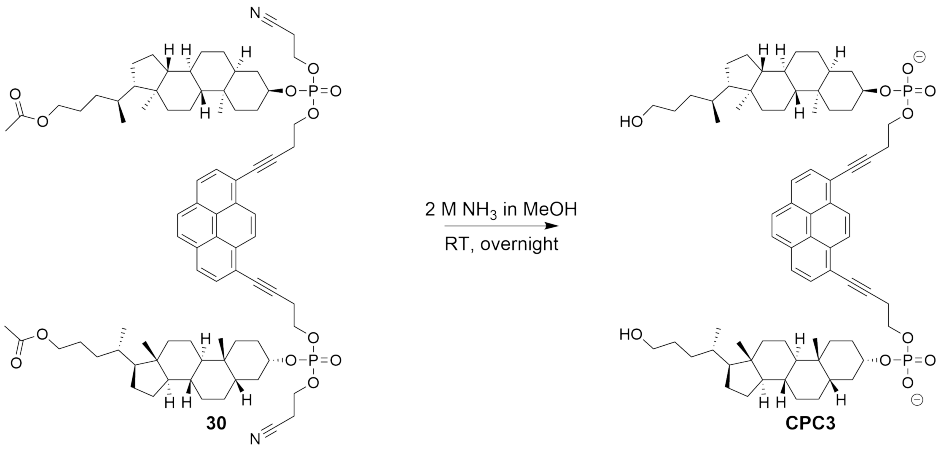

Scheme 7.16: Deprotection of **30** yielding **CPC3**.

Compound **30** was dissolved in a solution of 2 M NH_3 in MeOH (5 mL) and stirred at RT for 72 h. The sample was lyophilized and then purified by RP-HPLC (for conditions see Table 7.2 on page 112). HRMS-NSI (m/z): $[M-H]^-$ calcd for $C_{72}H_{98}O_{10}P_2$, 592.3323; found, 592.3312.

bis(2-cyanoethyl) (phenanthrene-3,6-diylbis(but-3-yne-4,1-diyl)) bis(diisopropylphosphoramidite) (32)

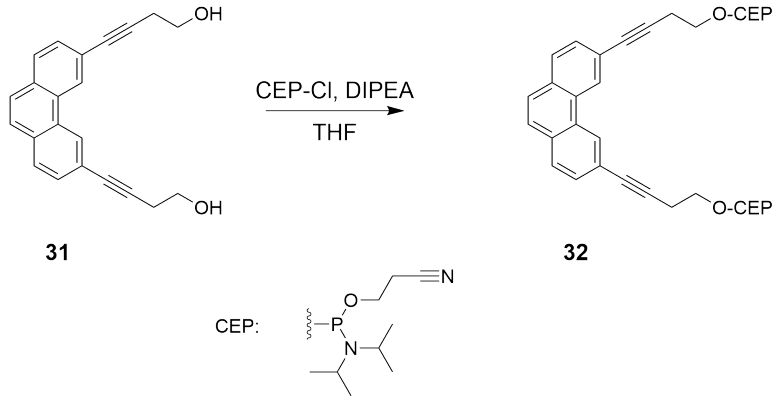

Scheme 7.17: Diphosphitylation of compound **31** to obtain compound **32**.

Compound **31** (50 mg, 0.2 mmol, 1 eq.) was dissolved in anhydrous THF (3 mL) and DIPEA (0.3 mL, 1.6 mmol, 10 eq.). CEP-Cl (78 µL, 0.4 mmol, 2.2 eq.) was added dropwise at RT and the reaction stirred for 1 h under argon. The reaction was concentrated under reduced pressure. The crude was purified by a short flash column chromatography on silica gel (heptane / EtOAc / NEt_3 7:3:1%). Product **32** was isolated as a colorless oil (118 mg, 97%). ^{1}H NMR **32** (300 MHz, $CDCl_3$) δ = 8.63 (d, J = 1.5

Hz, 2H), 7.72 (d, J = 8.2 Hz, 2H), 7.61 (s, 2H), 7.52 (dd, J = 8.2 Hz, 1.4 Hz, 2H), 3.82 (m, 7H), 3.59 (m, 3H), 2.75 (t, J = 7.0 Hz, 4H), 2.60 (m, 4H), 1.16 (dd, J = 6.8 Hz, 5.7 Hz, 29H). ^{31}P NMR **35** (121 MHz, $CDCl_3$) δ = 148.22.HRMS-NSI (m/z): $[M+H]^+$ calcd for $C_{40}H_{53}N_4O_4P_2$, 715.3537; found, 715.3546.

Protected Oligomer CPC4 (33)

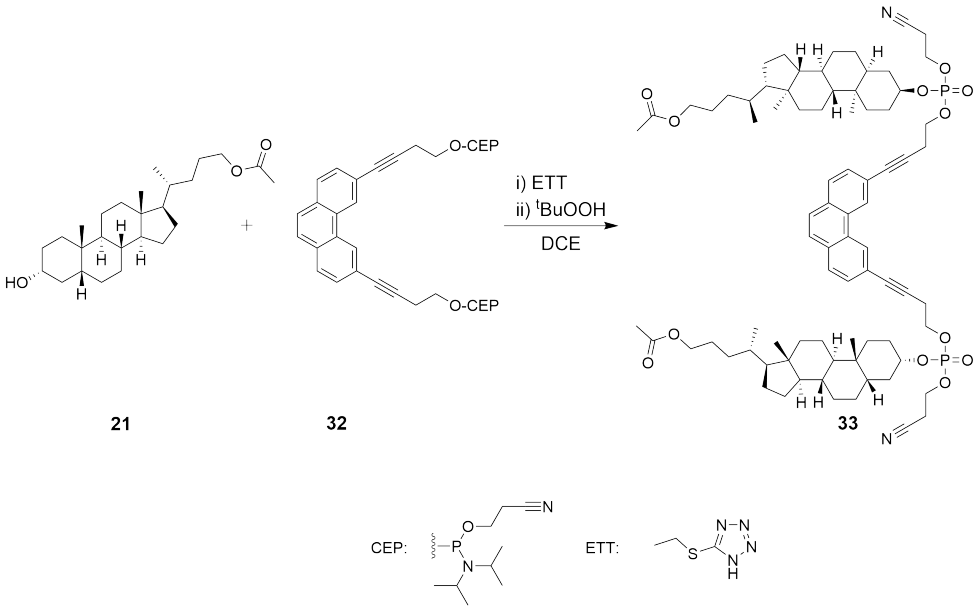

Scheme 7.18: Coupling of **21** and **32** to obtain compound **33**.

To a solution of **32** (20 mg, 0.03 mmol, 1 eq.) in DCE (0.19 mL), was added 5-(ethylthio)-1H-tetrazole (12 mg, 0.1 mmol, 3.5 eq.) in DCE (0.31 mL) under argon atmosphere. Compound **21** (32 mg, 0.1 mmol, 3 eq.) was dissolved in DCE (0.64 mL) and added to the activated compound **32**. The reaction was stirred at RT for 3 h. Tert-butyl hydroperoxide solution (70% in water, 23 µL, 0.2 mmol) was added. After 10 minutes, the reaction was diluted with $CHCl_3$ (15 mL) and washed with aq. sat. $NaHCO_3$ (15 mL) and brine (15 mL). The organic layer was dried over Na_2SO_4, filtered, and concentrated under reduced pressure. The crude was purified by a preparative TLC (DCM/toluene/MeOH 86:10:4) and subsequently used in the next step.

Oligomer CPC4

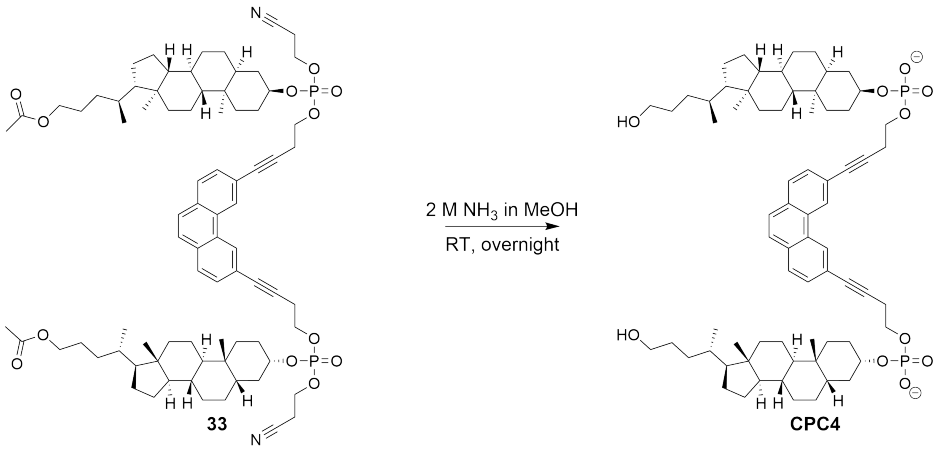

Scheme 7.19: Deprotection of **33** yielding **CPC4**.

Compound **33** was dissolved in a solution of 2 M NH_3 in MeOH (5 mL) and stirred at RT for 72 h. The sample was lyophilized and then purified by RP-HPLC (for conditions see Table 7.2 on page 112). HRMS-NSI (m/z): $[M-H]^-$ calcd for $C_{70}H_{98}O_{10}P_2$, 580.3323; found, 580.3310.

bis(2-cyanoethyl) (phenanthrene-2,7-diylbis(but-3-yne-4,1-diyl)) bis(diisopropylphosphoramidite) (35)

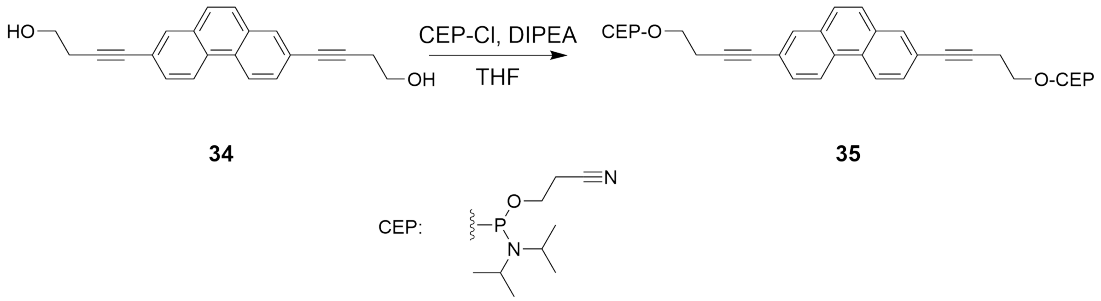

Scheme 7.20: Diphosphitylation of compound **34** to obtain compound **35**.

Compound **34** (50 mg, 0.2 mmol, 1 eq.) was dissolved in anhydrous THF (3 mL) and DIPEA (0.3 mL, 1.6 mmol, 10 eq.). CEP-Cl (78 µL, 0.4 mmol, 2.2 eq.) was added dropwise at RT and the reaction stirred for 1 h under argon. The reaction was concentrated under reduced pressure. The crude was purified by a short flash column chromatography on silica gel (heptane / EtOAc / NEt_3 7:3:1%). Product **35** was isolated as a colorless oil (104 mg, 91%). ^{1}H NMR **35** (300 MHz, $CDCl_3$; sample contained traces of heptane) δ = 8.53 (d, J = 8.7 Hz, 2H), 7.92 (d, J = 1.7 Hz, 2H), 7.69 – 7.59 (m, 4H), 4.01 – 3.74 (m, 8H), 3.65 (m, 4H), 2.80 (t, J = 6.9 Hz, 4H), 2.66 (m, 4H), 1.28 – 1.17 (m,

29H). ^{31}P NMR **35** (121 MHz, $CDCl_3$) δ = 148.21. HRMS-NSI (m/z): $[M+H]^+$ calcd for $C_{40}H_{53}N_4O_4P_2$, 715.3537; found, 715.3552.

Protected Oligomer CPC5 (36)

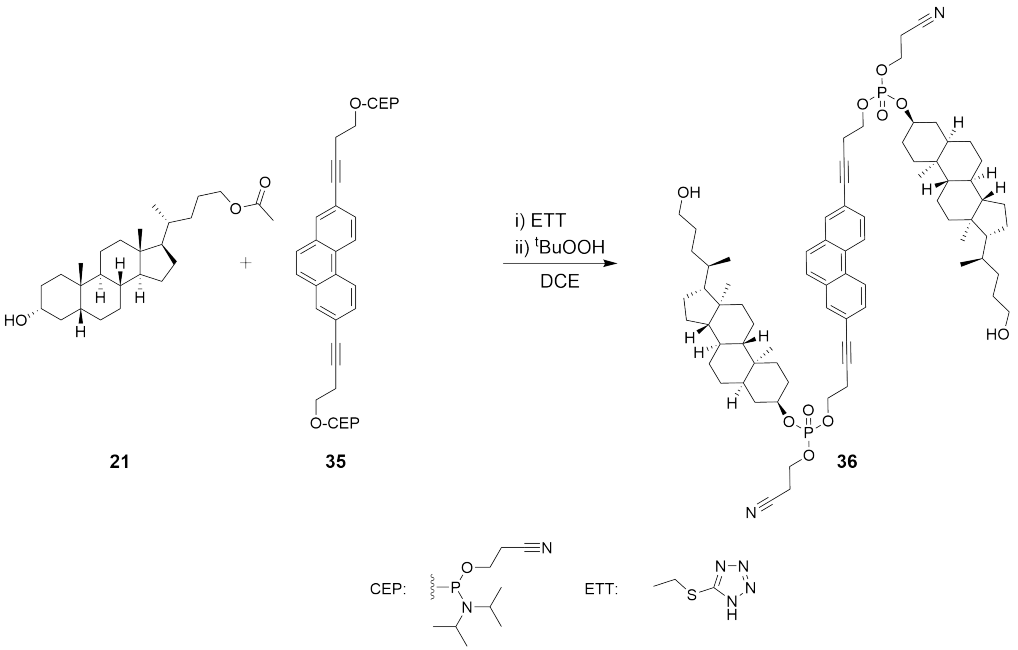

Scheme 7.21: Coupling of **21** and **35** to obtain compound **36**.

To a solution of **35** (20 mg, 0.03 mmol, 1 eq.) in DCE (0.20 mL) was added 5-(ethylthio)-1H-tetrazole (13 mg, 0.1 mmol, 3.5 eq.) in DCE (0.32 mL) under argon atmosphere. Compound **21** (34 mg, 0.1 mmol, 3 eq.) was dissolved in DCE (0.66 mL) and added to the activated compound **35**. The reaction was stirred at RT for 3 h. Tert-butyl hydroperoxide solution (70% in water, 23 µL, 0.2 mmol) was added. After 10 minutes, the reaction was diluted with $CHCl_3$ (15 mL) and washed with aq. sat. $NaHCO_3$ (15 mL) and brine (15 mL). The organic layer was dried over Na_2SO_4, filtered, and concentrated under reduced pressure. The crude was purified by a preparative TLC (DCM/toluene/MeOH 86:10:4) and subsequently used in the next step.

Oligomer CPC5

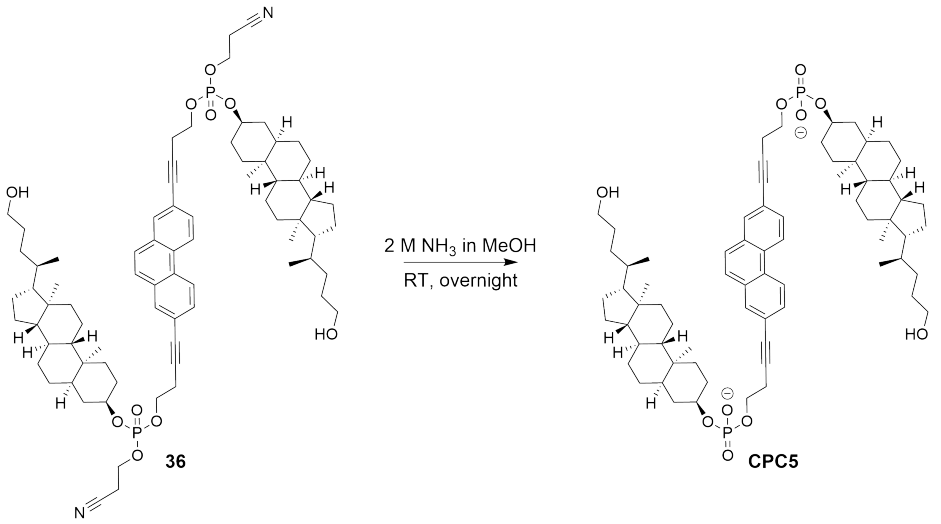

Scheme 7.22: Deprotection of **36** yielding **CPC5**.

Compound **36** was dissolved in a solution of 2 M NH_3 in MeOH (5 mL) and stirred at RT for 72 h. The sample was lyophilized and then purified by RP-HPLC (for conditions see Table 7.2 on page 112). HRMS-NSI (m/z): $[M-H]^-$ calcd for $C_{70}H_{98}O_{10}P_2$, 580.3323; found, 580.3312.

7.3.2 NMR Spectra

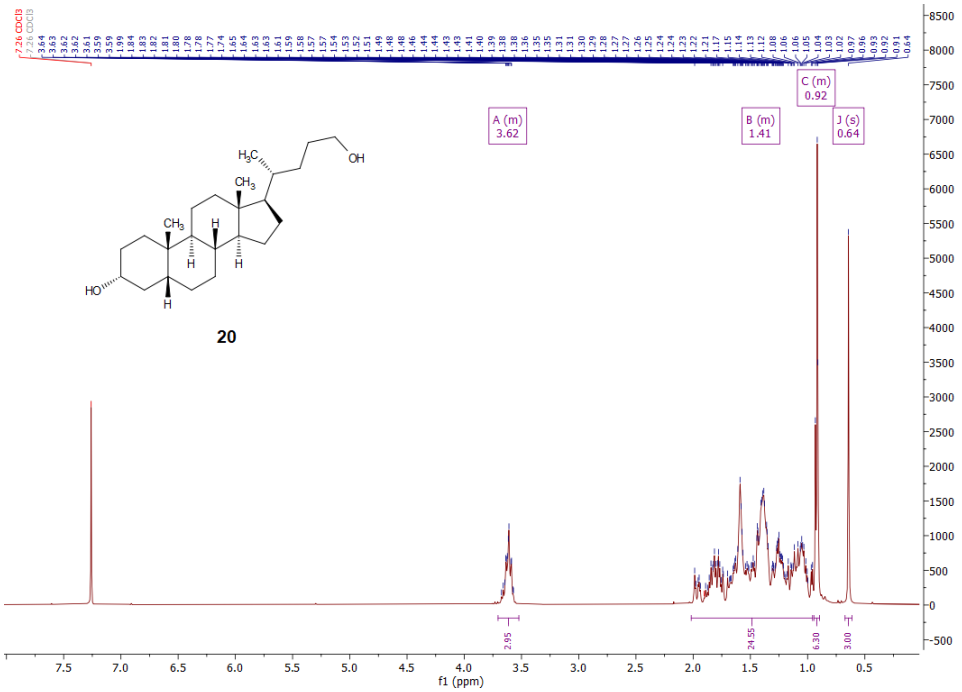

Figure 7.34: ^{1}H NMR of compound **20** in $CDCl_3$.

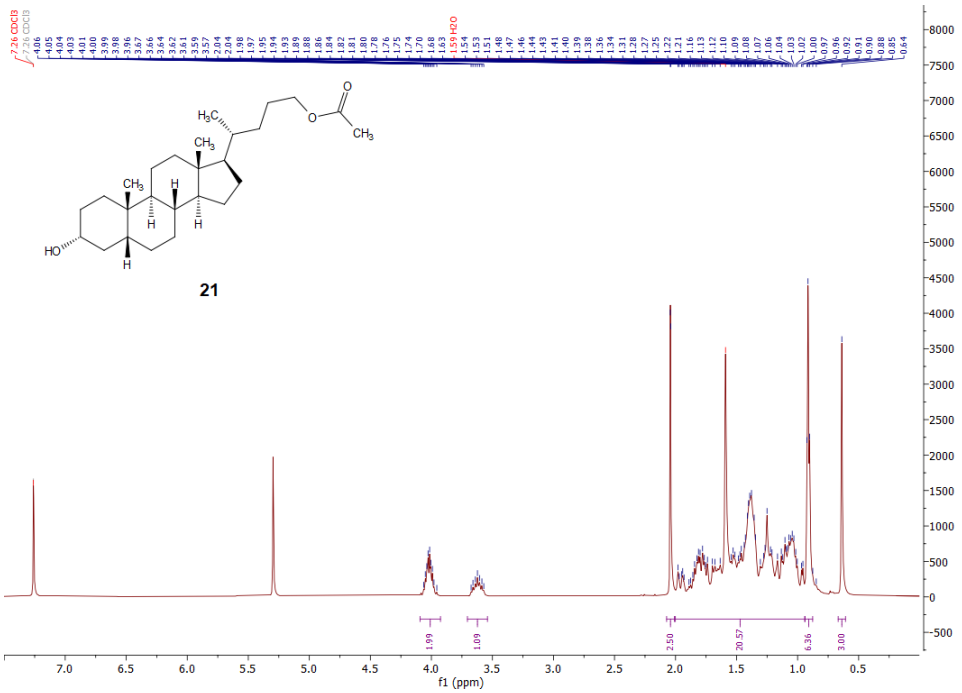

Figure 7.35: ^{1}H NMR of compound **21** in $CDCl_3$.

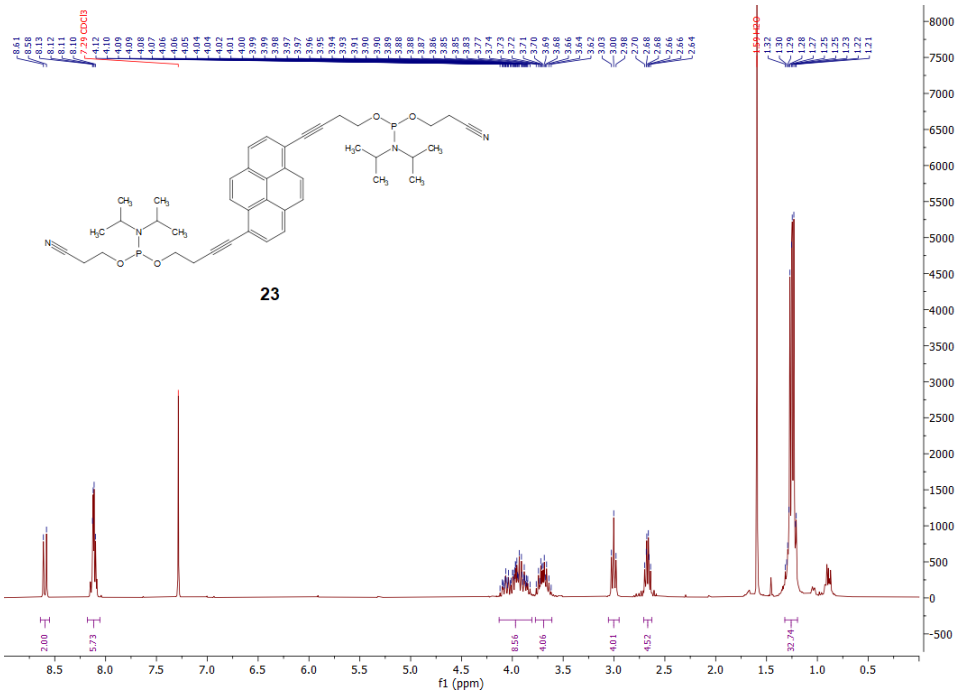

Figure 7.36: ^{1}H NMR of compound **23** in $CDCl_3$.

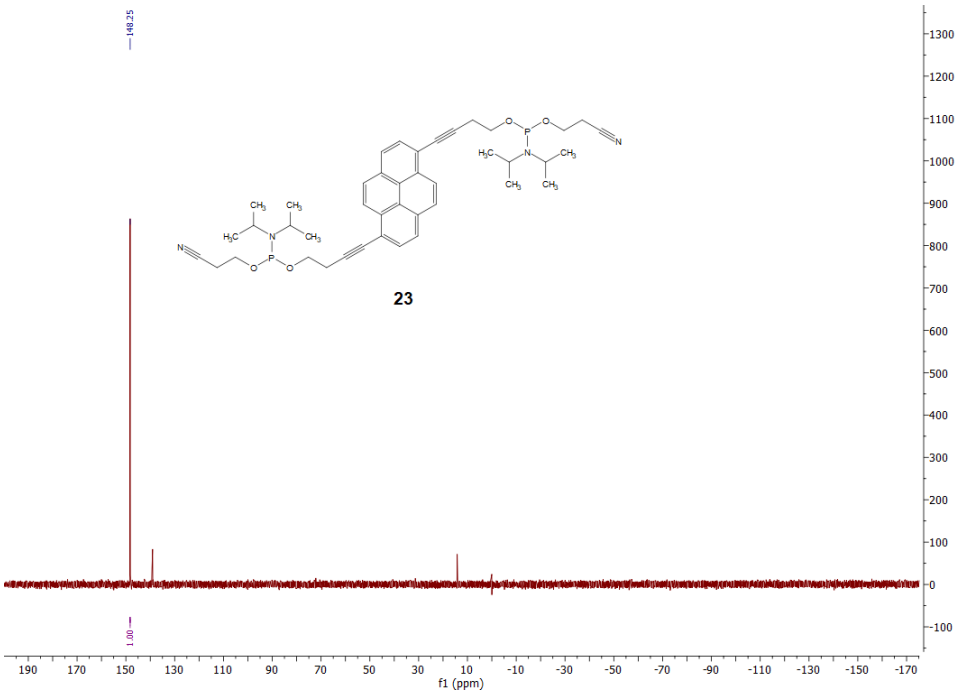

Figure 7.37: ^{31}P NMR of compound **23** in $CDCl_3$.

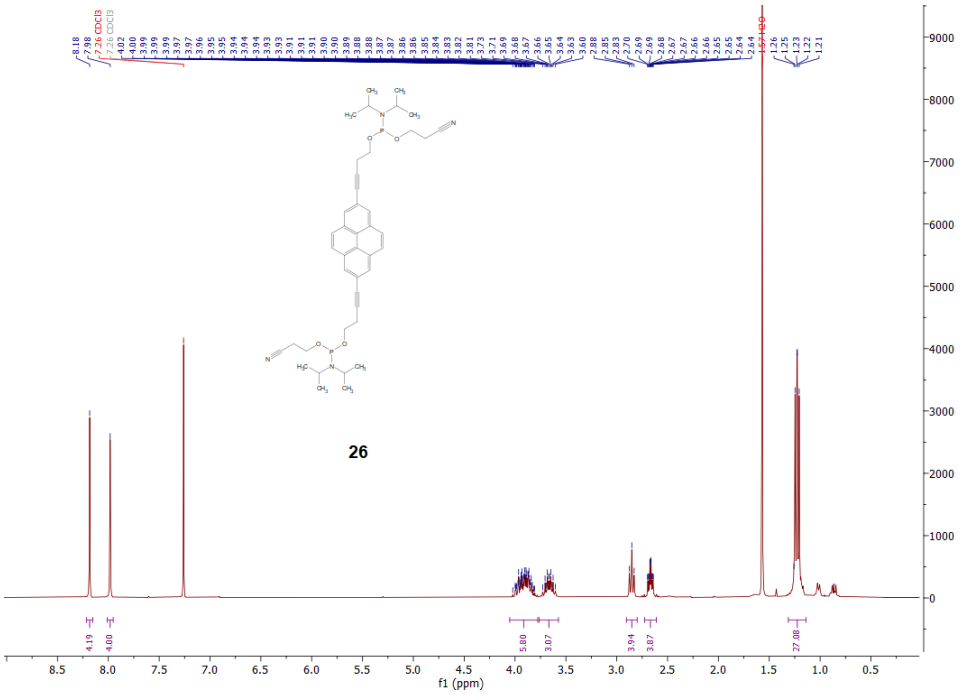

Figure 7.38: ^{1}H NMR of compound **26** in $CDCl_3$.

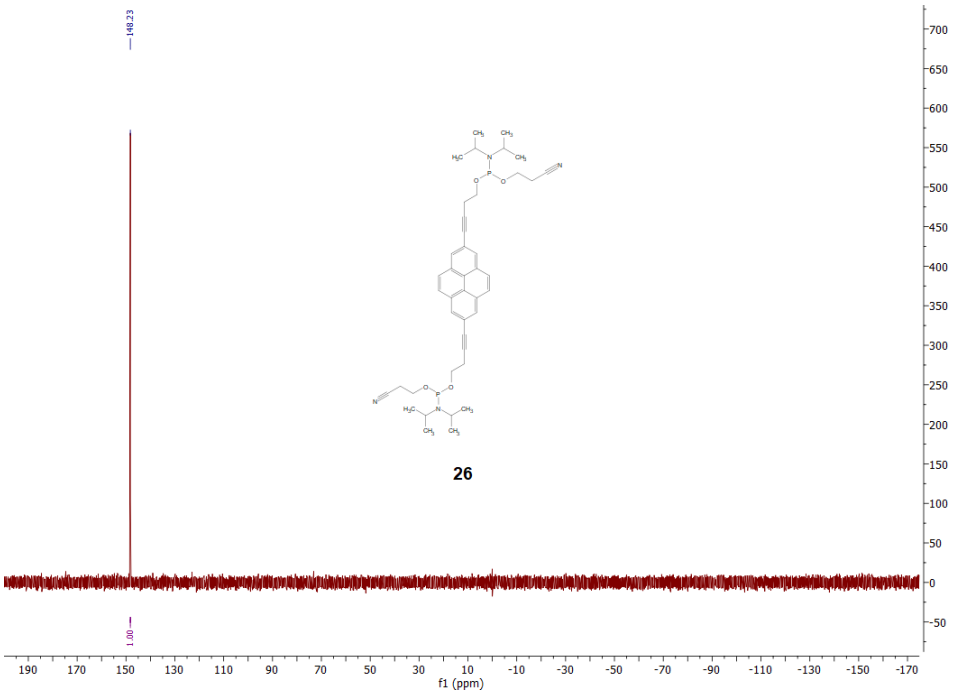

Figure 7.39: ^{31}P NMR of compound **26** in $CDCl_3$.

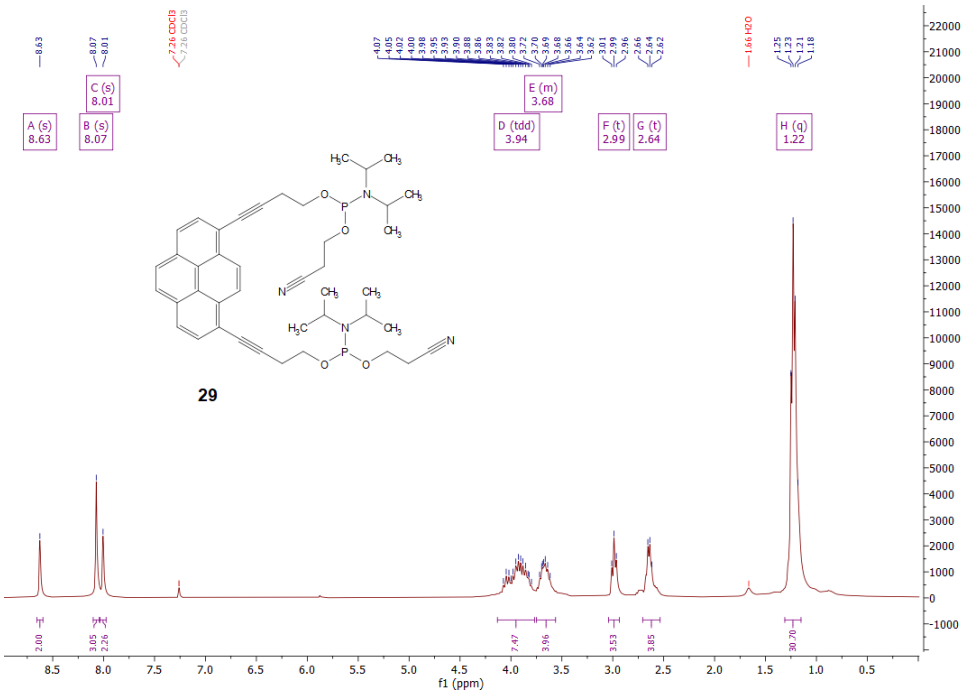

Figure 7.40: ^{1}H NMR of compound **29** in $CDCl_3$.

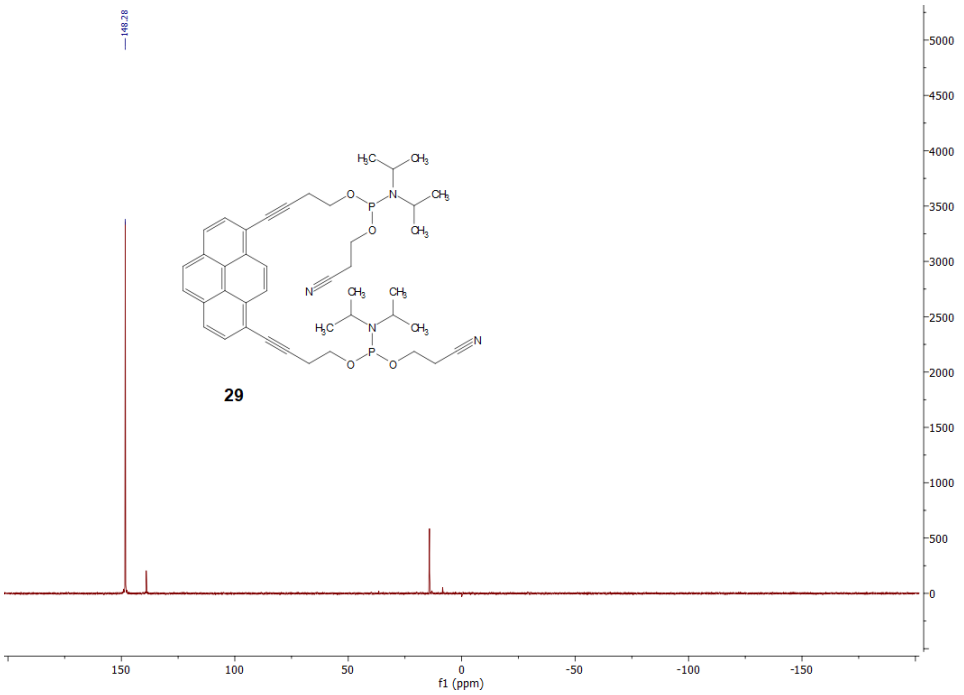

Figure 7.41: ^{31}P NMR of compound **29** in $CDCl_3$.

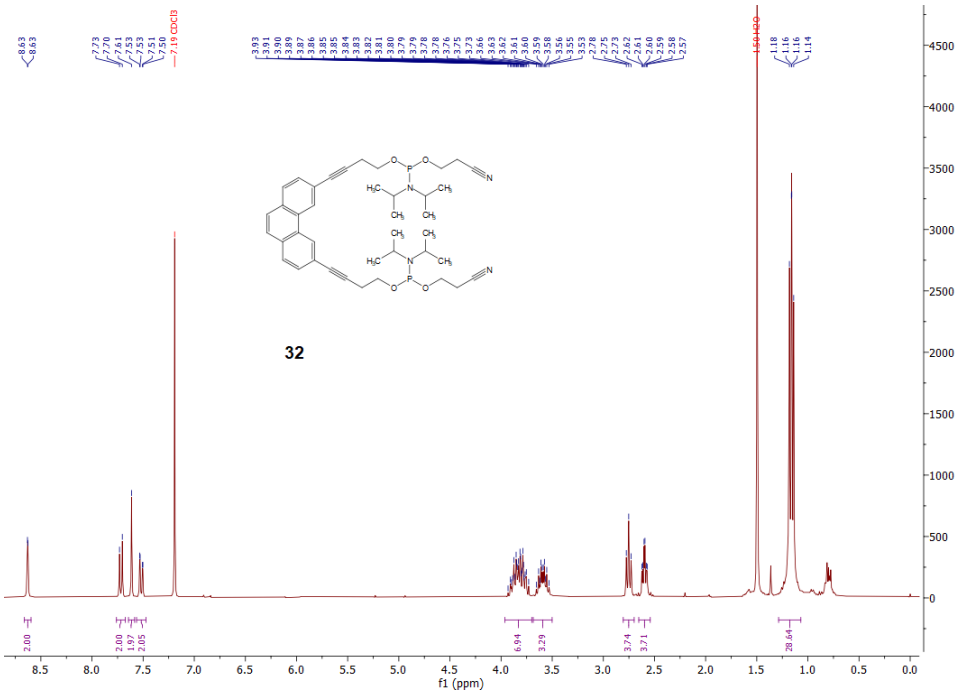

Figure 7.42: ^{1}H NMR of compound **32** in $CDCl_3$.

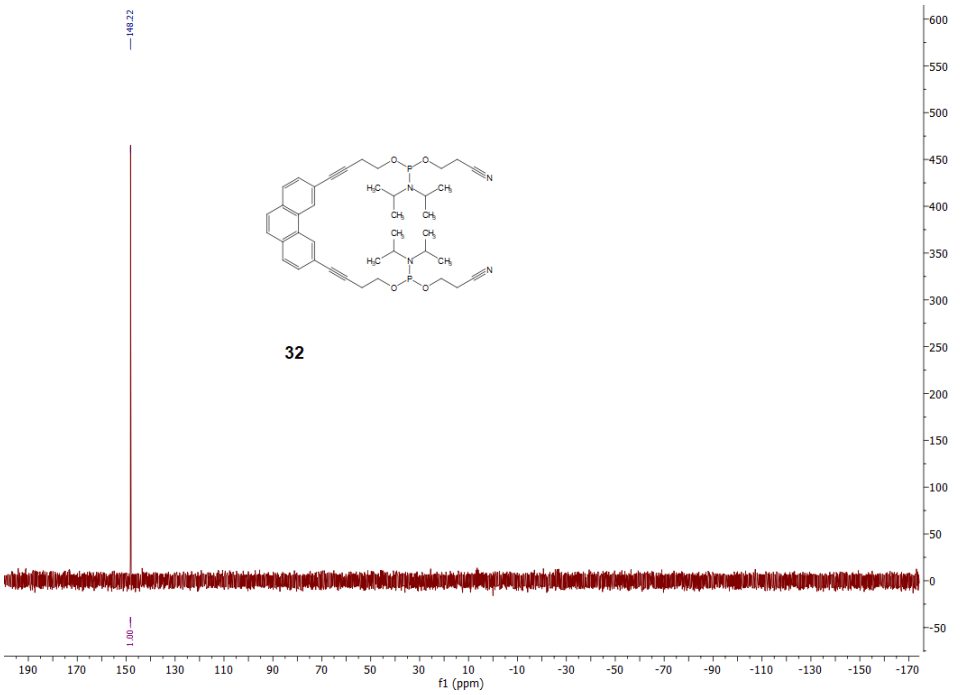

Figure 7.43: ^{31}P NMR of compound **32** in $CDCl_3$.

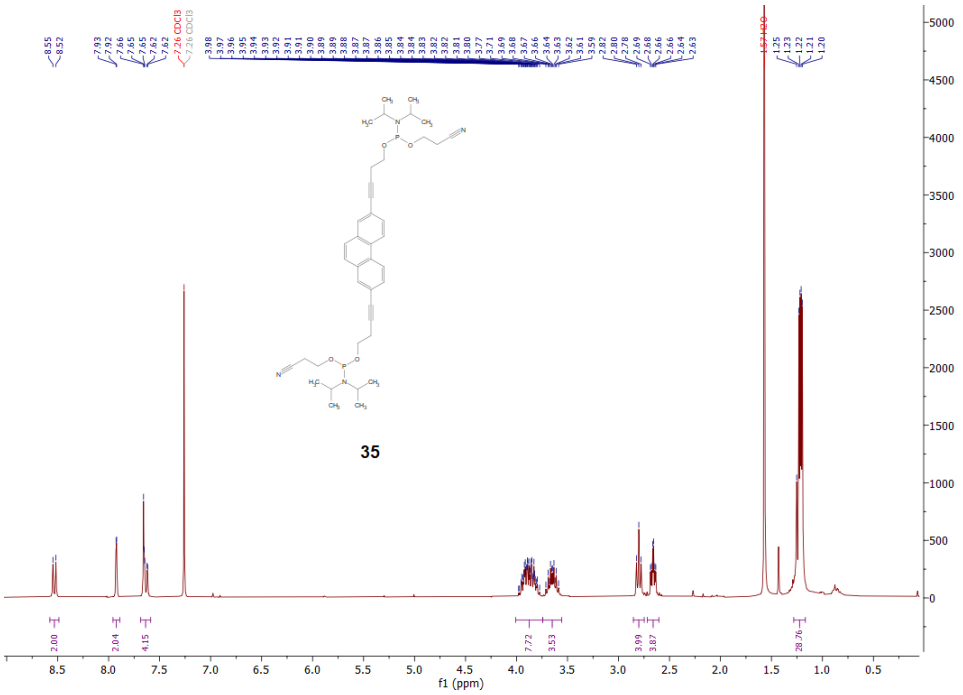

Figure 7.44: ^{1}H NMR of compound **35** in $CDCl_3$.

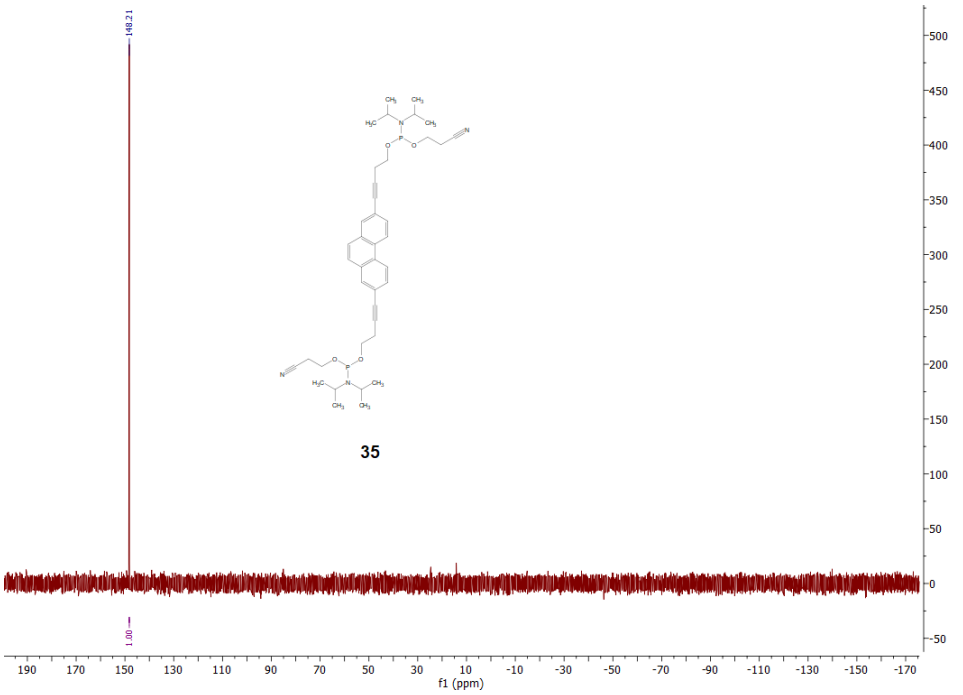

Figure 7.45: ^{31}P NMR of compound **35** in $CDCl_3$.

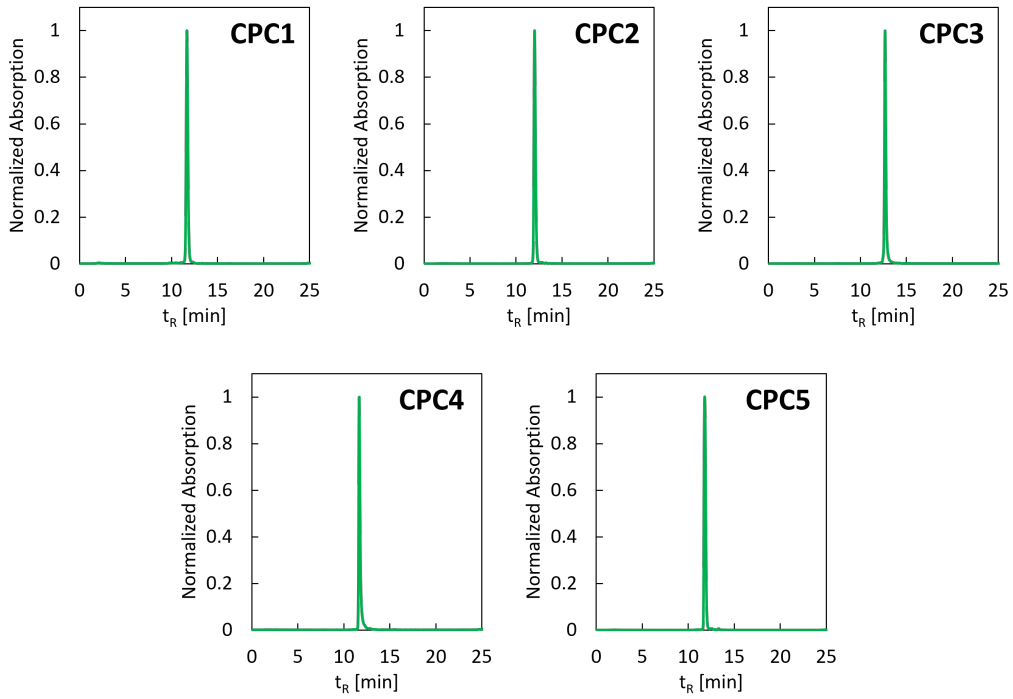

Figure 7.46: HPLC traces of the different oligomers.

Table 7.2: Cholane oligomers HPLC gradients, calculated and found masses by ESI-MS.

Oligomer	HPLC gradient B [%] ($t_{R\ [min]}$)	Calc. mass	Found mass
CPC1	40 (2), 60 (24)	592.3323	592.3315
CPC2	35 (2), 65 (24)	592.3323	592.3312
CPC3	35 (2), 65 (24)	592.3323	592.3312
CPC4	35 (2), 65 (24)	580.3323	580.3310
CPC5	40 (2), 60 (24)	580.3323	580.3312

7.3.3 MS Spectra

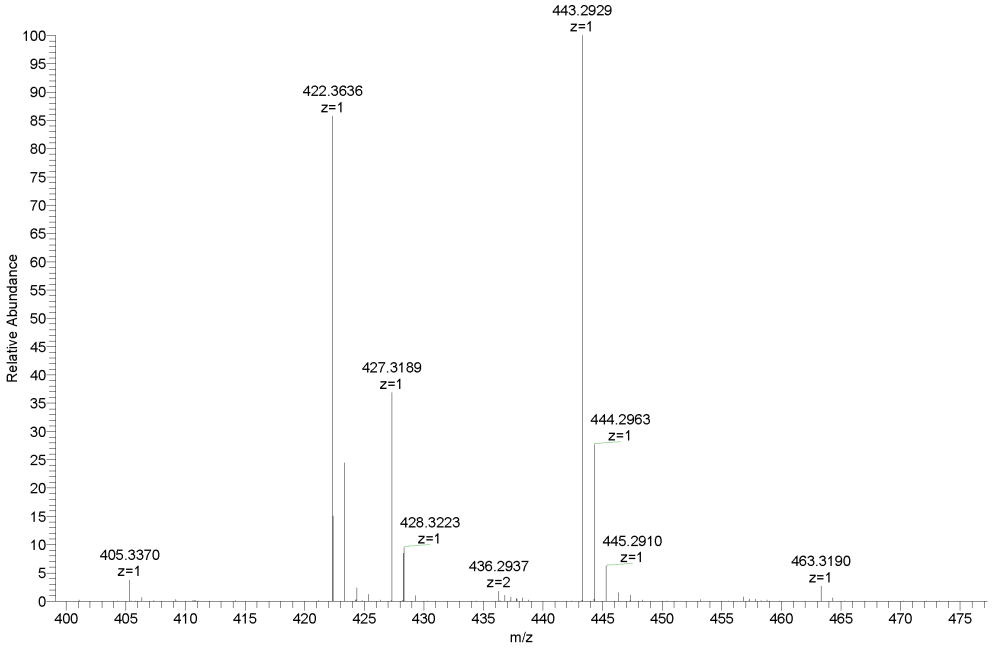

Figure 7.47: Mass spectrum of compound **21** in presence of a NH_4^+ and a K^+ adduct.

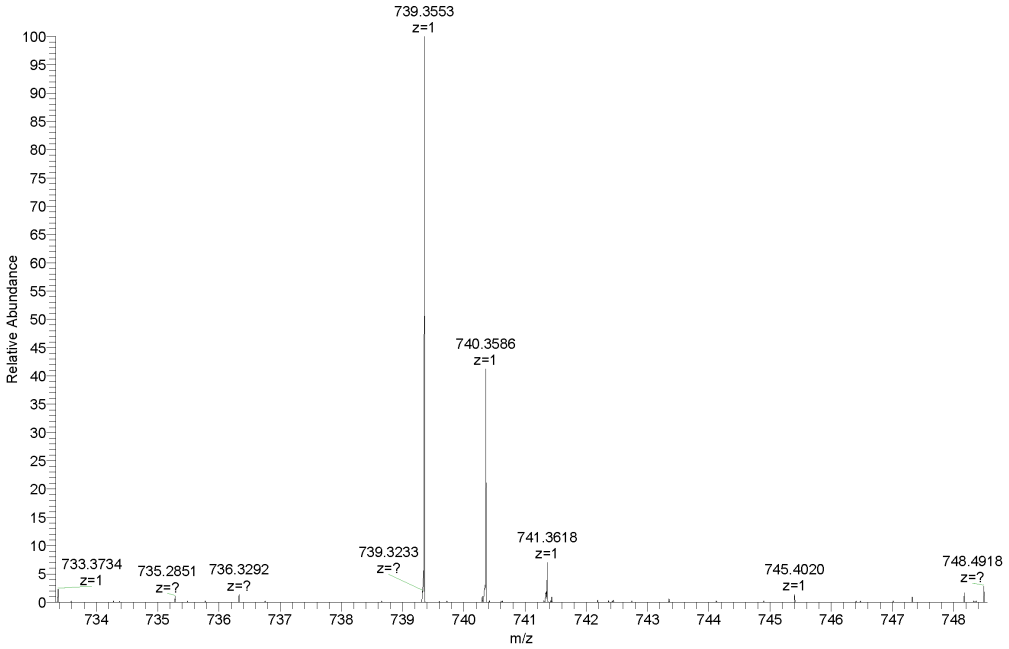

Figure 7.48: Mass spectrum of compound **23**.

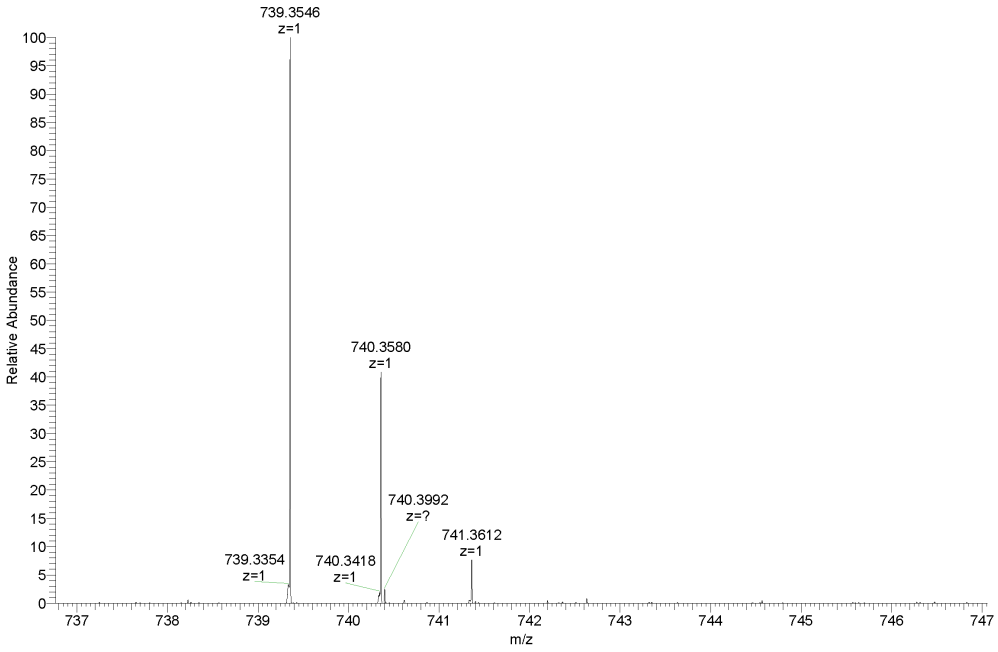

Figure 7.49: Mass spectrum of compound **26**.

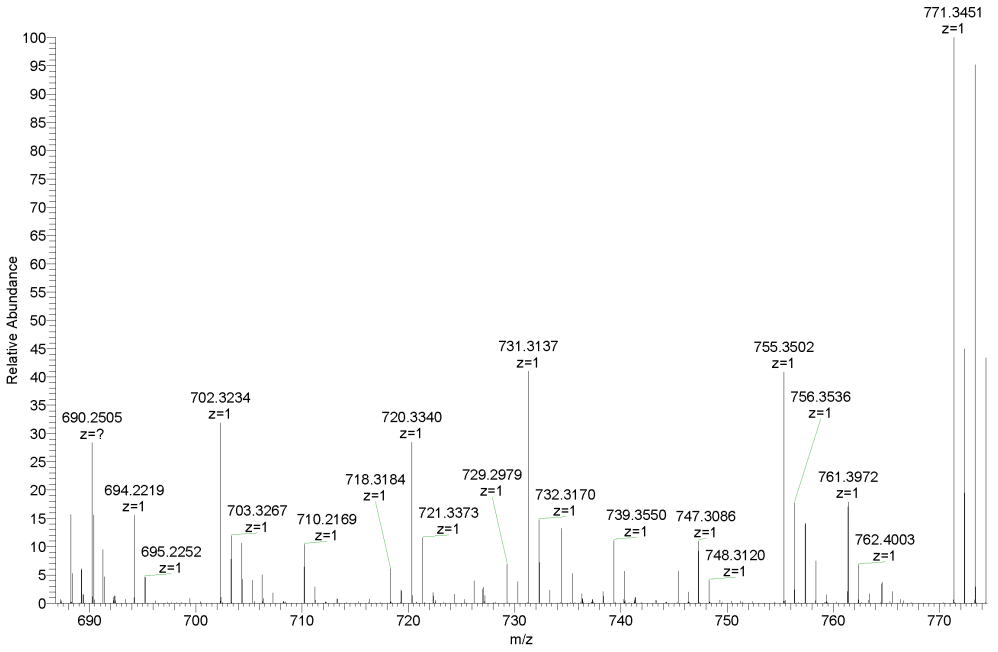

Figure 7.50: Mass spectrum of compound **29**.

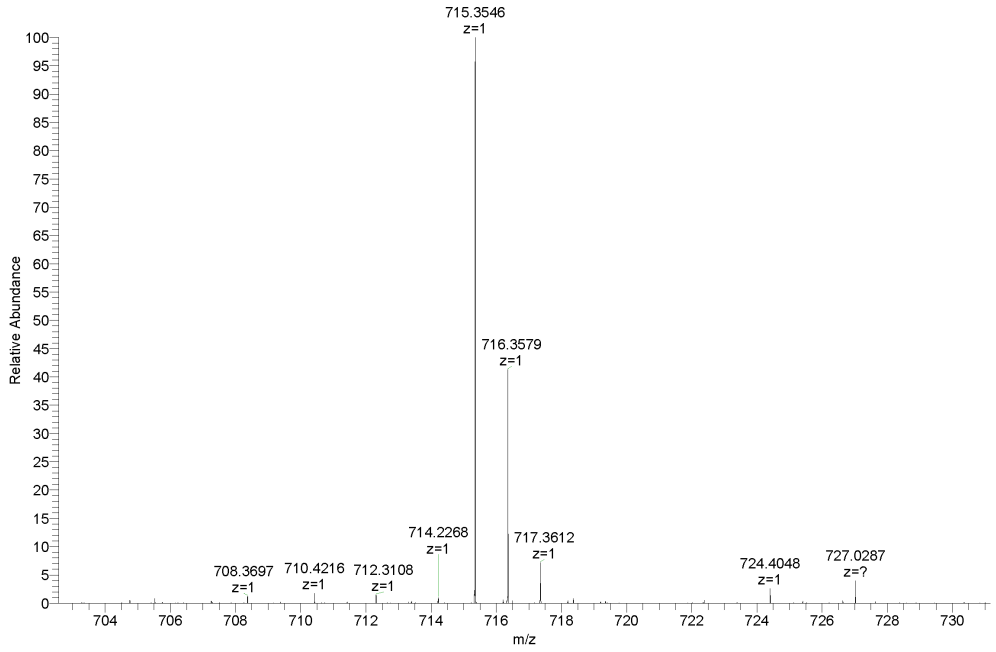

Figure 7.51: Mass spectrum of compound **32**.

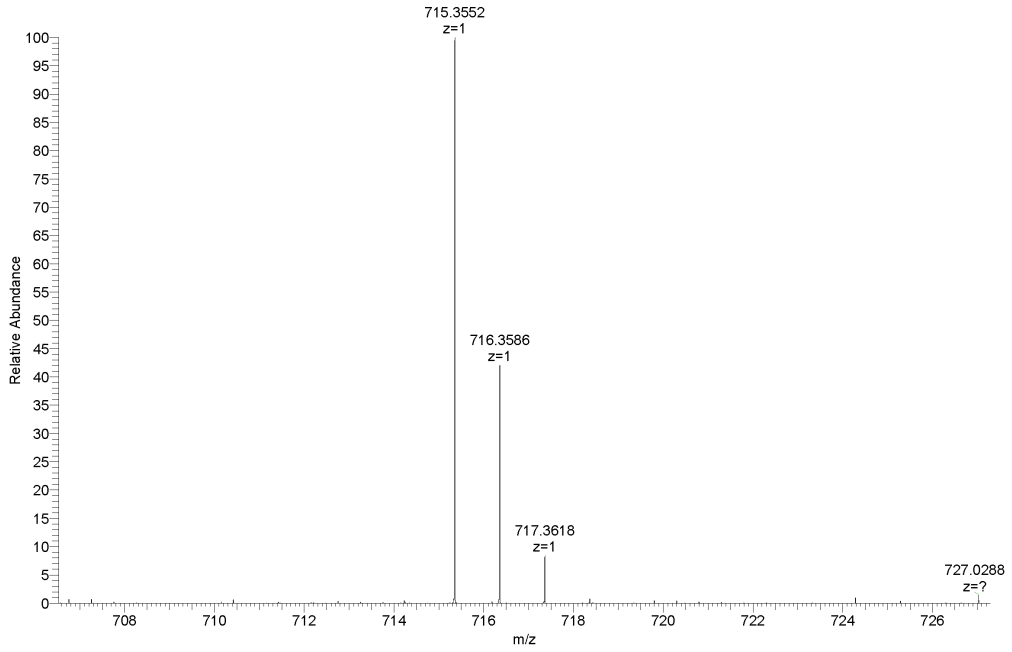

Figure 7.52: Mass spectrum of compound **35**.

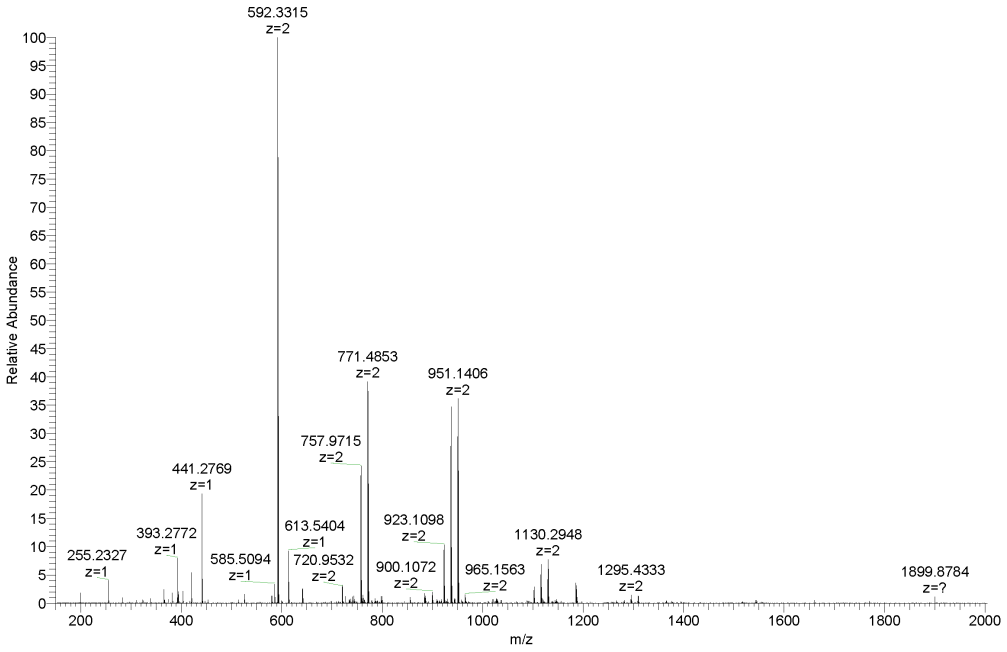

Figure 7.53: Mass spectrum of oligomer **CPC1**.

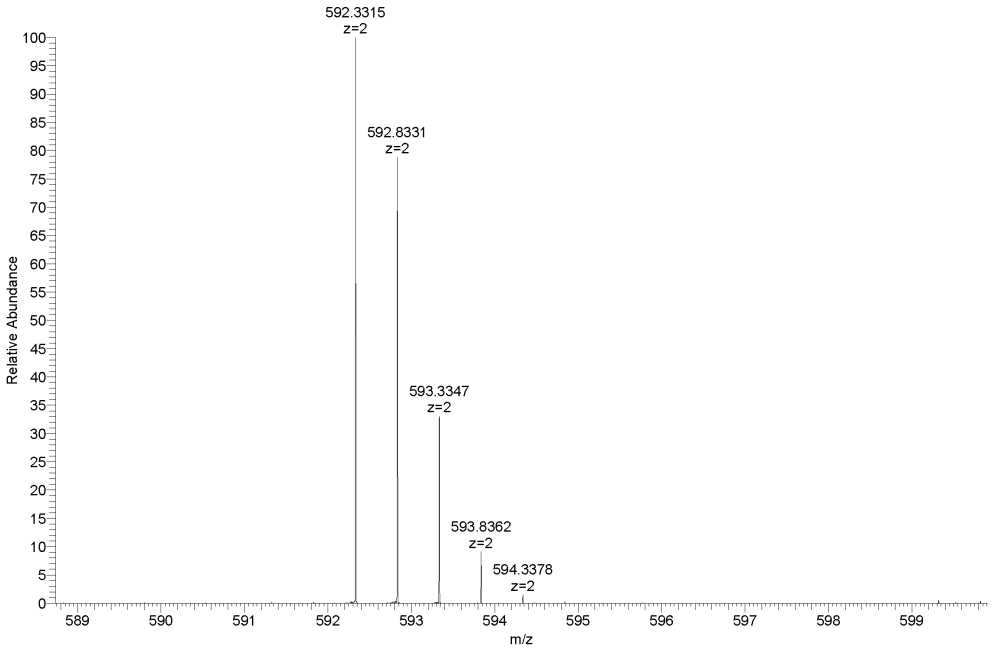

Figure 7.54: Mass spectrum (zoom) of oligomer **CPC1**.

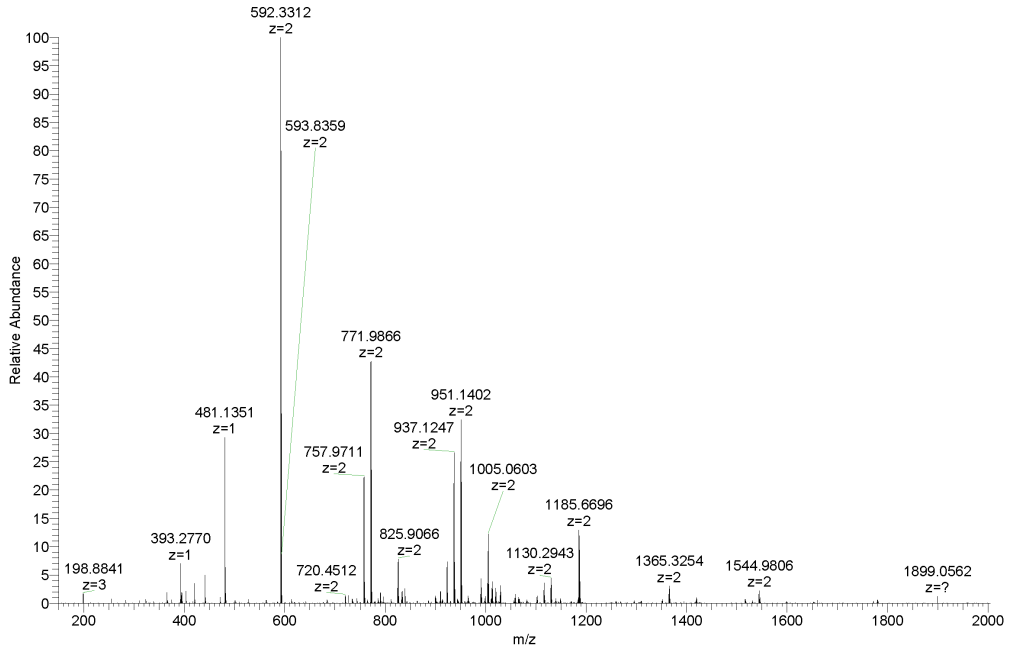

Figure 7.55: Mass spectrum of oligomer **CPC2**.

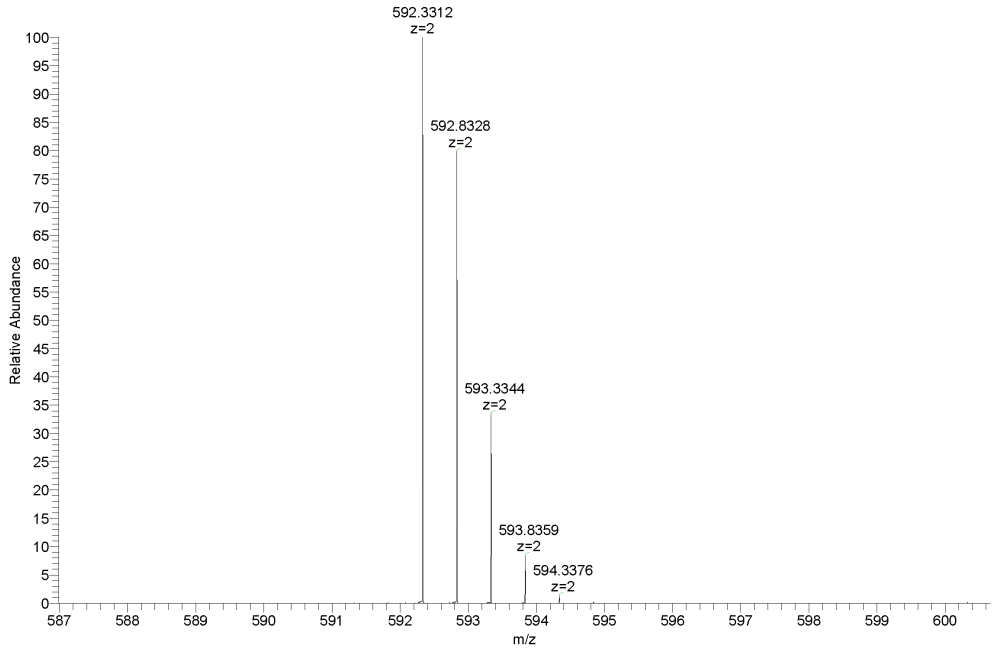

Figure 7.56: Mass spectrum (zoom) of oligomer **CPC2**.

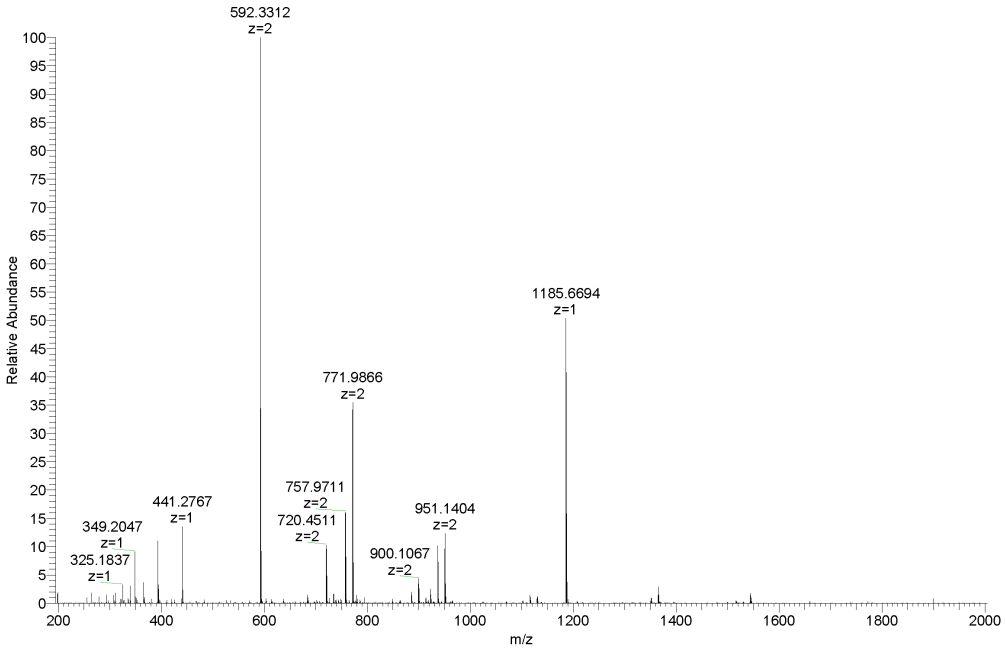

Figure 7.57: Mass spectrum of oligomer **CPC3**.

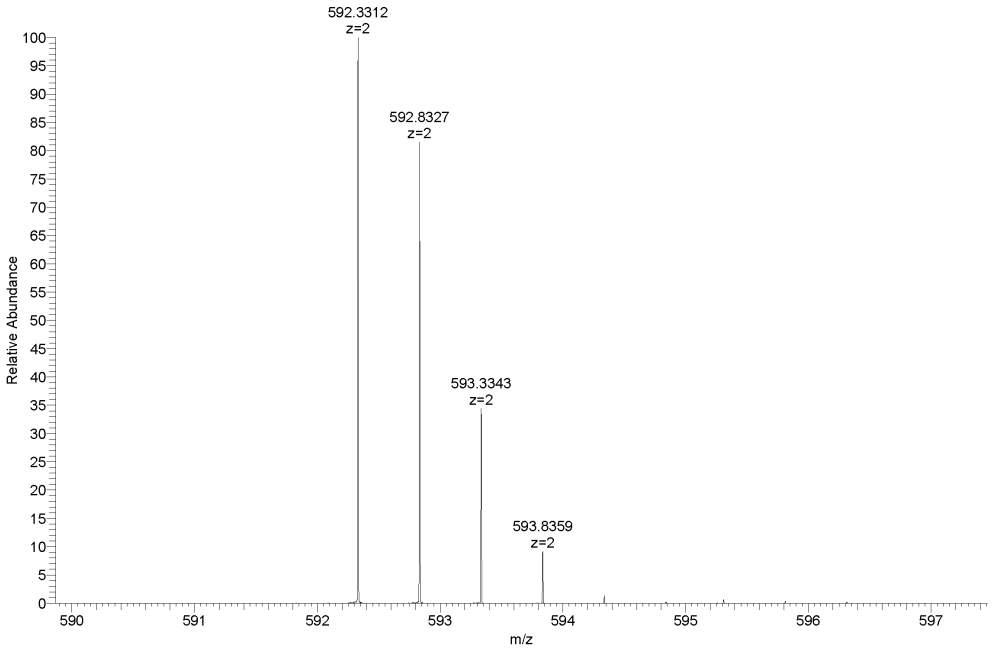

Figure 7.58: Mass spectrum (zoom) of oligomer **CPC3**.

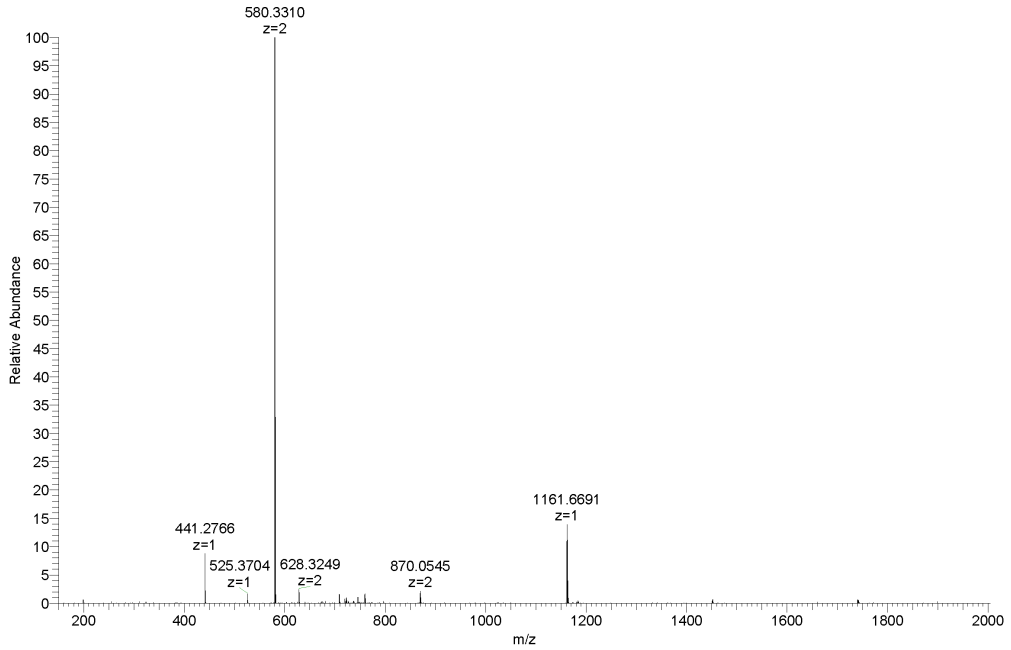

Figure 7.59: Mass spectrum of oligomer **CPC4**.

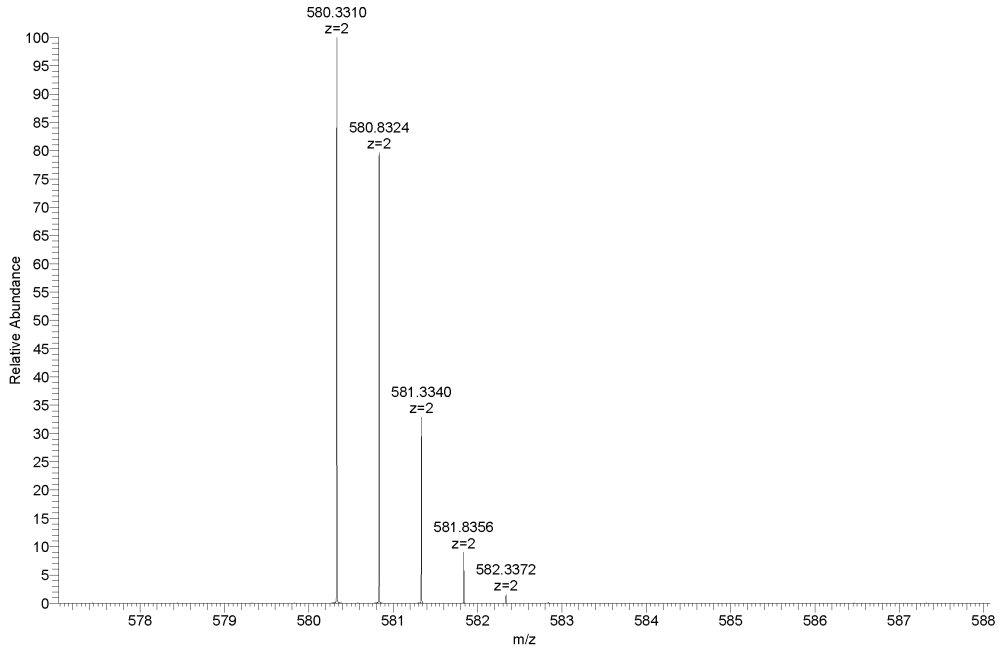

Figure 7.60: Mass spectrum (zoom) of oligomer **CPC4**.

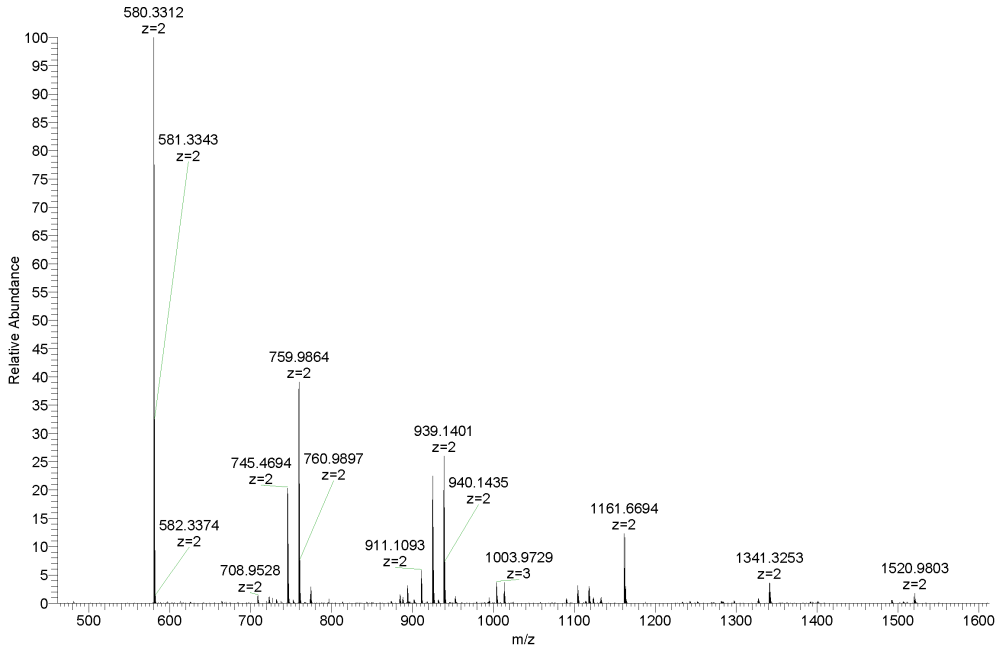

Figure 7.61: Mass spectrum of oligomer **CPC5**.

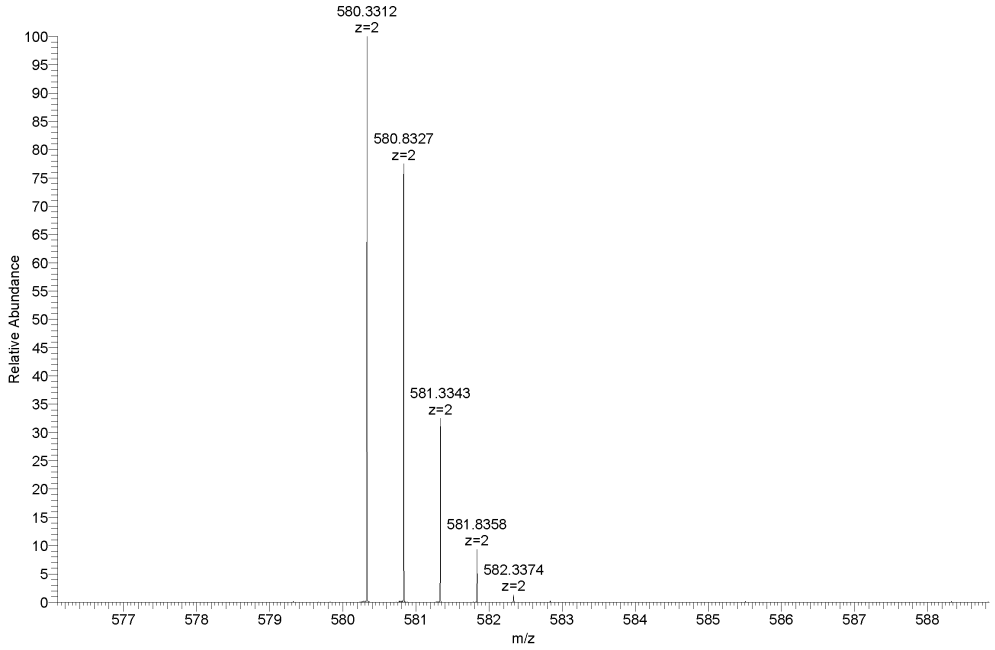

Figure 7.62: Mass spectrum (zoom) of oligomer **CPC5**.

7.3.4 Additional Measurements

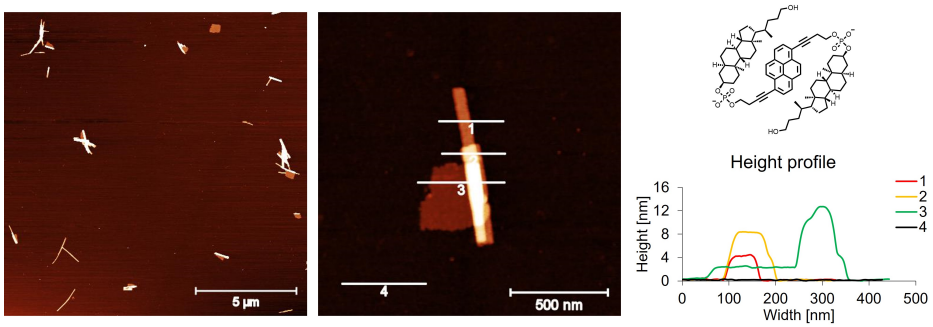

Figure 7.63: AFM images of the self-assembled **CPC1** with cross section on an APTES-modified mica sheet. Conditions: 3 µM oligomer, 10 mM sodium phosphate buffer, 10 mM NaCl and 20% EtOH.

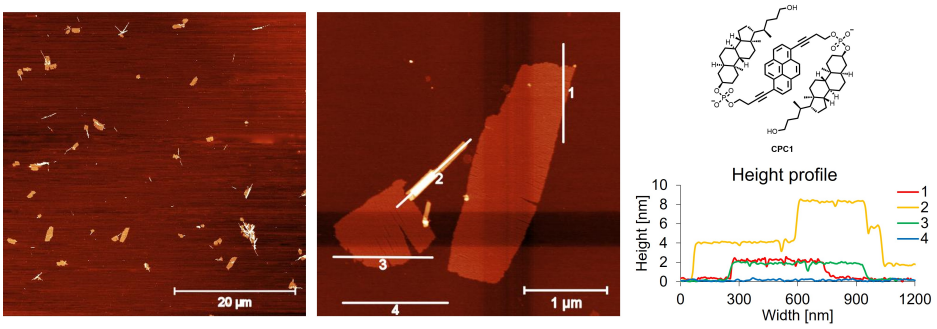

Figure 7.64: AFM images of the slow self-assembled **CPC1** (0.1 °C/min) with cross section on an APTES-modified mica sheet. Conditions: 3 µM oligomer, 10 mM sodium phosphate buffer, 10 mM NaCl and 20% EtOH.

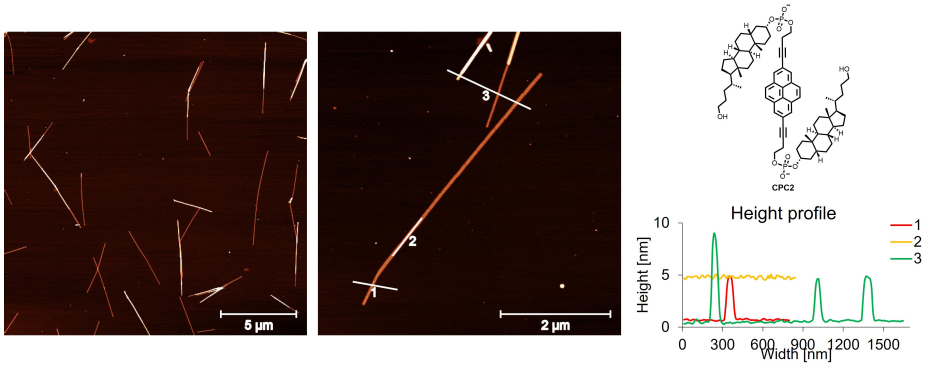

Figure 7.65: AFM images of the self-assembled **CPC2** with cross section on an APTES-modified mica sheet. Conditions: 3 µM oligomer, 10 mM sodium phosphate buffer, 10 mM NaCl and 25% EtOH.

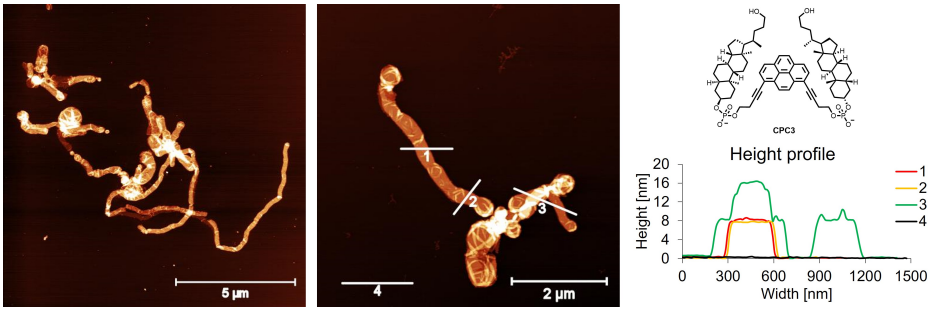

Figure 7.66: AFM images of the self-assembled **CPC3** with cross section on an APTES-modified mica sheet. Conditions: 3 µM oligomer, 10 mM sodium phosphate buffer, 10 mM NaCl and 15% EtOH.

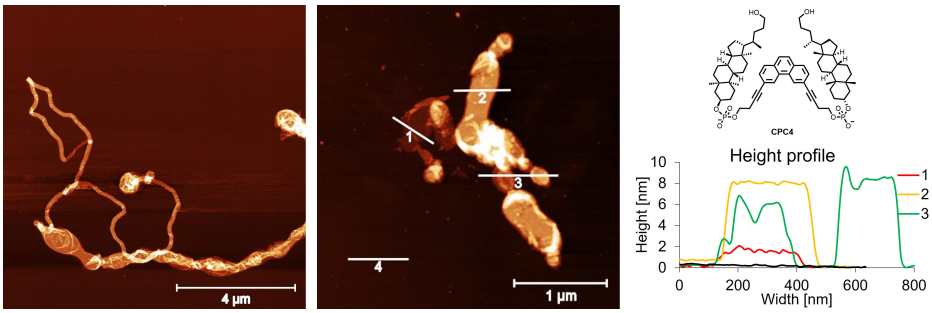

Figure 7.67: AFM images of the self-assembled **CPC4** with cross section on an APTES-modified mica sheet. Conditions: 3 µM oligomer, 10 mM sodium phosphate buffer, 10 mM NaCl and 15% EtOH.

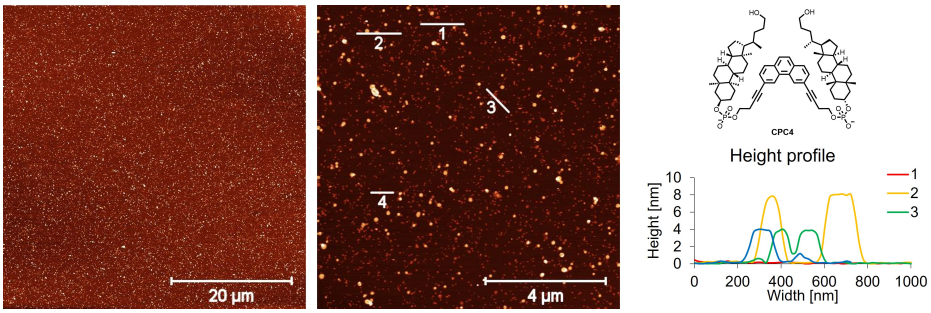

Figure 7.68: AFM images of the fast self-assembled **CPC4** (10 °C/min) with cross section on an APTES-modified mica sheet. Conditions: 3 µM oligomer, 10 mM sodium phosphate buffer, 10 mM NaCl and 15% EtOH.

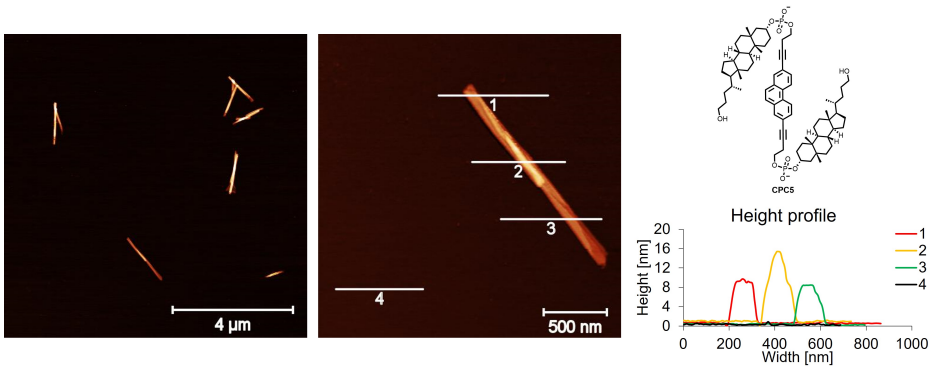

Figure 7.69: AFM images of the self-assembled **CPC5** with cross section on an APTES-modified mica sheet. Conditions: 3 µM oligomer, 10 mM sodium phosphate buffer, 10 mM NaCl and 20% EtOH.

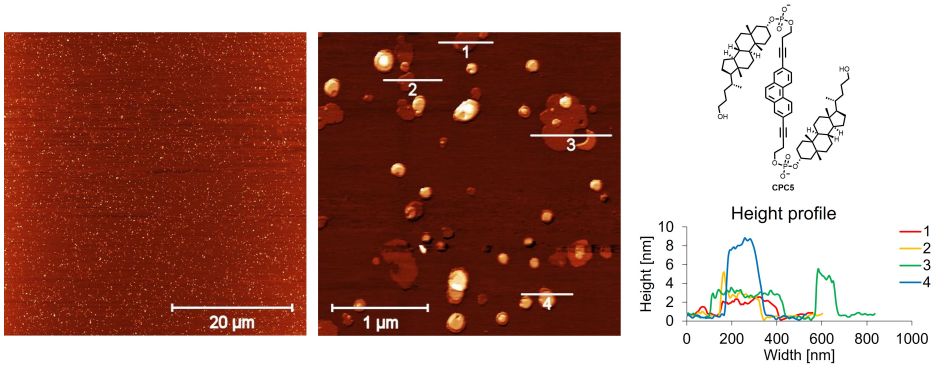

Figure 7.70: AFM images of the fast self-assembled **CPC5** (10 °C/min) with cross section on an APTES-modified mica sheet. Conditions: 3 µM oligomer, 10 mM sodium phosphate buffer, 10 mM NaCl and 20% EtOH.

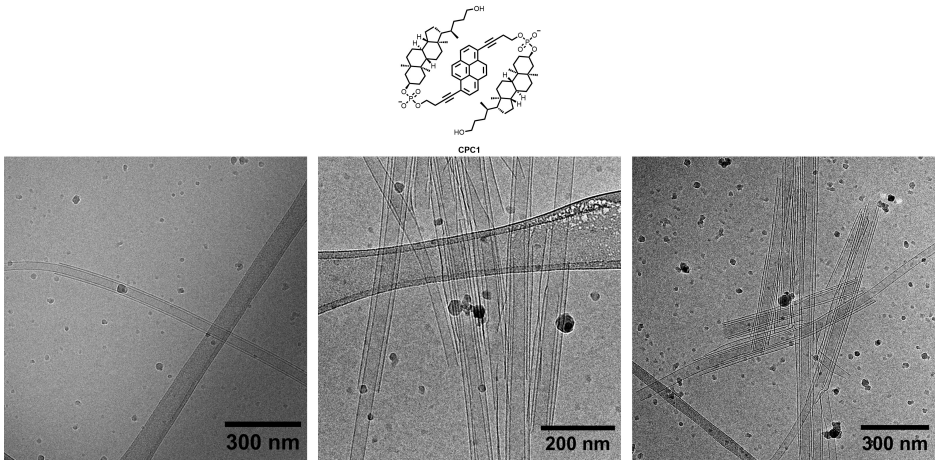

Figure 7.71: Cryo-EM images of the self-assemble **CPC1**. Conditions: 3 µM oligomer, 10 mM sodium phosphate buffer, 10 mM NaCl and 20% EtOH.

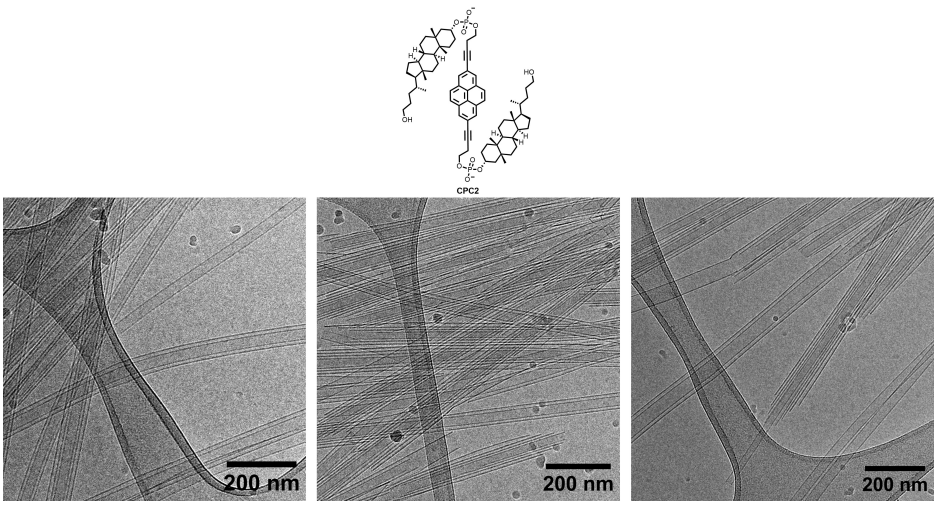

Figure 7.72: Cryo-EM images of the self-assemble **CPC2**. Conditions: 3 µM oligomer, 10 mM sodium phosphate buffer, 10 mM NaCl and 25% EtOH.

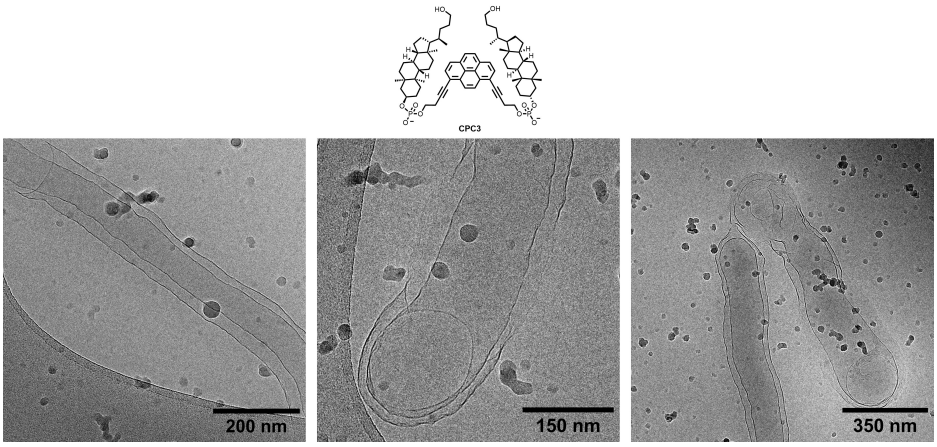

Figure 7.73: Cryo-EM images of the self-assemble **CPC3**. Conditions: 3 µM oligomer, 10 mM sodium phosphate buffer, 10 mM NaCl and 15% EtOH.

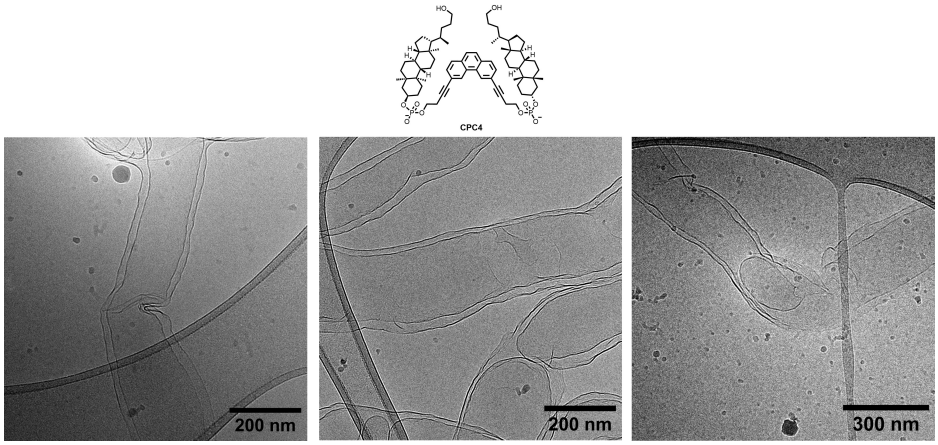

Figure 7.74: Cryo-EM images of the self-assemble **CPC4**. Conditions: 3 µM oligomer, 10 mM sodium phosphate buffer, 10 mM NaCl and 20% EtOH.

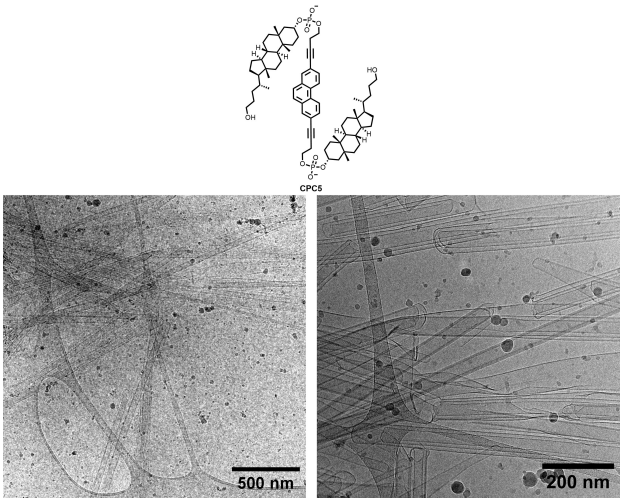

Figure 7.75: Cryo-EM images of the self-assemble **CPC5**. Conditions: 3 µM oligomer, 10 mM sodium phosphate buffer, 10 mM NaCl and 15% EtOH.

7.3.5 Control Measurements

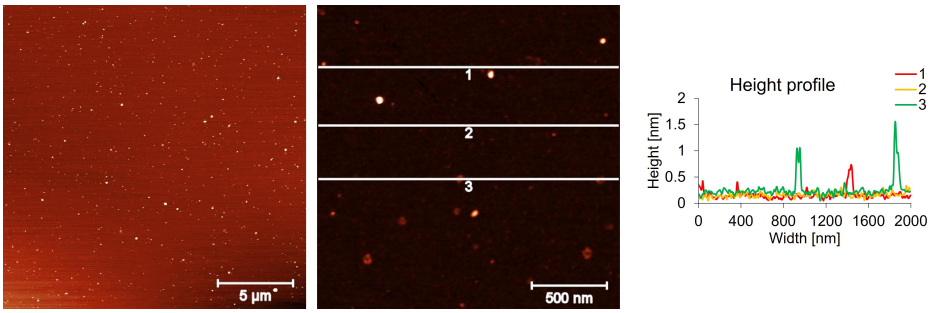

Figure 7.76: AFM images of the buffer conditions for **CPC1** and **CPC5** (0.5 °C/min) with cross section on an APTES-modified mica sheet. Conditions: no oligomer, 10 mM sodium phosphate buffer, 10 mM NaCl and 20% EtOH.

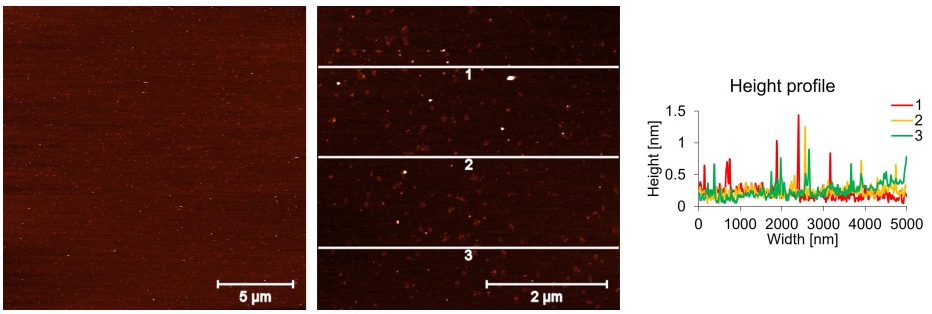

Figure 7.77: AFM images of the buffer conditions for **CPC2** (0.5 °C/min) with cross section on an APTES-modified mica sheet. Conditions: no oligomer, 10 mM sodium phosphate buffer, 10 mM NaCl and 25% EtOH.

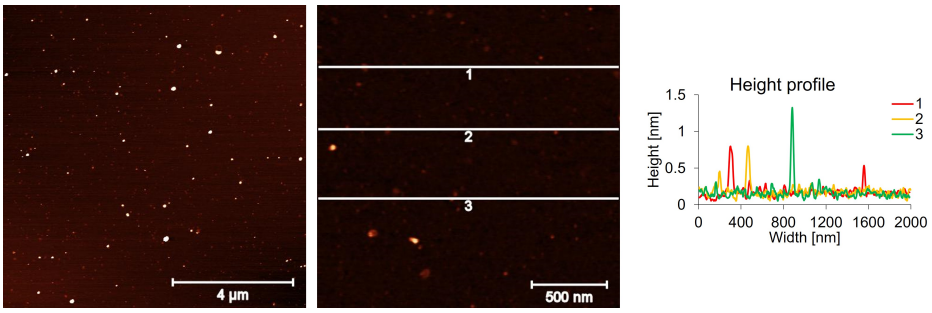

Figure 7.78: AFM images of the buffer conditions for **CPC3** and **CPC4** (0.5 °C/min) with cross section on an APTES-modified mica sheet. Conditions: no oligomer, 10 mM sodium phosphate buffer, 10 mM NaCl and 15% EtOH.

7.4 Appendix - Chapter 5

7.4.1 Quantum Yield Calculations

The quantum yield of the different systems has been calculated according to the following formula:

$$\Phi_{\mathrm{f}} = \frac{Number\ of\ photons\ emitted}{Number\ of\ photons\ absorbed} = Q_{\mathrm{R}} * \frac{I_{\mathrm{S}} * A_{\mathrm{R}} * {\eta_{\mathrm{S}}}^2}{I_{\mathrm{R}} * A_{\mathrm{S}} * {\eta_{\mathrm{R}}}^2} \qquad (1)$$

Where:

- $\mathrm{Q_R}$: Quantum yield of reference
- $\mathrm{I_S}$: Area under the fluorescence curve of sample
- $\mathrm{I_R}$: Area under the fluorescence curve of reference
- $\mathrm{A_S}$: Absorbance of the sample
- $\mathrm{A_R}$: Absorbance of the reference
- η_{S}: refractive index of sample
- η_{R}: refractive index of the reference

Table 7.3: Quantum yield calculation table for **CPC4** with increasing amounts of **CPC1**. Quinine sulfate in 0.5 M H_2SO_4 was used as a reference - ${\Phi_R}^{QS} = 0.546$.[145] Conditions: 10 °C/min cooling gradient, 3 µM oligomer, 10 mM sodium phosphate buffer, 10 mM NaCl and 15% EtOH.

	$Area_{sample}$	$Area_R$	$Absorption_S$	$Absorption_R$	Φ_F [%]	
0.0%	4496	41780	0.068	0.088	7.6	8.3 ± 0.6
	4770	42737	0.064	0.093	8.8	
	4804	42523	0.073	0.100	8.5	
0.3%	7241	41780	0.065	0.088	12.7	13.6 ± 0.9
	7373	42737	0.060	0.093	14.4	
	7453	42523	0.070	0.100	13.8	
0.6%	10068	41780	0.066	0.088	17.5	17.8 ± 1.8
	10442	42737	0.062	0.093	19.8	
	10263	42523	0.082	0.100	16.2	
1.5%	15630	41780	0.066	0.088	25.9	27.2 ± 1.7
	15487	42737	0.063	0.093	29.1	
	15630	42523	0.076	0.100	26.5	
3.0%	19732	41780	0.067	0.088	33.9	36.9 ± 2.7
	20961	42737	0.065	0.093	38.4	
	21775	42523	0.073	0.100	38.6	
6.0%	22149	41780	0.068	0.088	37.1	40.8 ± 3.2
	23504	42737	0.065	0.093	42.6	
	24991	42523	0.075	0.100	42.8	
12.0%	21735	41780	0.070	0.088	35.4	39.5 ± 3.7
	22891	42737	0.067	0.093	40.4	
	24952	42523	0.075	0.100	42.7	
24.0%	16797	41780	0.072	0.088	26.7	28.8 ± 2.4
	17456	42737	0.073	0.093	28.3	
	19036	42523	0.078	0.100	31.4	

Table 7.4: Quantum yield calculation table for **CPC4** with increasing amounts of **CPC1**. Quinine sulfate in 0.5 M H_2SO_4 was used as a reference - ${\Phi_R}^{QS} = 0.546$.[145] Conditions: 0.5 °C/min cooling gradient, 3 µM oligomer, 10 mM sodium phosphate buffer, 10 mM NaCl and 15% EtOH.

	$Area_{sample}$	$Area_R$	$Absorption_S$	$Absorption_R$	Φ_F [%]	
0.0%	4485	41780	0.67	0.088	7.6	8.2 ± 0.5
	4594	42737	0.064	0.093	8.5	
	4755	42523	0.073	0.100	8.4	
0.3%	6800	41780	0.067	0.088	11.6	12.2 ± 0.6
	6883	42737	0.063	0.093	12.8	
	6907	42523	0.073	0.100	12.1	
0.6%	8477	41780	0.067	0.088	14.4	14.4 ± 1.3
	8649	42737	0.065	0.093	15.8	
	8579	42523	0.084	0.100	13.1	
1.5%	13795	41780	0.068	0.088	23.4	23.9 ± 1.0
	13926	42737	0.066	0.093	25.1	
	14191	42523	0.078	0.100	23.3	
3.0%	19778	41780	0.069	0.088	32.7	35.0 ± 2.0
	20777	42737	0.067	0.093	36.5	
	21541	42523	0.078	0.100	35.8	
6.0%	22530	41780	0.070	0.088	36.8	40.4 ± 3.2
	24006	42737	0.067	0.093	42.2	
	25324	42523	0.077	0.100	42.3	
12.0%	18287	41780	0.072	0.088	28.9	33.6 ± 4.1
	20426	42737	0.069	0.093	35.0	
	22479	42523	0.079	0.100	36.8	
24.0%	13787	41780	0.074	0.088	21.3	23.2 ± 1.7
	14455	42737	0.072	0.093	23.6	
	15455	42523	0.081	0.100	24.6	

Table 7.5: Quantum yield calculation table for **CPC4** with increasing amounts of **CPC3**. Quinine sulfate in 0.5 M H_2SO_4 was used as a reference - ${\Phi_R}^{QS} = 0.546$.[145] Conditions: 10 °C/min cooling gradient, 3 µM oligomer, 10 mM sodium phosphate buffer, 10 mM NaCl and 15% EtOH.

	$Area_{sample}$	$Area_R$	$Absorption_S$	$Absorption_R$	Φ_F [%]	
0.0%	4854	41780	0.080	0.088	7.0	7.3 ± 0.4
	4915	42737	0.082	0.093	7.1	
	4975	42523	0.082	0.100	7.8	
0.3%	9456	41780	0.077	0.088	14.1	14.9 ± 1.4
	9471	42737	0.079	0.093	14.1	
	10149	42523	0.079	0.100	16.5	
0.6%	12774	41780	0.078	0.088	18.8	19.9 ± 1.2
	13228	42737	0.079	0.093	19.8	
	13528	42523	0.082	0.100	21.2	
1.5%	20320	41780	0.078	0.088	29.9	31.3 ± 1.6
	20409	42737	0.078	0.093	31.0	
	20448	42523	0.080	0.100	33.0	
3.0%	26298	41780	0.079	0.088	38.2	41.2 ± 3.0
	27569	42737	0.079	0.093	41.3	
	27752	42523	0.081	0.100	44.2	
6.0%	29695	41780	0.084	0.088	40.5	41.9 ± 2.6
	30382	42737	0.089	0.093	40.4	
	30848	42523	0.089	0.100	44.9	
12.0%	28129	41780	0.085	0.088	37.9	39.6 ± 2.3
	28594	42737	0.087	0.093	38.9	
	29477	42523	0.090	0.100	42.2	
24.0%	24146	41780	0.081	0.088	34.1	35.7 ± 1.7
	34632	42737	0.082	0.093	35.4	
	25355	42523	0.087	0.100	37.4	

Table 7.6: Quantum yield calculation table for **CPC4** with increasing amounts of **CPC3**. Quinine sulfate in 0.5 M H_2SO_4 was used as a reference - ${\Phi_R}^{QS} = 0.546$.[145] Conditions: 0.5 °C/min cooling gradient, 3 µM oligomer, 10 mM sodium phosphate buffer, 10 mM NaCl and 15% EtOH.

	$Area_{sample}$	$Area_R$	$Absorption_S$	$Absorption_R$	Φ_F [%]	
0.0%	3897	41780	0.083	0.088	5.4	5.5 ± 0.2
	3887	42737	0.083	0.093	5.5	
	3788	42523	0.085	0.100	5.7	
0.3%	9277	41780	0.079	0.088	13.4	13.7 ± 0.7
	9014	42737	0.081	0.093	13.2	
	9530	42523	0.085	0.100	14.5	
0.6%	12513	41780	0.080	0.088	17.9	19.1 ± 1.4
	12902	42737	0.081	0.093	18.8	
	13390	42523	0.084	0.100	20.6	
1.5%	20193	41780	0.079	0.088	29.2	30.2 ± 1.2
	20514	42737	0.081	0.093	30.0	
	20598	42523	0.084	0.100	31.5	
3.0%	26167	41780	0.082	0.088	36.7	39.4 ± 2.6
	27586	42737	0.082	0.093	39.6	
	27676	42523	0.085	0.100	41.9	
6.0%	29653	41780	0.088	0.088	38.4	40.9 ± 3.7
	30396	42737	0.092	0.093	39.1	
	30868	42523	0.088	0.100	45.1	
12.0%	27734	41780	0.082	0.088	38.5	40.6 ± 2.0
	28448	42737	0.083	0.093	40.6	
	29260	42523	0.089	0.100	42.6	
24.0%	22899	41780	0.083	0.088	31.7	33.0 ± 1.5
	23302	42737	0.084	0.093	32.7	
	24235	42523	0.090	0.100	34.7	

Table 7.7: Quantum yield calculation table for **CPC5** with increasing amounts of **CPC1**. Quinine sulfate in 0.5 M H_2SO_4 was used as a reference - ${\Phi_R}^{QS} = 0.546$.[145] Conditions: 10 °C/min cooling gradient, 3 µM oligomer, 10 mM sodium phosphate buffer, 10 mM NaCl and 20% EtOH.

	$Area_{sample}$	$Area_R$	$Absorption_S$	$Absorption_R$	Φ_F [%]	
0.0%	8492	41780	0.086	0.083	10.7	11.8 ± 1.1
	8892	42737	0.084	0.088	11.8	
	8619	42523	0.082	0.095	12.9	
0.3%	9846	41780	0.083	0.083	12.8	14.1 ± 1.4
	10655	42737	0.086	0.088	13.9	
	10419	42523	0.082	0.095	15.5	
0.6%	11629	41780	0.084	0.083	14.9	16.2 ± 1.5
	12323	42737	0.088	0.088	15.8	
	12101	42523	0.083	0.095	17.8	
1.5%	16345	41780	0.082	0.083	21.7	22.8 ± 1.7
	17143	42737	0.088	0.088	21.9	
	17021	42523	0.084	0.095	24.8	
3.0%	20756	41780	0.084	0.083	26.7	28.3 ± 1.8
	22749	42737	0.091	0.088	28.0	
	21382	42523	0.087	0.095	30.2	
6.0%	24710	41780	0.082	0.083	32.4	34.6 ± 2.5
	28108	42737	0.101	0.088	34.1	
	26293	42523	0.106	0.095	37.3	
9.0%	26828	41780	0.099	0.083	29.3	33.8 ± 4.3
	30195	42737	0.098	0.088	34.4	
	28438	42523	0.092	0.095	37.8	
30.0%	28681	41780	0.106	0.083	29.1	32.0 ± 2.7
	33252	42737	0.115	0.088	32.4	
	30630	42523	0.109	0.095	34.6	

Table 7.8: Quantum yield calculation table for **CPC5** with increasing amounts of **CPC1**. Quinine sulfate in 0.5 M H_2SO_4 was used as a reference - ${\Phi_R}^{QS} = 0.546$.[145] Conditions: 0.5 °C/min cooling gradient, 3 µM oligomer, 10 mM sodium phosphate buffer, 10 mM NaCl and 20% EtOH.

	$Area_{sample}$	$Area_R$	$Absorption_S$	$Absorption_R$	Φ_F [%]	
0.0%	7433	41780	0.089	0.083	9.0	10.0 ± 1.0
	6886	42737	0.077	0.088	10.0	
	6713	42523	0.074	0.095	11.1	
0.3%	12582	41780	0.089	0.083	15.3	17.6 ± 2.3
	12094	42737	0.077	0.088	17.5	
	12119	42523	0.075	0.095	19.9	
0.6%	15408	41780	0.091	0.083	18.4	20.5 ± 2.0
	15209	42737	0.083	0.088	20.5	
	14188	42523	0.078	0.095	22.4	
1.5%	20365	41780	0.089	0.083	24.6	27.9 ± 3.4
	20744	42737	0.084	0.088	27.7	
	20580	42523	0.081	0.095	31.3	
3.0%	22879	41780	0.088	0.083	28.0	31.7 ± 3.3
	24379	42737	0.083	0.088	32.7	
	22883	42523	0.081	0.095	34.5	
6.0%	24851	41780	0.086	0.083	31.4	35.1 ± 3.8
	27052	42737	0.086	0.088	35.1	
	25244	42523	0.080	0.095	38.9	
9.0%	25812	41780	0.098	0.083	28.6	33.8 ± 5.1
	28478	42737	0.094	0.088	34.0	
	26863	42523	0.085	0.095	38.8	
30.0%	24824	41780	0.102	0.083	26.4	29.0 ± 2.4
	28612	42737	0.107	0.088	29.8	
	25636	42523	0.102	0.095	30.9	

Table 7.9: Quantum yield calculation table for **CPC5** with increasing amounts of **CPC3**. Quinine sulfate in 0.5 M H_2SO_4 was used as a reference - ${\Phi_R}^{QS} = 0.546$.[145] Conditions: 10 °C/min cooling gradient, 3 µM oligomer, 10 mM sodium phosphate buffer, 10 mM NaCl and 20% EtOH.

	$Area_{sample}$	$Area_R$	$Absorption_S$	$Absorption_R$	Φ_F [%]	
0.0%	8400	41780	0.091	0.083	10.0	10.9 ± 1.7
	9979	42737	0.112	0.088	9.9	
	9766	42523	0.093	0.095	12.8	
0.3%	11986	41780	0.088	0.083	14.8	15.7 ± 1.9
	13972	42737	0.108	0.088	14.4	
	13865	42523	0.095	0.095	17.9	
0.6%	15046	41780	0.089	0.083	18.4	19.5 ± 1.8
	17838	42737	0.107	0.088	18.7	
	16931	42523	0.096	0.095	21.6	
1.5%	22338	41780	0.086	0.083	27.9	29.5 ± 2.7
	26456	42737	0.106	0.088	27.9	
	25994	42523	0.098	0.095	32.7	
3.0%	28215	41780	0.087	0.083	35.7	37.1 ± 3.0
	34216	42737	0.107	0.088	35.7	
	32476	42523	0.098	0.095	40.6	
6.0%	34376	41780	0.083	0.083	44.9	46.9 ± 4.1
	40789	42737	0.103	0.088	44.3	
	39657	42523	0.094	0.095	51.7	
9.0%	34598	41780	0.083	0.083	44.9	47.0 ± 3.8
	41325	42737	0.103	0.088	44.8	
	39696	42523	0.095	0.095	51.4	
30.0%	28585	41780	0.089	0.083	34.7	36.5 ± 3.0
	34409	42737	0.111	0.088	34.8	
	32521	42523	0.100	0.095	40.0	

Table 7.10: Quantum yield calculation table for **CPC5** with increasing amounts of **CPC3**. Quinine sulfate in 0.5 M H_2SO_4 was used as a reference - ${\Phi_R}^{QS} = 0.546$.[145] Conditions: 0.5 °C/min cooling gradient, 3 µM oligomer, 10 mM sodium phosphate buffer, 10 mM NaCl and 20% EtOH.

	$Area_{sample}$	$Area_R$	$Absorption_S$	$Absorption_R$	Φ_F [%]	
0.0%	7026	41780	0.080	0.083	9.5	10.4 ± 1.4
	8587	42737	0.100	0.088	9.6	
	8422	42523	0.086	0.095	12.0	
0.3%	7949	41780	0.080	0.083	10.7	11.3 ± 1.1
	9487	42737	0.100	0.088	10.6	
	9159	42523	0.089	0.095	12.6	
0.6%	9195	41780	0.086	0.083	11.6	11.9 ± 1.0
	10456	42737	0.105	0.088	11.2	
	10023	42523	0.094	0.095	13.0	
1.5%	10496	41780	0.086	0.083	13.1	12.8 ± 0.9
	10964	42737	0.104	0.088	11.8	
	10606	42523	0.096	0.095	13.6	
3.0%	12314	41780	0.085	0.083	15.6	14.9 ± 1.1
	12804	42737	0.105	0.088	13.7	
	12346	42523	0.097	0.095	15.5	
6.0%	15243	41780	0.084	0.083	19.6	18.2 ± 2.1
	14610	42737	0.104	0.088	15.8	
	14952	42523	0.096	0.095	19.1	
9.0%	14922	41780	0.087	0.083	18.6	17.4 ± 1.9
	14301	42737	0.105	0.088	15.2	
	14500	42523	0.097	0.095	18.3	
30.0%	26089	41780	0.088	0.083	32.1	29.8 ± 2.5
	27842	42737	0.115	0.088	27.2	
	25407	42523	0.103	0.095	30.3	

7.4.2 Fluorescence Spectra

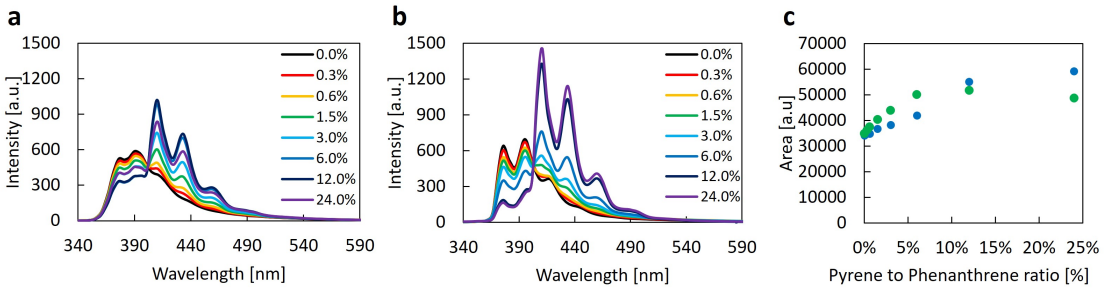

Figure 7.79: Fluorescence emission spectra of (a) **CPC4** and (b) **CPC5** in presence of increasing amounts of **CPC2** (0 to 24%) with a cooling rate of 10 °C/min. (c) Total area under the curves present in (a) in green and in (b) in blue. Conditions: 3 µM oligomer, 10 mM sodium phosphate buffer pH 7.2, 10 mM NaCl and EtOH (15 % for **CPC4** and 20 % for **CPC5**); $\lambda_{ex,\ \mathbf{CPC4}}$: 333 nm, $\lambda_{ex,\ \mathbf{CPC5}}$: 320 nm.

7.4.3 UV-Vis Absorption Spectra

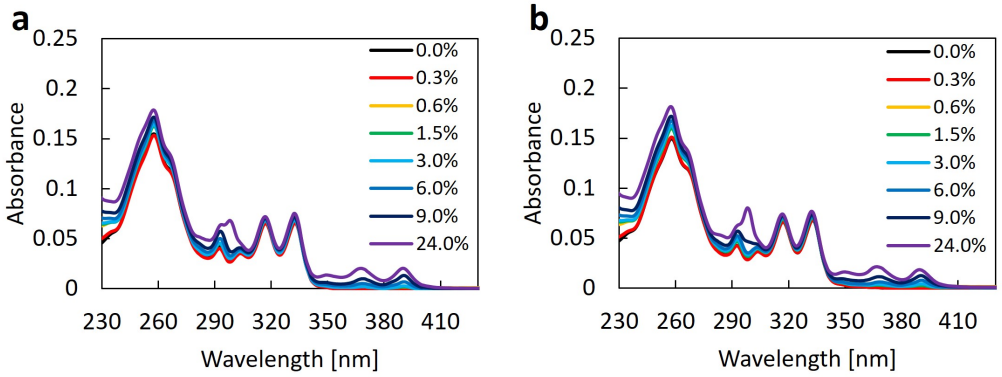

Figure 7.80: UV-Vis absorption spectra of **CPC4** at 20 °C with increasing amounts of **CPC1**. With temperature gradients of (a) 0.5 °C/min and (b) 10 °C/min. Conditions: 3 µM oligomer, 10 mM sodium phosphate buffer pH 7.2, 10 mM NaCl and 15% EtOH.

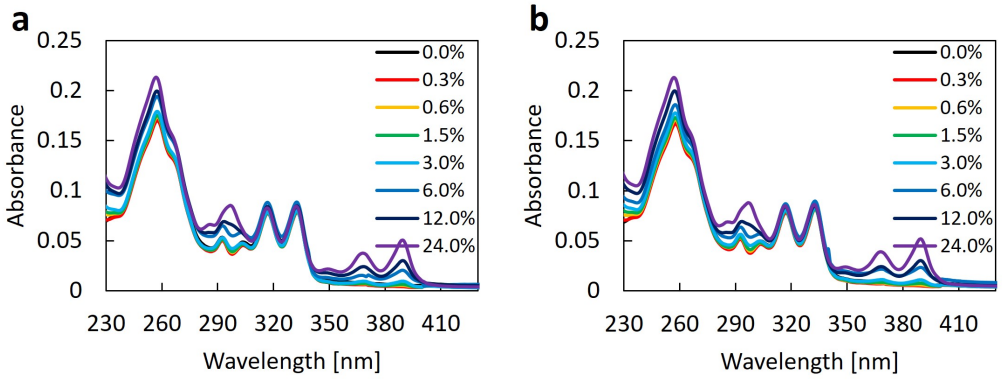

Figure 7.81: UV-Vis absorption spectra of **CPC4** at 20 °C with increasing amounts of **CPC3**. With temperature gradients of (a) 0.5 °C/min and (b) 10 °C/min. Conditions: 3 µM oligomer, 10 mM sodium phosphate buffer pH 7.2, 10 mM NaCl and 15% EtOH.

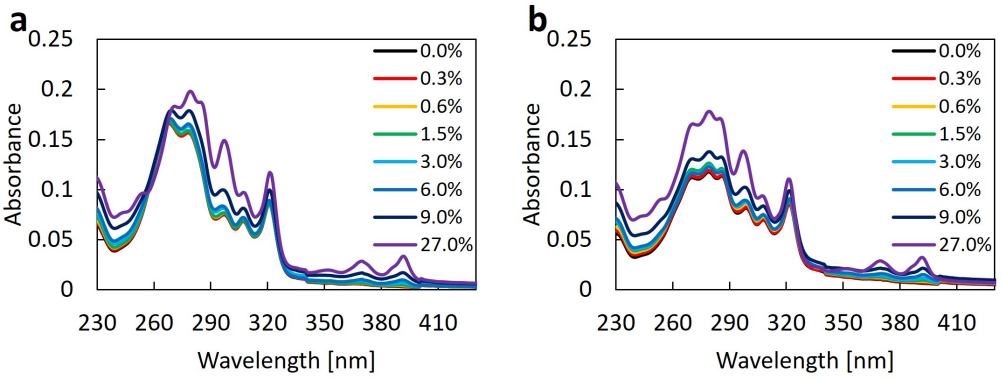

Figure 7.82: UV-Vis absorption spectra of **CPC5** at 20 °C with increasing amounts of **CPC1**. With temperature gradients of (a) 0.5 °C/min and (b) 10 °C/min. Conditions: 3 µM oligomer, 10 mM sodium phosphate buffer pH 7.2, 10 mM NaCl and 20% EtOH.

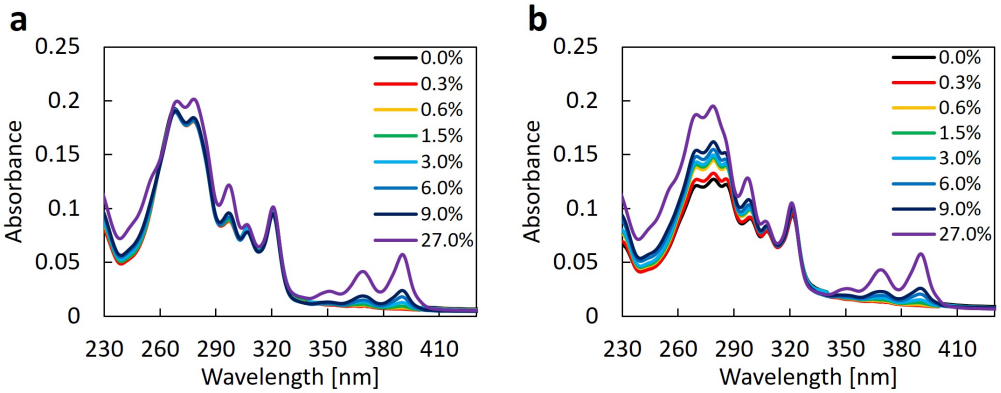

Figure 7.83: UV-Vis absorption spectra of **CPC5** at 20 °C with increasing amounts of **CPC3**. With temperature gradients of (a) 0.5 °C/min and (b) 10 °C/min. Conditions: 3 µM oligomer, 10 mM sodium phosphate buffer pH 7.2, 10 mM NaCl and 20% EtOH.

7.4.4 Control Experiments

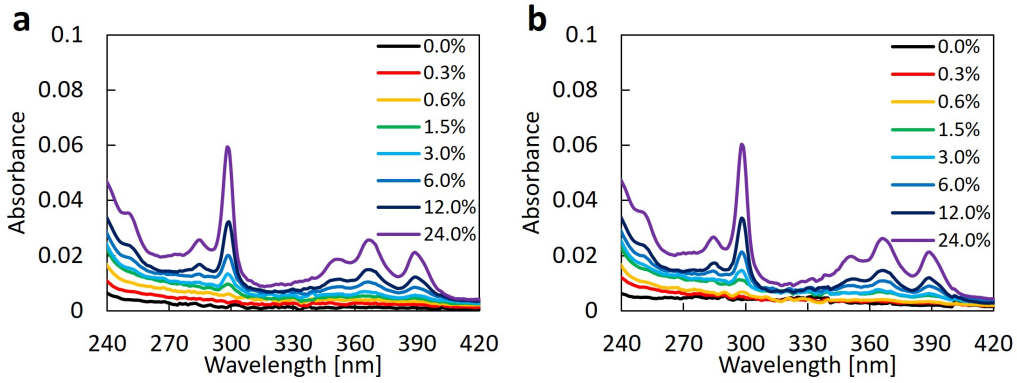

Figure 7.84: UV-Vis absorption spectra of buffer system at 20 °C with increasing amounts of **CPC1**. With temperature gradients of (a) 0.5 °C/min and (b) 10 °C/min. Conditions: no oligomer, 10 mM sodium phosphate buffer pH 7.2, 10 mM NaCl and 15% EtOH.

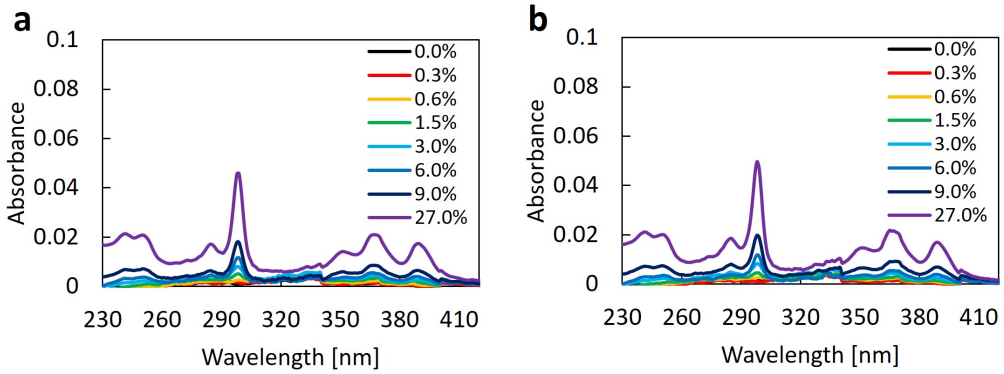

Figure 7.85: UV-Vis absorption spectra of buffer system at 20 °C with increasing amounts of **CPC1**. With temperature gradients of (a) 0.5 °C/min and (b) 10 °C/min. Conditions: no oligomer, 10 mM sodium phosphate buffer pH 7.2, 10 mM NaCl and 20% EtOH.

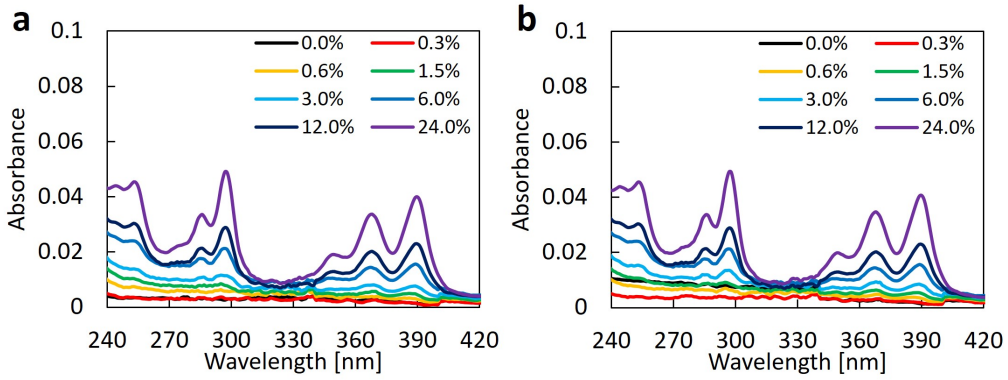

Figure 7.86: UV-Vis absorption spectra of buffer system at 20 °C with increasing amounts of **CPC3**. With temperature gradients of (a) 0.5 °C/min and (b) 10 °C/min. Conditions: no oligomer, 10 mM sodium phosphate buffer pH 7.2, 10 mM NaCl and 15% EtOH.

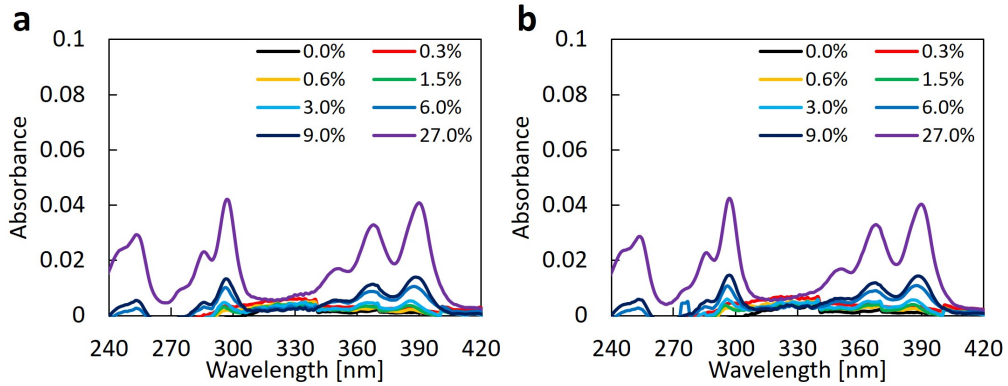

Figure 7.87: UV-Vis absorption spectra of buffer system at 20 °C with increasing amounts of **CPC3**. With temperature gradients of (a) 0.5 °C/min and (b) 10 °C/min. Conditions: no oligomer, 10 mM sodium phosphate buffer pH 7.2, 10 mM NaCl and 20% EtOH.

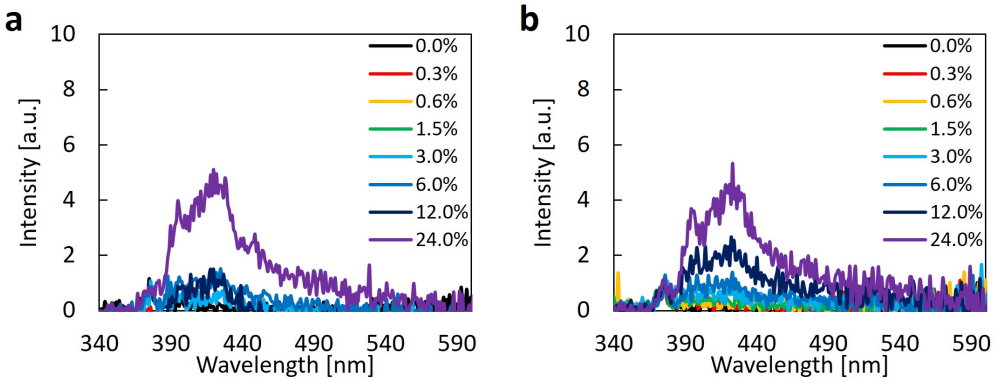

Figure 7.88: Fluorescence emission spectra of buffer system at 20 °C with increasing amounts of **CPC1**. With temperature gradients of (a) 0.5 °C/min and (b) 10 °C/min; λ_{ex}: 333 nm. Conditions: no oligomer, 10 mM sodium phosphate buffer pH 7.2, 10 mM NaCl and 15% EtOH.

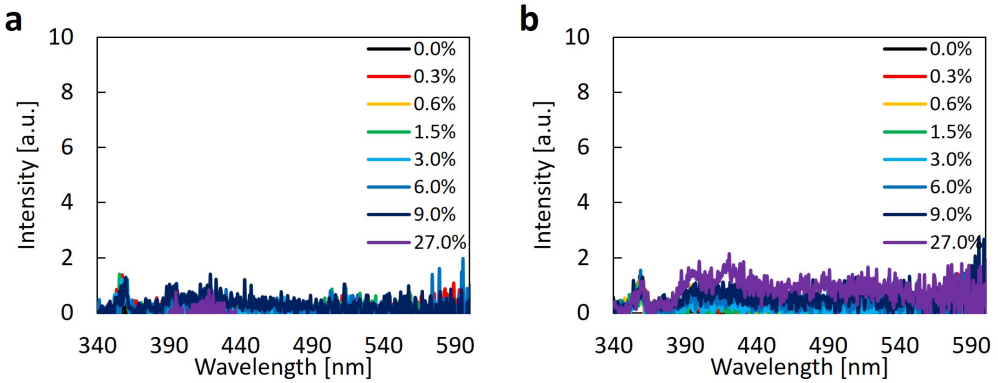

Figure 7.89: Fluorescence emission spectra of buffer system at 20 °C with increasing amounts of **CPC1**. With temperature gradients of (a) 0.5 °C/min and (b) 10 °C/min; λ_{ex}: 320 nm. Conditions: no oligomer, 10 mM sodium phosphate buffer pH 7.2, 10 mM NaCl and 20% EtOH.

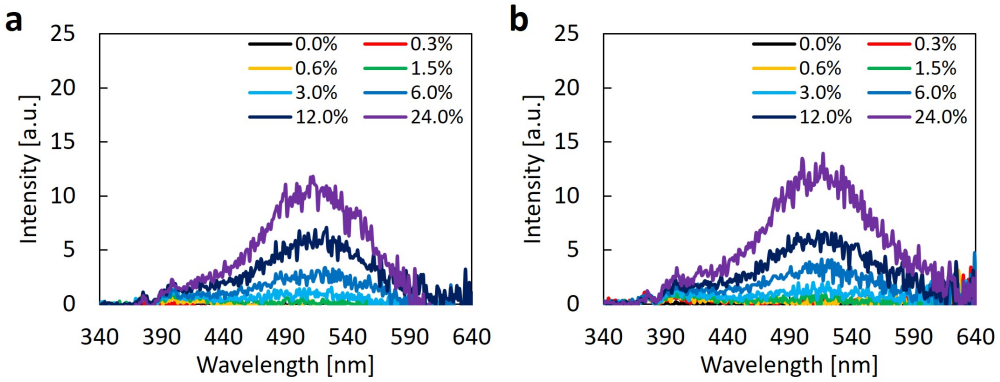

Figure 7.90: Fluorescence emission spectra of buffer system at 20 °C with increasing amounts of **CPC3**. With temperature gradients of (a) 0.5 °C/min and (b) 10 °C/min; λ_{ex}: 333 nm. Conditions: no oligomer, 10 mM sodium phosphate buffer pH 7.2, 10 mM NaCl and 15% EtOH.

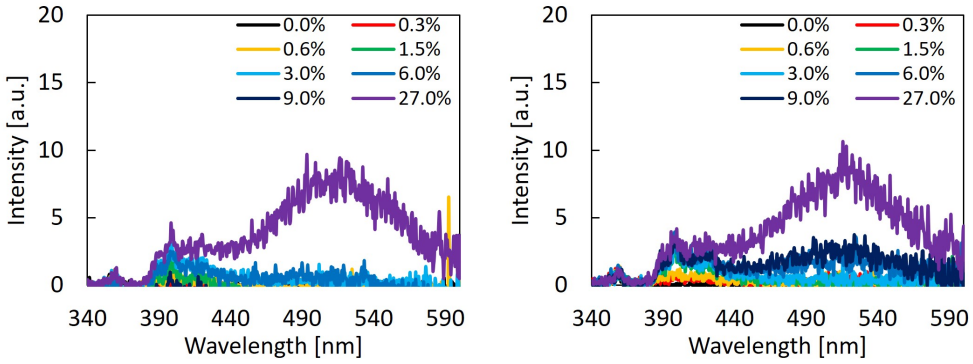

Figure 7.91: Fluorescence emission spectra of buffer system at 20 °C with increasing amounts of **CPC3**. With temperature gradients of (a) 0.5 °C/min and (b) 10 °C/min; λ_{ex}: 320 nm. Conditions: no oligomer, 10 mM sodium phosphate buffer pH 7.2, 10 mM NaCl and 20% EtOH.

Abbreviations

1,2-DCE	1,2-dichloroethane
ACN	Acetonitrile
AFM	Atomic force microscopy
ALHS	Artificial light-harvesting system
APTES	(3-aminopropyl)triethoxysilane
aq.	Aqueous
calcd	Calculated
CD	Cyclodextrin
CEP-Cl	2-cyanoethyl N,N-diisopropylchlorophosphoramidite
Con A	Concanavalin A
CPC	Cholane - pyrene - cholane or cholane - phenanthrene - cholane
CPT	Camptothecin
Cryo-EM	Cryogenic Electron Microscopy
DCM	Dicholoromethane
DIPEA	N,N-diisopropylethylamine
DMAP	4-dimethylaminopyridine
DMSO	Dimethyl sulfoxide
DMT	4,4'-dimethoxytrityl
DNA	Deoxyribonucleic acid
EET	Electronic energy transfer
ESI	Electronspray ionization
ETT	5-(Ethylthio)-1H-tetrazole
FRET	Förster resonance energy transfer
HBTU	3-[Bis(dimethylamino)methyliumyl]-3H-benzotriazol-1-oxide hexafluoro-phosphate
HFIP	1,1,1,3,3,3-hexafluoropropan-2-ol
HPLC	High performance liquid chromatography
HRMS	High resolution mass spectrometry
Hz	Herz
LCAA-CPG	Long-chain alkyl-amino controlled pore glass
LHC	light-harvesting complex

MS	Mass spectrometry
NMR	Nuclear magnetic resonance
NSI	Nano electronspray ionization
PAH	Polyaromatic hydrocarbon
PBS	Phosphate-buffered saline
PEG	Polyethylene glycol
ref	Reference
RT	Room temperature
RP-HPLC	Reverse phase high performance liquid chromatography
sat.	Saturated
SP	Supramolecular polymer
TCA	Trichloroacetic acid
TEA	Triethylamine
THF	Tetrahydrofuran
TLC	Thin layer chromatography
TMP	1,1,1-tris(hydroxymethyl)propane
UPy	Ureido-4-pyrimidinone
UV-vis	Ultraviolet-visible

Bibliography

[1] T. Aida, E. W. Meijer and S. I. Stupp, *Science*, 2012, **335**, 813–817.

[2] T. Aida and E. Meijer, *Isr. J. Chem.*, 2020, **60**, 33–47.

[3] L. Yang, X. Tan, Z. Wang and X. Zhang, *Chem. Rev.*, 2015, **115**, 7196–7239.

[4] S. P. Wijnands, E. W. Meijer and M. Merkx, *Bioconjugate Chem.*, 2019, **30**, 1905–1914.

[5] B. Rybtchinski, *ACS Nano*, 2011, **5**, 6791–6818.

[6] J. Xie, P. Yu, Z. Wang and J. Li, *Biomacromolecules*, 2022, **23**, 641–660.

[7] M.-H. Wei, B. Li, R. L. A. David, S. C. Jones, V. Sarohia, J. A. Schmitigal and J. A. Kornfield, *Science*, 2015, **350**, 72–75.

[8] S. Sivakova, D. A. Bohnsack, M. E. Mackay, P. Suwanmala and S. J. Rowan, *J. Am. Chem. Soc.*, 2005, **127**, 18202–18211.

[9] R. P. Sijbesma, F. H. Beijer, L. Brunsveld, B. J. B. Folmer, J. H. K. K. Hirschberg, R. F. M. Lange, J. K. L. Lowe and E. W. Meijer, *Science*, 1997, **278**, 1601–1604.

[10] L. Wang and Q. Li, *Chem. Soc. Rev.*, 2018, **47**, 1044–1097.

[11] Y. Wang, Z.-g. Zheng, H. K. Bisoyi, K. G. Gutierrez-Cuevas, L. Wang, R. S. Zola and Q. Li, *Mater. Horiz.*, 2016, **3**, 442–446.

[12] H. Wang, H. K. Bisoyi, L. Wang, A. M. Urbas, T. J. Bunning and Q. Li, *Angew. Chem., Int. Ed. Engl.*, 2018, **57**, 1627–1631.

[13] X.-M. Chen, S. Zhang, X. Chen and Q. Li, *ChemPhotoChem*, 2022, **6**, e202100256.

[14] *Encyclopedia of Materials: Science and Technology*, ed. K. H. J. Buschow, Elsevier, Amsterdam, 2001, vol. 4.

[15] *Encyclopedia of Physical Science and Technology*, ed. R. A. Meyers, Academic Press, San Diego, Third edition edn., 2001.

[16] X.-M. Chen, X.-F. Hou, H. K. Bisoyi, W.-J. Feng, Q. Cao, S. Huang, H. Yang, D. Chen and Q. Li, *Nat. Commun.*, 2021, **12**, 4993.

[17] Y. He, S. Lin, J. Guo and Q. Li, *Aggregate*, 2021, **2**, e141.

[18] H. Wang, H. K. Bisoyi, X. Zhang, F. Hassan and Q. Li, *Chem. Eur. J.*, 2022, **28**, e202103906.

[19] M. Yang, Y. Xu, X. Zhang, H. K. Bisoyi, P. Xue, Y. Yang, X. Yang, C. Valenzuela, Y. Chen, L. Wang, W. Feng and Q. Li, *Adv. Funct. Mater.*, 2022, **32**, 2201884.

[20] D. W. R. Balkenende, C. A. Monnier, G. L. Fiore and C. Weder, *Nat. Commun.*, 2016, **7**, 10995.

[21] Z. Chen, M. H.-Y. Chan and V. W.-W. Yam, *J. Am. Chem. Soc.*, 2020, **142**, 16471–16478.

[22] C. Kahlfuss, T. Gibaud, S. Denis-Quanquin, S. Chowdhury, G. Royal, F. Chevallier, E. Saint-Aman and C. Bucher, *Chem. Eur. J.*, 2018, **24**, 13009–13019.

[23] S. Chowdhury, Q. Reynard-Feytis, C. Roizard, D. Frath, F. Chevallier, C. Bucher and T. Gibaud, *J. Phys. Chem. B*, 2021, **125**, 12063–12071.

[24] S. Theis, A. Iturmendi, C. Gorsche, M. Orthofer, M. Lunzer, S. Baudis, A. Ovsianikov, R. Liska, U. Monkowius and I. Teasdale, *Angew. Chem., Int. Ed.*, 2017, **56**, 15857–15860.

[25] G. Weng, S. Thanneeru and J. He, *Adv. Mater.*, 2018, **30**, 1706526.

[26] C. Kulkarni, P. A. Korevaar, K. K. Bejagam, A. R. A. Palmans, E. W. Meijer and S. J. George, *J. Am. Chem. Soc.*, 2017, **139**, 13867–13875.

[27] Y.-K. Tian, Y.-F. Han, Z.-S. Yang and F. Wang, *Macromolecules*, 2016, **49**, 6455–6461.

[28] B. Adelizzi, P. Chidchob, N. Tanaka, B. A. G. Lamers, S. C. J. Meskers, S. Ogi, A. R. A. Palmans, S. Yamaguchi and E. W. Meijer, *J. Am. Chem. Soc.*, 2020, **142**, 16681–16689.

[29] W. Wagner, M. Wehner, V. Stepanenko and F. Würthner, *J. Am. Chem. Soc.*, 2019, **141**, 12044–12054.

[30] T. P. J. Knowles, M. Vendruscolo and C. M. Dobson, *Nat. Rev. Mol. Cell Biol.*, 2014, **15**, 384–396.

[31] M. D. Shoulders and R. T. Raines, *Annu. Rev. Biochem.*, 2009, **78**, 929–958.

[32] T. D. Pollard and G. G. Borisy, *Cell*, 2003, **112**, 453–465.

[33] E. Krieg, M. M. C. Bastings, P. Besenius and B. Rybtchinski, *Chem. Rev.*, 2016, **116**, 2414–2477.

[34] O. J. G. M. Goor, S. I. S. Hendrikse, P. Y. W. Dankers and E. W. Meijer, *Chem. Soc. Rev.*, 2017, **46**, 6621–6637.

[35] J. Szejtli, *Chem. Rev.*, 1998, **98**, 1743–1754.

[36] P. Evenou, J. Rossignol, G. Pembouong, A. Gothland, D. Colesnic, R. Barbeyron, S. Rudiuk, A.-G. Marcelin, M. Ménand, D. Baigl, V. Calvez, L. Bouteiller and M. Sollogoub, *Angew. Chem., Int. Ed.*, 2018, **57**, 7753–7758.

[37] C. D. Gutsche, *Acc. Chem. Res.*, 1983, **16**, 161–170.

[38] R. Castellano, D. Rudkevich and J. Rebek Jr., *Proc. Natl. Acad. Sci.*, 1997, **94**, 7132–7137.

[39] C. Xiong and R. Sun, *Chin. J. Chem.*, 2017, **35**, 1669–1672.

[40] G. Yu, X. Zhao, J. Zhou, Z. Mao, X. Huang, Z. Wang, B. Hua, Y. Liu, F. Zhang, Z. He, O. Jacobson, C. Gao, W. Wang, C. Yu, X. Zhu, F. Huang and X. Chen, *J. Am. Chem. Soc.*, 2018, **140**, 8005–8019.

[41] C. D. Bösch, S. M. Langenegger and R. Häner, *Angew. Chem., Int. Ed.*, 2016, **55**, 9961–9964.

[42] J. Thiede, S. Rothenbühler, I. Iacovache, S. M. Langenegger, B. Zuber and R. Häner, *Org. Biomol. Chem.*, 2023, **21**, 7908–7912.

[43] C. D. Bösch, J. Jevric, N. Bürki, M. Probst, S. M. Langenegger and R. Häner, *Bioconjugate Chem.*, 2018, **29**, 1505–1509.

[44] L. Markova, M. Probst and R. Häner, *RSC Adv.*, 2020, **10**, 44841–44845.

[45] S. Rothenbühler, I. Iacovache, S. M. Langenegger, B. Zuber and R. Häner, *Nanoscale*, 2020, **12**, 21118–21123.

[46] Y. Vyborna, M. Vybornyi and R. Häner, *J. Am. Chem. Soc.*, 2015, **137**, 14051–14054.

[47] S. Rothenbühler, I. Iacovache, S. M. Langenegger, B. Zuber and R. Häner, *Bioconjugate Chem.*, 2023, **34**, 70–77.

[48] A. L. Nussbaumer, D. Studer, V. L. Malinovskii and R. Häner, *Angew. Chem., Int. Ed.*, 2011, **50**, 5490–5494.

[49] M. Vybornyi, A. V. Rudnev, S. M. Langenegger, T. Wandlowski, G. Calzaferri and R. Häner, *Angew. Chem., Int. Ed.*, 2013, **52**, 11488–11493.

[50] M. Vybornyi, Y. Vyborna and R. Häner, *ChemistryOpen*, 2017, **6**, 488–491.

[51] C. B. Winiger, S. Li, G. R. Kumar, S. M. Langenegger and R. Häner, *Angew. Chem., Int. Ed.*, 2014, **53**, 13609–13613.

[52] O. Vybornyi, S.-X. Liu and R. Häner, *Angew. Chem., Int. Ed.*, 2021, **60**, 25872–25877.

[53] M. Vybornyi, A. Rudnev and R. Häner, *Chem. Mater.*, 2015, **27**, 1426–1431.

[54] M. Hartlieb, E. D. H. Mansfield and S. Perrier, *Polym. Chem.*, 2020, **11**, 1083–1110.

[55] B. Adelizzi, N. J. Van Zee, L. N. J. de Windt, A. R. A. Palmans and E. W. Meijer, *J. Am. Chem. Soc.*, 2019, **141**, 6110–6121.

[56] T. F. A. De Greef, M. M. J. Smulders, M. Wolffs, A. P. H. J. Schenning, R. P. Sijbesma and E. W. Meijer, *Chem. Rev.*, 2009, **109**, 5687–5754.

[57] *Supramolecular Polymer Chemistry*, ed. A. Harada, Wiley-VCH Verlag GmbH & Co. KGaA, Weinheim, Chichester, First edition edn., 2011.

[58] Y. Wang, X. Liu, R. Wang, J. Zhang, Y. Bai, Q. Chen, P. Guo, Z. Jing, Y. Wang, M. Cai, F. Guo and F. Zhou, *Tribol. Int.*, 2024, **191**, 109148.

[59] M. M. J. Smulders, M. M. L. Nieuwenhuizen, T. F. A. de Greef, P. van der Schoot, A. P. H. J. Schenning and E. W. Meijer, *Chem. Eur. J.*, 2010, **16**, 362–367.

[60] S. Datta, M. L. Saha and P. J. Stang, *Acc. Chem. Res.*, 2018, **51**, 2047–2063.

[61] N. Krishnan, M. Golla, H. V. P. Thelu, S. K. Albert, S. Atchimnaidu, D. Perumal and R. Varghese, *Nanoscale*, 2018, **10**, 17174–17181.

[62] M. A. Aleman Garcia, E. Magdalena Estirado, L.-G. Milroy and L. Brunsveld, *Angew. Chem., Int. Ed.*, 2018, **57**, 4976–4980.

[63] S. P. W. Wijnands, W. Engelen, R. P. M. Lafleur, E. W. Meijer and M. Merkx, *Nat. Commun.*, 2018, **9**, 65.

[64] T. A. Ngo, E. Nakata, M. Saimura and T. Morii, *J. Am. Chem. Soc.*, 2016, **138**, 3012–3021.

[65] H. Wang, Z. Feng and B. Xu, *Chem. Soc. Rev.*, 2017, **46**, 2421–2436.

[66] J. Zhou, J. Li, X. Du and B. Xu, *Biomaterials*, 2017, **129**, 1–27.

[67] F. Ishiwari, Y. Shoji and T. Fukushima, *Chem. Sci.*, 2018, **9**, 2028–2041.

[68] C. M. Niemeyer, *Angew. Chem., Int. Ed.*, 2010, **49**, 1200–1216.

[69] J. Müller and C. M. Niemeyer, *Biochem. Biophys. Res. Commun.*, 2008, **377**, 62–67.

[70] O. I. Wilner, Y. Weizmann, R. Gill, O. Lioubashevski, R. Freeman and I. Willner, *Nat. Nanotechnol.*, 2009, **4**, 249–254.

[71] C. Lin and H. Yan, *Nat. Nanotechnol.*, 2009, **4**, 211–212.

[72] M. Madsen and K. V. Gothelf, *Chem. Rev.*, 2019, **119**, 6384–6458.

[73] N. Z. Fantoni, A. H. El-Sagheer and T. Brown, *Chem. Rev.*, 2021, **121**, 7122–7154.

[74] K. Yamamoto and S. Kawanishi, *J. Biol. Chem.*, 1991, **266**, 1509–1515.

[75] Q. Wang, T. R. Chan, R. Hilgraf, V. V. Fokin, K. B. Sharpless and M. G. Finn, *J. Am. Chem. Soc.*, 2003, **125**, 3192–3193.

[76] S. I. Presolski, V. P. Hong and M. Finn, *Curr. Protoc. Chem. Biol.*, 2011, **3**, 153–162.

[77] M. C. Linder, *Mutat. Res., Fundam. Mol. Mech. Mutagen.*, 2012, **733**, 83–91.

[78] Y. Huang, J. Huang, Q. Xie and S. Yao, *Prog. Chem.*, 2008, **20**, 942–950.

[79] S. Cecioni, A. Imberty and S. Vidal, *Chem. Rev.*, 2015, **115**, 525–561.

[80] L. Johannes, R. Jacob and H. Leffler, *J. Cell Biol.*, 2018, **131**, jcs208884.

[81] M. Delbianco, P. Bharate, S. Varela-Aramburu and P. H. Seeberger, *Chem. Rev.*, 2016, **116**, 1693–1752.

[82] K. Petkau-Milroy and L. Brunsveld, *Org. Biomol. Chem.*, 2013, **11**, 219–232.

[83] Y.-b. Lim, K.-S. Moon and M. Lee, *Chem. Soc. Rev.*, 2009, **38**, 925–934.

[84] A. Olaya-Castro and G. D. Scholes, *Int. Rev. Phys. Chem.*, 2011, **30**, 49–77.

[85] X.-M. Chen, X. Chen, X.-F. Hou, S. Zhang, D. Chen and Q. Li, *Nanoscale Adv.*, 2023, **5**, 1830–1852.

[86] R. Croce and H. van Amerongen, *Nat. Chem. Biol.*, 2014, **10**, 492–501.

[87] K. V. Rao, K. K. R. Datta, M. Eswaramoorthy and S. J. George, *Chem. Eur. J.*, 2012, **18**, 2184–2194.

[88] Y.-X. Hu, P.-P. Jia, C.-W. Zhang, X.-D. Xu, Y. Niu, X. Zhao, Q. Xu, L. Xu and H.-B. Yang, *Org. Chem. Front.*, 2021, **8**, 5250–5257.

[89] C.-L. Sun, H.-Q. Peng, L.-Y. Niu, Y.-Z. Chen, L.-Z. Wu, C.-H. Tung and Q.-Z. Yang, *Chem. Commun.*, 2018, **54**, 1117–1120.

[90] X.-L. Li, S. Yu, M.-N. Chen, M. Jiang, R.-Z. Wang and L.-B. Xing, *J. Photochem. Photobiol., A*, 2021, **410**, 113182.

[91] J. Jiao, G. Sun, J. Zhang, C. Lin, J. Jiang and L. Wang, *Chem. Eur. J.*, 2021, **27**, 16601–16605.

[92] J.-J. Li, Y. Chen, J. Yu, N. Cheng and Y. Liu, *Adv. Mater.*, 2017, **29**, 1–5.

[93] S. Guo, Y. Song, Y. He, X.-Y. Hu and L. Wang, *Angew. Chem., Int. Ed. Engl.*, 2018, **57**, 3163–3167.

[94] P. K. Dutta, R. Varghese, J. Nangreave, S. Lin, H. Yan and Y. Liu, *J. Am. Chem. Soc.*, 2011, **133**, 11985–11993.

[95] M. Kownacki, S. M. Langenegger, S.-X. Liu and R. Häner, *Angew. Chem., Int. Ed.*, 2019, **58**, 751–755.

[96] Q. Song, S. Goia, J. Yang, S. C. L. Hall, M. Staniforth, V. G. Stavros and S. Perrier, *J. Am. Chem. Soc.*, 2021, **143**, 382–389.

[97] X. Fan, C. P. Teng, J. C. C. Yeo, Z. Li, T. Wang, H. Chen, L. Jiang, X. Hou, C. He and J. Liu, *Macromol. Rapid Commun.*, 2021, **42**, 2000716.

[98] X. Zhang, M. A. Ballem, M. Ahrén, A. Suska, P. Bergman and K. Uvdal, *J. Am. Chem. Soc.*, 2010, **132**, 10391–10397.

[99] Z. Cao, A. Hao and P. Xing, *Nanoscale*, 2021, **13**, 700–707.

[100] J.-J. Li, H.-Y. Zhang, X.-Y. Dai, Z.-X. Liu and Y. Liu, *Chem. Commun.*, 2020, **56**, 5949–5952.

[101] K. Zhong, S. Lu, W. Guo, J. Su, S. Sun, J. Hai, F. Chen, A. Wang and B. Wang, *J. Mater. Chem. A*, 2021, **9**, 10180–10185.

[102] R. van Grondelle, *Biochim. Biophys. Acta, Rev. Bioenerg.*, 1985, **811**, 147–195.

[103] T. Förster, *Ann. Phys.*, 1948, **437**, 55–75.

[104] H. Wang, B. Yue, Z. Xie, B. Gao, Y. Xu, L. Liu, H. Sun and Y. Ma, *Phys. Chem. Chem. Phys.*, 2013, **15**, 3527–3534.

[105] A. Hillisch, M. Lorenz and S. Diekmann, *Curr. Opin. Struct. Biol.*, 2001, **11**, 201–207.

[106] B. W. van der Meer, in *FRET – Förster Resonance Energy Transfer*, John Wiley & Sons, Ltd, 2013, pp. 23–62.

[107] E. Collini, *Chem. Soc. Rev.*, 2013, **42**, 4932–4947.

[108] G. S. Engel, T. R. Calhoun, E. L. Read, T.-K. Ahn, T. Mančal, Y.-C. Cheng, R. E. Blankenship and G. R. Fleming, *Nat.*, 2007, **446**, 782–786.

[109] E. Collini and G. D. Scholes, *Science*, 2009, **323**, 369–373.

[110] J. Strümpfer, M. Şener and K. Schulten, *J. Phys. Chem. Lett.*, 2012, **3**, 536–542.

[111] M. H. Caruthers, *Science*, 1985, **230**, 281–285.

[112] M. H. Caruthers, A. D. Barone, S. L. Beaucage, D. R. Dodds, E. F. Fisher, L. J. McBride, M. Matteucci, Z. Stabinsky and J. Y. Tang, in *Methods in Enzymology*, Academic Press, 1987, vol. 154 of Recombinant DNA Part E, pp. 287–313.

[113] M. H. Caruthers, *Acc. Chem. Res.*, 1991, **24**, 278–284.

[114] S. L. Beaucage and R. P. Iyer, *Tetrahedron*, 1992, **48**, 2223–2311.

[115] J. Goodchild, *Bioconjugate Chem.*, 1990, **1**, 165–187.

[116] *Nucleic Acids in Chemistry and Biology*, ed. G. M. Blackburn, J. M. Gait, D. Loakes and M. Williams, Royal Society of Chemistry, Cambridge, Third edition edn., 2006.

[117] D. v. d. Zwaag and E. W. Meijer, *Science*, 2015, **349**, 1056–1057.

[118] D. Straßburger, N. Stergiou, M. Urschbach, H. Yurugi, D. Spitzer, D. Schollmeyer, E. Schmitt and P. Besenius, *ChemBioChem*, 2018, **19**, 912–916.

[119] G. Picca, *Ph.D. thesis*, University of Bern, Bern, 2020.

[120] J. Jevric, S. M. Langenegger and R. Häner, *Eur. J. Org. Chem.*, 2020, **2020**, 4677–4680.

[121] T. M. Vandhana, J.-L. Reyre, D. Sushmaa, J.-G. Berrin, B. Bissaro and J. Madhuprakash, *New Phytol.*, 2022, **233**, 2380–2396.

[122] L. Su, Y. Feng, K. Wei, X. Xu, R. Liu and G. Chen, *Chem. Rev.*, 2021, **121**, 10950–11029.

[123] A. P. Dias, S. da Silva Santos, J. V. da Silva, R. Parise-Filho, E. Igne Ferreira, O. E. Seoud and J. Giarolla, *Int. J. Pharm.*, 2020, **573**, 118814.

[124] K. V. Mariño, A. J. Cagnoni, D. O. Croci and G. A. Rabinovich, *Nat. Rev. Drug Discovery*, 2023, **22**, 295–316.

[125] N. Cakir, G. Hizal and C. R. Becer, *Polym. Chem.*, 2015, **6**, 6623–6631.

[126] J. Hu, P. Wei, P. H. Seeberger and J. Yin, *Chem. Asian J.*, 2018, **13**, 3448–3459.

[127] A. Samanta, M. C. A. Stuart and B. J. Ravoo, *J. Am. Chem. Soc.*, 2012, **134**, 19909–19914.

[128] K. D. Hardman and C. F. Ainsworth, *Biochemistry*, 1972, **11**, 4910–4919.

[129] Z. Derewenda, J. Yariv, J. Helliwell, A. Kalb, E. Dodson, M. Papiz, T. Wan and J. Campbell, *EMBO J.*, 1989, **8**, 2189–2193.

[130] M. Vybornyi, Y. B.-C. Hechevarria, M. Glauser, A. V. Rudnev and R. Häner, *Chem. Commun.*, 2015, **51**, 16191–16193.

[131] J. Jevric, S. M. Langenegger and R. Häner, *Chem. Commun.*, 2021, **57**, 6648–6651.

[132] P. A. Korevaar, S. J. George, A. J. Markvoort, M. M. J. Smulders, P. A. J. Hilbers, A. P. H. J. Schenning, T. F. A. De Greef and E. W. Meijer, *Nat.*, 2012, **481**, 492–496.

[133] D. Zhao and J. S. Moore, *Org. Biomol. Chem.*, 2003, **1**, 3471–3491.

[134] H. C. Hsu, M.-T. Tsai, Y. Dyakov and C.-K. Ni, *Phys. Chem. Chem. Phys.*, 2011, **13**, 8313–8321.

[135] M. E. Walther and O. S. Wenger, *Dalton Trans.*, 2008, 6311–6318.

[136] J. R. Darwent, W. Dong, C. D. Flint and N. W. Sharpe, *J. Chem. Soc., Faraday Trans.*, 1993, **89**, 873–880.

[137] M. Lard, S. H. Kim, S. Lin, P. Bhattacharya, P. C. Ke and M. H. Lamm, *Phys. Chem. Chem. Phys.*, 2010, **12**, 9285–9291.

[138] H. Bittermann, D. Siegemund, V. L. Malinovskii and R. Häner, *J. Am. Chem. Soc.*, 2008, **130**, 15285–15287.

[139] M. Linkert, C. T. Rueden, C. Allan, J.-M. Burel, W. Moore, A. Patterson, B. Loranger, J. Moore, C. Neves, D. MacDonald, A. Tarkowska, C. Sticco, E. Hill, M. Rossner, K. W. Eliceiri and J. R. Swedlow, *J. Cell Biol.*, 2010, **189**, 777–782.

[140] J. Schindelin, I. Arganda-Carreras, E. Frise, V. Kaynig, M. Longair, T. Pietzsch, S. Preibisch, C. Rueden, S. Saalfeld, B. Schmid, J.-Y. Tinevez, D. J. White, V. Hartenstein, K. Eliceiri, P. Tomancak and A. Cardona, *Nat. Methods*, 2012, **9**, 676–682.

[141] G. A. Elsayed and G.-J. Boons, *Synlett*, 2003, **2003**, 1373–1375.

[142] J. B. H. Tok, W. Wong and N. Baboolal, *Bioorg. Med. Chem. Lett.*, 2002, **12**, 365–370.

[143] S. J. Kim, E.-K. Bang, H. J. Kwon, J. S. Shim and B. H. Kim, *ChemBioChem*, 2004, **5**, 1517–1522.

[144] K. Ishihara, H. Kurihara and H. Yamamoto, *J. Org. Chem.*, 1993, **58**, 3791–3793.

[145] W. H. Melhuish, *J. Phys. Chem.*, 1961, **65**, 229–235.

Declaration of consent

on the basis of Article 18 of the PromR Phil.-nat. 19

Name/First Name: Ehret Edouard

Registration Number: 13-825-781

Study program: DCBP Graduate Program

Bachelor ☐ Master ☐ Dissertation ☑

Title of the thesis: Self-assembly of amphiphilic oligophosphates into supramolecular polymers

Supervisor: Prof. Dr. Robert Häner

I declare herewith that this thesis is my own work and that I have not used any sources other than those stated. I have indicated the adoption of quotations as well as thoughts taken from other authors as such in the thesis. I am aware that the Senate pursuant to Article 36 paragraph 1 litera r of the University Act of September 5th, 1996 and Article 69 of the University Statute of June 7th, 2011 is authorized to revoke the doctoral degree awarded on the basis of this thesis.
For the purposes of evaluation and verification of compliance with the declaration of originality and the regulations governing plagiarism, I hereby grant the University of Bern the right to process my personal data and to perform the acts of use this requires, in particular, to reproduce the written thesis and to store it permanently in a database, and to use said database, or to make said database available, to enable comparison with theses submitted by others.

Bern, 23rd of July

Place/Date

Ehret

Signature

Digitally signed by Ehret
Date: 2024.07.23 12:14:40 +02'00'